



HAL
open science

Microstructural optimization of Solid Oxide Cells: a coupled stochastic geometrical and electrochemical modeling approach applied to LSCF-CGO electrode

Hamza Moussaoui

► **To cite this version:**

Hamza Moussaoui. Microstructural optimization of Solid Oxide Cells: a coupled stochastic geometrical and electrochemical modeling approach applied to LSCF-CGO electrode. Physics [physics]. Université Grenoble Alpes, 2019. English. NNT : 2019GREAI028 . tel-02186032

HAL Id: tel-02186032

<https://theses.hal.science/tel-02186032>

Submitted on 17 Jul 2019

HAL is a multi-disciplinary open access archive for the deposit and dissemination of scientific research documents, whether they are published or not. The documents may come from teaching and research institutions in France or abroad, or from public or private research centers.

L'archive ouverte pluridisciplinaire **HAL**, est destinée au dépôt et à la diffusion de documents scientifiques de niveau recherche, publiés ou non, émanant des établissements d'enseignement et de recherche français ou étrangers, des laboratoires publics ou privés.

THÈSE

Pour obtenir le grade de

DOCTEUR DE LA COMMUNAUTE UNIVERSITE GRENOBLE ALPES

Spécialité : **Matériaux, Mécanique, Génie civil, Electrochimie**

Arrêté ministériel : 25 mai 2016

Présentée par

« **Hamza MOUSSAOUI** »

Thèse co-dirigée par **Jérôme LAURENCIN** et **Johan DEBAYLE**

préparée au sein du **Laboratoire CEA-LITEN** et de l'**École des mines de Saint-Etienne**
dans l'**École Doctorale I-MEP²**

Microstructural Optimization of Solid Oxide Cells: A coupled stochastic geometrical and electrochemical modeling approach applied to LSCF-CGO electrode

Thèse soutenue publiquement le « **29 avril 2019** »,
devant le jury composé de :

Mme. Élisabeth SIEBERT

Directeur de recherche, LEPMI Grenoble, Présidente du Jury

M. Jan VAN HERLE

Professeur, EPFL Lausanne, Suisse, Rapporteur

M. Jean-Marc BASSAT

Directeur de recherche, ICMCB Bordeaux, Rapporteur

M. Volker SCHMIDT

Professeur, Université d'Ulm, Allemagne, Examineur

M. Jérôme LAURENCIN

Docteur, CEA-LITEN Grenoble, Directeur de thèse

M. Johan DEBAYLE

Professeur, École des mines de Saint-Etienne, Co-directeur de thèse

M. Gérard DELETTE

Ingénieur de recherche, CEA-LITEN Grenoble, Co-encadrant de thèse

M. Yann GAVET

Docteur, École des mines de Saint-Etienne, Co-encadrant de thèse



Remerciements

Ces travaux se sont déroulés au sein du Laboratoire des Technologies d'Hydrogène (LTH) du commissariat à l'énergie atomique et aux énergies alternatives (CEA) à Grenoble et ont été co-dirigés par le centre SPIN de l'École des Mines de Saint-Etienne (EMSE). Je remercie à ce titre **Julie Mougin** de m'avoir permis de réaliser ce travail de thèse au sein de son laboratoire et Monsieur le Haut-Commissaire du CEA, **Yves Bréchet** d'avoir financé ma thèse.

Je remercie vivement **Jan Van Herle**, professeur à l'EPFL Lausanne et **Jean-Marc Bassat**, directeur de recherche à l'ICMCB Bordeaux d'avoir accepté d'être rapporteurs de ce travail. Je tiens également à remercier **Volker Schmidt**, professeur à l'université d'Ulm, d'avoir participé au jury en tant qu'examinateur et **Élisabeth Siebert**, directrice de recherche au LEPMI de Grenoble, d'avoir présidé le jury. Enfin, je tiens à remercier tous les membres du jury d'avoir fait le déplacement jusqu'à Grenoble pour assister à ma soutenance et d'avoir enrichi les discussions par leurs interventions intéressantes.

Je tiens à exprimer ma profonde reconnaissance envers **Jérôme Laurencin**, directeur de thèse du CEA, de m'avoir fait confiance et de son accompagnement au quotidien. J'adresse également mes chaleureux remerciements à **Johan Debayle**, codirecteur de thèse de l'EMSE, pour sa disponibilité, ses conseils précieux, et de m'avoir permis d'avoir une belle expérience d'enseignement à l'EMSE. Enfin, je remercie **Gérard Delette** et **Yann Gavet**, encadrants de thèse du CEA et de l'EMSE respectivement, de m'avoir guidé à atteindre efficacement mes objectifs. C'était un plaisir de partager cette aventure qu'est la thèse avec vous.

Ce travail a été rendu possible grâce à de nombreuses collaborations. Je tiens à remercier à ce titre **Maxime Hubert** et **Peter Cloetens** du synchrotron de Grenoble (ESRF) de m'avoir donné la chance de participer à des travaux de reconstructions tomographiques. Je remercie également **Julien Vulliet**, ingénieur de recherche au CEA le Ripault, de tous les échanges pour fabriquer les microstructures optimales tant convoités. Je remercie **Florence Lefebvre-Joud**, directrice scientifique du Liten, pour ses encouragements et ses conseils édifiants. Enfin, je remercie **Elisa Effori**, **Rakesh Sharma** et **Federico Monaco** pour leur contribution à mes travaux à différents niveaux.

Mes sincères remerciements à mes collègues du LTH pour la bonne ambiance qui règne au sein du laboratoire. Je souhaite remercier **Marie, Pascal, Bertrand, Karine, Michel, Lionel, Philippe, Nathalie, Abdel, Patrick, Stéphane, Pierre, Olivier, Jérôme A, Guilhem, André, Charlotte, Thomas, et Denis**. Une pensée particulière pour l'équipe des jeunes chercheurs avec **Federico, Elisa, Amira, Youcef, Pauline, Sergii, Tika, Lydia, Thibaut, Paul, Delphine** et mes rencontres à travers l'association AITAP. Je souhaite bonne continuation à ceux qui sont en pleine thèse ou stage. Merci à **Sarah** et **Églantine** qui ont toujours été d'une aide précieuse pour tous les problèmes administratifs et d'organisation.

Ces trois ans de thèse m'ont permis également de faire de très belles rencontres hors du laboratoire, et qui m'ont beaucoup touchées. Je tiens à remercier tous mes amis du club 'Courir à Grenoble' avec qui j'ai partagé les meilleurs moments. En particulier **Amélie, Adrien, Alix, Aurore, Pauline, Julien, Christiane, PAF et Abdel** pour leur sorties en montagne pour me déconnecter des modèles des champs aléatoires. Toutes ces connaissances professionnelles et personnelles m'ont fait me sentir chez moi à Grenoble.

Pour terminer, je remercie mes **parents**, mes **frères (Khalid inclus)** et ma **sœur**, pour leur soutien derrière les coulisses, même si la microstructure des électrodes de cellules à oxydes solides reste un mystère pour eux.

Table of contents

Table of contents	5
List of Symbols	9
Résumé étendu en français	13
Introduction	19
General objectives	21
Layout of the manuscript.....	22
Chapter I: Context of high temperature Solid Oxide Cells	25
I.1 SOC operating principle.....	25
I.2 SOC materials and manufacturing	27
I.2.1 Electrolyte.....	28
I.2.2 Hydrogen electrode.....	29
I.2.3 Oxygen electrode	30
I.3 Physical phenomena in SOCs	31
I.3.1 Open circuit voltage (OCV)	32
I.3.2 Ohmic overpotential	32
I.3.3 Concentration overpotential	33
I.3.4 Activation overpotential	34
I.4 SOC durability and degradation mechanisms	36
I.4.1 SOC durability	36
I.4.1 Degradation mechanisms.....	36
I.5 Importance of microstructure	38
I.6 State-of-the-art review of the investigated fields	40
I.6.1 Overview on microstructure stochastic geometrical models.....	40
I.6.2 State of the art of microstructural correlations	42
I.6.3 Overview on LSCF-CGO reaction mechanisms	44
I.6.4 State of the art of LSCF-CGO microstructural optimization	45
I.7 Conclusion and methodology.....	46
Chapter II: 3D reconstruction and characterization of SOC electrodes microstructures	49
II.1 Presentation of the investigated cells	50
II.1.1 Cell-A: commercial complete cell in LSCF and Ni-YSZ	50
II.1.2 Cell-B: commercial complete cell in LSC and Ni-YSZ.....	51

II.1.3 Cell-C: in-house symmetrical cell in LSCF-CGO	52
II.2 Three-dimensional reconstruction of SOC electrodes	53
II.2.1 3D reconstruction via FIB-SEM tomography	54
II.2.2 3D reconstruction via synchrotron X-ray holotomography	55
II.3 Raw image processing and segmentation	56
II.4 Macropores separation from the micropores network in the diffusion layer.....	58
II.5 Microstructural quantitative characterization: properties measurement.....	59
II.5.1 Morphological parameters.....	60
II.5.2 Physical parameters.....	65
II.6 Representative Volume Element (RVE).....	66
II.7 Results and discussion	68
II.7.1 Results for Cell-A.....	68
II.7.2 Results for Cell-B.....	70
II.7.3 Results for Cell-C.....	74
II.8 Conclusion	76
Chapter III: Stochastic geometrical models and validation.....	77
III.1 Random Field model description and validation.....	77
III.1.1 Random Field model description for SOC electrodes	78
III.1.2 Validation of the random field model on 3D reconstructions.....	86
III.1.3 Discussion: model flexibility to various electrode microstructures.....	94
III.1.4 Conclusion	100
III.2 Particle-based model description and validation	102
III.2.1 Particle-based model description for SOC electrodes	102
III.2.2 Validation of the sphere-packing model on 3D reconstructions.....	108
III.2.3 Model flexibility: illustration for a diffusion layer with a bimodal pore distribution	116
III.2.4 Conclusion	121
III.3 Concluding remarks: models comparison	121
Chapter IV: Microstructural correlations	125
IV.1 Introduction	125
IV.2 Theoretical development and methodology	127
IV.2.1 Theoretical development: analytical expression for $S_{i/j}$ and S_i	127
IV.2.3 Methodology for calibrating and validating the microstructural correlations.....	133
IV.3. Calibration of the microstructural correlations	135
IV.3.1 Correlations for the electronic/pores and ionic/pores interfacial specific surface area.....	135

IV.3.2 Correlation for the electronic/ionic interfacial specific surface area.....	139
IV.3.3 Correlation for the density of TPBl	141
IV.4. Discussion and validation.....	144
IV.4.1 Model prediction with respect to the RF and SP microstructures	144
IV.4.2 Model validation on diverse electrodes reconstructions.....	145
IV.4.3 Model validation on the loss of TPBl after Ni agglomeration.....	146
IV.5 Conclusion.....	148
Chapter V: Impact of microstructure on the LSCF-CGO composite electrode performance	151
V.1 Experimental conditions, modeling and methodology	152
V.1.1 Testing conditions	152
V.1.2 Electrochemical model description.....	153
V.2. Experimental results and models validation	156
V.2.1 Electrochemical measurements.....	156
V.2.2 Calibration and validation of the electrochemical model	159
V.3. Role of the LSCF-CGO microstructure on the reaction mechanism.....	162
V.3.1 Reaction mechanism at 700°C and impact on the electrode performances	162
V.3.2 Role of microstructure on the electrode response: effect of composition, porosity and particle size.....	164
V.4 Conclusion	169
Conclusions & Perspectives.....	171
Appendix	177
A.1 Expression of the correlation $\rho_X(h)$ as a function of the weight function $\omega(h)$	177
A.2 Relation between $C_X(h)$, $\rho_X(h)$, and λ_X	177
A.3 Correlations for the specific surface area between the electronic and pore phases.....	179
A.4 Correlations for the Triple Phase Boundary lengths TPBl density	180
References	181

List of Symbols

Roman Symbols:

a	Scaling parameter in the correlations for $S_{io/el}$	–
C_i	The covariance function of i	–
C_{dl}	Double layer capacitance	F m ⁻²
$C_{O_o^x}$	Concentration of neutral oxygen atoms in LSCF	mol m ⁻³
$C_{O_o^x}^{eq}$	Concentration of neutral oxygen atoms in LSCF at equilibrium	mol m ⁻³
$C_{O_o^x}^{max}$	Maximum concentration of neutral oxygen atoms in LSCF	mol m ⁻³
$C_{V_o^{\bullet\bullet}}$	Vacancies concentration in LSCF	mol m ⁻³
$C_{V_o^{\bullet\bullet}}^{eq}$	Vacancies concentration in LSCF at equilibrium	mol m ⁻³
C_X	The covariance function of X	–
$\langle d_c \rangle$	Mean value of the contact diameter between the ionic and electronic particles	μm
d_p or $\langle D_i \rangle$	Mean phase diameter	μm
D_i	Domain or Cell related to the phase i	–
$\tilde{D}_{chem}^{eff}/\tilde{D}_{chem}^{bulk}$	Effective/Bulk oxygen chemical diffusion coefficient in LSCF	m ² s ⁻¹
D_{k,O_2}^{eff}	Effective Knudsen diffusion coefficient	m ² s ⁻¹
D_{O_2,N_2}^{eff}	Effective molecular diffusion coefficient	m ² s ⁻¹
$D_{O-SLSCF}$	Diffusion coefficient of oxygen adsorbates on LSCF	m ² s ⁻¹
E	Local electrode potential	V
F	Faraday's constant	C mol ⁻¹
G_i	Random Gaussian field of phase i	–
G_{ij}	Bi-Gaussian random field	–
$G_X(z)$	Gaussian random field	–
h	Electrode thickness	μm
h^\bullet	Hole defect in LSCF	–
i (or j)	Electrode phase: i =ionic (io), electronic (el), porosity (p)	–
$i=X, Y, Z$	Phase name	–

\bar{i}	Complementary phase of i	–
\vec{i}_{io}/e'	Ionic current density in CGO/Electronic current density in LSCF	A m ⁻²
k_{pow}	Rate constant for Ni coarsening	m ⁸ .s ⁻¹
K_{1i}	Shape factor for the surface area	–
K_{2i}	Shape factor for the volume	–
k_+	Forward reaction kinetic constants for R1	mol m ⁻² s ⁻¹
$k_{ox}^{LSCF/gas}$	Forward reaction kinetic constants for R2	m ³ mol ⁻¹ s ⁻¹
k_{ox}^{TPB}	Forward reaction kinetic constants for R3	m s ⁻¹
k_{des}	Forward reaction kinetic constants for R4	s ⁻¹
ℓ	Penetration length between two particles	m
ℓ_{LSCF}	Characteristic length	m
L_{TPBI}	Density of total TPBI	m ⁻²
M	Microstructure-factor	–
n	Exponent in the power law model for Ni coarsening	–
N_i	Number of ionic or electronic particles per unit volume	m ⁻³
N_c	Number of ionic and electronic contacts per unit volume	m ⁻³
N_{O_2}	Oxygen gas flux	mol m ⁻²
$N(0,1)$	Standard Normal Distribution	–
$O_o^x(LSCF)$	Oxygen atom in the LSCF lattice	–
$O_o^x(CGO)$	Oxygen atom in the CGO lattice	–
$O-S_{LSCF}$	Oxygen adsorbate on LSCF surface	–
O_2	Gaseous oxygen Molecule	–
P	Probability density function	–
P_{O_2}	Oxygen partial pressure	atm
P_t	Total pressure	Pa
R	Universal gas constant	J mol ⁻¹ K ⁻¹
S_{LSCF}	Adsorption site on LSCF surface	–
S_p	Specific surface area	m ⁻¹
S_i	Specific surface area for i	m ⁻¹
$S_{i/j}$	Interfacial specific surface area between i and j	m ⁻¹
S_i^{ex}	Specific surface area in the extended microstructure for i	m ⁻¹

$\langle S_i \rangle$	Mean surface area of the electronic or ionic particles	m^2
$S_p^{CGO/LSCF}$	Specific surface area between CGO and LSCF	m^{-1}
$S_p^{LSCF/gas}$	Specific surface area between LSCF and gas phase	m^{-1}
t	Time	s
T	Absolute temperature	K
$U(z)$	Non-correlated Gaussian random field	–
V_i	Volume of the phase i	m^3
$\langle V_i \rangle$	Mean volume of the electronic or ionic particles	m^3
V_i^{ex}	Volume of the phase i in the extended microstructure	m^3
V_{tot}	Total volume of the domain	m^3
V_Ω	Domain volume	μm^3
$V_o^{**}(LSCF)$	Oxygen vacancy in the LSCF lattice	–
$V_o^{**}(CGO)$	Oxygen vacancy in the CGO lattice	–
$Y_{(i)}$	Molar fraction of species (i)	–

Greek Symbols:

α	Ratio of the ionic to the electronic phase volume fractions	–
$\alpha_{(Ri)}^{ox/red}$	Symmetrical coefficient for reaction	–
β_i	Ratio of shape factors/scaling parameters in the semi-analytical correlations	–
β	Constrictivity parameter	–
γ_i	Skewness of the PSD _i	–
λ_X	Threshold	–
Γ	Surface density of available sites on LSCF	$mol\ m^{-2}$
δ	Oxygen under-stoichiometry in LSCF	–
ϵ_X	Phase volume fraction for the phase X	–
φ_{CGO}	Electrostatic potential in CGO	V
φ_{LSCF}	Electrostatic potential in LSCF	V
δ_X	Connectivity for the phase X	–
θ_i	Phase volume fraction	–
θ_{O-LSCF}	Coverage rate of oxygen atoms on LSCF	–

$\nu_{(i)}$	Kinetic rate of chemical/electrochemical reaction (i)	$\text{mol m}^{-3} \text{s}^{-1}$
ξ_{TPBs}	Density of triple phase boundary lengths	m^{-2}
$\sigma_{h_{LSCF}}^{eff} / \sigma_{h_{LSCF}}^{bulk}$	Effective/Bulk electronic conductivity of LSCF	S m^{-1}
$\sigma_{io, CGO}^{eff} / \sigma_{io, CGO}^{bulk}$	Effective/Bulk ionic conductivity of CGO	S m^{-1}
ρ_X	Correlation function	–
Ω	3D domain	–
π	Mathematical constant Pi ≈ 3.1416	–
τ_X^{geo}	Geometrical tortuosity for the phase X	–
ω_X	Weight function	–

List of Abbreviations

CE	Counter electrode
CGO	Ceria doped Gadolinium Oxide
CV _i	Coefficient of Variation of the PSD _i
EIS	Electrochemical impedance spectroscopy
FIB-SEM	Focused Ion Beam-Scanning Electron Microscopy
FFT	Fast Fourier Transform
PSD _i	Particle Size Distribution
LSCF	Lanthanum Strontium Cobalt Ferrite
MIEC	Mixed Ionic and Electronic Conductor
OCP	Open circuit potential
RE	Reference electrode
RF	Random Field
SEM	Scanning electron microscopy
SOCs	Solid Oxide Cells
SOEC	Solid Oxide Electrolysis Cell
SOFC	Solid Oxide Fuel Cell
SP	Sphere-Packing
TPBs	Triple Phase Boundary lengths
WE	Working electrode
YSZ	Yttria Stabilized Zirconia

Résumé étendu en français

Ce travail vise à étudier l'impact de la microstructure des électrodes des cellules à oxydes solides sur leur performance, en vue de les optimiser. Une approche numérique intégrée a été proposée pour atteindre cet objectif. Cette démarche couple une modélisation en géométrie stochastique des matériaux poreux à une modélisation électrochimique des mécanismes réactionnels au sein des électrodes.

L'utilisation démesurée et accélérée des combustibles fossiles au cours du dernier siècle, notamment du pétrole, du gaz naturel et du charbon, a déclenché une crise énergétique mondiale. En effet, les émissions de dioxyde de carbone provenant de la production d'électricité utilisant des combustibles fossiles sont directement responsables du changement climatique et des problèmes environnementaux associés. En outre, avec la croissante demande en énergie et l'épuisement des réserves, la production actuelle d'électricité à partir de ces ressources n'est plus durable. Par conséquent, il est urgent de développer les énergies renouvelables, telles que les éoliennes et les panneaux solaires. Néanmoins, le déploiement massif de ces nouvelles technologies nécessite de nouvelles solutions pour faire face aux fluctuations entre la demande et la production dues à son intermittence. Un nouveau vecteur énergétique flexible pour stocker l'énergie est donc nécessaire pour absorber les pics de production ou de consommation d'électricité.

Le dihydrogène se distingue comme un candidat très pertinent avec son rapport énergie / masse très élevé. De nos jours, le dihydrogène est principalement produit à partir du pétrole par des procédés qui émettent du gaz à effet de serre. Il existe pourtant des procédés non polluants comme l'électrolyse de l'eau. Le développement d'une filière de production de dihydrogène propre se révèle indispensable pour envisager le déploiement de ce vecteur énergétique à plus large échelle. Depuis sa découverte au XIX^{ème} siècle par Sir W. Grove, le procédé d'électrolyse a été développé à travers plusieurs technologies telles que l'électrolyse alcaline, les cellules à électrolyte polymère (PEM) ou les cellules à oxyde solide (SOC). Parmi ces différentes classes de cellules électrochimiques, la technologie SOC a suscité un grand intérêt dans le cadre de la transition énergétique. En effet, ce dispositif présente le rendement électrique le plus élevé par rapport aux autres solutions pour la production de dihydrogène. Cela s'explique en partie par le fait qu'une portion de l'énergie nécessaire à la dissociation de la molécule H₂O est fournie par la chaleur. Cette chaleur permet également d'éviter l'utilisation des catalyseurs coûteux comme le platine, car les vitesses cinétiques

électrochimiques sont favorisées à haute température. De plus, grâce à sa grande flexibilité, le même dispositif électrochimique peut alternativement être utilisé en mode pile à combustible pour la production d'énergie électrique et en mode électrolyseur pour la production de dihydrogène. Cette fonctionnalité est particulièrement convoitée pour pallier l'intermittence des énergies renouvelables.

De nombreux travaux ont été menés ces dernières années pour le développement de la technologie des convertisseurs électrochimiques haute température à oxydes solides (SOC). Cependant, la durée de vie de ces objets reste encore très limitée pour envisager leur déploiement à l'échelle industrielle. Le problème de durabilité est dû au fonctionnement à haute température (≈ 800 °C) qui favorise la décomposition des matériaux, la réactivité ou les évolutions microstructurales des électrodes. Dans ce contexte, la réduction de la température de fonctionnement (600-700 °C) a récemment fait l'objet d'un intérêt particulier. Néanmoins, le défi le plus important est de maintenir des performances élevées à ces températures «intermédiaires». Il est clairement établi que le rendement des SOCs dépend principalement des matériaux d'électrodes utilisés et de leur microstructure. Il est donc essentiel de mieux comprendre les processus à l'échelle de la microstructure et les relier aux performances macroscopiques des électrodes. C'est alors seulement qu'une optimisation microstructurale de ces électrodes pourrait être réalisée.

Ce travail de thèse s'inscrit dans ce contexte, et cherche à mieux comprendre l'impact de la microstructure des électrodes sur leur performance. Pour ce faire, une approche multi-échelle et multi-physique allant de la caractérisation microstructurale et électrochimique des électrodes, à la proposition et validation de modèles géométriques et électrochimiques a été proposée. Le présent manuscrit est organisé en cinq chapitres dont la synthèse est présentée ci-après.

Le premier chapitre présente le contexte des convertisseurs électrochimiques à oxydes solides. Tout d'abord, le principe de fonctionnement de ces objets est rappelé dans les deux modes (pile à combustible et électrolyseur). Une revue sur les matériaux classiquement utilisés pour les cellules et leur architecture est proposée. Les différentes surtensions qui surgissent en opération sont présentées ensuite et leur dépendance de la microstructure des électrodes a été soulignée. La limitation de la technologie en termes de dégradation est discutée par la suite en rappelant les mécanismes de vieillissement les plus prononcés de la littérature. Nous trouvons notamment la réactivité des matériaux, l'empoisonnement au chrome, la transformation cristallographique de phase, ou encore les évolutions microstructurales. Plusieurs facteurs sont soupçonnés de déclencher et accélérer ces mécanismes selon le mode de fonctionnement

tels que la polarisation, la température, ou encore l'humidité. Une stratégie pour réduire les taux de dégradation des électrodes au-dessous des seuils exigés pour l'industrialisation est donc de baisser la température de fonctionnement des cellules. Dans ce cas, une optimisation des composants des cellules est nécessaire pour maintenir de bonnes performances à ces températures 'intermédiaires'. Comme l'efficacité des cellules est directement pilotée par la composition des électrodes et leur microstructure, la stratégie proposée est de mener une optimisation microstructurale pour des matériaux de l'état de l'art. Dans le cadre de cette thèse nous avons choisi d'adresser l'optimisation de l'électrode à O₂. Le matériau retenu pour cet effet est le composite LSCF-CGO qui a montré récemment des propriétés très intéressantes pour potentiellement remplacer le pur LSCF classique. Ce choix est fait uniquement à titre illustratif et n'annule pas le caractère général de l'approche proposée. Une étude bibliographique complète a donc été réalisée, et un plan de travail a été défini en conséquence. L'approche proposée est articulée en quatre grands axes qui font l'objet des quatre chapitres suivants.

Une caractérisation précise et complète de la microstructure complexe des électrodes est primordiale dans un objectif de les optimiser. Le chapitre II porte sur les méthodes d'imagerie utilisées pour reconstruire les microstructures 3D des électrodes et les outils utilisés pour les quantifier. Tout d'abord, les cellules commerciales sont présentées et le protocole de mise-en-forme de celle fabriquée au sein du laboratoire est détaillé. Pour rappel, la méthode utilisée est basée sur de la sérigraphie et le frittage des poudres initiales. Les deux processus d'imagerie utilisés dans le cadre de cette thèse, à savoir l'holo-tomographie aux rayons X et la Microscopie Electronique à Balayage MEB couplée à un faisceau d'ions focalisé FIB (Focused Ion Beam), sont présentés. Les techniques de traitement d'image permettant l'identification des phases sont ensuite listées. Une attention particulière a été donnée à la séparation des macropores du réseau de micropores dans la couche collectrice de l'électrode. Cela nous a permis de quantifier la contribution de chaque échelle de grandeur de porosité au processus de diffusion des espèces gazeuses. Un aperçu des méthodes numériques permettant de calculer les propriétés morphologiques et physiques des volumes segmentés est fourni ensuite. Les propriétés morphologiques incluent les paramètres métriques tels que les fractions volumiques et les diamètres moyens de phase, et topologiques tels que la tortuosité géométrique et le facteur de constrictivité. Les propriétés physiques se réduisent dans le cadre de cette thèse à la conductivité électrique des phases solides et à la diffusivité effective de la porosité. Une section a été consacrée ensuite à l'évaluation de la taille du Volume Élémentaire

Représentatif RVE. Enfin, les résultats de caractérisation microstructurale des cellules testées sont synthétisés et discutés par rapport à la littérature.

Comme la mise en forme et l'imagerie 3D des matériaux sont des processus expérimentaux très coûteux en temps et en argent, une alternative est de générer des microstructures synthétiques représentatives. Le troisième chapitre porte sur le développement de deux outils de génération de microstructures numériques basés sur deux approches différentes. En effet, développer deux outils ne permet pas seulement de balayer une plus large gamme de microstructures mais aussi d'avoir deux approximations du même milieu pour tirer des conclusions indépendamment du modèle employé. Le premier modèle est basé sur « les champs aléatoires tronqués » issus de la géostatistique. En bref, chaque phase solide est représentée par un champ aléatoire obtenu par un produit de convolution d'un bruit blanc Gaussien avec une fonction de poids qui contient les informations morphologiques de la phase que nous souhaitons reproduire. Ces champs aléatoires sont ensuite seuillés pour obtenir la microstructure finale. La deuxième méthode est basée sur un empilement original de sphères représentatives de chaque phase solide. La distribution en taille des sphères, la façon de les positionner, leur degré de chevauchement, ainsi que leur morphologie de contact sont des paramètres d'ajustement du modèle. Les deux méthodes ont été validées sur plusieurs microstructures réelles, à deux et trois phases, en comparant les propriétés microstructurales des volumes synthétiques à ceux des reconstructions. Un très bon accord a été obtenu sur l'ensemble des propriétés morphologiques et physiques. Néanmoins, les deux modèles ont présenté la même 'limitation' à reproduire exactement les fortes constrictivités qui caractérisent les phases avec une faible fraction volumique et donc proches du seuil de percolation. La flexibilité des deux modèles à générer des microstructures 'non classiques' et prometteuses a été discutée par la suite. L'électrode à gradient de composition, l'électrode imprégnée, ou encore la couche collectrice ont été modélisées avec succès à l'aide de ces outils. Une discussion sur la comparaison de ces deux modèles a été fournie en conclusion de ce chapitre.

Le troisième objectif de cette thèse qui a fait l'objet du chapitre IV est l'établissement des corrélations entre les propriétés microstructurales. Cette étape permet de relier les paramètres 'primaires' qui sont facilement contrôlables par les équipes de mise-en-forme des matériaux (tels que la composition, la porosité et les diamètres moyens de phases) au paramètres 'clefs' qui pilotent les réactions électrochimiques (les surfaces spécifiques $S_{i/j}$ et la densité de points triples de contact entre les phases TPBs). Tout d'abord, les développements théoriques basés sur l'approche des « microstructures étendues » sont présentés. Ensuite, deux ensembles de

microstructures synthétiques générées à l'aide des deux modèles ont permis de calibrer les équations ainsi obtenues. Bien que les deux modèles stochastiques soient totalement différents, l'ajustement des équations sur les deux ensembles a conduit à des constantes assez proches. Enfin, la validité des relations a été vérifiée sur plusieurs reconstructions faites dans le cadre de la thèse ou provenant de la littérature. De plus, l'aptitude des équations semi-analytiques à estimer les évolutions microstructurales suite à une agglomération de Ni a été discutée. Ces corrélations constituent un guide très pratique aux fabricants de cellules pour concevoir des cellules de prochaine génération.

Le dernier objectif de la thèse est d'établir le lien entre les performances 'macroscopiques' des électrodes et leurs propriétés microstructurales, ce qui a été l'objet du dernier chapitre V. Un modèle électrochimique pour l'électrode à O₂ en LSCF-CGO, déjà développé au sein du laboratoire, a été exploité pour cet effet. Ce modèle propose un mécanisme de réaction composé de plusieurs étapes divisées en deux chemins en parallèle (un chemin en surface et un autre en volume). Le modèle permet de simuler à la fois la réponse stationnaire (courbes *i-V*) et dynamique (spectres d'impédances électrochimiques) de l'électrode en fonction de sa microstructure. Des tests électrochimiques ont été menés dans une configuration à trois électrodes avec une cellule symétrique de référence en LSCF-CGO afin de le calibrer. Les propriétés microstructurales de l'électrode de référence étant connues via la caractérisation 3D antérieure, seules les constantes cinétiques et la diffusivité de surface sont les paramètres inconnus du modèle à calibrer. Cette étape a été réalisée en ajustant les courbes de polarisation expérimentales à celles numériques à différentes températures. Le modèle a été ensuite validé en comparant les spectres d'impédance simulés et expérimentaux sans ajustement additionnel.

Dans nos conditions expérimentales, l'examen des résultats de caractérisations électrochimiques a révélé que le composite LSCF-CGO est contrôlé par le même mécanisme réactionnel quelles que soient les polarisations cathodiques ou anodiques à la température choisie de 700 °C sous air. Le modèle électrochimique a été utilisé pour analyser ces résultats expérimentaux. Les simulations ont montré que la réponse des électrodes était entièrement contrôlée par le transfert de charge aux TPBIs (chemin en surface) à 700°C, tandis que l'incorporation à la surface des particules LSCF (chemin en volume) est négligeable. Les phénomènes sous-jacents à l'origine de ce comportement des électrodes ont également été discutés.

Le couplage du modèle électrochimique et de microstructure a permis finalement d'investiguer le rôle de la microstructure sur les performances des électrodes. Un ensemble de

microstructures synthétiques a été généré en modifiant la composition de l'électrode, la porosité et la taille des particules. Toutes les propriétés calculées sur les volumes 3D ont été introduites dans le modèle électrochimique. Les simulations ont montré que les performances des électrodes sont principalement contrôlées par la densité de TPBI et la conductivité ionique effective du réseau de CGO. De plus, un optimum en termes de résistance de polarisation des électrodes a été identifié pour une composition de LSCF: CGO = 32:68% en volume. Les performances sont également améliorées en diminuant la porosité de 43% à 33% et en raffinant le réseau de LSCF dans le squelette CGO. Tous ces résultats servent à guider les équipes de mise-en-forme des matériaux à fabriquer des cellules à oxydes solides de meilleures performances.

Enfin, une conclusion générale est donnée pour rappeler les résultats essentiels de cette thèse, discuter de leur généralisation, et proposer quelques perspectives pour ce travail. Il est proposé notamment d'adresser en perspective la 'limitation' des modèles géométriques. Pour ce faire, une étude avancée de l'évolution morphologique d'une phase à proximité du seuil de percolation est requise, et des adaptations doivent être apportées aux modèles en conséquent. Il s'est avéré aussi très intéressant d'étudier la possibilité de générer un volume 3D à partir d'une section 2D représentative. Cette technique pourra réduire drastiquement le nombre de reconstructions 3D nécessaires dans une étude expérimentale. Les corrélations microstructurales proposées étant uniquement focalisées sur les propriétés électrochimiques, il sera intéressant de les étendre aux propriétés de transport et de mécanique par exemple. Une autre perspective sera de généraliser le modèle électrochimique utilisé en proposant un mécanisme réactionnel entièrement élémentaire, et d'étudier l'effet de la pression sur la réponse de l'électrode. En termes d'optimisation, il sera intéressant d'utiliser la même approche pour adresser de nouvelles architectures d'électrodes, comme l'électrode imprégnée, et de nouveaux matériaux, comme le cermet Ni-YSZ.

Introduction

The excessive and accelerated use of fossil fuels, especially oil, gas and coal, in the last century has triggered a global energy crisis (cf. Fig. 0.1). Indeed, carbon dioxide emission from power generation burning these sources is considered as a key contributor to climate change and related environmental problems. Besides, with increasing energy demand and depleting fuel reserves, the current power generation from these nonrenewable sources will not be sustainable.

Consequently, there is an urgent need to take advantage of the green energy sources, like wind turbines and solar panels, that are emerging in the energy production mix (cf. Fig. 0.1). Nevertheless, the massive development of these intermittent renewable technologies requires new solutions to match the fluctuations between the demand and the production. A new flexible energetic vector for storing energy is thus required to absorb the peaks of electricity production or consumption.

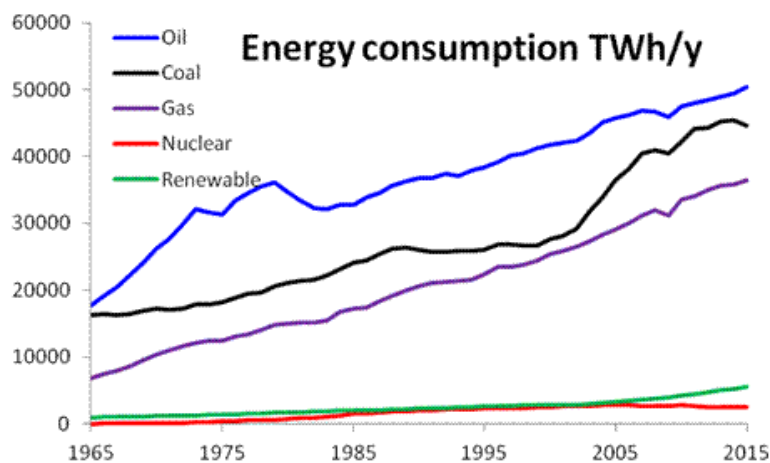


Fig. 0.1 The world's energy consumption by fuel or energy source from 1965 to 2015 (adapted from BP Statistical Review of World Energy 2018).

The dihydrogen gas, which presents a high ratio of energy to mass, is considered as one of the most relevant choices for this energy career. Nowadays, steam reforming of natural gas is the most common method of producing commercial hydrogen at about 95% of the world production [Ogden1999, USenergy.gov2017]. However, this process emits greenhouse gases as byproducts. Therefore, promoting cleaner techniques, like water electrolysis, seems a very

interesting strategy. Since its discovery in the 19th century by Sir W. Grove [Grove1842], the electrolysis process have been developed through several technologies such as Alkaline electrolysis cells, Polymer Electrolyte Membrane cells (PEM) or Solid Oxide Cells (SOC).

Of these several classes of electrochemical cells, the SOC technology has attracted great interest for promoting the energy transition. Indeed, this device exhibits the highest electrical efficiency compared to the other solutions for hydrogen production as shown in Fig. 0.2. This is partly explained by the fact that a portion of the required energy for the H₂O molecule splitting is provided through heat. Moreover, as the SOC operates at high temperature (750°C-850°C), the use of expensive electro-catalysts (like Platinum) is not requested to promote the electrochemical reactions. Besides, thanks to their high flexibility, the same electrochemical device can be alternatively used in fuel cell mode for electrical power generation and steam electrolysis mode for dihydrogen production [Graves2015] (i.e. in Solid Oxide Fuel Cell – SOFC – mode or in Solid Oxide Electrolysis Cell – SOEC – mode). This feature is especially sought for the renewable but intermittent energy sources.

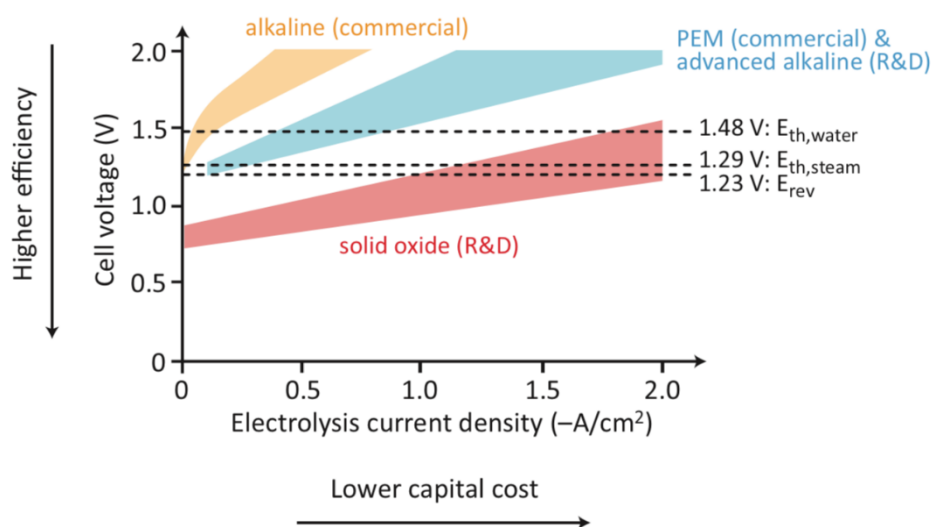


Fig. 0.2 Typical ranges of polarization curves for different types of state-of-the-art water electrolysis cells [Graves2011]

Nevertheless, SOCs still face some challenges to become economically competitive on the energy conversion marketplace. The high operating temperatures afford certainly several advantages for this technology, but they are also responsible for a number of its limitations. For instance, the cell degradation rates measured upon steady-state operation are still too high and constitute one of the main issues of this technology [Hjalmarsson2014, Hubert2018,

Laurencin2017, Lay-Grindler2014, Skafte2016]. These degradations are ascribed to various phenomena activated at high temperature like material decomposition, reactivity or electrode microstructural evolutions [Hubert2018, Uhlenbruck2009, Yokokawa1992, Yokokawa2008]. Moreover, the SOCs ability to withstand several thermal cycles imposed by the repetition of start and shutdown of the system remains nowadays insufficient [Hsiao1997]. In this frame, lowering the operating temperature (600-700°C) has recently attracted an increasing interest. Indeed, reduced temperature not only allows the use of low-cost interconnects and balance-of-plant components, but it could also mitigate significantly all the degradation issues related to both the thermal cycling and the material deterioration upon long-term operation [Murray2002]. In this case, work should be done to maintain high performances at these ‘intermediate’ temperatures.

It is clearly established that the efficiency of SOCs depends mainly on their material composition and their porous electrodes microstructure. It is therefore essential to improve the understanding of the processes taking place in the electrodes microstructure, and investigate their effect on performance. In this way a microstructural optimization of these electrodes will be held accordingly.

General objectives

Four milestones can be identified in the proposed approach aiming to optimize the SOC electrodes microstructure. As it is essential to obtain a detailed and reliable 3D reconstruction and quantification of the electrodes microstructure, the first goal is to achieve a relevant electrode “microstructural characterization”. In this frame, some in-house available tools and procedures should be taken advantage of, while new ones need to be developed to take into account the particularity of the studied cells. These tools are mainly dedicated to electrode imaging and microstructural quantification. The first point concerns the reconstruction procedure, from sample preparation and data acquisition up to the images stack processing and phases identification. The second sub-objective consists in developing and adapting appropriate methods for computing all the relevant morphological and transport properties on the segmented volumes.

The second milestone concerns “geometric microstructural modeling”. It is well known that electrode manufacturing and imaging are very time-consuming processes, especially in the frame of a microstructural optimization. In order to explore a large number of potential optimum microstructures, a relevant strategy is to develop stochastic geometrical models able

to mimic the morphology of actual SOC electrodes. These models ought to be representative of the real media, and should also be flexible to sweep a large range of promising microstructures.

The third milestone concerns “microstructural correlations”. Indeed, an electrode microstructure can be described through numerous morphological and physical parameters that are linked to each other. These relationships are still not clearly established, and are crucial to better understand the different dependences within a microstructure. In particular, the properties that are closely linked to the electrode performance (like active reaction sites density) can be expressed as a function of the parameters that are more easily controlled by the cell manufacturers (like materials composition, particle size and porosity).

The missing link in this approach is the one between the electrode microstructure and its performance, which brings us to the fourth and last milestone about “electrochemical modeling”. Indeed, once the correlations on the microstructural level are established, an up scaling is needed to assess the electrode macroscopic behavior based on its microstructural parameters. In this frame, an integrated modeling approach taking into account the plausible reaction mechanisms as well as the microstructural properties of an electrode is needed. At this stage, only the O₂ electrode will be addressed for illustrative purposes by taking advantage of an in-house model. The objective will be to experimentally validate this model on the studied cell in order to unravel the predominance of the reaction mechanisms occurring therein.

The achievement of these four milestones will allow a better understanding of the role of electrode microstructure on its performance, in an objective to optimize it.

Layout of the manuscript

The first chapter lays the groundwork for this thesis by presenting the context of high temperature Solid Oxide Cells. Firstly the working principle, the state of the art of materials and design, as well as the physical phenomena are presented. The technology’s limitation in terms of degradation is discussed afterwards. The suggested strategy to address this ‘weakness’ includes improving the understanding of the microstructural correlations for a later optimization. The proposed methodology to achieve this objective is presented at the end of this chapter, with an overview of the most recent advances on this subject.

The succeeding chapters address mainly the four milestones discussed previously. Chapter II tackles mainly the ‘microstructural characterization’ sub-objective. First, it presents the cells

that are used to calibrate and validate the modeling tools developed in this work. In this purpose, the employed tomographic processes for 3D reconstruction are presented in a first place. The image processing techniques allowing the phases identification are listed afterwards. Then an overview on the numerical methods allowing the extraction of the relevant morphological and physical properties from the segmented volumes is provided. A section has been dedicated to the assessment of the Representative Volume Element. Finally, the microstructural characteristics for the tested cells are summarized and discussed with respect to literature.

The third chapter addresses the ‘geometrical modeling’ goal. First, two proposed models are described and illustrated for two- and three-phase materials. The representativeness of the models to mimic the real microstructures introduced in the second chapter is examined afterwards. A discussion on the model flexibility to simulate ‘non-classical’, but promising, microstructures is provided afterwards. Finally, a comparison between the proposed models is given at the end of this chapter.

The fourth chapter deals with the ‘microstructural correlations’ topic. First, the theoretical developments leading to the different relationships are presented. Then, a large set of generated synthetic microstructures allows the calibration of the obtained equations. Finally, their validity is checked on several in-house and published reconstructions from the literature.

The fifth and last chapter addresses in a first part the ‘electrochemical modeling’ objective. The electrochemical testing setup, conditions and procedure are provided in a first place. The in-house model description for an O₂ electrode in LSCF-CGO is presented afterwards. Then, its calibration and validation are discussed secondly. Finally, an analysis of the reaction mechanisms is provided at the end of this part. The second half of this chapter concerns the investigation of the effect of microstructure on a composite O₂ electrode performance. The influence of composition, porosity, and particle size are discussed in this frame. This analysis is accompanied by several guidelines to cell manufacturers for electrode optimization.

Finally, a general conclusion is given to recall the essential findings of this thesis, and propose some outlooks to this work.

Chapter I: Context of high temperature Solid Oxide Cells

This chapter gives an outline of the fundamentals upon which this work is constructed. In particular, the operating principle, the materials and the basics of solid-state electrochemistry in SOCs are presented. As the electrode microstructure is closely linked to the different physical phenomena within this electrochemical device, a special attention has been paid throughout this chapter to highlight this dependence. The limitations of this technology, mainly linked to long-term degradation, are discussed afterwards. A strategy based on temperature reducing accompanied by an adapted microstructural optimization is proposed. Finally, an overview of the state-of-the-art of advances in this regard is provided with a detailed methodology to reach this goal.

I.1 SOC operating principle

The SOCs are high temperature electrochemical energy conversion devices composed of ceramic and metallic components. The same system can alternatively be operated in Solid Oxide Fuel Cell (SOFC) mode to produce electricity by electrochemical oxidation of hydrogen, or in Solid Oxide Electrolysis Cell (SOEC) mode to produce hydrogen from the reduction of steam under an electrical current. The global reversible reaction equation is given hereafter:



A SOC is a three layers setup made of a dense electrolyte sandwiched between two porous electrodes. The so-called hydrogen electrode is the cell layer in which hydrogen is oxidized in fuel cell mode or produced in electrolysis mode according to the reversible reaction (I.2a). The redox-reaction of O_2 takes place in the so-called oxygen electrode following the global reaction (I.2b).



The electrolyte ensures the conduction of the oxygen ions produced by the previous half-cell reactions from one electrode to the other. In SOFC mode, gaseous oxygen molecules are

reduced at the oxygen electrode into O^{2-} ions that migrate through the dense electrolyte to be oxidized at the hydrogen electrode into steam and electrons. In SOEC mode, the water molecules are dissociated to form hydrogen gas and oxygen ions that diffuse through the dense electrolyte to be oxidized at the O_2 electrode [Ni2008]. The schematic operating principle of a SOC, in fuel cell and electrolysis modes, is shown on Fig. I.1.

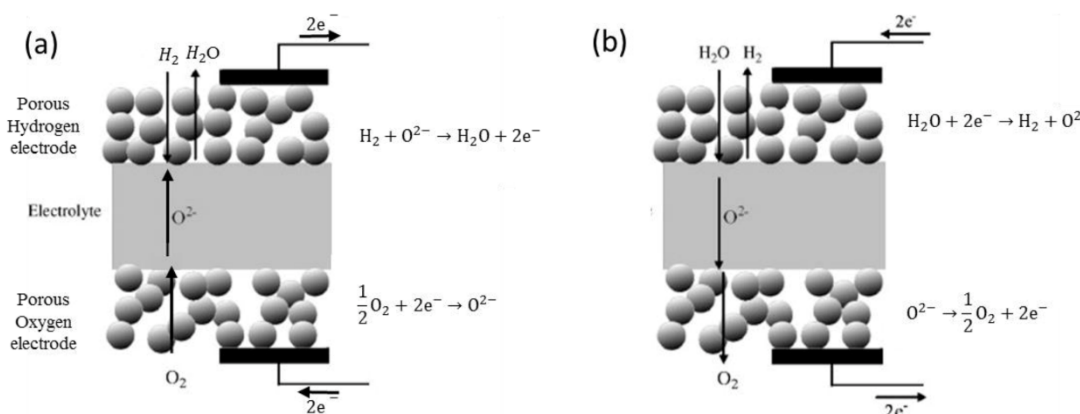


Figure I.1 Schematic operating principle of a SOC in (a) SOFC mode and in (b) SOEC with the half reactions for each electrode.

Operating conditions – Typical SOC operating temperatures are between 500°C and 1000°C . This high temperature level is crucial as the ionic conductivity of the solid electrolyte depends exponentially on temperature. In SOFC mode, this allows flexibility to run directly on hydrocarbon fuels such as methane via internal reforming [Vernoux2000, Zhu2003, Tu2004, Morel2005, Laurencin2008]. In SOEC mode, carbon dioxide and steam can simultaneously be co-electrolyzed to produce a syngas of carbon monoxide and hydrogen [O'Brien2008, Aicart2014].

Besides, conversely to low temperature technologies, like Polymer Electrolyte Membrane (PEM) fuel cells, no expensive catalysts like Platinum are required for the activation of the electrochemical reactions [Kiburakaran2009, Mekhilef2012]. Indeed, the high operating temperature promotes the efficiency of the electrochemical reactions by increasing kinetic rates, resulting in high performances. In addition, from a thermodynamic point of view, working at high temperature can also allow reducing the cost of hydrogen production if a heat source is available (nuclear power or renewable energy for example). Indeed, the electrical demand for the water splitting (Gibbs energy, ΔG) is reduced when increasing the operating temperature. As illustrated in Fig. I.2, the decrease in ΔG is then balanced by an increase in

the thermal need (entropy, $T\Delta S$) while the enthalpy ΔH is only slightly affected by the operating temperature [Hino2004, Ni2008, Laguna2012].

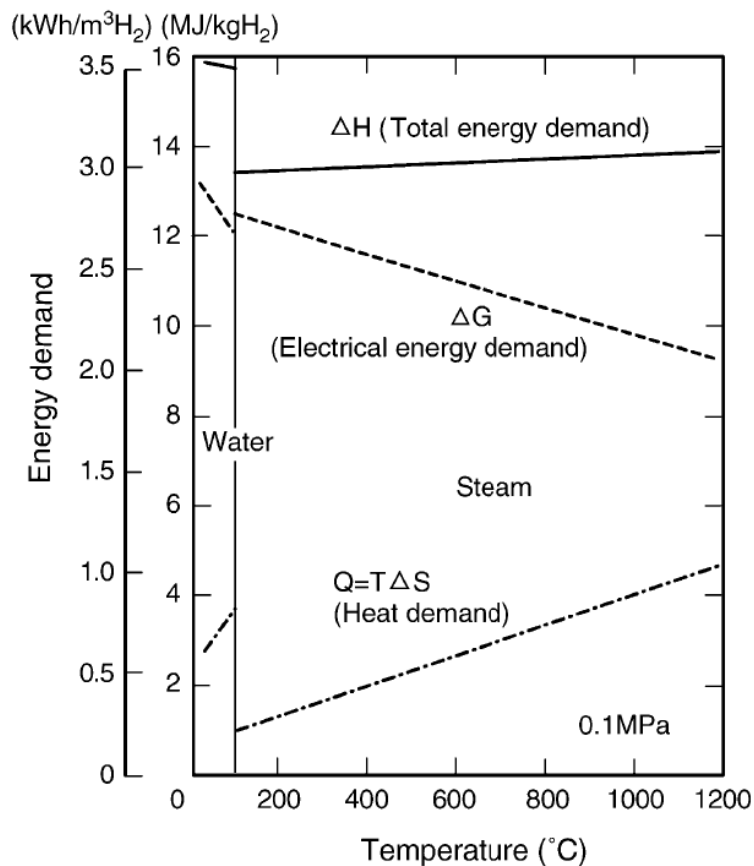


Figure I.2:
Evolution of the total energy demand, electrical energy demand and heat demand as a function of temperature illustrated for steam electrolysis [Hino2004].

Application areas – The most prominent application area for SOC-based systems is stationary power plants. At this relatively large scale (several kW to MW), the high temperatures and the associated structural problems during heating up and cooling down can be handled most effectively. This technology is particularly suitable to deal with the renewable energies intermittence (such as solar or wind energies). Indeed, the flexibility of this system between electrical energy storage and production allows matching the electricity consumption with the fluctuating energy production.

I.2 SOC materials and manufacturing

The choice of materials is of central importance for the cell reliability. Each SOC component (i.e. electrolyte, H₂ and O₂ electrodes) needs to fulfill several requirements that are sometimes conflicting, a compromise is then to find between these different constraints. They should allow highly efficient electrode reactions (Eqs. I.2a and I.2b) as well as ensure fast reactant

transport. Hence, the electrodes must have a high catalytic activity and high electronic and ionic conductivity, combined with sufficient reaction sites and good transport paths for the different species. The later point emphasizes the importance of an optimized electrode microstructure. A special attention is given throughout this work to address the microstructural requirements. Besides, the materials should be stable at high temperature either under oxidizing or reducing atmospheres at the O₂ or H₂ electrodes, respectively. The electrolyte material ought to exhibit a good ionic conduction and a negligible electronic one to prevent short circuits. However, each component cannot be optimized individually. Indeed, the whole materials assembly should also own compatible thermal expansion behavior to prevent the cracking and delamination that can result from the mismatch in thermal expansion coefficients. Finally, materials should not be reactive with other cell components during manufacturing or operation and to be stable over long-term operation.

The numerous requirements have promoted extensive material research in the course of the last decades to optimize the components of SOCs (i.e. electrolyte, H₂ and O₂ electrodes). Several comprehensive overviews over this subject can be found in the literature [Minh1993, Yamamoto2000, Tietz2002, Brandon2004, Haile2003, Weber2004]. The most prominent materials used in state-of-the-art SOC components will be briefly presented in the following subsections.

1.2.1 Electrolyte

The main function of the electrolyte is to separate the cell electrodes. It must be gas-tight and conduct oxide ions O²⁻ between the O₂ and the H₂ electrodes. Hence, it should provide significant ionic conductivity and negligible electronic conduction. A conventional choice of electrolyte material in SOCs is stabilized zirconia (YSZ, Y_{2x}Zr_{1-2x}O_{2-x}, where x is the concentration of the dopant in mol.% Y₂O₃ in ZrO₂). The doping of ZrO₂ with trivalent yttrium ions forms oxygen ion vacancies in the host lattice. This allows vacancy-mediated conduction of oxygen ions and stabilizes the cubic phase of zirconia at higher temperatures. The dopant concentration has a significant impact on the ionic conductivity of the electrolyte that ranges from 0.05 S.cm⁻¹ to 0.14 S.cm⁻¹ at 1000°C for a doping ratio between 5 %mol and 12 %mol [Yamamoto2000]. The electrolyte is classically doped with 8 %mol Y₂O₃ (denoted as 8YSZ in the following). Besides, 3YSZ (3 mol% Y₂O₃ in ZrO₂) has drawn attention due

to its higher mechanical stability. But it is not suitable for intermediate or low temperature usage because of its lower ionic conductivity.

In order to decrease the operating temperature, other ceria-based oxide materials are under investigation. Among these materials gadolinium-doped ceria (CGO, $\text{Ce}_{1-2x}\text{Gd}_{2x}\text{O}_{2-x-\delta}$, x =dopant concentration of Gd_2O_3 in CeO_2) is a promising candidate. However, one drawback is that for low oxygen partial pressures (particularly on the H_2 electrode side), they become electronically conductive, especially at temperatures above 600°C [Dalslet2006]. Nevertheless, these materials are still of interest for other applications (like LSCF-CGO composite O_2 electrode).

I.2.2 Hydrogen electrode

The role of the H_2 electrode is to provide an appropriate medium for the hydrogen reduction/oxidation reactions. Hence, the main material requirements are high catalytic activity, high electronic and ionic conductivities, compatible thermal expansion and chemical stability. For an H_2 -electrode-supported cell, this electrode provides additionally the mechanical support to the cell. It is usually composed of two layers; (i) a 300-1500 μm thick highly porous substrate which provides the mechanical stability and the transport of gases from and towards the second layer which is (ii) a 5-10 μm thin electrode functional layer where the reactions take place.

Thanks to its high electrical conductivity (e.g. $\sigma_{\text{el}} > 10^5 \text{ S.m}^{-1}$ under 1000°C [Ormerod2003]) and high electrochemical activity, the Nickel is considered as a standard material for the H_2 electrode. However, using the Ni alone limits the reactions (Eqs. I.2a and I.2b) to the Triple Phase Boundary lengths (TPBLs) in contact with the electrolyte. A porous composite of Ni and YSZ is classically used to extend the reactions into the volume of the electrode. Adding YSZ to Ni not only allows extending the reactions into the thickness of the electrode, but also leads to reduce the thermal expansion coefficient mismatch between the electrode and the electrolyte. The composition of this ceramic-metallic composite called ‘cermet’ is then a parameter that needs to be adjusted for an optimal electrode performance and robustness [Ni2008]. The Ni content usually varies between 30 and 50 %vol for ideal properties [Aruna1998].

It should be noticed that the H_2 electrode microstructure plays a huge impact on the cell performance. Indeed, while a fine microstructure is requested for the active layer to maximize the reaction sites (especially the TPBLs density), a coarse microstructure is praised for the

substrate to favor the gases diffusion. Both Ni-YSZ layers manufacturing involves classically the use of relatively cheap ceramic processing techniques like tape casting or screen printing [Tietz2000, Moon2008]. For detailed reviews about these ‘classical’ manufacturing processes, the reader is invited to refer to the following references [Thorel2015, moon2008, Somalu2017], and for less common processes [Tietz2002]. Moreover, in order to reach the high porosity levels expected for the substrate, pore-formers are usually mixed to the materials powder prior to sintering [Sanson2008]. The pore-formers consist in organic or polymer compounds that are burned before sintering. This operation leads to the creation of macropores in the final microstructure that facilitate the gases diffusion through the H₂ electrode.

I.2.3 Oxygen electrode

The components of this electrode are working under a highly oxidizing atmosphere at high temperature. Therefore, pure oxide ceramics are usually used in this case. The first designs for this electrode consisted of a composite of a good electronic conductor mixed with an electrolyte material for the ionic conduction. The microstructure of such a composite was similar to the hydrogen Ni-YSZ electrode with reactions taking place at the TPB lengths. A classical O₂ electrode was La_{1-x}Sr_xMnO_{3-delta} – YSZ (LSM-YSZ). A second-generation class of materials is the ABO₃-type perovskite manganites, cobaltates, and ferrates (A=La, Sr, Ca, Ba; B=Mn, Co, Fe) [Joos2017]. Depending on the configuration, these perovskites exhibit a Mixed Ionic and Electronic Conduction (MIEC). Their main advantage is that the entire MIEC surface contributes to the electrochemical reactions (Eqs. I.2a and I.2b) as discussed by Monaco et al. [Monaco2018]. La_{1-x}Sr_xCoO_{3-delta} (LSC) and La_{1-x}SrCo_yFe_{1-y}O_{3-delta} (LSCF) perovskites are the most used MIEC materials. These compounds exhibit improved electrochemical performances compared to the LSM-YSZ composite [Tietz2006]. However, the main drawback remains their chemical instability and their reactivity with YSZ (cf. Section I.4.2). In order to mitigate this problem, a thin CGO barrier layer of around 5 μm is commonly placed between the electrolyte and the MIEC. Finally, it should be noted that the addition of highly ionic conducting materials like Ceria doped Gadolinium Oxide (CGO) to LSCF or LSC has attracted much attention for improved O₂ electrode [Gao2016, Dusaster1999, Hwang2005]. Indeed, compared to the single solid-phase materials, the LSCF-CGO or LSC-CGO composite exhibits higher performances at intermediate temperatures and presents a better mechanical compatibility with the classical electrolyte in Ytria Stabilized

Zirconia (YSZ) [Kim17a, Kim17b, Leng08, Dusatre99]. For this reason, a special attention is given to the LSCF-CGO composite in the following.

I.3 Physical phenomena in SOCs

During operation, irreversible processes occur in the system, resulting in a drop of cell performances. In order to characterize these physical phenomena, classical techniques involve steady-state polarization measurements (i - V function) and electrochemical impedance spectroscopy (EIS). The i - V curve plots the cell voltage evolution as a function of the current density, $V_{\text{cell}}=f(i)$. This dependence gives relevant information about the cell performances. Regarding the EIS plot, this technique evaluates the transient behavior of the cell with a decomposition in the frequency range by applying a sinusoidal ‘small’ perturbation $i_{ac}(t)$ and measuring its answer. The plot of the impedance $Z(f)$ provides information on the reaction mechanisms.

From both types of measurements, EIS and i - V curves, the Area Specific Resistance ASR can be derived for SOC characterization. This property is widely used and corresponds to the derivative of the i - V curve at a given current density i^* ($ASR(i^*) = \left. \frac{dV_{\text{cell}}}{di} \right|_{i^*}$). The ASR can also be deduced from the impedance spectrum (for a given dc current $i_{dc} = i^*$). In the Bode plan, it corresponds to the intercept with the real axis at low frequencies. The polarization resistance R_{pol} is used to characterize the electrodes response without the ohmic losses. This parameter can be drawn from the impedance spectra. It corresponds to the difference between the intercepts with the real axis at low and at high frequencies (in the Bode plan). Finally, each irreversible mechanism occurring within a cell can be associated to a voltage drop that gives a specific contribution to the overall i - V curve. These ‘polarization overpotentials’, illustrated in Fig. I.3, can be sorted into different categories presented in the following.

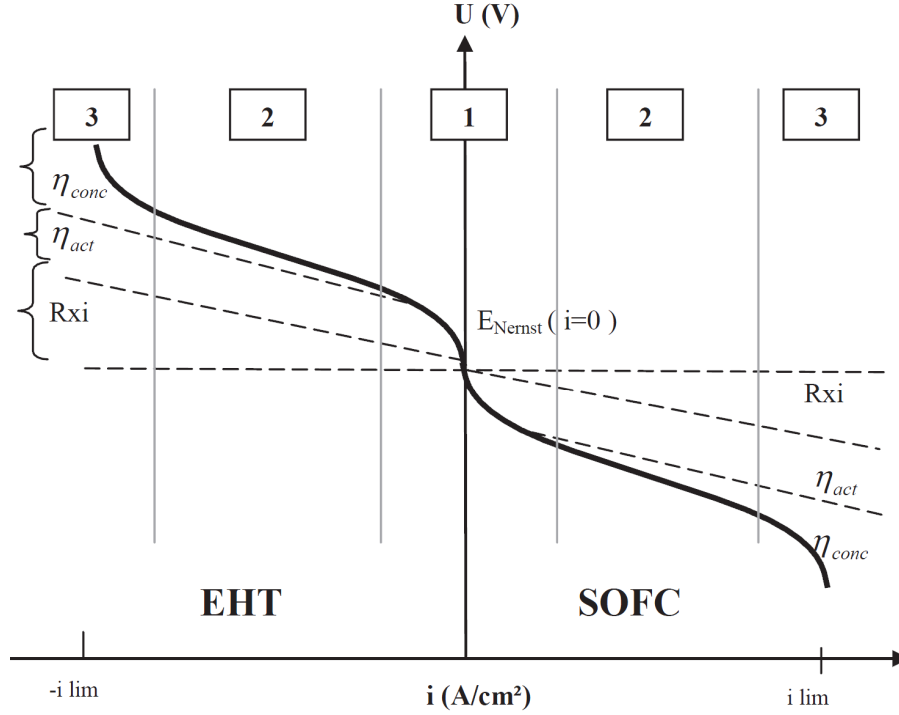


Figure 1.3: schematic plot of the different polarization overpotentials of a SOFC, in electrolysis and fuel cell modes [Mansuy2012]. i-V curves can usually be decomposed into 3 zones: zone 1 is mainly governed by activation, zone 2 by ohmic losses and zone 3 by mass transfer.

I.3.1 Open circuit voltage (OCV)

When the external circuit is open, the difference of oxygen partial pressure on each side of the dense electrolyte leads to an cell voltage $V_{i=0}$. This voltage can be expressed thanks to the Nernst law (Eq. (I.3)) [Godula-Jopek2015]. It corresponds to the thermodynamic equilibrium and depends on the gases conditions and the operating temperature as follows:

$$V_{i=0} = V^0(T) + \frac{RT}{2\mathcal{F}} \ln \left(\frac{y_{i=0}(H_2) \cdot \sqrt{y_{i=0}(O_2)}}{y_{i=0}(H_2O)} \right) \quad (I.3)$$

Where V^0 is the standard voltage, $y_{i=0}(x)$ is the molar fraction of the element x at the electrodes active sites under open circuit condition ($i=0$), \mathcal{F} is the Faraday's constant, and R is the gas constant ($R=8.314 \text{ J.mol}^{-1}.\text{K}^{-1}$). When the cell is under operation, several overpotentials arise changing the cell voltage.

I.3.2 Ohmic overpotential

Ohmic losses arise from the materials resistance to the electronic and ionic transport. The overall resistance R_{ohm} consists in the sum of the individual losses of each component. It is expressed proportionally to the current density via the classical Ohm's law:

$$\eta_{ohm} = R_{ohm} \cdot i \quad (I.4)$$

The resistance of the dense electrolyte represents the main contribution to R_{ohm} . A common solution is to use a very thin electrolyte ($\sim 10 \mu\text{m}$) and to delegate the mechanical support function to the H_2 electrode for example as discussed previously. The second contribution is related to the contact resistance between the cell electrodes and the current collectors. Current collecting grids are usually used in this frame to limit the associated ohmic losses.

I.3.3 Concentration overpotential

The concentration polarization arises in operation because of the change in gases composition in the vicinity of the electrochemically active sites. This contribution is dominant at high current densities when the gas composition close to the active sites is different from the inlet composition. This is due to gases production or consumption in the neighboring of the electro-active sites. It is convenient to take into account separately the composition gradient existing along the gas channel, above the electrodes, and the gradient encountered through the electrode thickness [Laurencin2015]. Following this convention, the concentration overpotential can be expressed as the sum of a gas conversion losses ΔV_{rev} and a diffusion overpotential η_{diff} :

$$\eta_{conc} = \Delta V_{rev} + \eta_{diff} \quad (I.5)$$

Gas conversion losses – This overpotential results from the change in gas composition with the current considering the conditions existing along the channel of the device under current [Laurencin2015]. It is expressed using the Nernst equation as follows:

$$\begin{aligned} \Delta V_{rev} &= \Delta V_{rev}^{H_2} + \Delta V_{rev}^{O_2} \\ &= \frac{RT}{2\mathcal{F}} \ln \left(\frac{y_{i=0}^{channel}(H_2) \cdot y_{i \neq 0}^{channel}(H_2O)}{y_{i \neq 0}^{channel}(H_2) \cdot y_{i=0}^{channel}(H_2O)} \right) + \frac{RT}{4\mathcal{F}} \ln \left(\frac{y_{i \neq 0}^{channel}(O_2)}{y_{i=0}^{channel}(O_2)} \right) \end{aligned} \quad (I.6)$$

Where $y_{i=0}^{channel}(x)$ and $y_{i \neq 0}^{channel}(x)$ are the molar fractions of the element x at the gas distribution channel under open circuit ($i=0$) and under current ($i \neq 0$). This expression does not consider the mass transport inside the porous electrode. It only reflects that the cell current density reaches a limiting value when all the reactants are consumed [Singhal2003]. Finally, it

is worth noting that the gas conversion losses depend only on the operating conditions defined by the current density and the gas feeding conditions. This ‘thermodynamic’ contribution is therefore the same whatever the SOC materials.

Gas diffusion losses – This contribution is related to gaseous transport limitations in the porous electrodes. Indeed, the paths for gas diffusion in an electrode are very entangled and imply a resistance to the gas transfer from the gas channel distribution to the electrochemical active sites. This limitation induces some partial pressure gradients that are strongly dependent on the microstructure morphology. These microstructure features can be characterized through the geometrical tortuosity and the constrictivity factor that describe the sinuous paths and the bottleneck effect, respectively (cf. Section II.5.1.2).

This phenomenon is exacerbated at high current densities since these operating conditions impose high gas fluxes through the electrodes. The associated overpotential can be described as follows (Eq. I.4) [Laurencin2011]:

$$\begin{aligned} \eta_{diff} &= \eta_{diff}^{H_2} + \eta_{diff}^{O_2} \\ &= \frac{RT}{2\mathcal{F}} \ln \left(\frac{y_{i \neq 0}^{channel}(H_2) \cdot y_{i \neq 0}^{sites}(H_2O)}{y_{i \neq 0}^{sites}(H_2) \cdot y_{i \neq 0}^{channel}(H_2O)} \right) + \frac{RT}{4\mathcal{F}} \ln \left(\frac{y_{i \neq 0}^{sites}(O_2)}{y_{i \neq 0}^{channel}(O_2)} \right) \end{aligned} \quad (I.7)$$

where $y_{i \neq 0}^{channel}(x)$, and $y_{i \neq 0}^{sites}(x)$ denote the molar fractions of the element x under current at the gas distribution channel, and at the vicinity of the active sites, respectively. It can be inferred that this overpotential is strongly dependent on the pore microstructure that is responsible for providing fast routes for gas transport. From this point of view, the effect of porosity level, along with the effect of having macropores are discussed in chapters V and II, respectively.

I.3.4 Activation overpotential

Beside the mass transfer limitation, the activation overpotential involves the irreversible phenomena occurring within the electrodes active layer. The activation losses include the limitations arising at each elementary step of the global electrochemical process (including interfacial ionic transfer, excorporation/incorporation of oxygen, oxidation/reduction reactions, or adsorption/desorption processes). These reaction pathways are discussed and illustrated for an O_2 electrode in LSCF-CGO in Section V.1.2.

At the ‘macroscopic’ cell level, it has been shown that the global activation overpotential could be modeled via the Butler-Volmer equation [Godula-Jopek2015]. In this phenomenological approach, the global activation overpotential is expressed as follows:

$$\eta_{act} = \eta_{act}^{H_2} + \eta_{act}^{O_2} = \frac{RT}{\mathcal{F}} \sinh^{-1} \left(\frac{i}{2i_0^{H_2}} \right) + \frac{RT}{\mathcal{F}} \sinh^{-1} \left(\frac{i}{2i_0^{O_2}} \right) \quad (I.8)$$

where i_0 is the “apparent” exchange current density in amperes normalized by the active electrode surface area, and it characterizes the electrode ability regarding its global electrochemical activity. In other words, its value is inversely proportional to the ‘global’ activation overpotential. This parameter is usually obtained by fitting the experimental data at low current densities. It depends mainly on the microstructure, the temperature and the gas composition. Indeed, the activation losses can be reduced by increasing the temperature, providing a catalyst, or more interestingly by providing more accessible reaction zones. This can be done by increasing the density of electrochemical active sites (TPBI density for example), which will enhance the electrode efficiency by providing more available sites for the electrochemical reactions.

Concluding this section, it should be retained that different losses occur within a SOC, which are responsible for the potential drop observed in the characteristic i - V curve evolution in Fig. I.3. Under operation, the ohmic losses induce a linear decrease in the electrode potential as a function of the current density. Besides, concentration polarization is responsible for the overpotential due to gas diffusion resistance in the porous electrodes. Finally, activation polarization emanates from the irreversible phenomena in the multi-step reaction mechanism, and has the particularity of being exponentially dependent on the temperature. The two last overpotentials are closely linked to the electrode microstructure. From this point of view, improving the SOC performances can be carried out thanks to a relevant microstructural optimization. Nevertheless, a reliable system requires also lasting performances over time. The following section deals with the central weakness of SOCs, which is their long-term durability.

I.4 SOC durability and degradation mechanisms

I.4.1 SOC durability

The high operating temperatures, along with the intense electrochemical potential gradients that a SOC withstands constitute an extreme environment for its components. This leads to materials degradation and thus a decline in cell performance over time. Nowadays, the durability of SOCs is the main limitation of this technology, which explains the ever-growing interest to quantify the degradation rates and to understand the underlying mechanisms. A large number of long-term experiments have been conducted in different conditions showing that the degradation rate of a SOFC (usually expressed as a percentage of cell voltage change in galvanostatic mode), is about 0.5 to 1 %. kh^{-1} [Tietz2006, Orui2008, Ghezal2013, Borglum2015, Hatae2015, Noponen2015, Trofimenko2015, Hubert2017]. However, higher percentages have been obtained in SOEC mode (i.e. $\sim 1\text{-}5\ \text{\%}\cdot\text{kh}^{-1}$) [Brise2008, Hauch2008, Schefold2013]. Even if these degradation rates are relatively low, they still need to be reduced in order to become economically competitive in the energy conversion marketplace [Blum2013]. The operating parameters affecting the degradation rates are still not precisely established [Hubert2017]. Nevertheless, a high operating temperature or thermal and redox cycling are believed to accelerate the cell degradation over time in both operating modes. Finally, the cell could also be a subject of contamination by the metallic interconnects, by impurities coming from the glass seal, or even by some raw materials during manufacturing.

I.4.1 Degradation mechanisms

In order to address the SOC ageing issue, several efforts have been paid to understand the underlying mechanisms of degradation. In practice, advanced post-test characterizations are required to investigate the changes in physico-chemical properties of materials or in electrode microstructure. Several degradation phenomena have been identified in the literature, affecting the different cell layers. The main reported processes include (i) materials reactivity, (ii) poisoning, or (iii) changing in material crystallography, and (iv) microstructural evolutions. A brief description of these phenomena is given hereafter for illustrative purposes. For more details the reader is invited to refer to the suggested references [Hubert2017].

(i) *Materials reactivity* – The electrochemical potential gradient inside an electrode induces the mobility of chemical or charged elements. For example, the reactivity of elements from the MIEC with the electrolyte creates secondary phases (SrZrO_3 , $\text{La}_2\text{Zr}_2\text{O}_7$), mainly localized at the interface between the two layers [Simner2006]. These new phases have a low conductivity and thus cannot be electrochemically active. Besides, its localization could favor the delamination of the electrode [Jiang1999]. As already mentioned, a thin CGO barrier layer is generally added between the electrode and the electrolyte to limit the material reactivity [Mai2006, Uhlenbruck2009, Adijanto2011].

(ii) *Poisoning* – The metallic interconnects are usually made in Chromium rich ferritic steel. It has been largely demonstrated that the Chromium can be released from interconnects under oxidizing atmosphere at high temperature and react with the O_2 electrode materials [Matsuzaki2001, Simner2005, Konyshева2006, Jiang2014]. While its transport process inside the electrode is still not conventional (between solid-state diffusion and volatilization and re-deposition) [Hilpert1996, Simner2005, Chen2010], gas humidity and high temperature are believed to accelerate this phenomenon [Hilpert1996, Chen2010, Tucker2006, Wei2015]. Finally, it should be noted that appropriate protective coatings on the interconnects are currently used to avoid the Cr poisoning. Moreover, using dry gas slows significantly down this process [Schuler2012].

(iii) *Changing in material crystallography* - The intrinsic properties of the dense electrolyte, classically made in YSZ, have been reported to undergo a loss in the ionic conductivity under reducing atmosphere [Linderoth2001, Haering2005, Kishimoto2012, Shimonosono2012]. A phase crystallographic transformation from cubic to tetragonal, which is less conducting has been observed after 20h of operation at 900°C [Kishimoto2012]. A high doping level of Zirconia has been suggested to limit this problem [Linderoth2001, Haering2005, Delaforce2007]. The contribution of this effect to the total cell degradation remains although negligible and limited over time [Aarberg1998, Liu2012].

(iv) *Microstructural evolutions* - Nickel coarsening and volatilization are considered as primary mechanisms for the H_2 electrode ageing. It was initially detected via Scanning Electron Microscopy (SEM) [Simwonis200, Jiang2003, Tanasini2009], then advanced 3D reconstruction techniques have been employed to investigate the complex microstructural evolutions of the cermet. This allowed quantifying the changes in terms of active TPBs

density, Ni phase size distribution, tortuosity and specific surface area. These studies revealed an increase in the mean particle diameter and a significant decrease in Ni percolation and active TPBLs density [Matsui2010, Cronin2011, Lay2014].

It is widely established that this phenomenon originates from the sintering of the metallic particles under high operating temperatures. Nevertheless, while the precise underlying mechanism is not yet conventional, it was systematically observed that it is strongly dependent on both the electrode microstructure and the operating conditions. Indeed, as expected, the temperature is a major accelerating factor for the Ni agglomeration [Sehested2006, Yokokawa2008, Pihlatie2011, Lee2014]. Besides, the mechanism was also found to be sensitive to the humidity [Jiang2003, Yokokawa2008, Holzer2011, Pihlatie2011, Lee2014], and polarization [Hagen2006].

Several attempts have been devoted to better understand this multi-variable complex problem by setting microstructural evolution laws, depending on the operating conditions. In practice, the decrease in electrochemical active sites is modeled by using some time-dependent laws fitted on data extracted from 3D reconstructions or 2D slice cuts [Faes2009, Nelson2012, Hubert2017].

In conclusion, the large-scale deployment of SOC technology is conditional upon the improvement of its long-term durability. Nowadays, an appropriate choice and integration of SOC materials allows alleviating a number of degradation processes as explained in Section I.2. Nevertheless, additional efforts should be done to decrease the degradation rates down to the industry requirements level. As the material deterioration in operation is associated to thermally activated processes, the decrease in the operating temperature should allow mitigating the degradation in performances. In this case, an electrode microstructural optimization approach is particularly relevant in order to maintain the high performances at these ‘intermediate’ temperatures. It appears then that the microstructure plays a major role in the SOC reliability as it is discussed in the following section.

I.5 Importance of microstructure

The SOC's performances are highly sensitive to the complex 3D microstructure of both the H₂ and O₂ electrodes [Kim2017, Abe2006, Ostergard1995, Suzuki2009, Virkar2000, Usseglio-Viretta2014]. This can be inferred from the dependence of the polarization overpotentials on the microstructure as explained in Section I.3. Indeed, the activation overpotential depends on

the available active sites for the electrochemical reactions (cf. Section I.3.4). One of the key parameters is the active Triple Phase Boundaries lengths (TPBl) defined by the lines where the percolated ionic, electronic and gas phases meet (cf. Section II.5.1.1). For example, the density of active TPBl directly controls the efficiency of the H₂ electrode, since the electrochemical reactions in the Ni-YSZ cermet take place at these electro-active sites [Hanna2014]. For the O₂ electrode, the higher performances of the LSCF-CGO composite with respect to the pure LSCF can be explained by the extension of TPBl in the bulk of the electrode [Dusastre1999, Kim2017]. Indeed, it has been suggested that the oxygen oxidation/reduction at TPBl according to the so-called “surface path” could control the global electrochemical reaction for the LSCF-CGO electrode [Hubert2016, Laurencin2015]. Aside from the TPBl, the interfacial specific surface areas $S_{i/j}$ between the electrode phases can also contribute to the global reaction mechanism (with i/j =electronic/pore, ionic/pore or electronic/ionic interfaces). For instance, it is suspected that the charge transfer at TPBl in the Ni-YSZ cermet can be co-limited by a gas interaction step with the YSZ or Ni surface [Hanna2014]. For the O₂ electrode, the reaction of oxygen reduction under SOFC mode is assumed to occur on the whole LSCF/pore interfacial surface area according to the so-called “bulk path” [Adler1996, Monaco2018]. In this reaction mechanism, the ionic charge transfer between LSCF and CGO is proportional to the contact surface area between the two materials. Aside from maximizing the active sites density, an easy access of charge carriers should also be provided to them. This can be achieved by offering well-connected paths throughout the electrodes with a minimum tortuosity and constrictivity (cf. Section II.5.1.2). This allows insuring fast transport and avoiding charge accumulation.

As discussed in Section I.3.3, the concentration overpotential is also strongly dependent on the pore microstructure. Indeed, the porosity is responsible for providing fast routes for gas transport throughout the electrodes. Similarly to the charge holders routes, the gas paths need to satisfy the same criteria for a fast transport. Nevertheless, it is worth pointing out that, unlike the activation overpotential, gas diffusion losses are less dependent on the operating temperature.

In addition to the strong impact on the performance, electrodes microstructure plays a key role on the cell durability as discussed in the previous section. Therefore, a clear understanding of the effect of microstructure on SOC electrodes macroscopic behavior is of central importance

for improving their reliability. An overview of the state-of-the-art of advances in this frame is given in the following section before presenting the proposed approach in the last one.

I.6 State-of-the-art review of the investigated fields

This section aims at giving a clear overview of the state-of-the-art of advances in the investigated fields. Four topics can be distinguished from the four milestones defined in the previous introducing chapter: “microstructure geometrical modeling”, “microstructural correlations”, “LSCF-CGO electrochemical modeling”, and “LSCF-CGO microstructural optimization”.

I.6.1 Overview on microstructure stochastic geometrical models

A lot of attempts have been devoted to the development of relevant 3D geometrical models able to mimic the actual microstructure of both two-phase electrodes (i.e. porous LSCF and LSC for example) and three-phase composite electrodes (i.e. Ni-YSZ cermet and LSCF-CGO composite for example). The published methods can be classified according to whether they involve a particle-based process or they adopt another geostatistical approach.

I.6.1.1 Particle-based models

Most available models are based on random sphere packing algorithms [Nishida2011, Prakash2014]. In this frame, many authors have assumed a uniform particle size whereas only few studies have taken into account a more realistic distribution on the sphere radii [Kenney2009, Zhang2011]. As a general matter, the sphere packing algorithms are decomposed into two steps. The first one is related to the creation of “seeds” corresponding to the positioning of the spheres. The second step is dedicated to the simulation of the “sintering” process in order to densify the microstructure up to the desired porosity. The first step can be done by the so-called “drop & roll” algorithm [Bertei2013, Kenney2009, Bertei2012, Zheng2016] or by the random positioning of “seeds” on a lattice structure [Nishida2011, Golbert2008, Metcalfe2010]. However, these methods are too much constrained, and hence, they are not able to account for the full stochastic nature of the actual SOC electrodes. For example, the positioning of spheres on a lattice results in a structuration of the final microstructure that is not realistic regarding the SOC microstructure. Furthermore, the “drop and roll” method yields an irrelevant anisotropy in the synthetic microstructures

[Ali2008]. To overcome this issue, some authors have developed algorithms with a pure random positioning of spheres [Cai2011, Rhazaoui2011]. The second step of the sphere packing methods is based on basic geometrical operations to increase the surface contact between particles (i.e. sphere radius expansion [Zheng2016, Golbert2008, Cai2011, Ali2008] or overlapping [Bertei2013, Kenney2009, Bertei2012] and creation of necks [Metcalf2010]). Aside from these pure geometrical approaches, the Discrete Element Method (DEM) has also been employed to simulate the initial sphere packing by computing the mechanical contact between the particles [Liu2011, Sanyal2010]; while the densification can be simulated by modeling the physical sintering process [Liu2011]. All these iterative methods need rather intensive CPU (Central Processing Unit) resources especially for the DEM computations.

I.6.1.2 Geostatistical-based models

In addition to the particle-based methods, other stochastic models based on geostatistical simulations can be used to generate synthetic microstructures [Lantuéjoul2002]. This approach can be used in an iterative process, based on the minimization of correlation functions between the synthetic microstructure and a real segmented image [Suzue2008, Baniassadi2011]. However, it is more usually used in a non-iterative process to take advantage of its very fast execution time. For this purpose, Neumann et al. [Neumann2016] have proposed a generalization of a multi-steps model decomposed in a homogeneous Poisson point process, a beta skeleton algorithm followed by the voxel phase labeling. With the same objective, Lanzini et al. [Lanzini2009] have applied the truncated Gaussian random field model to the SOC electrodes by considering a medium constituted of two phases (i.e. the pores with one solid phase). Abdallah et al. [Abdallah2016] have applied the Boolean random sets and the truncated plurigaussian random field model to generate a porous Ni-YSZ composite electrode. In the last case, the three sets related to the three electrode phases were obtained with set operations on the two underlying segmented independent Gaussian random fields.

I.6.1.3 Microstructure stochastic geometrical models validation

It is worth noting that few studies have been devoted to validate the morphological representativeness of the numerical SOC microstructures compared to the real ones. As a general matter, the sphere packing methods yield a final microstructure that keeps the geometry of the initial spheres. Therefore, as pointed out in [Prakash2014], the relevance of this morphology can be questionable if compared to the real SOC electrode microstructure in

which the phases exhibit a complex and continuous shape. Nevertheless, as discussed in Neumann et al. [Neumann2016], these approaches allow qualitative conclusions for the microstructural relationships even if ‘their applicability to real materials are still unclear’. For instance, Nishida et al. [Nishida2011] have succeeded with a random sphere-packing model to reproduce the experimental dependence of TPBs density with the solid phase volume fraction. However, Choi et al. [Choi2011] have compared a FIB-SEM reconstruction to a numerical microstructure generated by sphere packing. They obtained significant differences in the resulting structures.

For the other approaches based on geostatistical simulations, Neumann et al. [Neumann2016] have validated their model on a 3D reconstruction of a real Ni-YSZ electrode. The virtual microstructure fitted on the reconstruction presents a good agreement not only visually but also quantitatively in terms of morphological parameters (geometrical tortuosity factors, constrictivity parameters, density of TPBs after smoothing) and phase effective conductivities. Nevertheless, they found a significant mismatch for the interfacial specific surface area. Abdallah et al. [Abdallah2016] have fitted their 3D synthetic microstructures on the covariance function measured on 2D SEM micrographs of a Ni-YSZ cermet. They have shown that the Boolean sets method is not relevant for SOC electrode modeling. However, the microstructure generated with the plurigaussian model was found ‘to be visually very close to the materials’. Moreover, in addition to the fitted covariance functions, they also found a good agreement in terms of phase size distributions and the linear erosion functions (measured on the 2D SEM images).

I.6.2 State of the art of microstructural correlations

In order to establish the electrode microstructural correlations, a first strategy is based on the manufacturing of several electrodes by changing both the composition and the Particle Size Distribution (PSD) of the initial powder. The microstructural properties (L_{TPB} and $S_{i/j}$) can be measured on 3D reconstructions obtained by X-ray Computed Tomography (XCT) [Cronin2013, Grew2010, Hubert2018, Shearing2012, Villanova2013] or by Focused Ion Beam Scanning Electron Microscopy (FIB-SEM) [Holzer2011, Vivet2011, Wilson2006]. This experimental approach requires a large number of samples for parametric studies. However, the number of experiments is generally very limited since this method is time

consuming. Therefore, the dataset is usually insufficient to fully validate the complex microstructural relationships [Chen2013, Gokhale2009].

An alternative approach consists in theoretical developments based on geometrical considerations. In this frame, numerical approaches can be used to derive some pure phenomenological microstructural relationships. They are based on the generation of synthetic 3D microstructures obtained by the random packing of initial spheres (Section I.6.1.1) or by geostatistical simulations (Section I.6.1.2). As a general matter, these methods require intensive computational means for the generation of a large dataset of 3D microstructures and must also involve complex optimization algorithms of data mining [Stenzel2017].

Aside from these numerical computations, some analytical developments based on the percolation theory have been proposed to establish the microstructural correlations. Most of them are focused on the density of TPBI [Chen2013, Bertei2011, Chan2004, Chen2011, Janardhanan2008, Sunde2000, Sunde1996, Zhang2011], while Chen et al. [Chen2013] and Costamagna et al. [Costamagna1998] have dealt with the interfacial specific surface area between the electronic/pore and ionic/electronic phases, respectively. All these mathematical models, which are based on pure geometrical considerations, are free from the computational cost of 3D simulations but require some simplifications. All these models consider spherical particles for the electronic and ionic conductors that are loosely packed. The particles of each constituent have the same coordination number while the distance between the particle centers (or the contact angle) depicting the spheres intersection is constant. In the first studies, the spheres of each phase were assumed to have the same size [Chan2004, Costamagna1998, Sunde2000]. This simplification has been recently improved by extending the modeling to poly-dispersed particles [Chen2013, Bertei2011, Chen2011, Janardhanan2008, Zhang2011]. Nevertheless, they still do not capture the effects of particle shapes/morphologies and the distribution on the coordination number. However, a distribution of the coordination number is expected in real microstructures exhibiting a scattering on the particle size. Indeed, there is a clear correlation between the particle size and the number of bonds in the lattice. Moreover, a distribution on the contact angles related to the particles intersection could also affect the distribution on the coordination number. Finally, it is worth noting that all these models rely on the knowledge of the particles intersection and/or the coordination number. Nevertheless, the definition and the computation of these properties for real partially sintered

microstructures is not straightforward and requires further simplifying assumptions [Gokhale2009].

To overcome these issues, Gokhale et al. [Gokhale2009] have proposed a stochastic geometry based analytical expression for the total L_{TPB} related to the overall phases (i.e. including the percolated phases and the disconnected clusters). The model is applicable for particles of any convex shapes and size distribution. For this purpose, they have used the notion of “extended” microstructure, widely employed in modeling phase transformations [Avrami1939, Avrami1940, Avrami1941, Fanfoni1998, Gokhale1980, Gokhale1984, Jones1997]. With such an approach, the effects of the particle shape and size distribution can be taken into account. This geometrical method has been initially employed by Gokhale et al. [Gokhale2009] to express L_{TPB} in composite electrodes, taking into account the actual PSD of spheres (eq. IV.4). The consistency of this theoretical relation has been checked by Zhang et al. [Zhang2012] thanks to 3D simulated volumes generated by an algorithm developed to produce the same microstructure as defined in the analytical model. As expected, they have found a very good agreement between the simulated and predicted TPBI. They have also checked that this correlation stands to accurately predict the active density of TPBI as long as the electrode phases are well connected (i.e. solid phase volume fraction higher than 30 % and porosity higher than 10% in their case). From our best knowledge, no correlation has been proposed for the interfacial specific surface areas.

I.6.3 Overview on LSCF-CGO reaction mechanisms

In some recent attempts, some models have been proposed in literature to better understand the electrochemical behavior of LSCF-CGO composite. However, for most of them, a mechanism fully controlled by the ‘bulk’ path has been assumed whereas the potential role of TPBIs has been ignored [Mortensen2014, Nielsen2011, Yurkiv2014]. For example, Mortensen et al. [Mortensen2014] have derived an analytical expression for impedance at Open Circuit Potential (OCP) for the composite electrodes. The model takes into account effective oxygen vacancy diffusion for the two solid phases, a global reaction of oxygen exchange at the surface of the MIEC particles and gas diffusion in the porosity of the electrode. Yurkiv et al. [Yurkiv2014] have developed an elementary dynamic kinetic model in which they have also supposed that the oxygen reduction only proceeds via the bulk path. The oxygen is at first adsorbed, dissociated and ionized on the surface of the LSCF before to be

directly incorporated into the bulk of CGO. Çelikbilek et al. [Çelikbilek2016] have proposed a steady-state 3D model for hierarchically nanostructured composite electrode considering a mechanism based on the bulk path. For our best knowledge, only Kim et al. [Kim2017] have recently investigated the potential role of TPBIs by using a stationary model for which ‘macroscopic’ exchange current densities for the bulk and surface paths have been fitted on experimental i - V curves recorded in fuel cell mode. They have inferred from their analysis that ‘electrochemical reaction in LSCF-CGO cathode cannot be explained only by the surface reaction but that additional contribution such as TPBIs reaction must be considered’ [Kim2017]. From this point of view, it appears that the detailed reaction mechanism for the LSCF-CGO composite electrode and the role of microstructure is still a subject of investigation.

I.6.4 State of the art of LSCF-CGO microstructural optimization

Despite the lack of knowledge of the LSCF-CGO reaction mechanisms, several experimental works have been conducted in order to identify the optimum content of CGO into LSCF. All the studies have been carried out with the classical $\text{La}_{0.6}\text{Sr}_{0.4}\text{Co}_{0.2}\text{Fe}_{0.8}\text{O}_{3-\delta}$ material. By adding a $\text{Ce}_{0.9}\text{Gd}_{0.1}\text{O}_{1.95}$, Kim et al. [Kim2017] have found that the lowest polarization resistance was achieved for a weight ratio of LSCF:CGO = 34:66 wt% at 700°C under 100% O_2 (corresponding to a volume ratio of LSCF:CGO = 30:70 vol%). On the same material, Leng et al. [Leng2008] have reported an optimum in performances at 600°C under air for a slightly lower content of CGO (i.e. 60 wt%).

By using a stoichiometric $\text{Ce}_{0.8}\text{Gd}_{0.2}\text{O}_{2-\delta}$, Murray et al. [Murray2002] reported a minimum in polarization resistance for a composition of LSCF:CGO = 50:50 wt% over a temperature range of 500-750°C in air, while Qiang et al. [Qiang2007] obtained the lowest polarization resistance when 40wt% CGO was added to $\text{La}_{0.58}\text{Sr}_{0.4}\text{Co}_{0.2}\text{Fe}_{0.8}\text{O}_{3-\delta}$ over a temperature range of 650-800°C under air.

The relative scattering in the optimal composition of the LSCF-CGO composite electrode can be obviously explained by the difference in the CGO stoichiometry and in the operating testing conditions. Nevertheless, it can be also suspected that other microstructural parameters could have a significant influence on the optimization. For instance, it is well established that a fine microstructure could increase the performances by increasing the density of TPBIs and the specific surface area. Leng et al. [Leng2008] have thus suggested that any substantial

decrease of the LSCF particle size could lower the optimum content of CGO to beyond 50 wt%.

The porosity can also have an influence on the optimization by promoting the gas diffusion into the electrode. For example, Çelikkilek et al. [Çelikkilek2016] have shown that the polarization resistance at 500°C of nanostructured composite electrode is highly sensitive to the porosity with a minimum at around 20 % for a composition of LSCF:CGO = 43:57 wt%. As a consequence, the composition, the porosity and the particle size are expected to affect the electrode global performances by changing the effective ionic/electronic conductivity, gas diffusivity and the active sites for the electrode reactions (i.e. density of TPBIs and specific surface area). A thorough study is then required to decorrelate the effect of each microstructural parameter on the electrode performances and to identify the best compromise between the composition, the particle size and the porosity.

I.7 Conclusion and methodology

This chapter was dedicated to introduce the context of high temperature Solid Oxide Cells. The operating principle, the state of the art of electrode materials and design, as well as the physical phenomena have been recalled. It was particularly highlighted that the different cell overpotentials, arising under operation, are intimately dependent on the porous electrodes microstructure.

The long-term degradation, which constitutes the central limitation for this technology, has been addressed secondly. In this frame, a quick overview of the main degradation mechanisms has been provided. In order to face these thermally activated processes, it was proposed to lower the operating temperature. In this case, an electrode microstructural optimization is necessary to maintain the high performances at these ‘intermediate’ temperatures.

As the microstructure plays a major role on both cell performance and durability, our course of action is mainly centered on this electrode characteristic. In this objective, a coupled experimental and numerical approach has been adopted to better understand the microstructural correlations and to unravel the role of electrode microstructure on its performance.

The experimental part has a first microstructural facet including the tomographic imaging employed to reconstruct the electrodes microstructure, the post-processing of the raw data, and the fine quantification of the segmented volumes. In this frame in-house multi-scale tools need to be adapted, and others need to be developed to take into account the specific microstructural characteristics of the studied electrodes. The extracted morphological and physical data are valuable for the later models validation. A second electrochemical facet includes the measurements undertaken on a symmetrical LSCF-CGO cell in order to record the steady (i - V curve) and transient (EIS) answers at various operating conditions. This allows drawing some preliminary conclusions on the reactions mechanisms in this composite electrode. Besides, it serves primarily to validate an in-house electrochemical model employed later in this study.

The modeling part consists in morphological and electrochemical simulations. Stochastic geometrical models able to mimic the specific morphology of SOC electrodes microstructures have been developed. Two models based on different considerations are considered for this purpose; an original stochastic particle-based model and a geostatistical-based method founded on the Gaussian Random Fields. A special attention is paid to fully validate both methods on the reconstructions obtained for both O₂ and H₂ electrodes. The models flexibility to simulate ‘non-classical’, but promising, microstructures is discussed afterwards. It can be noticed that the proposed particle-based model has been developed with the participation to the work of a Mater internship student (Luca Rinaldi).

Once validated, the geometrical models are used to generate a large set of synthetic volumes for the calibration and validation of some proposed microstructural correlations. In this purpose, the notion of “extended microstructures” is employed to propose some relationships between the microstructural parameters. This allows particularly a better understanding of the complex link between the reaction sites density (like TPBIs and $S_{i/j}$), and the “basic” electrode parameters (like composition, porosity, and particle diameter). Finally, the reliability of the semi-analytical expressions needs to be checked with real 3D electrode reconstructions.

Since the reaction mechanism of O₂ electrodes is still not precisely understood, an in-house model is used to analyze the electrode operating pathways and their dependence on the electrode microstructure. The model is built by considering an equivalent homogenous medium of the composite porous electrode for which the effective properties are computed on

the 3D reconstruction. The model needs to be calibrated and validated by using both morphological and electrochemical, experimental results. This will allow assessing more precisely the predominance of the reaction mechanisms and understanding the link between the electrode microstructure and its performances. In the frame of this work, we chose to address the LSCF-CGO composite electrode microstructural optimization for illustrative purposes. It is worth noting that this electrochemical part has been conducted in collaboration with the thesis of Elisa Effori, aiming to evaluate the effect of pressure on the LSCF-CGO reaction mechanism.

This coupled experimental and modeling methodology based on microstructural and electrochemical considerations enables to better understand the effect of microstructure on the LSCF/CGO composite reaction mechanism. Besides it allows addressing some numerical microstructural optimizations, thus providing useful recommendations for the electrode design and manufacturing.

Chapter II: 3D reconstruction and characterization of SOC electrodes microstructures

It is clearly recognized that the microstructure of porous SOC electrodes governs their performances and long-term stability (cf. Section I.4.1). From this point of view, the full characterization of these complex microstructures seems imperative in an objective of electrode performance optimization. The Scanning Electron Microscopy (SEM) has been used for a long time to obtain two-dimensional SEM micrographs of fractured or polished cross-sections. This technique provides some useful microstructural information and enables the extraction of some basic metric properties like the phase volume fractions (cf. Section II.4.1). However, the true nature of these media cannot be assessed accurately without a three-dimensional reconstruction. Indeed, a fundamental understanding of some microstructural effects (like charge and gas transport phenomena) requires a 3D characterization. Indeed, some structural parameters of higher order topology can only be computed on a 3D volume of the porous electrode. For instance, the phase tortuosity and constrictivity (cf. Section II.5.1.2), which quantify the pathways convolution and the bottleneck effect respectively, cannot be measured from 2D micrographs. Besides, only a 3D analysis can show whether the phases are percolating or not.

The ceramic components of SOCs present highly absorbent materials, and a large field of view is usually required to be statistically representative of the whole electrode [Laurencin12]. For these reasons, two adapted tomographic methods are commonly used to reconstruct the spatial structure of these porous media, i.e. FIB-SEM tomography and X-ray tomography. Considering the advantages and drawbacks of each method [Laurencin12], the selection of the technique is driven by a necessary compromise between the volume size and the image resolution. Irrespective of the chosen method, the following progression has been systematically performed after image acquisition: firstly, raw data generally require a specific treatment to improve the quality of the 3D reconstruction and then to facilitate the thresholding step. A Representative Volume Element (RVE) of the segmented microstructure has to be estimated afterwards using here a volume expansion method described by Yan et al. [Yan17]. Finally, a set of electrode morphological and physical parameters is computed on the extracted volume. These properties allow quantifying the specific surface areas, the density of

electrochemical active sites, and the effective transport properties in the porous electrodes that are the main microstructural input data for a proposed electrochemical model. In this chapter, the studied cells are presented in a first step, then the methodology for image acquisition, segmentation and characterization is presented subsequently, and finally the results are presented and discussed in a last section.

II.1 Presentation of the investigated cells

Three different cells were analyzed in the frame of this study, two commercial complete cells (electrolyte sandwiched between an O₂ and H₂ electrodes) and one in-house symmetrical cell (electrolyte sandwiched between two O₂ electrodes). This section describes these cells in terms of design, material composition, and layered structuration.

II.1.1 Cell-A: commercial complete cell in LSCF and Ni-YSZ

The first investigated cell, later named Cell-A, is a commercial circular cell (multi-layered disc-shaped object) with a hydrogen electrode used as mechanical support. The electrolyte and hydrogen electrode have a diameter of 50 mm whereas the oxygen electrode presents an active surface of 9.08 cm². The electrolyte is made of a dense 5 μm thick layer of 8%mol Yttria stabilized Zirconia (YSZ). The hydrogen electrode is a ceramic-metallic composite of nickel and YSZ (Ni-YSZ) with a thickness of about 260 μm. The oxygen electrode is composed of several layers. A barrier layer made of 10%mol Gadolinium doped Ceria (Gd_{0.1}Ce_{0.9}O_{1.95} abbreviate CGO) is first added on the electrolyte to avoid chemical reactivity. It should be noticed that this layer is not fully dense. Then, a composite active layer of CGO and La_{0.6}Sr_{0.4}Co_{0.2}Fe_{0.8}O_{3-δ} (LSCF) is deposited. The LSCF-CGO composite material ensures a good matching between the thermal expansion coefficients of the cell layers. A single phase LSCF porous layer of about 18 μm thickness is added to the oxygen electrode. Finally, a La_{0.5}Sr_{0.5}CoO₃ (LSC) layer of about 20 μm is present on the surface of the oxygen electrode to improve the current collection. All the thicknesses and compositions are summarized on the Figure II.1 obtained by SEM.

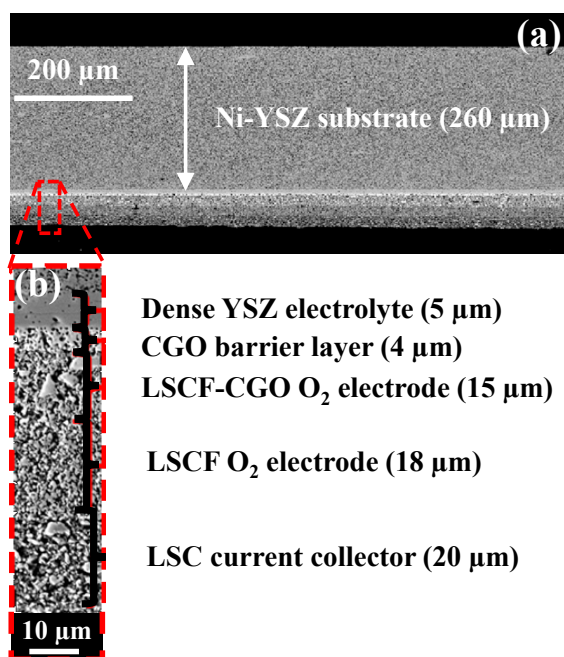


Figure II.1 Cell-A imaging: (a) SEM cross-section image obtained with Secondary Electron Detector of Cell-A, (b) zoom over the cell showing the materials and dimensions of the different cell layers.

II.1.2 Cell-B: commercial complete cell in LSC and Ni-YSZ

The second studied cell is also a H₂ electrode Supported Cell, referenced as Cell-B in the following of this work. The substrate consists of a thick Ni-8YSZ layer (Ni with 8 mol.% Y₂O₃—ZrO₂) with a thickness of 500 μm and a diameter of 35 mm. A polished cross section image of this layer was obtained using a Scanning Electron Microscope (Philips XL30) in Back Scattering Electron mode. The obtained greyscale image is shown in Fig. II.2a with the black region representing porosity, and grey region being the solid phase. It can be seen that this substrate contains large scale porosities of some micrometers size which distinguish this current collecting layer.

Higher magnification SEM images in Fig II.2b and II.2c allow distinguishing the other constitutive cell layers. A Ni-8YSZ functional layer of 10 μm with a fine microstructure is deposited on the substrate. The electrolyte consists in a dense and thin 8YSZ layer (5 μm) whereas the O₂ electrode is made of LaSrCoO_{3- δ} (20 μm). An intermediate layer of CGO (Gd doped CeO₂, 2 μm) is also added between the electrolyte and the O₂ electrode.

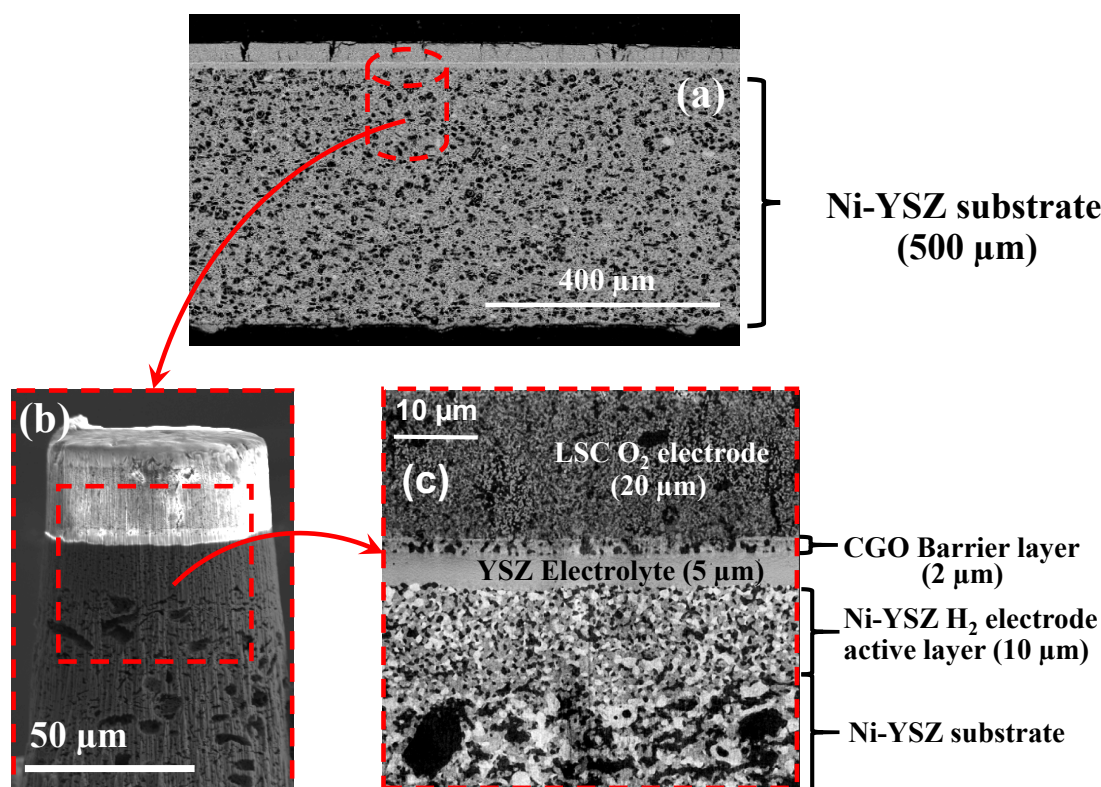


Figure II.2 Cell-B imaging: (a) SEM cross-section image of Cell-B observed in BSE mode, (b) cylindrical sample prepared by Xe PFIB for the tomographic experiment (Scanning Electron Image taken in secondary electron mode at 15kV), and (c) 2D cross section taken in the 3D reconstruction (image in grey level with porosity in black, Ni in dark grey and YSZ in bright grey).

II.1.3 Cell-C: in-house symmetrical cell in LSCF-CGO

The third studied cell is an in-house symmetrical button cell manufactured with LSCF-CGO electrodes deposited on each side of a circular and dense electrolyte in Yttria Stabilized Zirconia YSZ (cf. Fig. II.3). The electrodes were fabricated using a powder mixture composed of 50 wt.% of $\text{La}_{0.6}\text{Sr}_{0.4}\text{Co}_{0.2}\text{Fe}_{0.8}\text{O}_{3-\delta}$ and 50 wt.% of $\text{Ce}_{0.8}\text{Gd}_{0.2}\text{O}_{2-\delta}$ layered by screen printing and sintered under air. In order to avoid any misalignment in the position of the CE (Counter Electrode) with respect to WE (Working Electrode), a special attention has been paid to center the electrodes (thickness = 35 μm and diameter = 11.3 mm) onto the YSZ disk (thickness = 260 μm and diameter = 25 mm). Finally, a thin $\text{Ce}_{0.8}\text{Gd}_{0.2}\text{O}_{2-\delta}$ barrier layer of 2 μm was added between the electrodes and the electrolyte in order to avoid the formation of secondary phases between LSCF and YSZ [Anderson04].

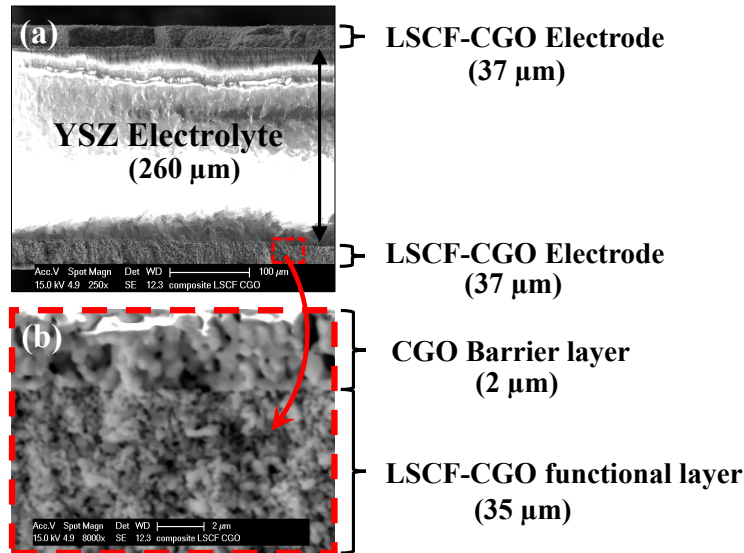


Figure II.3 Cell-C imaging: (a) SEM cross-section image obtained with Secondary Electron (SE) Detector of Cell-C, (b) materials and dimensions of the different cell layers.

II.2 Three-dimensional reconstruction of SOC electrodes

Two techniques were used in the frame of this study to obtain 3D reconstructions of the investigated electrodes microstructures, the FIB-SEM tomography and X-ray tomography. The choice of the method to use depends on the desired volume size and resolution. As a general matter, FIB-SEM is well adapted to reconstruct cell electrodes with a fine microstructure, requiring high image resolution (the electrode functional layer for example). Indeed, this method allows imaging volumes of around 10^3 - $15^3 \mu\text{m}^3$ size with a very fine resolution of down to 10 nm. The X-ray holotomography on the other hand leads to overall lower resolutions of around 50 nm. However, this method allows reconstructing volumes with a large field of view of up to $50^3 \mu\text{m}^3$ (which is well adapted for the electrode substrate for instance). An appropriate spatial resolution is required to accurately describe the electrode microstructure. Indeed, an optimal resolution is needed to catch all the microstructural details of different length scales in an electrode without leading to excessive computational time for image processing. The spatial resolution has been discussed by Joos et al. [Joos2012] and Usseglio et al. [Usseglio15]. It has been shown by Joos et al. [Joos2012] that 10-15 voxels are necessary on a particle diameter to determine accurately the specific surface area. Usseglio et al. [Usseglio15] showed from a sphere-packing model that the theoretical value of the specific surface area is reached at 10 voxels per particle diameter. Besides resolution, a relevant

reconstruction volume size is necessary to be statistically representative of the whole electrode without leading to superfluous computational time as well. A study on the RVE determination has been carried out in Section II.6. Finally, depending on the desired resolution and RVE size, one of the two methods has been adopted. In this section, a description of the protocol of both methods is presented, from sample preparation up to the final raw images stack processing.

II.2.1 3D reconstruction via FIB-SEM tomography

Since its first deployment in SOC electrodes imaging in 2006, the interest in Focused Ion Beam – Scanning Electron Microscopy (FIB-SEM) has been growing continuously. The first 3D reconstruction, reported by Wilson et al [Wilson2006], was based on 82 consecutive images of a Ni-YSZ H₂ electrode with a reported distance between images of about 50 nm. It was not then common to impregnate the electrode with contrast-enhancing epoxy resin prior to imaging, making it hard to distinguish the solid phase from porosity. Nonetheless, a manual segmentation of the raw data allowed computing a number of microstructural properties, giving therefore a rough idea of the electrode architecture. Nowadays, a particular attention is being paid for sample preparation and image processing giving more confidence to the obtained reconstructions, while keeping a reasonable acquisition time [Vivet2011, Kanno2011, Joos2014]. In the frame of this work, this technique was used for the O₂ electrodes of both Cell-B and Cell-C in order to catch accurately their fine microstructure. The procedure from sample preparation to image acquisition is presented hereafter for Cell-C as an illustration.

The sample was first impregnated under vacuum conditions in order to fill the pores with an epoxy resin. This enables to minimize the undesirable damage of the specimen, to avoid accumulation of gallium ions in the pores during the FIB milling and to improve the contrast between the porosity and the solid phases [Vivet2011]. The serial sectioning and the image acquisition were carried out in a FEG-SEM NVISION 40 from Carl ZEISS® microscope. For SEM observation, Energy selective Backscatter (EsB) detector with a low acceleration voltage of 1.5 kV was used in order to clearly distinguish the LSCF and CGO solid phases. Then, images with a pixel size of 10 nm were captured sequentially with a z-axis slice pitch of 10 nm using a milling current of 1.5 nA (Fig. II.4). A stack of 1987 images, each having a size of 1115x1115 pixels was collected. The resulting reconstruction exhibits a dimension of

$19.87 \times 11.15 \times 11.15 = 2470 \mu\text{m}^3$ with a cubic voxel size of 10 nm. Following the same protocol, a larger volume of $17^3 = 4919 \mu\text{m}^3$ was obtained for the LSC O₂ electrode of Cell-B, with a fine spatial resolution of 16.5 nm.

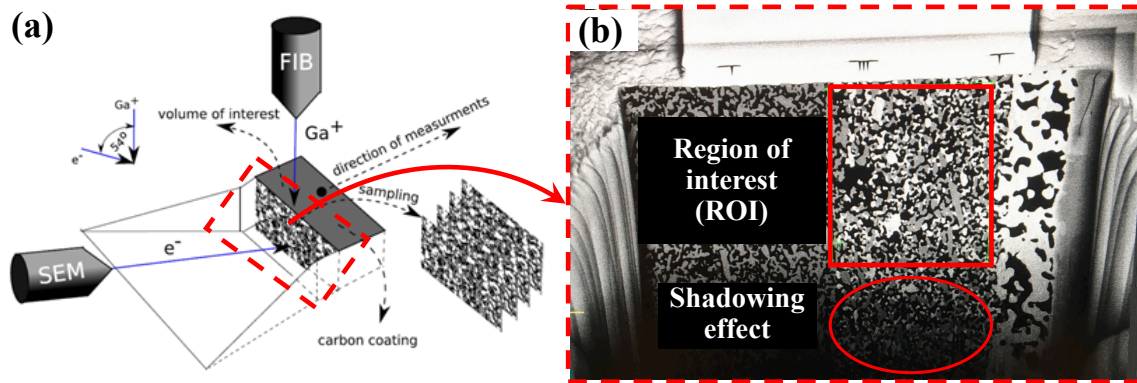


Figure II.4 (a) FIB-SEM working principle [Brus2014], (b) SEM image of the Cell-C sample during the “milling and imaging” process. The region of interest (ROI) is displayed in the red rectangle, and the shadowing effect is highlighted in the red ellipse.

II.2.2 3D reconstruction via synchrotron X-ray holotomography

Less widely used for SOC imaging compared to FIB-SEM tomography, the synchrotron X-ray nano-holotomography presents an interesting solution for electrode reconstruction when a particularly large volume size is required. This technique is well adapted for electrodes with coarser microstructures or large-scale porosities (the electrode diffusion layer for example). The new Nano-Imaging beamline ID16A of the European Synchrotron Radiation Facility (ESRF) has been used in this context for the magnified SOC holotomographic experiments. A special attention has been paid within the framework of a previous thesis [Hubert2017a] to improve the sample preparation procedure, the recording process and the spatial resolution measurement. This method has been used to reconstruct both O₂ and H₂ electrodes of Cell-A in the frame of previous work [Hubert2017a] while the H₂ electrode of Cell-B (with both functional and diffusion layers) have been especially acquired for the present study. An overview of this method procedure is presented hereafter.

An accurate X-ray nanotomography measurement lies on an adequate sample preparation. Both size and geometry of the sample influence the accuracy of the projections recorded during a scan. In practice, a compromise should be reached for the sample thickness in order to limit absorption while keeping a large volume size to be statistically representative of the

whole electrode. In this work, the samples were prepared by milling cylindrical pillars in the cells with a plasma Focused Ion Beam (PFIB) working with Xenon ions (Fig. II.2.b). This relatively fast method [Hubert2017a] results in a pillar that is welded on a needle support to handle the specimen for the tomographic scan. Afterwards, the diameter of the sample is reduced down to $\sim 50\mu\text{m}$ in a P-FIB chamber. A low current of 59 nA is used to obtain a smooth and undamaged surface sample with a cylindrical geometry. The sample is then scanned at the ID16A nano-Imaging beamline (ESRF) with selected X-ray energies of 17.05 keV and 33.60 keV for the O_2 and H_2 electrodes, respectively. The detailed protocol for data acquisition and the procedure for the electrode reconstruction can be found in. [Hubert2016, Hubert2017a, Hubert2017b]. The 3D images after reconstruction present a volume as large as $\sim 50\ \mu\text{m} \times 25^2\ \mu\text{m}^2 \times \pi = 98174\ \mu\text{m}^3$ with a voxel size of 25 nm. The reconstructed greyscale image stacks are thus ready for the subsequent image processing before segmentation.

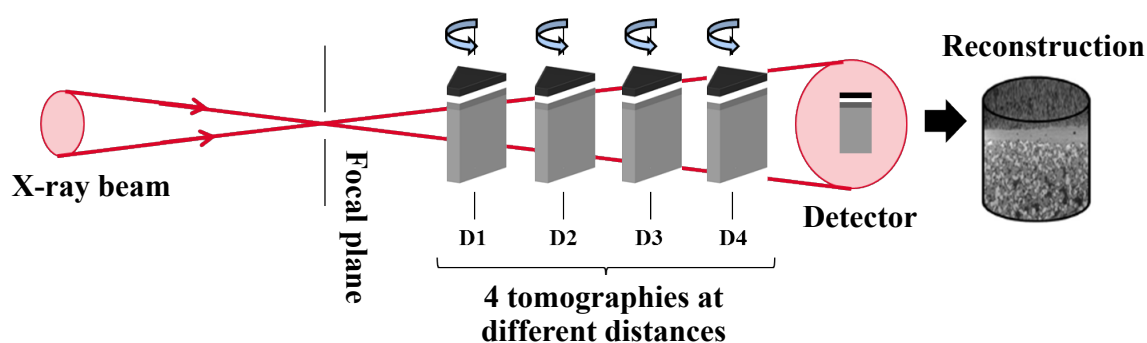


Figure II.5 Working principle of X-ray nano-holotomography.

II.3 Raw image processing and segmentation

In order to compute the microstructural parameters on the reconstructed volumes, the greyscale images need to be segmented. This step is of capital importance to separate the different phases that compose an electrode. Nevertheless, a series of image processing and data analyses are required to enhance the image quality before proceeding to the thresholding step. The aim of this section is to give an overview of the steps undertaken in this frame.

The grey level within the same phase in the raw images stack is usually heterogeneous and noisy. Therefore, the first step is to apply a smoothing filter to homogenize the grey intensity within the same phase, while preserving sharp edges between the phases. This practically allows enhancing the peak separation in the histogram and having a good contrast between

phases. For this end, an anisotropic diffusion filtering proposed by Malik and Perona [Perona90] was retained. This filter has been shown to be suitable for similar SOC materials image processing [Villanova13]. Once this filtering process is applied to the full 3D volume, the segmentation of the different phases is made easier. An automated segmentation method is used for the identification of the phases. The approach is based on Otsu's method [Otsu1979], which determines the optimal threshold value to maximize the between-class variance. This general method is appropriate whatever the number of phases, and thus is applicable for both O₂ and H₂ electrodes. However, in the case of a three-phase material, an artefact arises during the segmentation step between the brightest phase and the darkest one. Indeed, a thin layer of an intermediate grey level is created in-between. This unreal transition zone is due to the finite spatial resolution and the finite voxel size [Holzer2011]. The correction of this border is done via an in-house program dividing these voxels between the two adjacent phases [Usseglio-Viretta2015]. Finally, in the case of a FIB-SEM reconstructed electrode, an undesired misalignment of 2D slice images is observed (cf. Fig. II.7a). This random shift can add up to a significant number of pixels in the whole stack, leading to errors in the microstructural parameters computation [Joos2010, Joos2012]. In order to fix this undesired drift, a program has been developed in order to readjust the image stack and the resulting volume was cropped to keep only the ROI common to all slices (cf. Fig. II.7b). In practice, the correction is carried out with an opening-closing morphological operation. The geometry of the structuring element is a thin plate allowing the image realignment without changing the microstructure as shown in Fig. II.7.

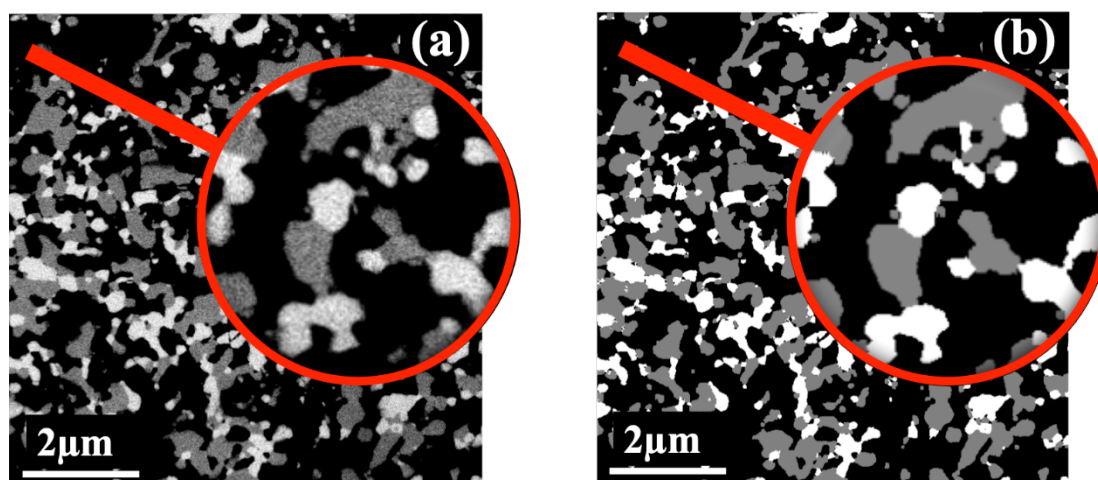


Figure II.6 Slice from the raw greyscale images stack (a), and from the final segmented stack for LSCF-CGO O₂ electrode of Cell-C (b): black color represents porosity, grey LSCF and white CGO.

The proposed image processing and thresholding steps allow obtaining 3D segmented reconstructions on which it is possible to directly compute all the microstructural properties. However, for a fine characterization of the diffusion layer of Cell-B (containing a bi-modal pore size distribution), it is important to characterize the micro- and macro-pores separately as they result from different manufacturing processes. In this objective, a morphological procedure has been developed to separate these two different length-scale voids.

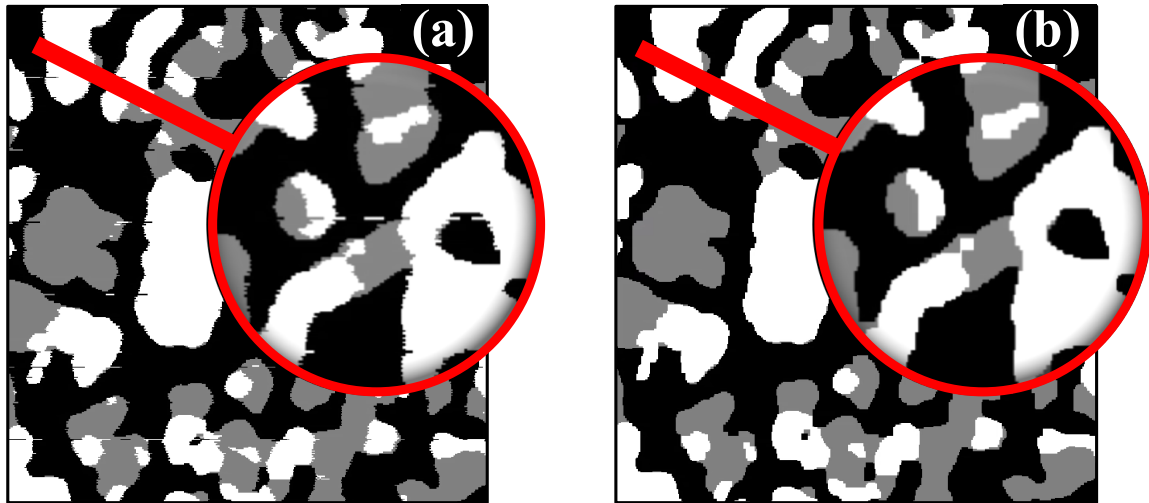


Figure II.7 FIB-SEM images stack before drift correction (a), and after alignment (b) for LSCF-CGO O₂ electrode of Cell-C (black color represents porosity, grey LSCF and white CGO).

II.4 Macropores separation from the micropores network in the diffusion layer

A procedure based on mathematical morphology [Serra1988] has been proposed to separate the large-scale porosities from the micropores network. The main operations applied on the porous phase of the substrate reconstruction are summarized hereafter:

- (1) Apply a morphological erosion: a small spherical structuring element has been used in this first step to remove the very small porosities leading to discontinuities within the microporosity network. Moreover, the volume of the remaining pore phase (micro and macro pores) is shrunk according to the radius of the structural sphere.

- (2) Remove small disconnected porosities: Once the micropores are disconnected, it becomes easy to delete them. Indeed, all the disconnected pores are identified and then removed if their size is smaller than a critical value.
- (3) Apply a morphological dilatation on the pore phase: This operation allows retrieving the external part of the macropores that was erased by the morphological erosion of step (1). Therefore, a spherical structuring element of the same size was used in this case.

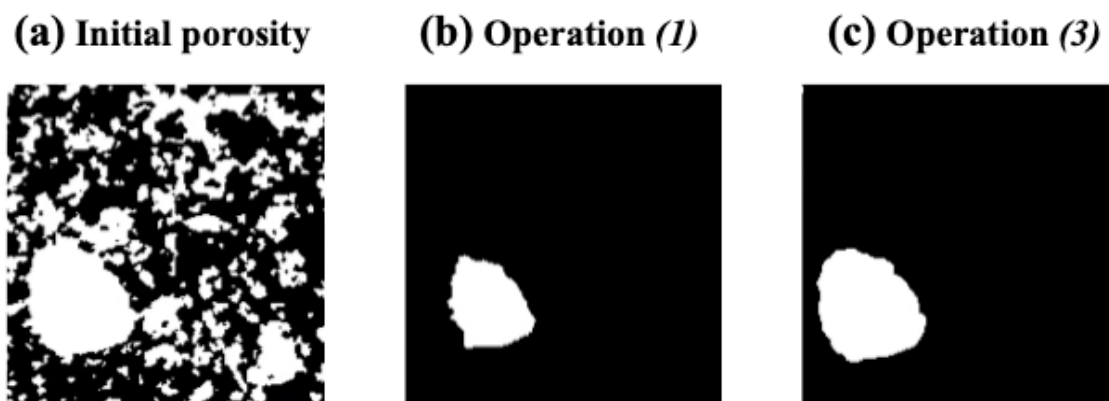


Figure II.8 Illustration of the different steps for the separation of the macropores from the micropores network. Step (2) was not necessary in this particular illustrative case, as the fine micropores were deleted using step (1).

II.5 Microstructural quantitative characterization: properties measurement

After the raw image processing, the electrode reconstruction consists in a 3D matrix where each voxel represents a given phase (porosity, ionic/electronic conductor or mixed ionic/electronic conductor). Significant microstructural properties can be calculated on these segmented data to characterize the charge/gas transport process and the reaction sites of the electrode. These parameters are assumed to ‘fully’ characterize the electrode microstructure, and are particularly crucial to understand the impact of microstructure on the cell performances. This section presents numerous methods and algorithms developed for the calculation of these parameters. A literature review of other available methods is also given. Two sets of microstructural parameters can be distinguished, morphological and physical ones. The morphological parameters allow quantifying the geometrical attributes of the electrode microstructure and particularly the electrochemical reaction sites. The physical parameters allow assessing mainly the gas and charge transport phenomena.

II.5.1 Morphological parameters

The electrode morphological properties define the shape of each phase and how it is distributed in the 3D space. These parameters can be classified into two subsets, metric and topological parameters. The metric properties have the particularity to hold a unit, in general a distance in μm , a line density in $\mu\text{m}/\mu\text{m}^3$, a surface density in $\mu\text{m}^2/\mu\text{m}^3$, or a volume density in $\%.\text{vol}$. On the other side, the topological properties are usually expressed as a measure of objects number, connectivity, or proximity.

II.5.1.1 Metric properties

There are two ways to compute the metric properties from a given 3D microstructure. The first method consists in counting the number of voxels (3D pixels) that satisfy a condition on phase nature or proximity. This direct method usually requires correction terms to overcome the approximation induced by the image voxelization, and it needs a relatively high computational time as it involves numerous loops with checking conditions on each voxel. An alternative method is to compute these parameters in an indirect way by using statistical morphology functions [Matheron1971, Jeulin1981, Serra1982, Coster1989, Jeulin2001]. In this frame, the covariance function allows to draw accurately several morphological properties, like the volume fraction, specific surface area and the phase characteristic length, within a fast computational time [Moussaoui2018a]. Finally, it is worth noting that these properties can be estimated quite precisely on a representative 2D microstructure slice by slice using image stereology assumptions.

(i) Phase volume fraction

The phase volume fraction ε_i is the most primary characteristic of porous electrodes. Indeed, the solid phase volume fractions are the direct results of the powder mix proportions used for the electrode manufacturing, while the porosity is closely linked to the sintering rate. Therefore, the accuracy of the reconstruction segmentation can directly be checked on this parameter. In practice, it is simply given by the percentage of voxels belonging to the phase i , and can be computed on a 3D volume as well as on a 2D image [Russ2001]:

$$\varepsilon_i = \frac{N_i}{N} \quad \text{and} \quad \sum_i \varepsilon_i = 1 \quad (\text{II.1})$$

With N_i being the number of voxels belonging to the phase φ_i and N the total number of voxels.

Nevertheless, a representative volume or surface element is needed to obtain a good statistical information (cf. Section III.6). Besides, ε_i can also be deduced from the phase covariance function introduced further in this section.

(ii) Specific Surface Area

The phase specific surface area S_p^i is one of the most important properties of porous electrodes as all the kinetics of the surface reactions depend on this parameter. For instance, the kinetic rates of adsorption and desorption are directly expressed as a function of this density, and so the electrode performances as well. S_p^i is simply defined as the contact area of the phase φ_i with its complementary $\bar{\varphi}_i$ normalized by the total volume [Wilson2010]. The interfacial specific surface area $S_{i/j}$ between φ_i and φ_j phases is thus directly linked as follow:

$$S_p^i = \frac{A_{i/\bar{i}}}{V} \quad \text{and} \quad S_p^i = \sum_{j \neq i} S_{i/j} \quad (\text{II.2})$$

Where $A_{i/\bar{i}}$ is the contact area between the phase φ_i and its complementary $\bar{\varphi}_i$, and V is the total reconstruction volume.

In practice, the most direct way to compute this parameter is to sum the voxel faces areas between two adjacent phases. However, a rescaling factor is required in this case to take into account the digitized nature of the phase [Rajon2002]. Under simple geometrical considerations, it can be shown that the scaling corresponds to a factor of $\pi/6$ in the case of spherical particles (this factor is equal to the ratio of a sphere to a cube surface). Therefore, the real specific surface area ranges between the rough data deduced directly from the numerical reconstruction and the corrected value by a factor of $\pi/6$.

In order to bypass the discretization-induced problems, an alternative method is to use the phase covariance function. This mathematical morphology function is assumed to ‘fully’ characterize the morphology of a given microstructure [Serra1988]. From a mathematical point of view, the phase covariance function $C_i(h)$ is defined as the probability that two points

distant by a distance h drop within the same phase φ_i . It is expressed as follows (illustrated in the x direction):

$$C_i(h) = P\{x \in \varphi_i, x + h \in \varphi_i\} = \frac{1}{N} \times \sum_{n=1}^N k(x, y, z) \times k((x + h), y, z) \quad (\text{II.3})$$

with $k(x, y, z) = 1$ if $(x, y, z) \in \varphi_i$ or 0 if $(x, y, z) \notin \varphi_i$, and N is the number of draws.

Practically, the covariance function is deduced from a second function called the ‘‘Geometric Covariogram’’ K_i . This function computes the volume intersection between the studied phase and its translation by a distance h :

$$C_i(h) = \frac{K_i(h)}{V_i} \quad \text{and} \quad K_i(h) = \iiint_{V_i} k(x, y, z) \times k((x + h), y, z) \times dV \quad (\text{II.4})$$

where V_i is the phase φ_i total volume.

As expected, $C_i(h)$ is equal to the phase volume fraction ε_i at the origin: $C_i(h = 0) = \varepsilon_i$, and tends towards an asymptotic value corresponding to the square volume fraction: $C_i(h \rightarrow \infty) = \varepsilon_i^2$ [Haas1967, Kanit2003]. The distance h^* to reach this asymptotic value is called ‘‘the covariance range’’ and it corresponds to a loss of correlation. This characteristic length can be attributed to the mean particle diameter of the studied phase [Haas1967, Kanit2003]. Finally, S_p^i is directly deduced from the geometric covariogram as follows [Haas1967]:

$$S_p^X = \frac{-4}{V_i} \times \left. \frac{dK_i}{dh} \right|_{h=0} \quad (\text{II.5})$$

The specific surface area can be estimated from a representative 2D image slice as well by stereological means. Indeed, a correcting factor of $4/\pi$ should be multiplied by the 2D contact length to estimate the corresponding 3D surface as described in [Russ2001]. Finally, it is worth noting that the covariance function is used in the rest of this work to compute the specific surface areas S_p^i , allowing therefore overcoming the discretization issue. However, the particle/pore size distribution, more adapted to catch the length scales within in a microstructure, is used for the phase mean diameter measurement.

(iii) Particle and Pore Size Distribution

In order to obtain an accurate characterization of the different length scales present in a microstructure, the continuous Phase Size Distribution (c-PSD) is the most adapted tool [Holzer2011, Serra1988]. While a discrete particle size distribution of the initial powder is a more easily accessible function, the continuous PSD of the sintered phase is far from being straightforward. This is mainly because the sintering process results in overlapping particles with some contact ‘necks’, making it very difficult, if not impossible, to distinguish the constitutive particles [Ghokale2012]. Several c-PSD methods are available in the literature to characterize the SOC electrodes [Gelb1999, Holzer2011, Serra1988, Ender98, Joos2014]. For example, Gelb et al. [Gelb1999] developed a pure geometrical approach where the phase is represented by a set of overlapping spheres, each one being tangent to the complementary phase. In the current work, a method detailed by Serra et al. [Serra1988] was adopted over its very quick time execution (compared to the one proposed by Gelb et al. [Gelb1999] for example). The PSD, called also ‘granulometry’, is computed by applying a sequence of morphological openings with a spherical structuring element of increasing size. The structuring element allows ‘removing’ the particles with the same size. The resulting PSD allows extracting some valuable data, such as the arithmetic mean diameter $\langle D_i \rangle$, the standard deviation σ_i^2 , the Coefficient of Variation (CV_i) and the skewness γ_i . Considering the probability density function p , these parameters are expressed as follows:

$$\begin{aligned} \langle D_i \rangle &= \int_0^\infty D_i p(D_i) dD_i \quad ; \quad \sigma_i^2 = \int_0^\infty [D_i - \langle D_i \rangle]^2 p(D_i) dD_i \\ CV_i &= \frac{\sigma_i}{\langle D_i \rangle} \quad ; \quad \gamma_i = \frac{1}{\sigma_i^3} \int_0^\infty [D_i - \langle D_i \rangle]^3 p(D_i) dD_i \end{aligned} \quad (\text{II.6})$$

(iv) Triple Phase Boundary lengths (TPBLs) density

The density of TPBLs ξ_{TPBLs} is defined for a composite electrode as the length of the ionic/electronic/gas phases intersections normalized by the volume size. These lines play a major role in the electrode performance as the electrochemical reactions occur in the vicinity of these sites. It can be directly calculated by identifying and summing each voxel edge at the triple phase contacts. A correction factor of 1.455 is then introduced because of the domain cubic discretization [Wilson2010]. The number of these triple phase junctions can also be estimated based on a 2D image slice. Indeed, the density of these lines can be measured using

the stereological principle that the length of a linear feature per unit volume is equal to twice the number of intercepts of the feature with sectioning planes per unit area [Russ2001, Zhang2012]. Finally, it is worth mentioning that only the percolating TPBs contribute to the electrode reactions as the disconnected ones are electrochemically inactive. The connectivity is taken into account in the later electrochemical model by considering only the percolated phases.

II.5.1.2 Topological properties

(i) Phase connectivity

Phase contiguity δ_i is calculated by analyzing the phase connectivity from one side of the volume to the other [Laurencin2012]. A portion of a phase φ_i is connected if it belongs to a cluster that contains a continuous path from one side of the electrode to the other. Otherwise, it is considered inactive and does not contribute to the electrochemical reactions and transport phenomena.

(ii) Geometrical tortuosity

The geometrical tortuosity τ_i^{geo} takes into account the fact that the mass or charge transport in one phase is hampered since the pathway for diffusion is not straight but sinuous and entangled [Bathia1985, Epstein1989]. This parameter is thus defined as the ratio of the effective pathway length ℓ^{eff} over the length of the sample ℓ and can be seen as a measure of the deviation from the shortest possible pathway:

$$\tau_i^{\text{geo}} = \ell^{\text{eff}} / \ell \quad (\text{II.7})$$

This parameter is calculated by using the so-called ‘centroid’ path method from the ‘geodesic distance’ notion [Gostovic2007, Smith2009, Cooper2014]. For a given phase, the algorithm is based on the calculation of the center of mass within each 2D slice of the reconstruction along the in-plane direction of the flow. The effective length is then deduced by following the path from one centroid to the other.

(iii) Constrictivity factor

The transport can be also hindered by some constrictions in the microstructure since the cross sections area for diffusion is not constant. This bottleneck effect is described through the constrictivity parameter that can be defined as follows [Holzer2013]:

$$\beta_i = (r_{\min}/r_{\max})^2 \quad (\text{II.8})$$

By definition, the constrictivity β_i ranges between 0 and 1 (the lower the parameter is, the higher the constriction in the microstructure). As proposed by Holzer et al. [Holzer2013] and Gaiselmann et al. [Gaiselmann2014], the statistically averaged value for r_{\min} is calculated by the simulation of the Mercury Intrusion Porosimetry (MIP) while r_{\max} , which is defined as the radius of the phase size median, is determined with the PSD.

II.5.2 Physical parameters

This set of morphological parameters is finally completed by the computation of the effective gas diffusivities or effective charge conductivities σ_i^{eff} for the percolated phases. Since the transport is limited by the complex microstructure, the effective conductivities σ_i^{eff} are lower than the intrinsic values for the dense materials σ_i^{bulk} . This effect is taken into account through a microstructure-factor M_i defined as follows [Holzer2013]:

$$M_i = \sigma_i^{\text{eff}}/\sigma_i^{\text{bulk}} \quad (\text{II.9})$$

The ratio M_i is correlated to the electrode morphological parameters controlling the diffusional process. For instance, Stenzel et al. [Stenzel2016] have fitted on Ni-YSZ reconstructions a law which depends on the volume fraction, the geometrical tortuosity and constrictivity: $M_i = 2.08 (\varepsilon_i^{1.62} \beta_i^{0.49}) / (\tau_i^{geo})^{2.26}$. It can be noticed that the microstructural factor is also classically used to express an ‘apparent’ tortuosity τ_i that encompasses both the transport pathway (geometrical tortuosity) and the bottleneck effect (constrictivity): $M_i = \varepsilon_i / \tau_i^2$ [Bathia1985, Epstein1989]. In the present work, the effective conductivities have been determined by using a classical homogenization technique [Laurencin2012]. For each conducting phase, the equations for diffusion are solved in the digitized domain with the Finite Element Method (FEM). The effective conductivity is then deduced from the numerical

analysis by equating the macro homogeneous flux to the average value computed from the FEM simulation.

II.6 Representative Volume Element (RVE)

In order to obtain good statistics, it is worth noting that the microstructural properties have to be quantified on the electrode Representative Volume Element (RVE), or if it is not possible, on several independent Stochastic Volume Elements (SVEs) extracted from the whole reconstructions [Usseglio-Viretta2014, Harris2015a, Harris2015b]. In the present study, the RVE has been evaluated for each electrode by using the volume expansion method described by Yan et al. [Yan2017]. The volume fraction, the TPBIs density, and the M-factors for each phase have been computed on several sub-volumes taken from the whole reconstructions. The evolutions of the mean value as well as the standard deviation for iso-volumes taken from the whole reconstructions have been plotted as a function of their size. Fig. II.9 illustrates the volume expansion method applied for the Ni phase of Cell-A, which is the phase with the least volume fraction and then the most constraining one. The RVE is reached when the standard deviation for each investigated parameter becomes negligible. Correspondingly, the requested number of SVE has been estimated in such a way that the standard deviation is very low after averaging on these independent volumes. Therefore, the microstructural parameters of the O₂ electrodes have been computed on a RVE estimated to $\approx 9 \times 9 \times 9 \mu\text{m}^3$ for both Cell-A and Cell-B [Hubert2017a], and $\approx 8 \times 8 \times 8 \mu\text{m}^3$ for the finer Cell-C. The microstructural properties for the H₂ electrode of Cell-A have been calculated on a RVE evaluated to $\approx 15 \times 15 \times 15 \mu\text{m}^3$ [Hubert2017a]. Since the H₂ electrode active layer of Cell-B has a thickness limited to 10 μm (Fig. II.2), the computation of its microstructural properties has been carried out by averaging the data computed on 16 independent SVEs of $\approx 8.5 \times 8.5 \times 8.5 \mu\text{m}^3$ (for which the standard deviation becomes negligible). Finally, a large cubic volume of $36 \times 36 \times 36 \mu\text{m}^3$ was considered for the Cell-B substrate in order to be representative of its coarse microstructure (due to the large scale porosities for this diffusion layer).

Except for the substrate of Cell-B, all the properties including the effective conductivities have been calculated without changing the initial image voxel size. Therefore, all the computations have been carried out by keeping a voxel size (or element size for the FEM mesh) of at least 25 nm. As already discussed in [Hubert2016], a discretization of 25 nm is

adequate to correctly describe the morphological details in the microstructure and then to accurately compute its properties. Nevertheless, because of its very fine microstructures, it has been chosen to compute the properties of the O₂ electrodes of Cell-B and Cell-C on the FIB-SEM volumes by keeping voxel sizes of 16.5 nm and 10 nm, respectively.

Concerning the diffusion layer of Cell-B, with a coarser microstructure, the resolution has been downsized to 50 nm. For this purpose, each set of $2^3 = 8$ voxels was replaced by one voxel containing the dominant phase for time optimization reasons. Indeed, the phases and pore mean diameters are higher for this layer, so the spatial resolution coarsening does not affect the microstructural properties measurement accuracy as long as the number of voxels per particle is kept constant.

Moreover, both the covariance functions and the M-factors for each phase have been calculated in the three spatial directions. They have been found to be very close to each other, meaning that the electrodes can be considered as an isotropic medium. As a consequence, all the electrodes properties have been averaged on the three spatial directions. All the parameters for the three cells are given in the next section for both the O₂ and H₂ electrodes.

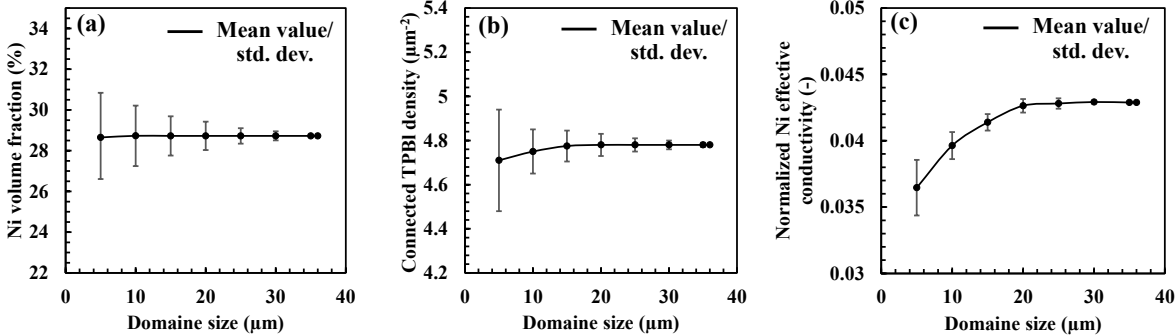


Figure II.9 Estimation of the Representative Volume Element for Cell-A H₂ electrode in Ni-YSZ with respects to the Ni volume fraction (a), the connected TPBI density (b), and the normalized Ni effective conductivity (c). A volume of $15^3 \mu\text{m}^3$ was retained for this electrode.

II.7 Results and discussion

In this section, the 3D rendering volumes of the final segmented volumes are presented in a first place. All the microstructural properties computed for each reconstructed layer of the three cells are summarized in Tables II.1-3. The size of the analyzed RVE and the requested number of SVE, which were considered for the computations, were determined thank to the sensitivity analysis presented in the previous section. Finally, the morphological and physical parameters obtained on the different cells are discussed and compared and their consistency with the literature is examined.

II.7.1 Results for Cell-A

The Cell-A, introduced in the first section of this chapter, consists in a commercial complete cell, with an O₂ electrode in LSCF and a H₂ electrode in Ni-YSZ. The rendering volumes of these two electrodes are presented in Fig. II.10.a-b, with respective RVEs of 9x9x9 μm³ and 15x15x15 μm³. These two reconstructions were characterized by computing all the microstructural properties defined in Section II.5 (Table II.1).

a) Results for the O₂ electrode

The solid volume fraction of 56.36% drops within the typical LSCF O₂ electrodes values. Indeed, the optimal ratio between the MIEC and porosity is a compromise between the solid phase requirements of good charge conductivity and mechanical stability, and the pore phase requirements of a good gas diffusion and large surface area density. For instance, an equally distributed volume fractions, i.e. 50:50 vol.%, allows maximizing $S_{LSCF/gas}$ as it is generally sought (cf. Section IV). In our case, the obtained value of 3.80 μm⁻¹ drops within the lower bound of the literature values [Joos2014]. Moreover, with no surprise for a two-phase material with almost the same proportions, the percolation of both phases is excellent. The pore and particle mean diameters of 0.26 μm and 0.32 μm respectively are in the same range of the literature values around 0.3μm. The LSCF phase presents more tortuous paths for charge transport compared to the gas paths ($\tau_{LSCF}^{geo} = 1.34$; $\tau_{Pore}^{geo} = 1.22$). However, the LSCF phase presents slightly less bottlenecks and dead ends compared to the porosity ($\beta_{LSCF} = 0.11$; $\beta_{Gas} = 0.10$). Finally, the LSCF has more effective diffusivity compared to the gas phase ($M_{LSCF} = 0.289$; $M_{Gas} = 0.194$), which can be explained by the combination of a larger volume fraction and less constrictive paths.

b) Results for the H₂ electrode:

The cermet Ni-YSZ microstructural parameters drop within the range of literature values. The porosity constitutes 44% of the H₂ electrode volume, while the solid phases have a close volume fraction of around 28%. The phases mean diameters are almost in the same range ($d_{pore} = 0.28 \mu\text{m}$, $d_{YSZ} = 0.28 \mu\text{m}$, and $d_{Ni} = 0.33 \mu\text{m}$). A relatively high density of TPBLs density of $4.78 \mu\text{m}^{-2}$ has been obtained. Finally, it can be noticed that the connectivity is very good with a minimum of around 94%.

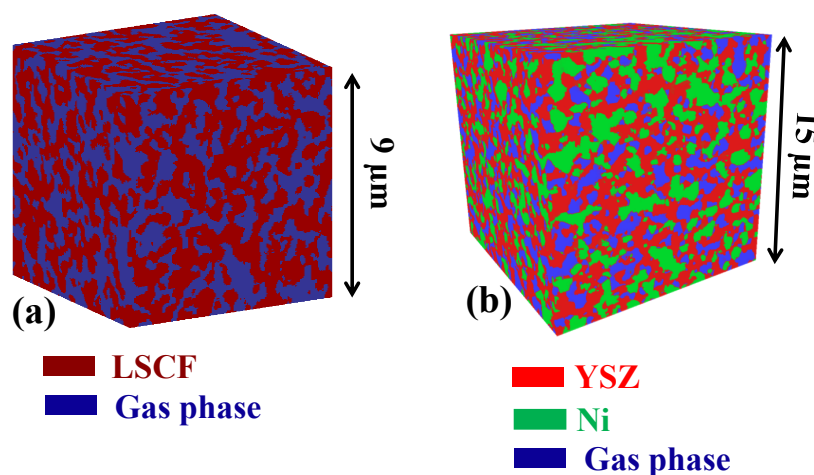


Figure II.10 3D visualization of the reconstructed volumes for the Cell-A O₂ electrode in LSCF (a) (red representing LSCF and blue the pore phase) and H₂ electrode in Ni-YSZ (b) (red representing the YSZ phase, green the Ni phase and blue the pore phase).

Table II.1

Microstructural properties for the O₂ and H₂ electrodes of Cell-A computed on the tomographic reconstructions. The specific surface area, the connectivity, the volume fraction, the mean particle/pore diameter, the geometrical tortuosity, the constrictivity factor, the M-factor, and the connected TPBL density are given for each electrode phase.

Properties Units	Cell-A								
	S_p μm^{-1}	δ %	ε %	d_p μm	τ^{geo} -	β -	M-factor -	TPBL density μm^{-2}	
Gas phase	3.80	99.96	43.64	0.26	1.22	0.10	0.194	n/a	O ₂ electrode
LSCF phase		99.99	56.36	0.32	1.34	0.11	0.289		
Gas phase	2.67	94.74	28.04	0.28	1.67	0.09	0.03	4.78	H ₂ electrode
YSZ phase	2.68	99.78	44.08	0.28	1.43	0.13	0.189		
Ni phase	3.30	97.45	27.88	0.33	1.75	0.08	0.041		

II.7.2 Results for Cell-B

The second investigated cell consists in a complete commercial one as well, with an O₂ electrode in LSC, and a H₂ electrode in Ni-YSZ. Only the microstructural properties of this cell and those of Cell-A have been used in this work for the microstructural model validation (cf. next chapter). However, the electrochemical performances of these two cells have already been evaluated in dedicated studies [Bernadet2015, Hubert2015], showing that Cell-B exhibits a much lower polarization resistance compared to Cell-A. A first visual inspection of the cell functional layers (Fig. II.11a for LSC and Fig. II.11.b for Ni-YSZ) shows that the microstructures are finer than those of Cell-A. Concerning, the H₂ electrode diffusion layer, a notably large RVE of 36x36x36 μm³ was required to catch the characteristic bimodal distribution of porosity. Indeed, the large voids created by the use of specific pore formers are revealed in Fig. II.11.c. In order to quantify these results, all the relevant microstructural properties have been summarized in Table II.2.

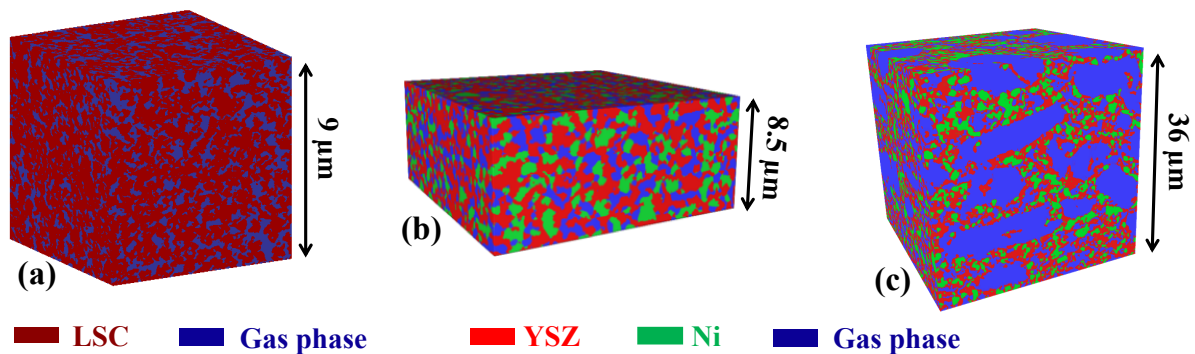


Figure II.11 3D visualization of the reconstructed volumes for Cell-B. (a) O₂ electrode in LSC (red representing LSC and blue the pore phase) and both active (b) and diffusion (c) layers of the H₂ electrode in Ni-YSZ (red representing the YSZ phase, green the Ni phase and blue the pore phase).

a) Results for the O₂ electrode

As expected, the MIEC specific surface area of 6.28 μm⁻¹ is much higher than 3.80 μm⁻¹ found for Cell-A. This result is in good accordance with the much finer O₂ electrode of Cell-B. The cell is also considerably less porous than Cell-A (28.83% compared to 43.64%). This unbalanced volume fraction repartition between the solid and pore phases results in a significant difference in the phase tortuosity, constrictivity and diffusivity (cf. Table II.3).

b) Results for the H₂ electrode functional layer:

Concerning the H₂ electrode functional layer, slightly lower mean diameters than the one for Cell-A were obtained ($d_{Pore} = 0.24 \mu\text{m}$, $d_{YSZ} = 0.31 \mu\text{m}$, and $d_{Ni} = 0.28 \mu\text{m}$), while the volume fractions remained in the same range (around 50% porosity and 25% for each solid phase). This result explains the overall slightly higher specific surface areas ($Sp_{Pore} = 2.94 \mu\text{m}^{-1}$, $Sp_{YSZ} = 3.42 \mu\text{m}^{-1}$, and $Sp_{Ni} = 2.46 \mu\text{m}^{-1}$) while the transport properties are in the same order of magnitude. Nevertheless, the finer microstructure results in a relatively high active TPBI density of $6.20 \mu\text{m}^{-2}$ compared to $4.78 \mu\text{m}^{-2}$ for Cell-A, which can explain in part the higher performances of this cell.

Table II.2

Microstructural properties for the O₂ electrode and the active and diffusion layers of the H₂ electrode of Cell-B computed on the tomographic reconstructions. The specific surface area, the connectivity, the volume fraction, the mean particle/pore diameter, the geometrical tortuosity, the constrictivity factor, the M-factor, and the connected TPBI density are given for each electrode phase. It can be noted that the porosity is divided into microporosity and macroporosity

Properties	Cell-B							TPBI density μm^{-2}	
	S_p μm^{-1}	δ %	ϵ %	d_p μm	τ^{geo} -	β -	M-factor -		
Gas phase	6.28	99.76	28.83	0.12	2.27	0.23	0.078	n/a	O ₂ electrode
LSCF phase		100	71.17	0.22	1.31	0.31	0.474		
Gas phase	2.94	94.23	26.55	0.24	1.74	0.39	0.021	6.20	H ₂ electrode (functional layer)
YSZ phase	3.42	99.92	49.55	0.31	1.14	0.44	0.243		
Ni phase	2.46	92.81	24.13	0.28	1.81	0.34	0.018		
Microporosity	1.92	99.94	31.25	0.61	1.62	0.20	0.131	3.19	H ₂ electrode (Diffusion layer)
Macroporosity	0.28		14.21	2.48					
YSZ phase	1.79	99.22	34.85	0.56	1.78	0.43	0.100		
Ni phase	1.25	96.71	19.69	0.42	2.20	0.35	0.011		

c) Results for the H₂ electrode substrate:

The current collector of Cell-B in Fig II.11.c exhibits a coarser microstructure compared to the functional layer of this cell. Indeed, the YSZ and Ni solid phases have mean respective diameters of $0.56 \mu\text{m}$ and $0.42 \mu\text{m}$ (compared to $\sim 0.3 \mu\text{m}$ for the functional layer). This obviously leads to lower specific surface areas of $Sp_{YSZ} = 1.79 \mu\text{m}^{-1}$ and $Sp_{Ni} = 1.25 \mu\text{m}^{-1}$ that are almost two times lower for this layer. As expected, the volume proportions of the solid phases are lower compared to the functional layer ($\epsilon_{YSZ} = 34.85 \%$, $\epsilon_{Ni} = 19.69 \%$), with more content of Ni in the solid phase $\epsilon_{Ni}/(\epsilon_{YSZ} + \epsilon_{Ni}) = 36.10\%$ compared to 32.75% for the functional layer. Indeed, a higher Ni proportion is needed in the current collecting layer to ensure a good electronic conductivity and electrical contact with the interconnects. Besides, all the phases are well connected as the different volume fractions do not drop below the percolation threshold. Moreover, both solid phases show more tortuous phases and close constrictive

factors leading to lower conductivities compared to the functional layer ($M_{YSZ} = 0.100$, $M_{Ni} = 0.011$). Finally, the coarse microstructure of this layer has obviously a lower connected TPBLs density of $3.19 \mu\text{m}^{-2}$.

A special attention has been paid to finely characterize the porosity of the substrate of Cell-B. For this objective, it was crucial to separate the macropores resulting from the burning-off of specific pore-formers from the microporosity network arising from the incomplete electrode densification and NiO reduction. This step is important to characterize separately the two radically different morphologies and therefore investigate the properties of each porosity length-scale. This allows evaluating the individual contribution of the pore formers to the mass transfer. This work is particularly valuable in a microstructural optimization framework of the diffusion layer.

The visual results of this operation are shown in Fig. II.12. The extracted macropores can be characterized in terms of morphology, orientation, amount, and repartition. These geometrical characteristics allow investigating the transport routes of this diffusion layer. The close examination of Fig. II.12 shows that these void volumes have an ellipsoid-like shape, with a variable degree of flattening going from an almost spherical to an oblate geometry. It can also be noticed that they seem homogeneously distributed within this diffusion layer and disconnected from each other (cf. Figs. II.2.a and II.12).

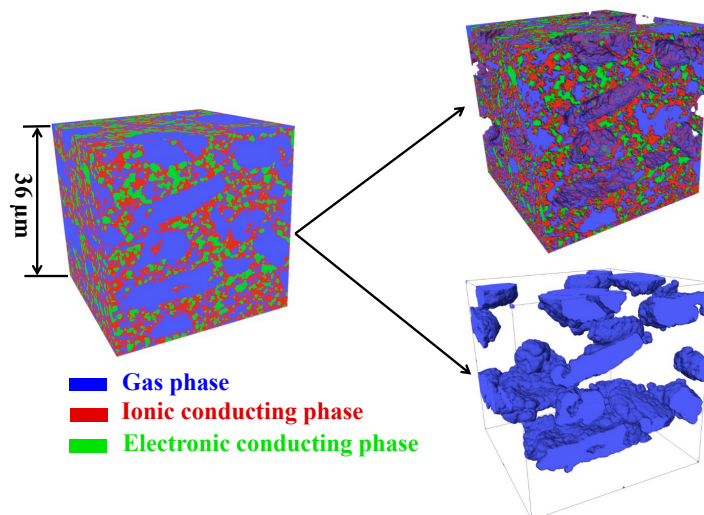


Fig. II.12 Illustration of the macropores separation for the current collector of Cell-B.

To go further in the substrate characterization, all the microstructural properties have been computed and summarized in Table II.3. This diffusion layer has a high porosity of 45.46 %,

with a contribution of 14.21 % due to the macro-porosities. As expected for a high volume fraction phase, the porosity is almost fully connected to up to 99.94%. The macropores segregation allows also separating the contribution of each porosity length-scale to the whole porosity bimodal distribution in Fig. II.13. A mean diameter of $0.61 \mu\text{m}$ was identified for the microporosity network, whereas the larger-scale porosities exhibit a mean size of $2.48 \mu\text{m}$. The macropore size distribution reveals also a relatively high standard deviation of $\sigma = 1.18 \mu\text{m}$ and a positive skewness of $\gamma = 0.50$. The difference in pore size and volume fraction between the two porosity length scales leads to a pronounced unbalance between the specific surface area developed by the microporosity $Sp_{micropore} = 1.92 \mu\text{m}^{-1}$, and the one by the macroporosity $Sp_{macropore} = 0.28 \mu\text{m}^{-1}$. It is worth reminding that the macropore size distribution can also be related to the employed pore-formers distribution as their morphology is quite conserved after sintering in the final microstructure [Horri2012]. Concerning the orientation, it can be remarked visually from Fig. II.12 that the macropores are almost parallel to the electrode plan. To quantify this statement, each volume was fitted to an ellipsoid geometry as illustrated in Fig. II.14. This allowed obtaining an approximation of the distribution of these voids dimensions and orientation. It was found that the volumes have a mean tilt angle of $\sim 6^\circ$, while no privileged orientation has been detected within the parallel plane to the electrode (xy-plane).

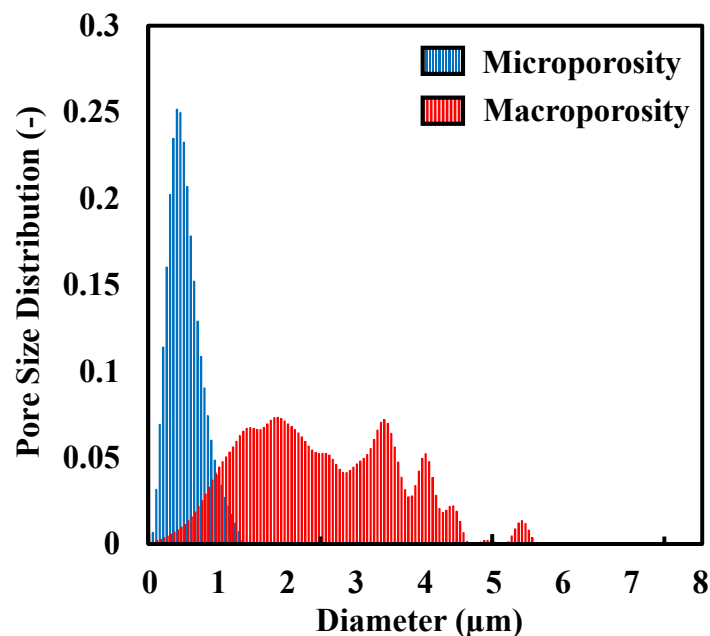


Fig. II.13 Pore Size Distribution (PSD) separated in microporosity PSD in blue and macroporosity PSD in red.

As expected for a highly porous layer, the gas paths are less tortuous compared to the functional layer, with $\tau_{pore}^{geo} = 1.62$. However, because of the large bimodal pore size distribution (Fig. II.13), a large difference was obtained between the maximum section S_{max} , dominated by the macroporosity and the necks size S_{min} controlled by the microporosity. This leads to a pronounced bottle-neck effect quantified to $\beta_{pore} = 0.20$. Finally, the physical transport process of the gas phase was evaluated, and a notable difference was obtained between the three space directions. Indeed, a very close M-factor was obtained in the two parallel directions to the electrode surface $M_{pore}^x \approx M_{pore}^y = 0.156$, while a lower diffusivity was obtained in the orthogonal direction to the electrode $M_{pore}^z = 0.100$. This anisotropy can be explained by the privileged macropores orientation reported before. This trend was also observed for the YSZ and Ni phases ($M_{YSZ}^{x,y} = 0.112$; $M_{YSZ}^z = 0.083$ and $M_{Ni}^{x,y} = 0.012$; $M_{Ni}^z = 0.009$). This tendency is opposed to the desired cell characteristics, as the transport phenomena in the electrode are supposed to be favored in the orthogonal direction to the electrode (i.e. z-direction). This anisotropy of the substrate could be related to its manufacturing method by tape casting [Nojonen15] that induces a privileged orientation as discussed in [Jabbari16].

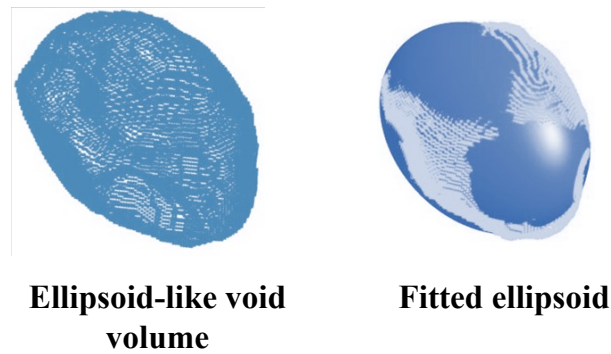


Fig. II.14 Illustration of a macropore volume fitting to an ellipsoid.

II.7.3 Results for Cell-C

A 3D rendering volume of the segmented reconstruction of Cell-C is given in Fig. II.15 where the blue, red and green represent the pore, LSCF and CGO phases, respectively. The Representative Volume Element (RVE) of the microstructure was estimated on the reconstruction by using a volume expansion method described in the previous section. In our

case, it has been shown that a cubic volume of $8 \times 8 \times 8 \mu\text{m}^3 = 512 \mu\text{m}^3$ is sufficient to be statistically representative of the heterogeneous LSCF-CGO electrode microstructure. A volume of this dimension was extracted from the whole reconstruction and used for the microstructural properties computation.

All the values of the microstructural parameters are given in Table II.3. First of all, it can be noticed that the relative volume fractions of the solid phases, ε_{LSCF} and ε_{CGO} , match quite perfectly the weight proportion of LSCF and CGO used for the electrode manufacturing. This preliminary remark means that the overall procedure from the raw data acquisition up to the final segmentation of the 3D image is valid.

As observed in Fig. II.15, the 3D rendering volume reveals a fine microstructure of the electrode. This statement is confirmed by the quantification of the microstructural properties with (i) some rather low mean diameters for all the phases ($d_i < 190\text{nm}$), (ii) a high active TPBLs density of $\xi_{TPBLs} = 9.06 \mu\text{m}^{-2}$, and (iii) some quite large specific surface areas ($S_{i/j} > 3.2 \mu\text{m}^{-1}$). It can also be noticed in Table II.3 that the solid phases M-factors are rather low. According to the microstructural correlation given in [Holzer2013], $Mfactor \approx \delta \varepsilon \frac{\beta}{\tau^{geo}}$, these low values could be ascribed to the fairly low phase volume fractions ε_i and the low constrictivity parameters β_i for the two solid phases. However, the geometrical tortuosity τ_i^{geo} for each phase is close to the unity indicating a more constrictive than tortuous microstructure. Nevertheless, it is found that all the electrode phases are quite perfectly percolated since the phase connectivity remains higher than 91%. As a consequence, the connected density of TPBLs remains as high as the total one of $12.09 \mu\text{m}^{-2}$. Therefore, the studied LSCF-CGO composite exhibits a suitable microstructure in such a way that it can be considered as a ‘standard’ SOC electrode.

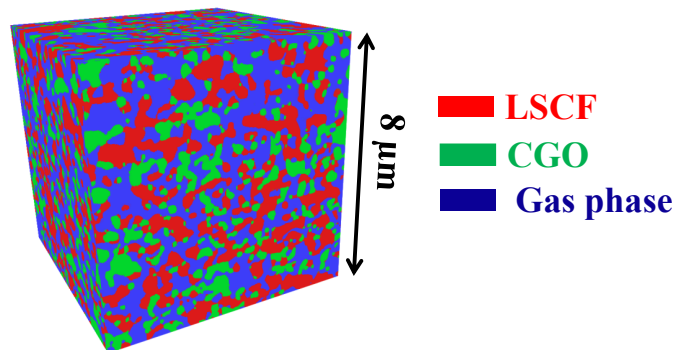


Fig. II.15 3D visualization of the FIB-SEM reconstructed O₂ electrode of Cell-C. Red representing the LSCF phase, green the CGO phase, and blue the pore phase).

Table II.3

Microstructural properties for the O₂ electrode of Cell-C computed on the tomographic reconstruction. The specific surface area, the connectivity, the volume fraction, the mean particle/pore diameter, the geometrical tortuosity, the constrictivity factor, the M-factor, and the connected TPBI density are given for each electrode phase.

Properties Units	Cell-C							TPBI density μm^2	
	S _p μm^{-1}	δ %	ε %	d _p μm	τ^{geo} -	β -	M-factor -		
Gas phase	4.41	99.99	43.45	0.17	1.55	0.53	0.2441	9.06	O ₂ electrode
LSCF phase	3.26	97.86	30.15	0.19	1.77	0.51	0.0428		
CGO phase	3.27	91.56	26.40	0.16	1.81	0.55	0.0183		

II.8 Conclusion

A relevant electrode microstructural characterization is of central importance to accurately understand the complex link between the electrode microstructure and its performance. From this point of view, two tomographic methods have been used in the frame of this work to reconstruct different layers of electrodes from three tested cells. This allowed obtaining relevant 3D reconstructions that have been processed and then segmented. A set of morphological and physical properties was then computed. A particular attention has been paid to characterize the substrate of Cell-B that has a bimodal pore distribution. Indeed, the macropores have been for the first time separated from the microporosity network and quantified accurately. It should be noted that although the image reconstruction and characterization procedure is liable to introduce some bias with respects to reality during the image-processing course, it provides a relevant knowledge of the electrode morphology and transport behavior. However, the image acquisition is a very time- and resource-consuming procedure; the sample preparation, reconstruction, and processing may take more than two full days to obtain a single volume. From this point of view, developing a representative microstructure generation tool seems a relevant strategy to reduce the number of required reconstructions. For this end, two complementary stochastic geometrical models are proposed in the following chapter. The microstructural properties are computed on the generated synthetic media and compared to the real ones in order to validate these two morphological models.

Chapter III: Stochastic geometrical models and validation

This chapter presents the stochastic geometrical models that have been developed to simulate SOC electrodes microstructure. As discussed in the previous chapter, the electrode manufacturing and reconstruction processes are so time-consuming and labor-intensive that the number of achievable reconstructions is very limited. Nevertheless, a large number of microstructures is needed in the present sensitivity analysis aiming to investigate the complex microstructural correlations. An alternative approach consists in generating synthetic representative microstructures. For this purpose, two models have been proposed and adapted to emulate SOC porous electrodes. The models have been inspired from the two main classes discussed in the literature review in Section I.6.1, namely ‘geostatistical models’ and ‘particle-based models’. The first model is an adaptation of the so-called ‘plurigaussian random fields’ method, while the second one is based on an original sphere-packing algorithm. The fundamental difference between the two models allows providing two approximations of a same microstructure and hence drawing conclusions that are independent of the chosen model. Besides, using two models allows sweeping a larger range of microstructures and thus evaluating various promising electrode architectures. The chapter is organized as follow: the first two sections are dedicated to present the two models, their validation, and a discussion about their flexibility to generate ‘non-classical’ microstructures, while the third and last section provides a discussion about the models comparison.

III.1 Random Field model description and validation

In the present section, the truncated plurigaussian random field model has been employed to generate synthetic microstructures of SOC electrodes. A specific attention has been paid to fully validate the method on X-ray holotomography and FIB-SEM 3D reconstructions obtained for both O₂ and H₂ electrodes (cf. Section II.7). The model validation step has been carried through a set of morphological and physical parameters presented in the previous chapter (Section II.5). It is worth noting that the present model includes a generalization, which was initially proposed in Galli et al. [Galli1994] and detailed in Armstrong et al. [Armstrong2011], for the combination and thresholding of independent random fields. This method was adapted here to the SOC electrodes in order to improve the relevance and the representativeness of the synthetic microstructures. The method also offers the possibility to

have a more flexible numerical tool. Two correlation lengths have been thus introduced for the electrode solid phases. The capacity of the approach to mimic different kinds of electrode microstructures and architectures is illustrated and discussed on several examples. This work has been valued by a published article entitled “Stochastic geometrical modeling of solid oxide cells electrodes validated on 3D reconstructions” in Computational Materials Science journal [Moussaoui2018].

III.1.1 Random Field model description for SOC electrodes

III.1.1.1 Two-phase materials for O₂ electrode

The truncated Gaussian random field model has been used to generate 3D microstructures of typical O₂ electrodes made of porous LSCF or LSC. As the mathematical definition of a random field falls outside the scope of the current work, the reader is invited to refer to the following references for more details [Lantuéjoul2002, Lang2011]. For a two-phase material, a general description of the method can be found in [Lantuéjoul2002, Abrahamsen1997, Adler2010]. Only the main steps of the procedure are thus reminded hereafter by underlying the specificities that were adopted to model the SOC electrode microstructures.

Main model assumptions – A statistically stationary, isotropic and homogeneous porous microstructure has been considered in the model. Such assumption is well verified on ‘typical’ commercial SOC electrodes obtained by screen printing or tape casting [Laurencin2012, Delette2013]. Moreover, the covariance function contains the most relevant morphological information required to reconstruct a microstructure [Serra1988]. As a consequence, it has been assumed that the microstructure of a two-phase electrode (X and \bar{X} , where X refers to one phase and \bar{X} the other) can be characterized through the covariance function $C_X(h)$ which is used as the only input data for the simulations. This function is introduced in Section II.5.1.1, only a brief description is given hereafter: from a mathematical point of view, $C_X(h)$ is expressed as the probability that two points separated by a distance h belong to the same phase X :

$$C_X(h) = P(z \in X, z+h \in X) \quad \text{for } z \in \Omega \quad (\text{III.1})$$

Where Ω denotes the 3D domain. The covariance function provides information on the phase volume fraction ε_X :

$$0 \leq C_X(h) \leq \varepsilon_X = C_X(0) \quad (\text{III.2})$$

It is also linked to the phase specific surface area S_p^X , which is simply defined as the total surface area of the interface between this phase X and its complementary \bar{X} normalized by the domain volume V_Ω [Serra1988] through the ‘‘Geometric Covariogram’’ K_X (cf. Section II.5.1.1):

$$S_p^X = -\frac{4}{V_\Omega} \times \frac{dK_X}{dh} \Big|_{h=0} \quad \text{with} \quad C_X(h) = \frac{K_X(h)}{V_X} \quad (\text{III.3})$$

In a general point of view, the covariance function describes how the phase is distributed in the 3D space. It tends to an asymptotic value corresponding to the square of the volume fraction: $\lim_{h \rightarrow +\infty} C_X(h) = \varepsilon_X^2$. The distance to reach this asymptotic bound is defined as the range of the covariance and can be ascribed to the phase characteristic length [Serra1988].

Description of the model steps – Basically, the model consists in the generation of a stationary and normal centered Gaussian random field $G_X(z)$ that exhibits the same spatial correlation than the real homogenous microstructure (described with the correlation and covariance functions, respectively). The two phases, X and \bar{X} , of the synthetic microstructure are thus obtained by thresholding $G_X(z)$:

$$X = \{z; G_X(z) \geq \lambda_X\} \quad (\text{III.4})$$

where λ_X denotes the threshold.

(i) In order to determine λ_X , it is reminded that $G_X(z)$ follows the law of a standard normal distribution (of mean value $\mu=0$ and variance $\sigma^2=1$): $G_X(z) \sim N(0,1)$. Therefore, the threshold can be related to the phase volume fraction with the following relation:

$$\varepsilon_X = P\{G_X(z) \geq \lambda_X\} = \int_{\lambda_X}^{\infty} p(x) dx \quad (\text{III.5})$$

Where $p(x)$ is the continuous probability density function of the normal distribution $N(0,1)$. The threshold can be easily deduced from (III.5) as illustrated in Fig. III.1:

$$\varepsilon_X = 1 - \int_{-\infty}^{\lambda_X} \frac{1}{\sqrt{2\pi}} \exp\left(-\frac{1}{2}x^2\right) dx \quad (\text{III.6})$$

(ii) As described for the first time by Alder et al. [Alder1990] and further developed by Liang et al. [Liang1998], the field $G_X(z)$ can be generated by the convolution of an uncorrelated Gaussian random noise $U(z)$ with a normalized and symmetric weight function $\omega(h)$:

$$G_X(z) = U(z) * \omega(h) = \int_{h \in \Omega} U(z-h) \omega(h) dh \quad (\text{III.7})$$

$$\text{with : } \sum_{\Omega} \omega^2(h) = 1 \quad \text{and} \quad \omega(h) = \omega(-h) \quad \forall h$$

This operation can be interpreted as the filtering of the normal centered uncorrelated random noise $U(z) \sim \mathcal{N}(0,1)$ with the weight function $\omega(h)$. The objective of this operation is to introduce the requested spatial correlation in $G_X(z)$. Therefore, $\omega(h)$ is linked to the correlation function $\rho_X(h)$ of the Gaussian random field defined as follows:

$$\rho_X(h) = \text{cov}\{G_X(z), G_X(z+h)\} \quad (\text{III.8})$$

(iii) To determine the weight function, it can be shown that the auto-convolution of $\omega(h)$ is equal to $\rho_X(h)$ (cf. Appendix A.1):

$$(\omega * \omega)(h) = \rho_X(h) \quad (\text{III.9})$$

(iv) The correlation function $\rho_X(h)$ of the random field is associated to the covariance function of the real microstructure $C_X(h)$ through the following relation (cf. demonstration in Appendix A.1):

$$C_X(h) - \varepsilon_X = \frac{1}{2\pi} \int_1^{\rho_X(h)} \frac{1}{\sqrt{1-r^2}} \exp\left\{\frac{-\lambda_X^2}{1+r}\right\} dr \quad (\text{III.10})$$

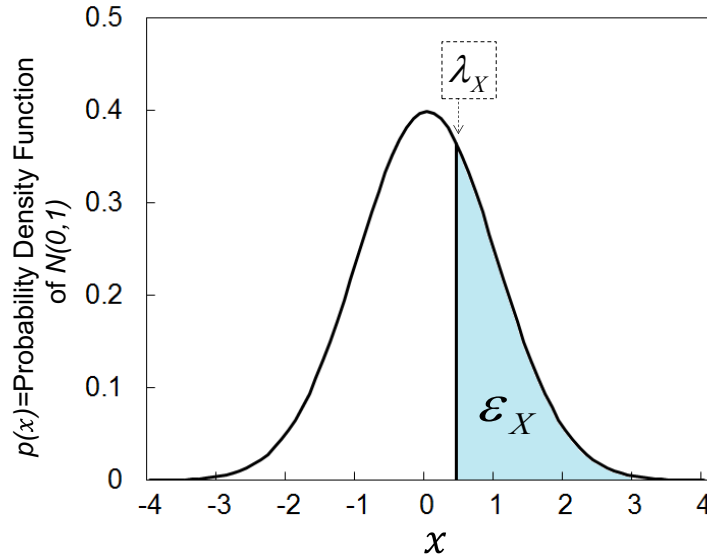


Fig. III.1 Distribution and definition of the threshold for a two-phase electrode: the Gaussian field is proportion to a normal distribution segmented with a constant threshold.

To summarize, the method is decomposed into a sequence of successive steps consisting of:

- (1) The determination of the threshold λ_X with the phase volume fraction (eq. (III.6)),
- (2) The computation of the correlation function $\rho_X(h)$ with the covariance $C_X(h)$ of the real microstructure (eq. III.10),
- (3) The generation of the random field $G_X(z)$ by combining eqs. (III.7) and (III.9),
- (4) The segmentation of $G_X(z)$ with the threshold λ_X to obtain the final synthetic microstructure.

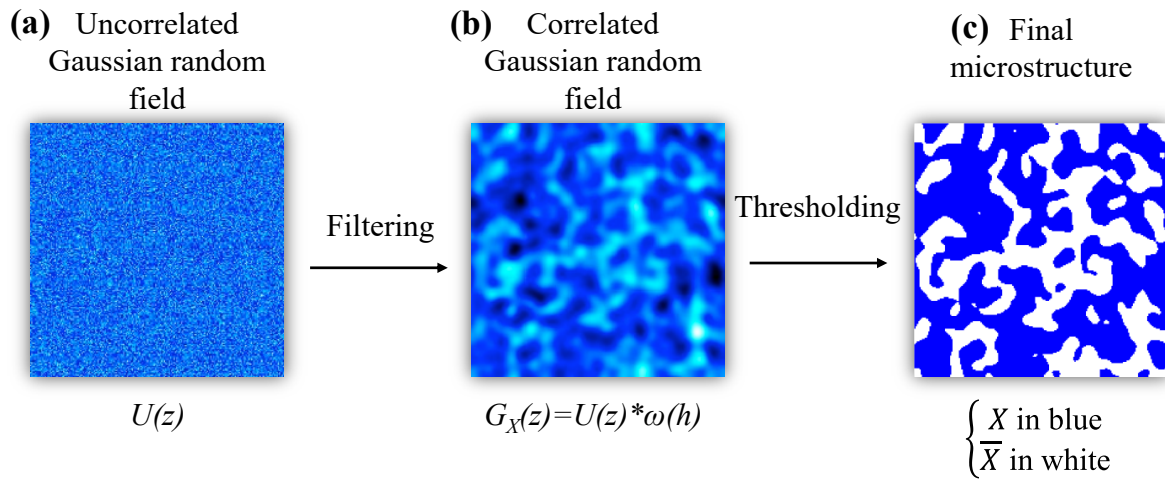


Fig. III.2 2D Illustration of the random field model methodology for a two-phase material (a) uncorrelated Gaussian field, also called ‘white noise’, (b) correlated Gaussian random field obtained by a product of convolution of the ‘white noise’ with a weight function ω (eq. (III.10)), and (c) the binary image, representing the final microstructure, obtained by segmenting the correlated random field with the computed threshold from eq. (III.6).

Numerical implementations – Instead of directly calculating computationally expensive convolutions, the use of Fast Fourier Transform (FFT) must allow to drastically reduce the time for generating the microstructure. For this purpose, the convolution products (III.7) and (III.9) have been carried out in the Fourier space by using FFT transforms:

$$G_X(z) = FFT^{-1} \left\{ FFT(U(z)) \times \sqrt{FFT(\rho(h))} \right\} \quad (III.11)$$

Thanks of the symmetry of $U(z)$ and $\rho(h)$, it is worth mentioning that their FFT transforms in eq. (III.11) lead to positive and real numbers (the imaginary part is nil). Moreover, it has been shown by Lang et al. [Lang2011] that the error induced by the FFT approximation is

negligible for a sufficiently fine discretization of the domain. Thanks to this model implementation, the simulations are very fast and allow the generation of virtual microstructures in a very short time compared to other iterative methods. For example, considering a volume of $9 \times 9 \times 9 \text{ } \mu\text{m}^3$ with a voxel size of 25 nm (corresponding to a $360 \times 360 \times 360$ voxels volume), the virtual microstructure of the studied two-phase electrode (for Cell-A: cf. Section III.4.1) is created in ~ 8 seconds by using only one CPU (Intel[®] Xenon[®]). It is worth noting that the FFT execution time is even further optimized when the total number of points is a power of 2 for example [Duhamel1990]. In the objective to quantitatively compare the iterative and non-iterative methods, the same microstructure has been generated by using the in-house overlapping sphere-packing algorithm presented in the next section (cf. III.2). With the same computational resources, a time of ~ 90 minutes is needed to obtain the synthetic microstructure. This result highlights the low computational expense requested by the random field methods in comparison to other iterative techniques. It can be noticed in both cases, the memory usage is about 756 Megabytes. Moreover, the time and the memory linearly increase with the number of voxels.

It can be noticed that a least square method is used to solve eq. (III.10) and to compute the discrete correlation function $\rho_x(h)$ by minimization on $C_x(h)$. However, it has been found that the direct use of the numerical expression of $\rho_x(h)$ to generate the microstructure yields an irrelevant noise (due to the non-derivability of $\rho_x(h)$ at the origin [Lantuéjoul2002]) at the interface between the phases (Fig. III.2). To overcome this issue, Abdallah et al. [Abdallah2016] have applied a low pass Gaussian filter on the random field $G_x(z)$ to remove the small-length artifacts. Alternatively, an analytical model for the correlation function (derivable at the origin) [Lantuéjoul2002, Abrahamsen1997, Wilson2001] can be fitted on the discrete values of $\rho_x(h)$ and used in the procedure. Different noise-free models and their combinations [Lantuéjoul2002, Abrahamsen1997] have been tested. It has been found that the exponential correlation of second order (Gaussian) is the most suitable function to obtain a good fit of $\rho_x(h)$:

$$\rho(h) = \exp\left\{\frac{-h^2}{2\ell^2}\right\} \quad (\text{III.12})$$

Where ℓ is the fitted correlation length. As illustrated in Fig. III.3, the resulting microstructure does not present noise at the phase interface.

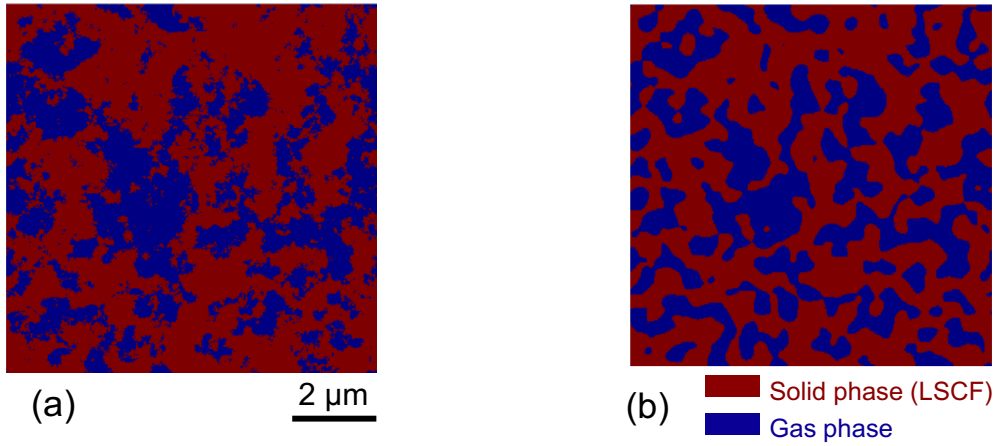


Fig. III.3 2D slice extracted from the 3D virtual microstructure for the LSCF electrode of Cell-A (cf. Section II.7.1). (a) Image obtained with the discrete correlation function $\rho_x(h)$ after minimization on $C_x(h)$ (without fitting). (b) Image obtained by fitting the Gaussian exponential function on the discrete values of $\rho_x(h)$ after minimization on $C_x(h)$.

The virtual microstructure for the two-phase electrode can be built either by generating the solid or the gas phase. In practice, no significant differences have been found for the typical tested electrodes. Besides, taking into account the stochastic nature of the method, different realizations result in different microstructures. Nevertheless, it has been found that the microstructures exhibit the same characteristics (in average) if considering a volume large enough to be statistically representative.

III.1.1.2 Three-phase materials for Ni-YSZ cermet or LSCF-CGO composite electrodes

Description of the model steps – In this section, a method [Galli1994, Armstrong2011] allowing the combination and thresholding of two independent Gaussian random fields has been used to simulate typical three-phase SOC electrode microstructures. The method is based on the generation of two fields $G_X(z)$ and $G_Y(z)$ with the covariance functions $C_X(h)$ and $C_Y(h)$ related to the phases X and Y of the real microstructure (i.e. for instance $X=Ni$, $Y=YSZ$ and porosity= $\overline{X \cup Y}$).

The process to compute $G_X(z)$ or $G_Y(z)$ is the same than the one depicted in the previous section. The two fields are then combined to form a bigaussian random field $G_{XY} = \{G_X(z); G_Y(z)\}$ that follows a standard normal bivariate distribution $G_{XY}(z) \sim$

$N\left(\mu = \begin{bmatrix} 0 \\ 0 \end{bmatrix}, \Sigma = \begin{bmatrix} 1 & 0 \\ 0 & 1 \end{bmatrix}\right)$ whose probability density function $p(x,y)$ is (Fig. III.4a):

$$p(x, y) = \frac{1}{2\pi} \exp\left\{-\frac{(x^2 + y^2)}{2}\right\} \quad (\text{III.13})$$

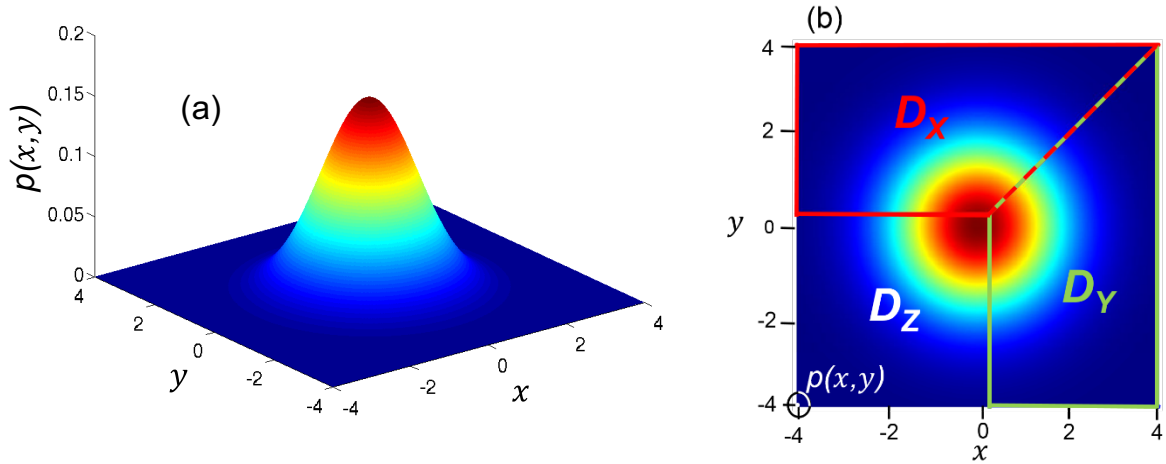


Fig. III.4 Distribution and definition of the thresholds for a three-phase electrode: the Gaussian field follows a normal bivariate distribution with probability density function $p(x,y)$ (a) segmented with a domain partitioning shown in (b). The angles at the triple point between D_X , D_Y , and D_Z allow controlling the specific surface areas between the three phases X, Y, and Z.

In order to get the synthetic microstructure, the bigaussian random field $G_{XY}(z)$ has to be segmented. The attribution of each voxel of $G_{XY}(z)$ to one of the three phases is carried out by the partitioning of the bivariate distribution $p(x,y)$. As illustrated in Fig. III.4b, the distribution is divided in three cells or domains D_X , D_Y and D_Z associated to the three electrode phases. The sets X , Y and Z of the synthetic microstructure are thus obtained by thresholding $G_{XY}(z)$ as follows:

$$X = \{z; G_{XY}(z) \in D_X\}; \quad Y = \{z; G_{XY}(z) \in D_Y\}; \quad Z = \overline{X \cup Y} \quad (\text{III.14})$$

The integrals of $p(x,y)$ on D_X and D_Y are equal to the volume fractions of X and Y :

$$\varepsilon_X = \int_{D_X} p(x,y) dx dy \quad \text{and} \quad \varepsilon_Y = \int_{D_Y} p(x,y) dx dy \quad (\text{III.15})$$

While the volume fraction of the complementary phase Z is simply given by $\varepsilon_Z = 1 - \varepsilon_X - \varepsilon_Y$. As detailed in Lantuéjoul [Lantuéjoul2002], the shape of the partitioning domains controls the contact surface between the phases. For example, angles of 120° at the triple point, defined as the intersection between the three domains, lead to an equal interfacial specific surface area between the phases (i.e. $S_p^{X,Y} = S_p^{X,Z} = S_p^{Y,Z}$). It could be interesting to investigate in a future work the eventual mathematical relationship between the angles at the triple point and the specific surface areas $S_{i/j}$.

To summarize, the model consists in the generation of two random fields $G_X(z)$ and $G_Y(z)$ corresponding to two of the three electrode phases. Then, the fields are combined and jointly thresholded on the basis of the domain partitioning of $p(x, y)$. This step is carried out in such a way that the properties of the synthetic microstructure satisfy the volume fraction and the interfacial specific surface area measured on the real reconstruction. However, since the threshold is not constant for both phases, a bias is introduced in the model so that the covariance functions of the resulting microstructure are liable to not match perfectly the real ones. This error is minimized during the segmentation step by using a third constraint on the covariance functions.

Numerical implementations – The random fields $G_X(z)$ and $G_Y(z)$ are generated with the same procedure detailed in the previous section. In this case, two distinct Gaussian exponential correlation functions are used to fit the discrete values of $\rho_X(h)$ and $\rho_Y(h)$ with two different correlation lengths. The partitioning of $p(x, y)$ and the thresholding of $G_{XY}(z)$ are carried out by minimizing the errors E on the interfacial specific surface area $S_p^{i,j}$ and the covariance functions $C_i(z)$ between the synthetic and real microstructures:

$$E = \sum_{i,j \in \{X,Y,Z\}; i \neq j} \frac{|S_p^{i,j} - S_{p_real}^{i,j}|}{S_{p_real}^{i,j}} + \sum_{0 \leq z \leq z_{\max}} \sum_{i \in \{X,Y,Z\}} \frac{|C_i(z) - C_{i_real}(z)|}{C_{i_real}(z)} \quad (\text{III.16})$$

This minimization is conducted by respecting the phase volume fractions. This sequence of the method is performed into an iterative loop that does not require the generation of a new random field. Indeed, the loop is only carried out after the generation of $G_{XY}(z)$ and only concerns the partitioning and thresholding of the random field. As a consequence, the time necessary to simulate a virtual three-phase material remains very short. Considering a volume of $15 \times 15 \times 15 \mu\text{m}^3$ with a voxel size of 25 nm (corresponding to a $600 \times 600 \times 600$ voxels volume), the virtual microstructure of the studied three-phase electrode (for Cell-A: cf. Section II.7.1) is created in ~ 230 seconds by using only one CPU (Intel[®] Xenon[®]), while, a time of several hours is needed to obtain the same microstructure with our sphere packing algorithm. For both cases, the memory usage is about ~ 3.5 Gigabytes.

Finally, without any constraints on the partitioning, the permutation of X and Y does not change the final synthetic microstructure. Therefore, only three combinations are possible to produce the synthetic microstructure depending on the choice of the complementary phase

(i.e. Z=Ni, YSZ or Gas). As for the two-phase electrodes, no significant difference has been found whatever the selected combination.

III.1.2 Validation of the random field model on 3D reconstructions

III.1.2.1 Validation for the two-phase O₂ electrodes

The model for the two-phase materials has been validated on the LSCF and LSC O₂ electrodes of Cell-A and Cell-B. The 3D rendering volumes of the real and synthetic microstructures are compared in Fig. III.5. As a first approach, the visual inspection of the 3D volumes for both electrodes reveals that the virtual microstructures seem to mimic quite perfectly the real ones. Therefore, it seems that the model would be able to accurately describe the coarse microstructure of Cell-A as well as the finer microstructure of Cell-B. As illustrated in Fig. 6a, this first statement is confirmed by the very good agreements between the covariance functions calculated on the synthetic volumes and the tomographic reconstructions. As it was expected, this result highlights on one hand the possibility to accurately compute the correlation $\rho_x(h)$ with eq. (III.10), and on the other hand, to have a good fit of $\rho_x(h)$ with the exponential correlation function.

To go further in the model validation, the cumulative PSD and all the key electrode microstructural parameters of the virtual electrodes have been determined in the same conditions than the data computed with the tomographic reconstructions (i.e. for the same RVE and voxel size). As shown in Table III.1, a very good agreement is achieved for all the parameters calculated for both electrodes. Indeed, the relative errors listed in Table 1 remain restricted in a range of few percent. For instance, the disagreement in respect of the electrode specific surface area, which is a crucial parameter controlling the electrode kinetic rate for the oxygen incorporation [Larencin2015], does not exceed 5% for both cells. Actually, the highest mismatch is found for the geometrical tortuosity and the constrictivity factor related to the pore phase of Cell-B. In this case, the error on these two parameters reaches values around +/-10%. It can be noticed that the mismatch between the virtual and real volumes arises for the phase that exhibits the finest microstructure characterized by the lowest mean particle size diameter and phase volume fraction. Therefore, for the two-phase electrode, the model yields the highest discrepancies on the geometrical tortuosity and constrictivity factor for the finest electrode microstructure.

It can also be remarked that the M-factor presents an error ranging between +/-5% and +/-10% whatever the investigated electrode phase (Table III.1). Indeed, this parameter combines the errors on the phase volume fraction, the geometrical tortuosity and constrictivity as discussed previously. Nevertheless, despite this discussion on its limitation, it is worth underlining that the model is able to statistically reproduce the main LSCF or LSC O₂ electrode microstructural properties with a high level of confidence.

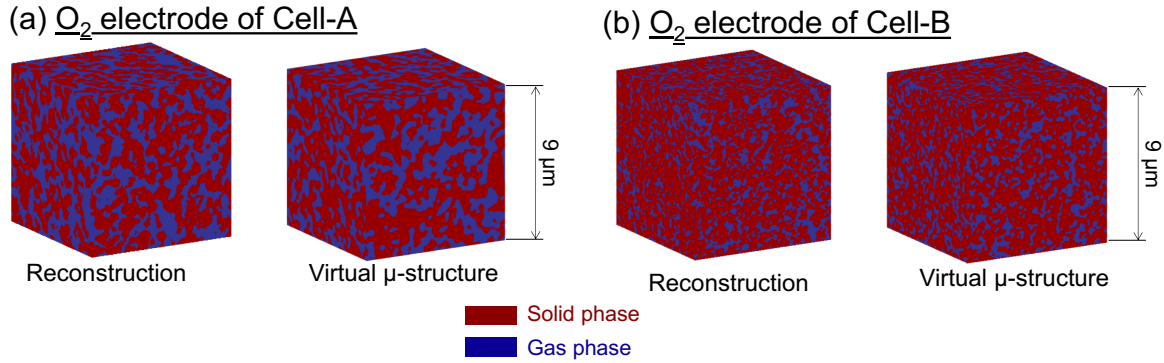


Fig. III.5. Visual comparison between the synthetic RF microstructures and the reconstructed volumes for the O₂ electrodes of (a) Cell-A and (b) Cell-B.

Table III.1

Microstructural properties for the O₂ electrodes of Cell-A and Cell-B computed on the tomographic reconstructions and the synthetic volumes.

O ₂ electrode of Cell-A													
Properties	S _p μm ⁻¹	Gas phase						Solid phase (LSCF)					
		δ (%)	ε (%)	d _p ^(*) (μm)	τ ^{gco} (-)	β (-)	M-factor (-)	δ (%)	ε (%)	d _p ^(*) (μm)	τ ^{gco} (-)	β (-)	M-factor (-)
Real μ-structure	3.80	99.96	43.64	0.26	1.22	0.10	0.194	99.99	56.36	0.32	1.34	0.11	0.289
Virtual μ-structure	3.78	99.94	43.61	0.27	1.23	0.11	0.185	99.98	56.39	0.32	1.46	0.12	0.319
Error	~0%	~0%	~0%	+4%	~0%	+4%	-5%	~0%	~0%	~0%	+9%	+6%	+10%
O ₂ electrode of Cell-B													
Properties	S _p μm ⁻¹	Gas phase						Solid phase (LSC)					
		δ (%)	ε (%)	d _p ^(*) (μm)	τ ^{gco} (-)	β (-)	M-factor (-)	δ (%)	ε (%)	d _p (μm)	τ ^{gco} (-)	β (-)	M-factor (-)
Real μ-structure	6.28	99.76	28.83	0.12	2.27	0.23	0.078	100	71.17	0.22	1.31	0.31	0.474
Virtual μ-structure	5.97	99.47	28.85	0.13	2.03	0.26	0.084	100	71.15	0.24	1.22	0.33	0.497
Error	-5%	~0%	~0%	+8%	-11%	+13%	+7%	~0%	~0%	+9%	-7%	+6%	+5%

^(*) mean phase diameter taken from the PSD.

Finally, as shown in Fig. III.6c and III.6d for both cells, a good agreement is also observed between the cumulative PSDs of the virtual and real electrodes. It is worth mentioning that these curves characterize all the morphological details of the microstructure at different length scales. From that point of view, they integrate an important portion of the errors for the morphological parameters listed in Table III.1. Therefore, the PSD plots can be seen as one of

the toughest criteria to validate the model. Since the mismatch with the real electrodes is rather limited for both cells, it is claimed that the microstructure generated with truncated Gaussian random field is fully representative for the two-phase electrode materials.

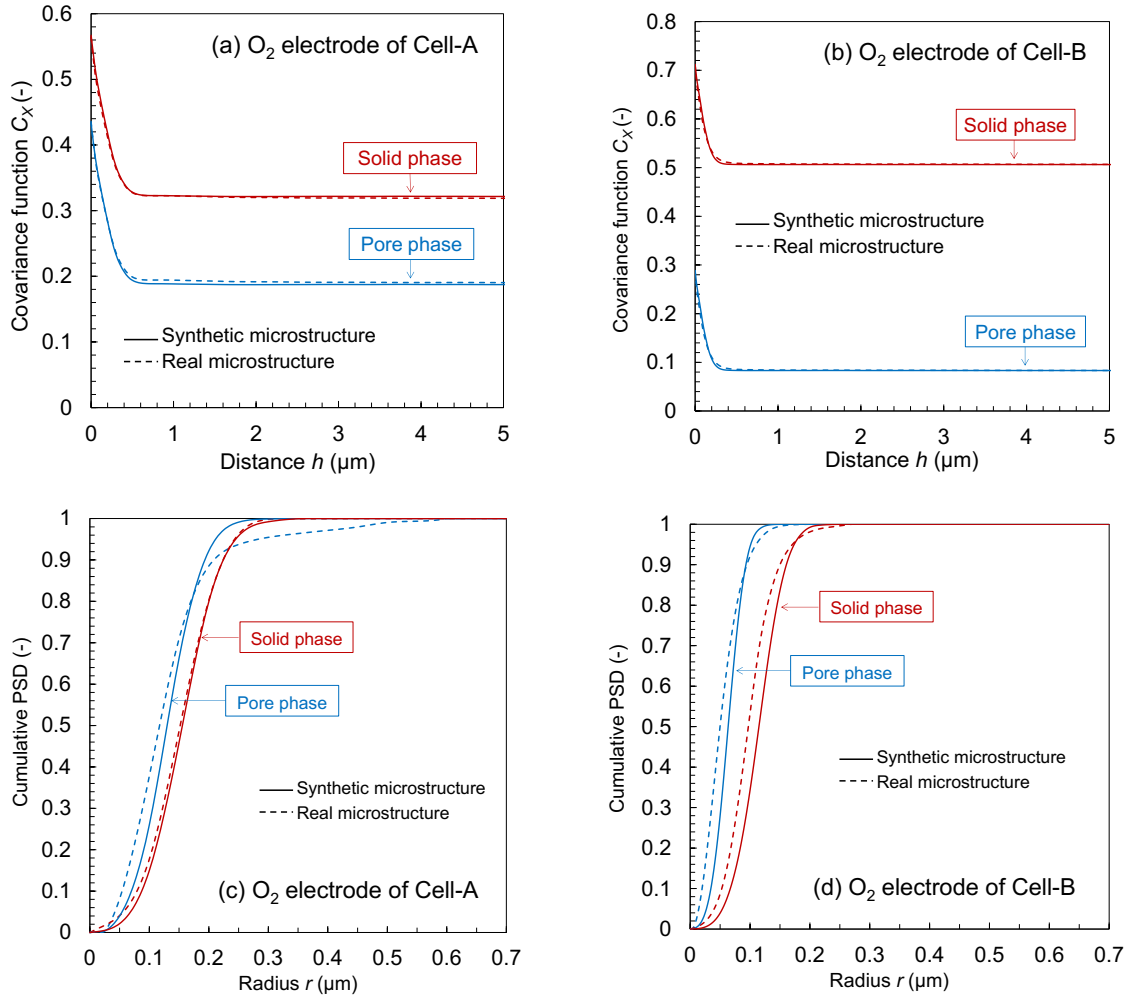


Fig. III.6. Comparison between the synthetic and real O₂ electrode microstructures in respect of (a,b) the covariance functions and (c,d) the cumulative PSDs for both Cell-A and Cell-B.

III.1.2.2 Validation for the three-phase electrodes

a) Validation for the Ni-YSZ H₂ electrodes of Cell-A and Cell-B

The Ni-YSZ synthetic microstructures have been generated with the two independent random fields G_X and G_Y related to the two solid phases and the porosity as the complementary set. As already mentioned, no large difference in terms of representativeness has been found whatever the considered combination. The 3D rendering volumes of the synthetic

microstructures are compared to the Ni-YSZ cermet reconstructions in Fig. III.7. As for the LSCF or LSC electrode, the visual inspection shows that the model would be able to correctly describe the more complex microstructure of the three-phase electrodes. This preliminary observation is also supported by the good agreement found between the covariance functions of the real and synthetic microstructures (Fig. III.8a and III.8b).

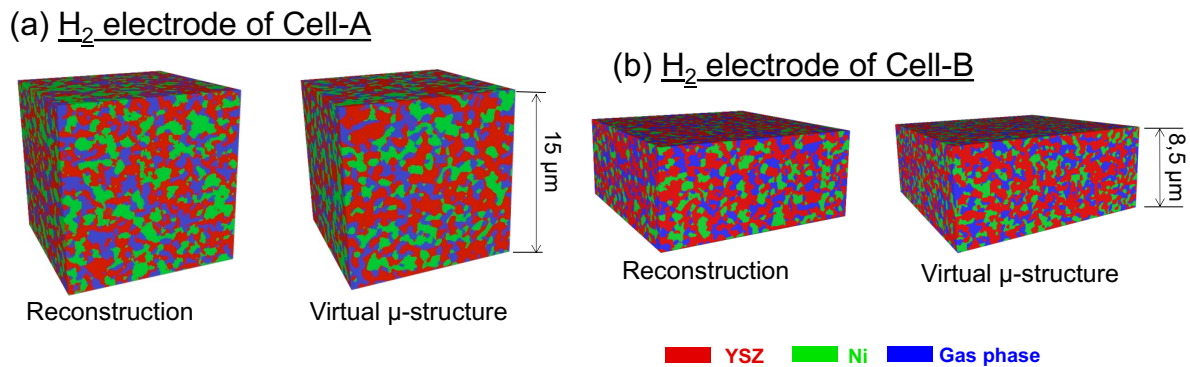


Fig. III.7. Visual comparison between the synthetic microstructures and the reconstructed volumes for the H_2 electrodes of (a) Cell-A and (b) Cell-B.

To check more precisely the model representativeness, the microstructural properties of the synthetic volume have been compared to the real values in Tables III.2 and III.3. As a general matter, a rather good accordance is found for all the parameters. More specifically, it can be remarked that the model is able to accurately reproduce the density of TPBs which is of central importance as it controls the efficiency of the Ni-YSZ electrode [Lay-Grindler2013]. Indeed, the error on the density of TPBs is less than $\pm 2.5\%$ for the two studied cells. Moreover, the model is also able to capture correctly the electrodes specific surface areas for both electrodes with a mismatch that does not exceed $\pm 2\%$. Actually, the highest discrepancy arises for the transport properties of the pore and Ni phases of Cell-A and Cell-B. In this case, the errors on the M-factor ranges between 20-25% while the one for the YSZ phase of both electrodes remains negligible ($\leq 1\%$). This noticeable discrepancy on the microstructural factor for the Ni and pore phases is clearly related to the error on the constrictivity parameter (cf. Table III.2). This mismatch on the constrictivity seems to be correlated with the phases that exhibit the lowest volume fraction ($< 30\%$ for the Ni and pores and $> 45\%$ for the YSZ). In other words, it appears that the model is able to accurately reproduce the metric properties (i.e. volume fractions, specific surface areas, mean phase

diameters and density of TPBs), whereas a higher discrepancy on the topological parameters (i.e. constrictivity and tortuosity) is detected for the phases with a low volume fraction (cf. Ni phase in Table III.2 and III.3). As the topological properties are related to the connectivity [Russ2001], a large variation in their values can be expected when the volume fractions get closer to the percolation threshold. This remark could explain the apparent correlation between the error on tortuosity and constrictivity for low phase volume fractions. However, some authors [Jouannot-Chesney2017] have proved, for some random spatial structures, that there does not exist any direct link between the percolation threshold and its topology described by the Euler-Poincaré characteristic. We recall that this parameter is a topological invariant that describes the shape of a topological space or structure regardless of the way it is bent [Armstrong1997]. From this point of view, it appears that further investigations are still needed to better understand the evolution of the electrode topology close to the percolation limit. Nevertheless, as a general comment for the three-phase electrode, it turns out that the model exhibits a limitation to reproduce with a high level of confidence a microstructure composed of very high constrictive phases associated with low volume fraction.

The cumulative PSDs are plotted in Fig. III.8c and III.8d for Cell-A and Cell-B. There is a relatively good agreement between the curves. As expected, the highest discrepancies arise for the Ni and pore phases of Cell-A and Cell-B. In this case, the curves for the real microstructure are more widespread than the ones for the synthetic volume. It means that the Ni and pore phases present a large distribution of particle lengths which is well correlated with their low constrictivity parameters. This result highlights the limitation to perfectly model the high constriction effect associated with a large distribution of particle size. Nevertheless, it is worth mentioning that this limitation of the model remains acceptable for the investigated SOCs electrodes (in the worst case, the error on the microstructural factor does not exceed 25% for Cell A and 24% for Cell-B: cf. Tables III.2 and III.3). As a consequence, despite the limitation on the constrictivity factor, it can be then concluded that the adapted plurigaussian random field model is able to accurately simulate the main electrode properties, and then to provide a realistic and representative Ni-YSZ synthetic microstructure.

Table III.2

Microstructural properties for the H₂ electrodes of Cell-A computed on the tomographic reconstruction and the synthetic volume.

H ₂ electrode of Cell-A														
Properties	Gas phase							Electronic conducting phase (Ni)						
	S _p μm ⁻¹	δ (%)	ε (%)	d _p ^(*) (μm)	τ ^{geo} (-)	β (-)	M-factor (-)	S _p μm ⁻¹	δ (%)	ε (%)	d _p ^(*) (μm)	τ ^{geo} (-)	β (-)	M-factor (-)
Real μ-structure	2.67	94.74	28.04	0.28	1.67	0.09	0.030	2.30	97.45	27.88	0.33	1.75	0.08	0.041
Virtual μ-structure	2.64	99.43	28.14	0.28	1.62	0.11	0.036	2.32	99.21	27.78	0.34	1.70	0.10	0.051
Error	-1%	+4%	~0%	~0%	-3%	+22%	+21%	+1%	+2%	~0%	+3%	-3%	+25%	+25%
Properties	Ionic conducting phase (YSZ)							Density of TPBIs (Ni/YSZ/gas contact lengths)						
	S _p μm ⁻¹	δ (%)	ε (%)	d _p ^(*) (μm)	τ ^{geo} (-)	β (-)	M-factor (-)	ξ _{TPBIs} ^(**) (μm ⁻²)						
Real μ-structure	3.68	99.78	44.08	0.28	1.43	0.13	0.189	4.78						
Virtual μ-structure	3.65	99.94	44.08	0.29	1.43	0.13	0.190	4.73						
Error	-1%	~0%	~0%	+3%	~0%	~0%	~0%	-1%						

(*) mean phase diameter taken from the PSD. (**) density of 'active' TPBIs computed on the connected phases.

Table III.3

Microstructural properties for the H₂ electrodes of Cell-B computed on the tomographic reconstruction and the synthetic volume.

H ₂ electrode of Cell-B														
Properties	Gas phase							Electronic conducting phase (Ni)						
	S _p μm ⁻¹	δ (%)	ε (%)	d _p ^(*) (μm)	τ ^{geo} (-)	β (-)	M-factor (-)	S _p μm ⁻¹	δ (%)	ε (%)	d _p ^(*) (μm)	τ ^{geo} (-)	β (-)	M-factor (-)
Real μ-structure	2.94	94.23	26.55	0.24	1.74	0.39	0.021	2.46	92.81	24.13	0.28	1.81	0.34	0.018
Virtual μ-structure	2.87	98.65	26.80	0.25	1.66	0.45	0.026	2.41	97.75	24.82	0.28	1.74	0.41	0.021
Error	-2%	+4%	+1%	+4%	-4%	+15%	+24%	-2%	+5%	+2%	~0%	-4%	+21%	+17%
Properties	Ionic conducting phase (YSZ)							Density of TPBIs (Ni/YSZ/gas contact lengths)						
	S _p μm ⁻¹	δ (%)	ε (%)	d _p ^(*) (μm)	τ ^{geo} (-)	β (-)	M-factor (-)	ξ _{TPBIs} ^(**) (μm ⁻²)						
Real μ-structure	3.42	99.92	49.55	0.31	1.14	0.44	0.243	6.20						
Virtual μ-structure	3.45	99.98	48.38	0.31	1.13	0.47	0.246	6.07						
Error	+1%	~0%	-2%	~0%	-1%	+7%	+1%	-2%						

(*) mean phase diameter taken from the PSD. (**) density of 'active' TPBIs computed on the connected phases.

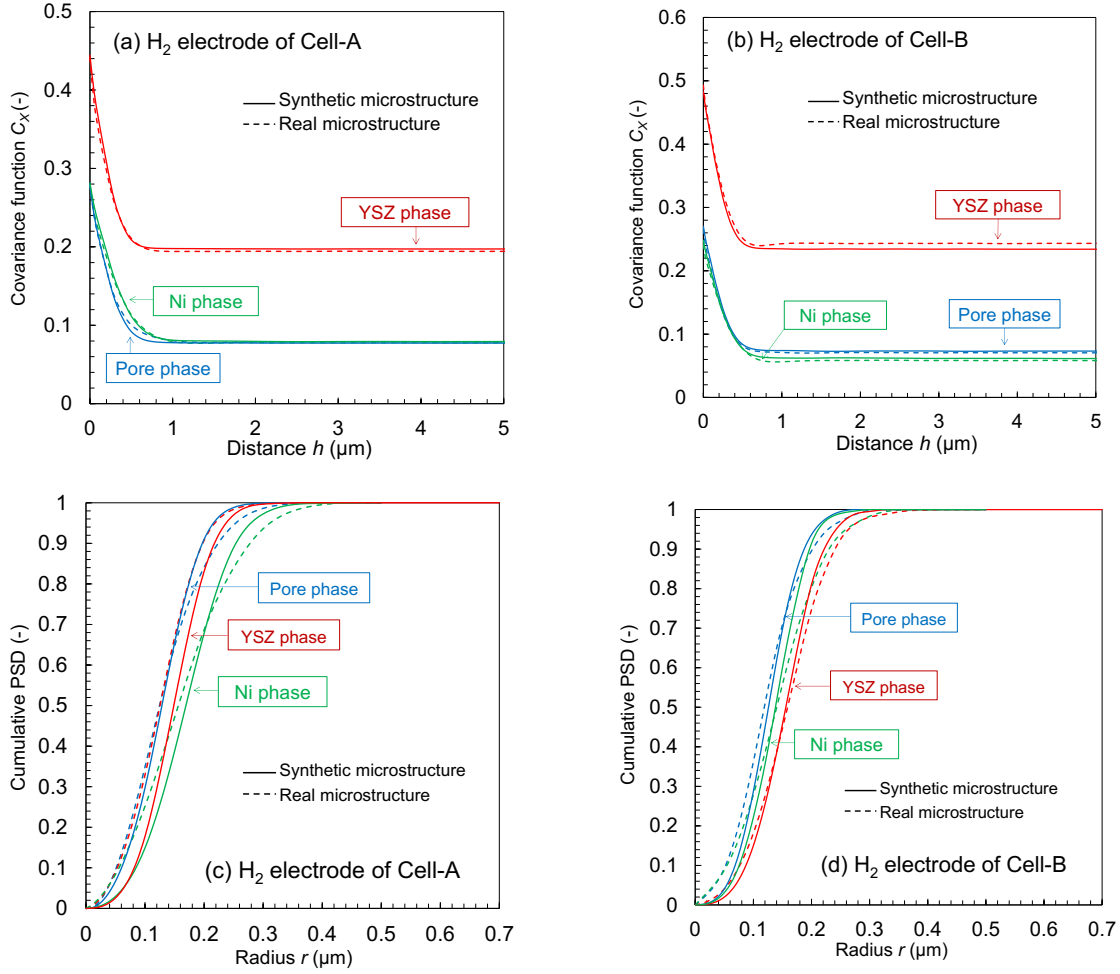


Fig. III.8. Comparison between the synthetic and real H₂ electrode microstructures in respect of (a,b) the covariance functions and (c,d) the cumulative PSDs for both Cell-A and Cell-B.

In ref. [Moussaoui2017], the authors have investigated the representativeness of the model proposed by Abdallah et al. [Abdallah2016] who considered an alternative method based on two underlying independent Gaussian random fields with two constant thresholds for the segmentation. The validation was performed on the same Ni-YSZ electrode reconstruction of Cell-A. The deviation from the real microstructural properties was significantly higher than the one reported in Table III.2. For instance, the error on the density of TPBs and the constrictivity for the Ni phase reaches 11% and 38%, respectively [Moussaoui2017]. Therefore, the proposed model based on an adjusted partitioning of the bigaussian field G_{XY} , is more accurate to simulate representative microstructures, and hence it can be seen as an improved method regarding the SOC application.

b) Validation for the LSCF-CGO electrodes of Cell-C

The method validity has been also checked for a composite electrode made of two ceramic components. For this purpose, the LSCF-CGO O₂ electrode of Cell-C has been used. The same procedure than for the Ni-YSZ cermet has been followed.

The 3D rendering volumes of the real and synthetic microstructures are compared in Fig. III.9. The visual inspection of the two volumes reveals that the virtual microstructure seems to mimic quite accurately the complex and fine microstructure of the real electrode. For a full model validation, the electrode microstructural properties have also been computed on the synthetic volume and compared to the real parameters in Table III.4. As expected, a general good agreement between the two sets of parameters has been found. More precisely, the metric properties are retrieved by the geometrical model with a high level of confidence. Indeed, the relative errors on the predicted properties with respect to the real ones do not exceed a few percent (Table III.4). As an illustration, the error on the active TPBLs is only 2% for this particular electrode.

Concerning the topological properties, the relative errors remain very low for the porosity and the LSCF phase. The highest discrepancy is found for the CGO backbone. In this case, the relative errors on the geometrical tortuosity, connectivity and constrictivity reach -2%, 6% and 9%, respectively. The combination of these errors in the M-factor leads to a rather high level of uncertainty on the prediction of this parameters (up to 20%). This deviation could be assigned with the low volume fraction of the CGO phase which is not so far from its percolation threshold (only 91% of CGO phase is connected).

To conclude, the model is also able to reproduce accurately the microstructure of the porous LSCF-CGO electrode. The uncertainties are roughly in the same order than the Ni-YSZ cermet with the same limitation on the transport properties when reaching the phase percolation threshold.

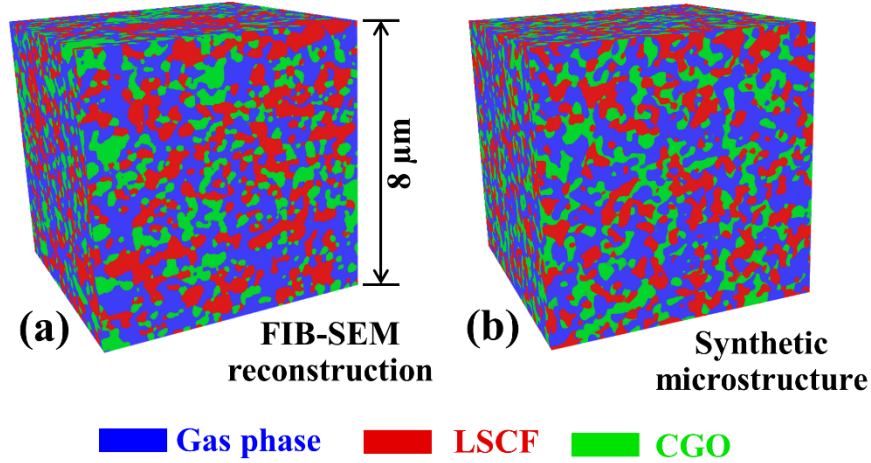


Figure III.9: Rendering volumes for the real and synthetic microstructures of the LSCF-CGO electrode of Cell-C

Table III.4

Microstructural properties of the LSCF-CGO composite O₂ electrode of Cell-C computed on the FIB-SEM reconstruction and the synthetic volume (S_p =specific surface area, δ =connectivity, ϵ =volume fraction, d_p = mean phase diameter, τ^{geo} =geometrical tortuosity, β =constrictivity factor, M-factor=ratio effective/bulk conductivities, ξ_{TPB} =density of TPBs).

LSCF-CGO electrode														
Properties	Gas phase							MIEC (LSCF)						
	S_p μm^{-1}	δ_{gas} (%)	ϵ (%)	$d_p^{(*)}$ (μm)	τ^{geo} (-)	β (-)	M-factor (-)	S_p μm^{-1}	δ_{LSCF} (%)	ϵ (%)	$d_p^{(*)}$ (μm)	τ^{geo} (-)	β (-)	M-factor (-)
FIB-SEM	4.41	99.99	43.45	0.17	1.55	0.53	0.2441	3.26	97.86	30.15	0.19	1.77	0.51	0.0428
Synthetic	4.37	99.94	43.35	0.17	1.53	0.54	0.2449	3.23	99.55	30.14	0.19	1.75	0.52	0.0442
Error	<1%	<1%	<1%	-0%	-1%	2%	<1%	-1%	2%	<1%	-0%	-1%	2%	3%
Properties	Ionic conducting phase (CGO)							Density of TPBs						
	S_p μm^{-1}	δ_{CGO} (%)	ϵ (%)	$d_p^{(*)}$ (μm)	τ^{geo} (-)	β (-)	M-factor (-)	Total ξ_{TPBs} (μm^{-2})			Active (**)			
FIB-SEM	3.27	91.56	26.40	0.16	1.84	0.52	0.0183	12.09			9.06			
Synthetic	3.24	99.42	26.51	0.16	1.81	0.55	0.0219	12.57			9.24			
Error	-1%	9%	<1%	-0%	-2%	6%	20%	4%			2%			

(*) mean phase diameter taken from the Phase Size Distribution. (**) density of 'active' TPBs computed on the connected phases.

III.1.3 Discussion: model flexibility to various electrode microstructures

With the present validated numerical tool, different synthetic microstructures could be generated by changing the model input parameters. If considering the 3D reconstructions as the reference electrode, the set of synthetic volumes could be used to establish the microstructural relationships for the classical SOC electrodes. For instance, the effect of phase volume fractions can be easily investigated by changing the random field thresholding. Moreover, in order to investigate a finer or a coarser microstructure, the mean diameter of each phase can be tuned by changing its correlation length in the expression of $\rho_i(h)$ (cf. eq.

(III.12)). This kind of sensitivity analysis can be used for a numerical optimization of the SOC electrode microstructures in order to provide guidelines for the cell manufacturing. Nevertheless, aside from this classical optimization, the relevance of the 3D microstructure model must also stand in its capacity to generate a large variety of innovative electrode architectures. In the following, the model flexibility is illustrated and discussed on different examples of promising electrode designs.

III.1.3.1 Impact of domain partitioning

As mentioned in Section III.1.1.2, the contact surface areas between the phases in the three-phase electrode depend on the domain partitioning of the bivariate distribution. This property of the model can be useful to control the ‘coverage rate’ of one phase to the other, and hence, to adapt the interfacial specific surface areas between the electrode phases. This model property is illustrated on Fig. III.10: by changing the domain partitioning, the specific surface areas can be easily tuned by keeping the same phase volume fractions and phase characteristic lengths. As expected, the density of TPBIs is maximal when the three interfacial specific surface areas are equal (Fig. III.10). Nevertheless, knowing that the volume fractions and characteristic lengths are not modified, it can be remarked that the density of TPBIs is not strongly affected by changing the domain partitioning. Advantage could be taken of this model specificity regarding the microstructural optimization. Indeed, as an illustration for the LSCF/CGO composite, the maximization of the LSCF/gas interface by keeping a sufficiently high density of TPBIs would be necessary to promote the oxygen adsorption and incorporation [Hubert2016]. Correspondingly for the Ni/YSZ cermet operated in electrolysis mode, it could also be interesting to increase the Ni/gas interface area to favor the suspected limiting step of steam adsorption on the Ni surface [Godula-Jopek2015].

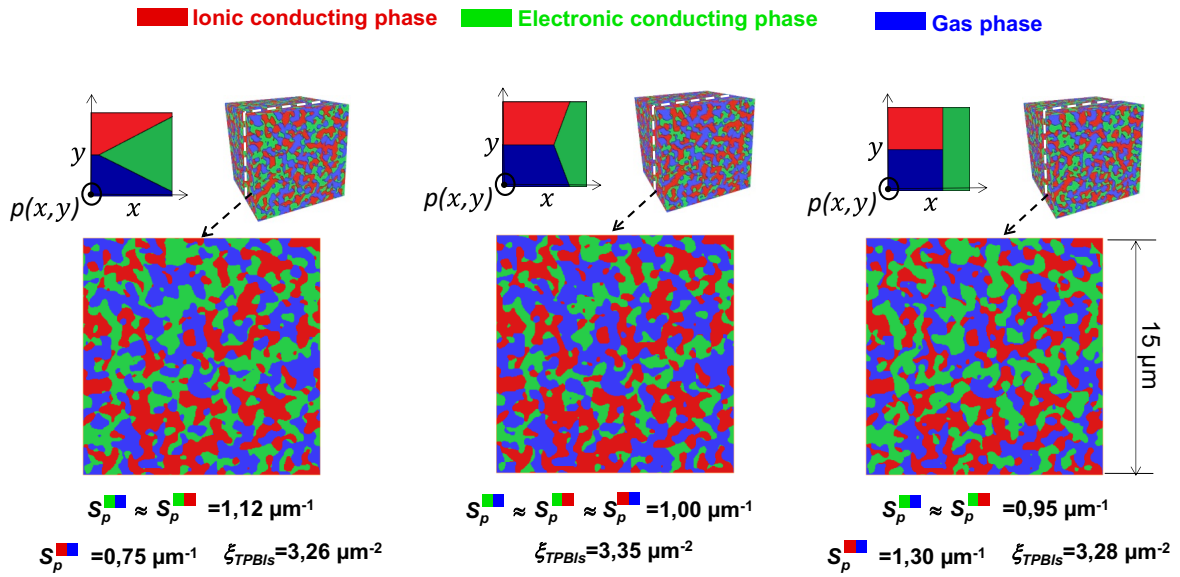


Fig. III.10 Impact of domain partitioning for a composite electrode. The ‘coverage rate’ between the phases can be tuned to control the specific surface areas and density of TPBs (simulated microstructure with the same volume fraction for each phase).

Furthermore, the particular situation of constant parallel thresholds leads to divide the domain into three horizontal regions resulting in a microstructure with one intermediate phase that surrounds the other (Fig. III.11). By taking advantage of this model specificity, it becomes possible to model the electrodes prepared by infiltration which have the potentiality to be the next generation of functional active layers replacing the classical composite [Irvine2016]. Indeed, depending of the manufacturing process, the infiltration results in a continuous thin film deposited on an electrode scaffold [Ding2014, Bidrawn2011]. As shown in Fig. III.11, this particular materials architecture can be easily modeled by reducing the volume fraction of the intermediate phase with the partitioning in three parallel strips of the bivariate distribution.

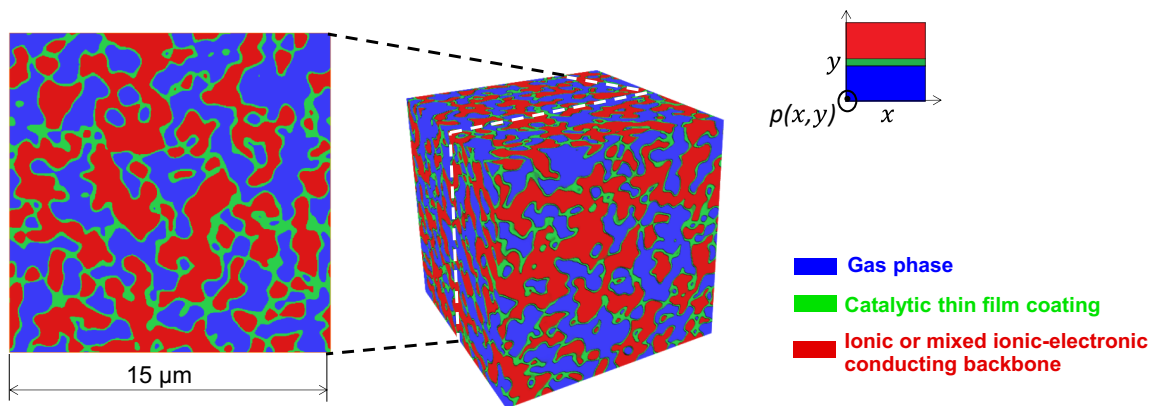


Fig. III.11 Simulation of a thin film coating impregnated onto the surface of the electrode backbone (simulated microstructure with: $\epsilon=0.41$ for the ionic conducting scaffold, $\epsilon=0.19$ for the catalytic coating).

III.1.3.2 Introduction of a local thresholding: illustration on the graded electrodes

With the random field model, spatial heterogeneities can be introduced in the microstructure with a threshold that depends on the local position in the material. This model feature offers the possibility to generate specific architectures for optimizations by material design. In this frame, the Functionally Graded Materials (FGM), which exhibit a spatial distribution in the composition and/or in the structure, are nowadays widely studied as advanced engineering materials [Naebe2016]. The concept of FGM has been applied to the SOC electrodes in an attempt to enhance the cell efficiency and reliability [Kong2007, Nie2015]. With a gradient in composition and/or particle size for both electronic and ionic conducting phases, it has been shown that the electrode performances may be improved by optimizing the ohmic losses in the active layer [Deseure2005, Schneider2007]. Besides, by mitigating the thermal expansion mismatch with the electrolyte, it has been shown that the graded electrodes present an enhanced mechanical stability [Anandakumar2010]. Nevertheless, the best compromise between the mechanical robustness and electrochemical efficiency needs to be identified [Schneider2007].

As an illustration of the local thresholding for the SOC application, the graded electrodes have been simulated with the model. For the two phase materials, a gradient in composition can be easily introduced in the microstructure by considering a threshold that evolves continuously along the thickness of the active layer (Fig. III.12a). This method allows obtaining a good spatial continuity in the final structure, as sought for the SOC application. For the composite electrodes, the microstructure should exhibit two opposite compositional gradients for the electronic and ionic conducting phases in order to maximize the collection of both electronic and ionic currents [Schneider2007]. This structure can be simulated by using a space dependent partitioning of the bivariate distribution in order to get the targeted local electrode composition. Moreover, this mapping can be done by controlling the angle around the triple point to optimize the interfacial specific surface areas (cf. previous section). For a sake of clarity, the evolution of domain partitioning is illustrated in Fig. III.12b for two constant thresholds. As expected, the resulting microstructure presents two continuous and opposite gradients for the ionic and electronic conducting phases (Fig. III.12c) that are assumed to be well representative of real graded electrodes. Thanks to the model flexibility, the compositional gradients in association with the local morphological characteristics such as interfacial surface area are liable to be optimized.

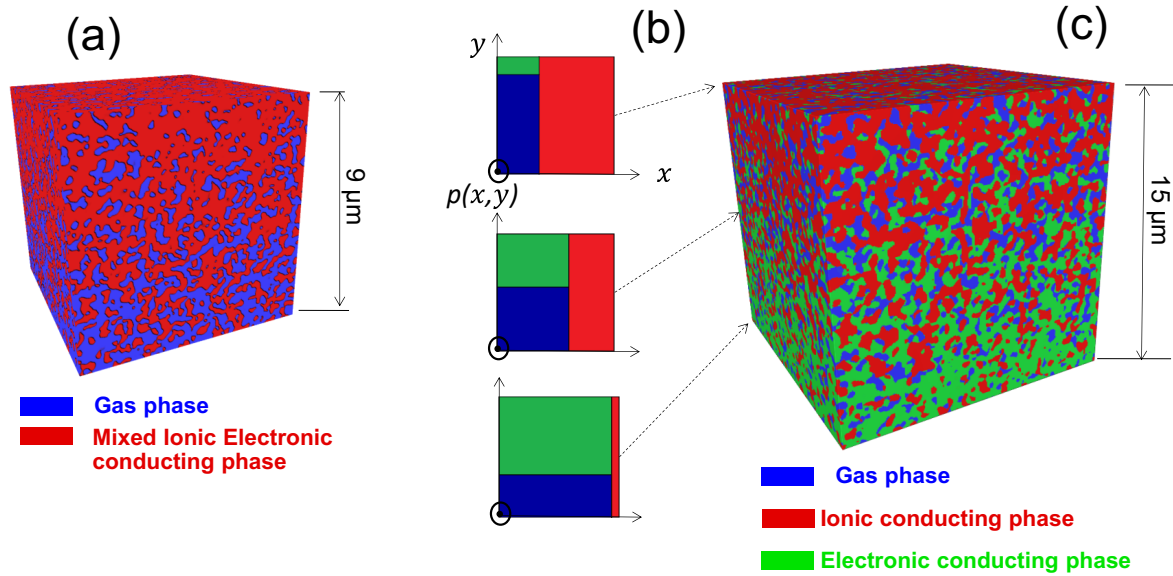


Fig. III.12 Graded electrodes simulated with the local thresholding: (a) 3D rendering volume for a two-phase electrode, (b) Evolution of the domain partitioning: illustration of the thresholding maps taken at three different locations along the electrode thickness and (c) 3D rendering volume for a three-phase electrode.

III.1.3.3 Introduction of a multi-correlation length: impact on interfacial roughness

The morphology of the solid/solid or gas/solid interface plays a major role in the SOC electrode efficiency. Indeed, a high surface exchange between the phases is generally required to favor the reactions of mass and/or charge transfers. Aside from the classical ceramic manufacturing routes, various deposition techniques such as the Electrostatic Spray Deposition (ESD) [Sharma2016] have been recently used to control the electrode surface morphology. For example, the ESD has allowed to produce LSCF nanostructured porous coatings for the O₂ electrode with a high surface area [Marinha2011].

In order to reproduce such kind of electrodes, it can be interesting to produce virtual microstructures by controlling the local topology of the gas/solid interface. This can be achieved with the random field model by introducing a second correlation length ℓ^* related to the electrode local roughness. This possibility has been investigated for the O₂ electrode. The method is based on the generation of two random fields, $G_{X,\ell}(z)$ and $G_{X^*,\ell^*}(z)$, containing the information on the characteristics lengths at the ‘microscopic’ and ‘nanoscopic’ scales, ℓ and ℓ^* , respectively. Typically, the characteristic length ℓ of the microstructure is around 0.25-

0.75 μm while the dimension of the local roughness ℓ^* could be in the range of few tens of nanometers [80]. In practice, $G_{X,\ell}(z)$ and $G_{X^*,\ell^*}(z)$ are combined in a bigaussian field and then segmented considering a specific diagonal domain partitioning defined by the threshold $G_X + G_{X^*} = \lambda$. This domain partitioning allows giving the same weight for the characteristics of $G_{X,\ell}(z)$ and $G_{X^*,\ell^*}(z)$ in the final synthetic microstructure. It is equivalent to add the two fields and use a constant threshold as follows:

$$G_{solid}(z) = G_{X,\ell}(z) + G_{X^*,\ell^*}(z) \quad \text{with } \ell^* < \ell \quad \text{and } \varepsilon_{solid} = P\{G_{solid}(z) \geq \lambda\} \quad (\text{III.17})$$

As the method is based on the sum of two independent random fields $G_{X,\ell}(z)$ and $G_{X^*,\ell^*}(z)$ associated to their correlation functions $\rho_{X,\ell}(z)$ and $\rho_{X^*,\ell^*}(z)$, it is also equivalent to the generation of one single field $G_{XX^*,\ell,\ell^*}(z)$ defined by the correlation $\rho_{XX^*,\ell,\ell^*}(z) = \rho_{X,\ell}(z) + \rho_{X^*,\ell^*}(z)$. Note the procedure leads to add some few small disconnected inclusions in the phases that are removed by simple morphological operation [Serra1988].

To illustrate the method, the O₂ electrode microstructures obtained with one and two correlation lengths have been generated and compared in Fig. III.13a and III.13b. In order to make the comparison relevant, it is worth noting that the two microstructures have been generated in such a way that they present the same phase volume fraction and the same mean particle size. As expected, the microstructure which combines the two correlation lengths presents a much higher surface roughness than the one obtained with the classical method. Indeed, the electrode specific surface area is increased from 3.89 μm^{-1} for the classical microstructure to 5.12 μm^{-1} for the second one. This evolution is in good agreement with the PSD of the solid phase plotted in Fig. III.13c: the microstructure obtained with two correlation lengths exhibits a dissymmetry in the distribution due to the appearance of small particles related to the surface roughness. This result highlights the flexibility of the method to control the morphology of the electrode interfaces.

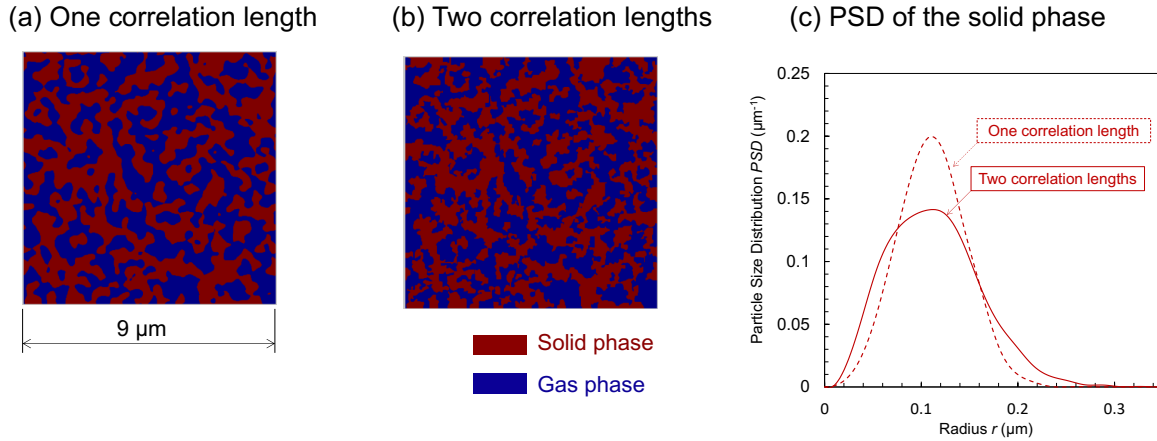


Fig. III.13. 2D slices taken in the 3D synthetic volume for a two-phase electrode simulated with: (a) one correlation length and (b) two correlation lengths. (c) PSD plots for the two microstructures. Both electrodes have been simulated so that they have the same phase volume fraction ($\epsilon_{\text{solide}}=0.5$) and mean phase diameter ($d_p=0.2 \mu\text{m}$).

III.1.4 Conclusion

An original 3D stochastic model, based on the truncated plurigaussian random fields, has been adapted to simulate the complex microstructure of SOC electrodes. To improve the relevance of the method regarding to the application, the model includes a generalization consisting in an *Ad hoc* partitioning of the combined random fields. A special attention has also been paid to the numerical implementation in order to generate the electrode virtual microstructure in a very short time. This criterion is of central importance for forthcoming studies devoted to the microstructural optimization or to the assessment of the complex relationships linking the morphological electrode properties.

The representativeness of the virtual microstructures has been checked on five synchrotron X-ray and FIB-SEM tomographic reconstructions obtained on typical LSCF, LSC, Ni-YSZ, and LSCF-CGO electrodes. The validation step has been carried out by comparing a set of relevant electrode morphological properties as well as the phase effective conductivities or diffusivities. It has been found that the model is able to accurately reproduce the density of TPBs and the specific surface areas which are the main parameters controlling the reaction kinetic rates in the electrodes. For both of these microstructural properties, the mismatch between the synthetic material and the real reconstruction do not exceed a +/- 5% whatever the tested electrode. Although the model fails to reproduce perfectly very high constrictive phases, the characteristic parameters controlling the mass and charge transport in the virtual

microstructures have been found to be in rather good agreement with the properties of the real electrodes. As a general matter, it was inferred from this analysis that the synthetic media correctly mimic the complex microstructure of typical SOC electrodes.

Finally, the model flexibility for simulating different types of SOC microstructural architectures has also been illustrated on different examples. Aside from the classical properties such as the volume fractions or the characteristic lengths of the phases, a specific domain partitioning of the bigaussian random field allows controlling the coverage rate of one solid phase to the other. This characteristic of the model is particularly useful to generate SOC electrode prepared by infiltration resulting in a uniform and continuous thin layer covering a scaffold. With a local thresholding depending on the position, continuous graded electrodes can be also produced. Finally, the model offers the possibility to introduce different correlation lengths for each phase in order to control the local topology of the interfaces. All these cases illustrate the model capability to be adapted to the different kind of promising electrode designs for further numerical microstructural optimizations.

III.2 Particle-based model description and validation

In complementarity with the non-iterative mathematical model based on the Random Field method, an original particle-based algorithm has been developed to generate synthetic microstructures. In this objective, the packed structures must mimic the characteristics of two-phase and three-phase electrodes commonly fabricated with the sintering of powder materials. Ionic-conducting and electronic-conducting particles are used to emulate the solid phases, while the porosity constitutes the complementary phase of the partially densified medium. With this approach, the model steps and the morphological input data can be related to the real electrode manufacturing process. Indeed, initial particles, following a desired size distribution, are positioned in the 3D space and then a numerical procedure is applied to obtain the sintered microstructure. In this approach, the particle size distribution chosen for the simulations can be roughly ascribed to the distribution of the real powder particles used for the electrode manufacturing. For the densification, some additional geometrical and numerical parameters are introduced to control the homogeneity of the microstructure and the particles interpenetration into the synthetic medium. These parameters are also depending on the conditions of the slurry preparation and the electrode sintering.

The model description is given in the following Section III.2.1, then its validation is summarized in Section III.2.2, and finally an illustration of its flexibility is presented in Section III.2.3.

III.2.1 Particle-based model description for SOC electrodes

III.2.1.1 Two-phase materials for O₂ electrode

The three main steps to generate a two-phase synthetic microstructure are listed below:

(a) *Initial sphere allocation* – The particle structure generation starts with an empty volume V in which are positioned some initial spheres with a given particle size distribution. The choice of this distribution is of capital importance to control the geometrical characteristic of the final microstructure. In practice, different distributions were tested and it has been found that the Weibull function is the best compromise to reproduce the SOC electrode microstructures (eqn. III.18):

$$f_{Weibull}(r; \lambda, k) = \frac{k}{\lambda} \left(\frac{r}{\lambda}\right)^{k-1} e^{-(r/\lambda)} \quad (\text{III.18})$$

where r is the random variable for the sphere radius, and k and λ are respectively the shape and scale parameters. The characteristics of the spheres population (mean, standard deviation, skewness, etc.) are expressed directly as a function of these two parameters. This distribution is consistent with the one of the classical powder particles used for the electrode manufacturing. Indeed, the real distribution of the powders usually follows a non-symmetrical repartition [Nelson2011, Hubert2017], which is well captured by the Weibull function.

The positioning of the initial spheres in the domain is also crucial to control the pattern of the microstructure and the possibility to have some local aggregation in the final medium. For this purpose, a specific procedure has been implemented by dividing the domain V into n_{seed}^3 cubic sub-volumes $U_{i \in \llbracket 1, n_{seed}^3 \rrbracket}$. In each sub-volume, an initial sphere is randomly placed as illustrated for a 2D slice cross-section in Figure III.14a. The number of initial spheres or seeds, n_{seed} , is then a model parameter that needs to be adapted depending on the microstructure to emulate. An initial domain division in a large number of sub-volumes will yield a homogeneous microstructure whereas a low number of initial spheres will result in the creation of aggregates. Indeed, in order to achieve a good connectivity of the final microstructure, any new sphere added in the generation process (cf. next step) needs to be in contact with an existing sphere. In that condition, the number of seeds enables to control the level of clustering in the final microstructure.

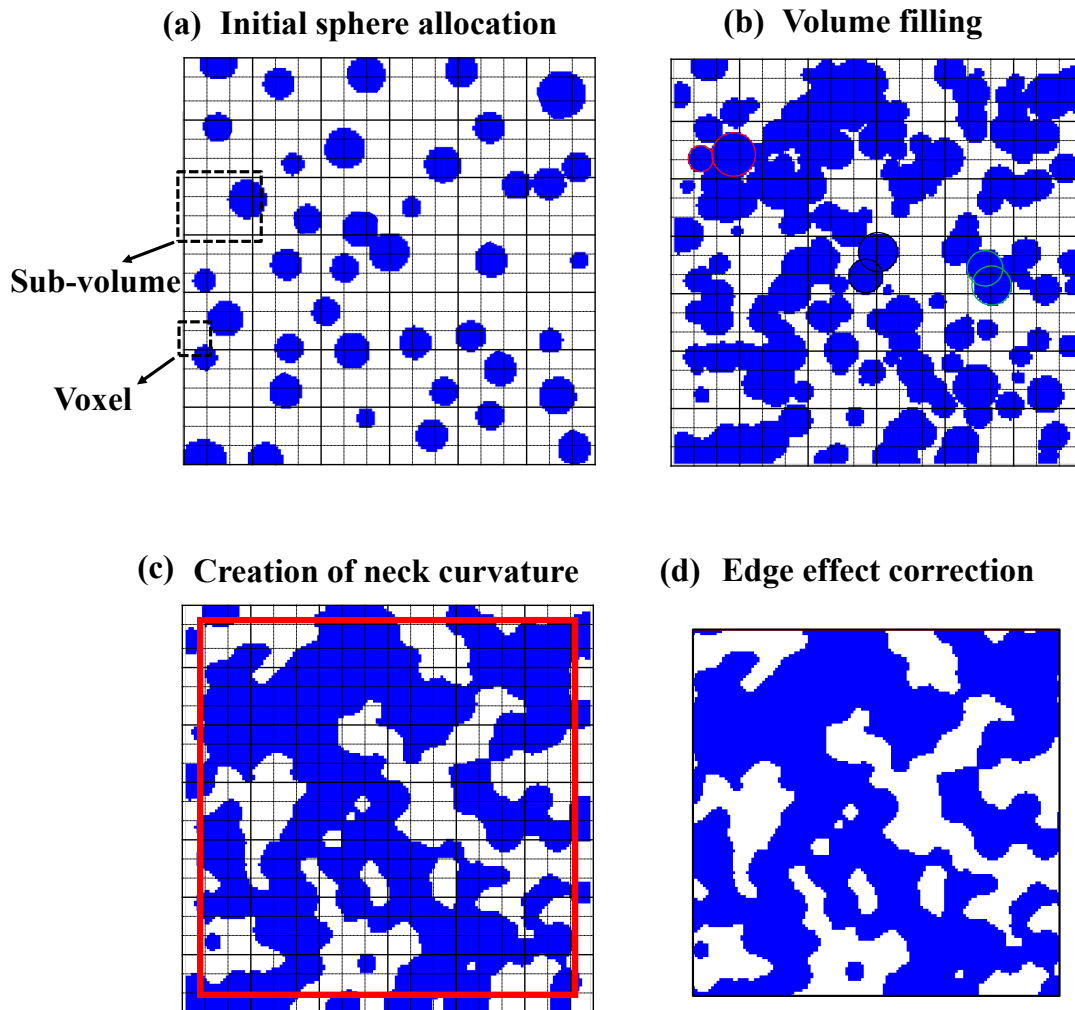


Figure III.14 2D Illustration of the three steps for building the particle-based two-phase microstructure; (a) Initial spheres allocation, (b) volume filling (with three examples of spheres overlap extend: high, medium and low in green, black and red respectively), (c) creation of neck curvature, and (d) edge effect correction by volume cropping.

(b) *Volume filling* – In order to fill the volume and reach the targeted pore volume fraction, new spheres are added in the domain in an iterative process. Assuming that they are also related to the powder particles used for the electrode fabrication, the diameters of the new spheres follow the same Weibull distribution than the initial one. As previously mentioned, each sphere is added in the domain to be in contact with an existing one, already positioned in the volume. This constraint ensures a good solid phase connectivity as it is generally observed in real microstructures (cf. chapter II). In order to take into account the partially densified nature of the SOC electrodes, some conditions of the particle interaction/contact have to be fulfilled and are described hereafter.

Firstly, a controlled overlap is allowed between particles during the volume filling process. In practice, the distance between two overlapping spheres S_i and S_j with respective radii r_i and r_j (cf. Figure III.15) is defined as following:

$$d_{ij} = \frac{r_i + r_j}{2} (1 + rand^{n_{overlap}}) \quad (\text{III.19})$$

where $rand$ denotes a uniformly distributed random variable in the interval $[0,1]$, and $n_{overlap}$ a variable controlling the overlap distribution. In fact, values of $n_{overlap}$ higher than unity lead to high degrees of spheres overlap while lower values lead to more punctual contacts. A sensitivity analysis has been conducted over this parameter, and a value of 1 was retained. This means that the overlap extend is equally distributed between the two bounded positions (i.e. between the maximum overlap $d_{ij} = (r_i + r_j)/2$ and the punctual contact $d_{ij} = (r_i + r_j)$).

Secondly, the direction of each new sphere with respects to the old one needs to be totally random in order to account for the isotropy of the sintered electrode. Therefore, the azimuth and elevation angles, Φ and θ , have been expressed in the spherical coordinates system as follows:

$$\Phi = 2 * \pi * rand_1 \quad \text{and} \quad \theta = \arcsin(rand_2) \quad (\text{III.20})$$

Where $rand_1$ and $rand_2$ are two uniformly distributed random variables in the interval $[0,1]$. It can be noticed that the elevation angle θ is not expressed directly as a function of the random variable, but through the inverse sine function. The reason behind this choice is to avoid a privileged position close to the poles and thus to obtain uniformly distributed directions [Yan2017].

Finally, the number of interconnections is constrained in the model. Indeed, the coordination number is computed for each sphere, and a maximum value n_{coord} is set to avoid non-realistic local heterogeneities. In practice, before counting the number of coordination, it is necessary to test if two spheres are overlapping or not. This preliminary step is carried out by checking the following condition (eq. III.21):

$$\sqrt{(c_{j,x} - c_{i,x})^2 + (c_{j,y} - c_{i,y})^2 + (c_{j,z} - c_{i,z})^2} \leq (r_i + r_j) \quad (\text{III.21})$$

Where $(c_{i,x}, c_{i,y}, c_{i,z})$ and $(c_{j,x}, c_{j,y}, c_{j,z})$ are the Cartesian coordinates of the spheres i and j centers.

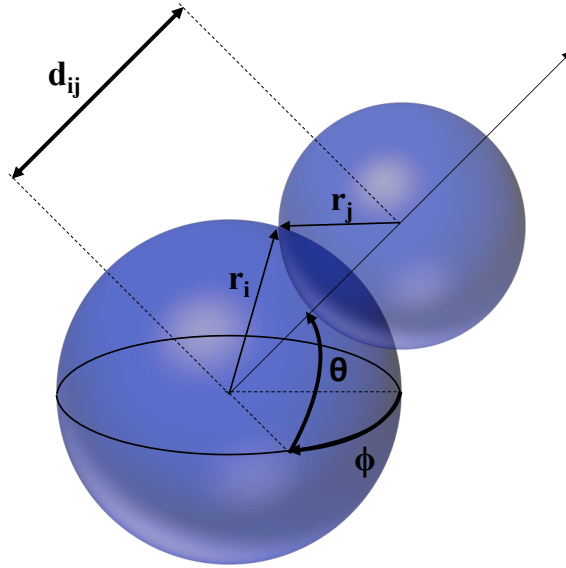


Figure III.15 Schematic representation of the contact geometry between two particles i and j in the spherical coordinate system.

The iterative process for the volume filling is ended when the targeted volume fraction is reached. However, for time machine optimization, the phase volume fraction ε_p is not computed at each step of the simulation at the beginning of the procedure, but only when $n_{opti} \sim 500$ spheres are added within the domain. Then the frequency of volume fraction, assessment is increased continuously when the simulation get closer to the targeted value.

(c) *Creation of neck curvature* between sintered particles – The sintering leads to the formation of neck between the particles, which have been already taken into account in the previous step of the algorithm (i.e. thanks to the volume filling by the sphere overlap). Nevertheless, the mass transfer resulting from the diffusion of solid mater to the particle intersections also yields the creation of neck curvature as illustrated in Fig. III.14c. For instance, Metcalfe et al. [Metcalfe2010] have proposed to set the radius of this neck curvature to one-twentieth of the particle diameter based on SEM observations of SOC electrodes. In our case, this radius is created by applying a morphological opening defined as the dilation of the erosion of the microstructure [Serra1988]. For this operation, a spherical structuring element has been employed. The diameter of the sphere, which is one of the model parameters, is of central importance to control the geometry of the curvature. In practice, a diameter of one-sixth to one-fifth of the mean particle diameter provides good results for typical SOC electrodes. It can also be noticed that the morphological opening induces a slight change of the electrode phase volume fractions, which is taken into account in the algorithm.

Finally, it should be mentioned that an edge effect has been observed on the resulting synthetic microstructures. Indeed, the spheres have less probability to occupy the regions close to the external faces of the simulated domain. Therefore, slices with a thickness of around a phase mean diameter has been removed from the volume sides as shown in Fig. III.14d. This edge effect could be avoided as well by considering a simulation volume larger than the actual observation window [Baum2017].

III.2.1.2 Three-phase materials for Ni-YSZ electrode

The particle-based model has been extended to simulate the Ni-YSZ porous composite electrodes. For this purpose, two kinds of sphere populations related to the two electrode solid phases were used to generate the synthetic microstructure. For each case, the particles are assumed to follow a distinct Weibull distribution. The initial sphere positioning is carried out in order to respect the volume fraction of the solid phases. Then, the ionic and electronic particles networks are built step by step to fill the volume. In this iterative procedure, the addition of a new sphere in the domain follow the same rules than the ones defined for the two-phase electrode. However, at each step of the process, the attribution of the ionic or electronic nature of the new particle is carried out with a constraint added to fulfill the targeted electrode composition. Besides, in order to maintain a high phase connectivity, each new sphere is positioned in contact with an existing particle of the same nature. The neck curvature between the spherical particles of the microstructure is subsequently created by applying a morphological opening for the two solid phases. For the last operation, the same structuring element has been considered for the phases. Finally, to remove the edge effect, the thickness of the slices (which are removed from the simulated microstructure) is set to the highest mean diameter of the ionic or electronic spheres.

As a general matter, the simulation of the electrode microstructure requires as input data (i) the phase volume fractions, (ii) the size of the structuring element for the morphological opening and (iii) the parameters of the Weibull distributions for the ionic and electronic conducting spheres. As already discussed, these last parameters could be roughly ascribed to the ones describing the particles distribution for the powders used for the cell manufacturing. Moreover, if the sintering is not too high, the geometrical characteristics of the particles used for the simulation should not be too far from the phase size measured on the 3D

reconstruction. Therefore, these last distributions for the ionic and electronic conducting phase could be taken for the simulation. However, it has been observed that the sintering leads to a linear shift between the distribution of the particles used for the simulation and the one measured on the 3D reconstruction. Thus, the input sphere size distribution needs to be shifted to accurately reproduce the microstructure as follows (Eqn. III.22):

$$\left. \frac{dP}{dr} \right|^{model\ input}(r) = \left. \frac{dP}{dr} \right|^{Reconstruction}(r + r^{shift}) \quad (III.22)$$

For the model validation presented in the following section, the distributions of the solid phases have been thus measured on the 3D reconstructions and then shifted with a value equal to 20% of the mean radius measured on the 3D volumes.

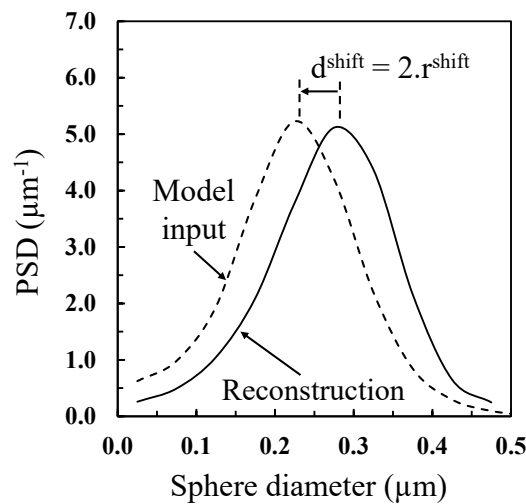


Figure III.16 Illustration of the shift between the model input spheres size distribution and the reconstruction PSD for the LSCF O₂ electrode of Cell-A.

III.2.2 Validation of the sphere-packing model on 3D reconstructions

The sphere-packing algorithm has been validated on the reconstructions of Cell-A and Cell-B. The same volume size and spatial resolution than the ones used for the Random Field model has been considered hereafter.

III.2.2.1 Validation for the two-phase O₂ electrodes

The model for the two-phase materials has been validated on the LSCF and LSC O₂ electrodes of Cell-A and Cell-B. With Representative Volume Elements (RVEs) of 9x9x9

μm^3 , it has been checked with the sphere-packing model that the criterion on the repetitiveness is satisfied meaning that only one realization is required to obtain good statistics.

The 3D rendering volumes of the real and synthetic microstructures are compared in Fig. III.17. As a first approach, the visual inspection of the 3D volumes for both electrodes reveals that the virtual microstructures seem to mimic quite perfectly the real ones. Therefore, it seems that the model would be able to describe accurately the coarse microstructure of Cell-A as well as the finer microstructure of Cell-B.

As illustrated in Fig. III.18a and III.18b, this first statement is confirmed by the very good agreements between the cumulative solid phase size distributions calculated on the synthetic volumes and the tomographic reconstructions. This good agreement is expected and logical as the LSCF or LSC phase size distribution was introduced in the model as input data. Nonetheless, this result highlights the model capability to adjust accurately this distribution and then to capture all the length scales of the solid phase. Furthermore, the size distribution of the complementary phase, i.e. porosity, is also well retrieved by the model (Fig. 18a,b). Indeed, a very good agreement is found for both cells, albeit a slight discrepancy on the last part of the pore cumulative PSD of Cell-A. This can be explained by some large-scale porosities in the real reconstruction of cell-A that was not caught perfectly by the model.

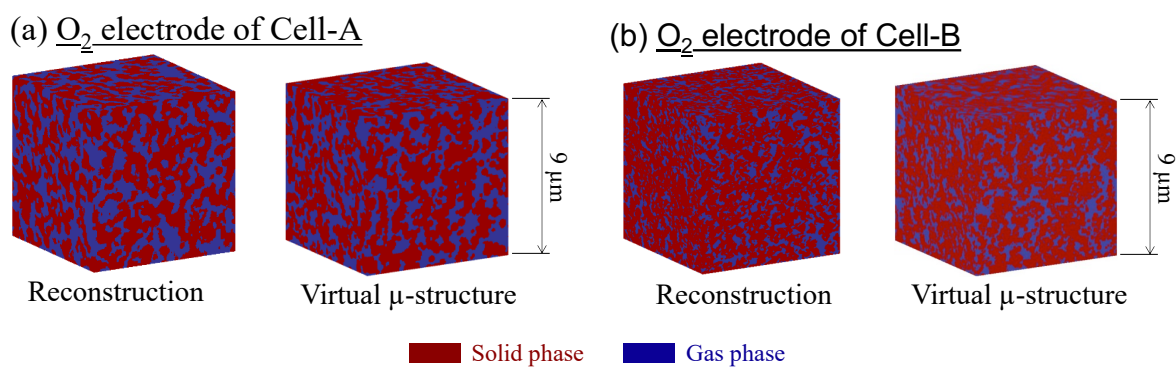


Fig. III.17 Visual comparison between the synthetic SP microstructures and the reconstructed volumes for the O_2 electrodes of (a) Cell-A and (b) Cell-B.

To go further in the model validation, the covariance functions and all the electrode morphological and physical parameters of the virtual electrodes have been determined in the same conditions than the data computed with the tomographic reconstructions.

A very good agreement can be highlighted in Fig. III.18 between the real and numerical covariance functions for both phases of each cell. This first statement is confirmed by the general good consistency regarding the metric properties. Indeed, negligible errors are obtained over the phase volume fractions and the specific surface areas (Table III.4), which are directly deduced from the covariance functions (c.f. Section III.4.1). For instance, the disagreement with respect to the electrode specific surface area, which is a crucial parameter controlling the electrode kinetic rate for the oxygen incorporation [Laurencin2015], does not exceed 4% for both cells. Still on the metric property, the phase mean diameters are perfectly retrieved by the model as this parameter is directly inferred from the granulometry (size distribution).

A general good agreement is also achieved for the topological properties calculated for both electrodes. First of all, as computed on the real electrodes, the virtual microstructures are almost totally percolated (more than 99.90% is connected for both solid and pore phases). Besides, the discrepancy on the geometrical tortuosity and the constrictivity factor remains very limited since the error ranges from 2 to 8%.

It can be inferred from this analysis on the metric and topological properties that the proposed particle-based model is able to correctly predict the morphological characteristics of the studied microstructure.

Table III.5

Microstructural properties for the O₂ electrodes of Cell-A and Cell-B computed on the tomographic reconstructions and the synthetic SP volumes.

O ₂ electrode of Cell-A													
Properties	S _p μm ⁻¹	Gas phase						Solid phase (LSCF)					
		δ (%)	ε (%)	d _p ^(*) (μm)	τ ^{gco} (-)	β (-)	M-factor (-)	δ (%)	ε (%)	d _p ^(*) (μm)	τ ^{gco} (-)	β (-)	M-factor (-)
Real μ-structure	3.80	99.96	43.64	0.26	1.22	0.10	0.194	99.99	56.36	0.32	1.34	0.11	0.289
Virtual μ-structure	3.95	99.97	43.71	0.26	1.24	0.11	0.209	99.99	56.29	0.32	1.39	0.12	0.252
Error	+4%	~0%	~0%	~0%	+2%	+5%	+8%	~0%	~0%	~0%	+4%	+8%	-13%
O ₂ electrode of Cell-B													
Properties	S _p μm ⁻¹	Gas phase						Solid phase (LSC)					
		δ (%)	ε (%)	d _p ^(*) (μm)	τ ^{gco} (-)	β (-)	M-factor (-)	δ (%)	ε (%)	d _p (μm)	τ ^{gco} (-)	β (-)	M-factor (-)
Real μ-structure	6.28	99.76	28.83	0.12	2.27	0.23	0.078	100	71.17	0.22	1.31	0.31	0.474
Virtual μ-structure	6.09	99.99	28.79	0.12	2.15	0.25	0.082	100	71.21	0.22	1.27	0.32	0.498
Error	-3%	~0%	~0%	~0%	-5%	+8%	+6%	~0%	~0%	~0%	-3%	+5%	+5%

(*) mean phase diameter taken from the PSD.

Regarding the physical properties, the M-factor, which describes the transport phenomena in the solid and pore phases (c.f. Section II.5.2) have been examined. This comparison shows low relative errors that does not exceed $\pm 13\%$ (Table III.5). Indeed, this mismatch combines the errors obtained on all topological properties (the geometrical tortuosity, the constrictivity factor and the phase percolation) as discussed previously in Section II.5.2. Nevertheless, considering the general good agreement between the real reconstructions and their digital twins over the large range of investigated morphological and physical properties, it can be claimed that the model is able to statistically reproduce the main single solid-phase O_2 electrode microstructural properties, with a high level of confidence.

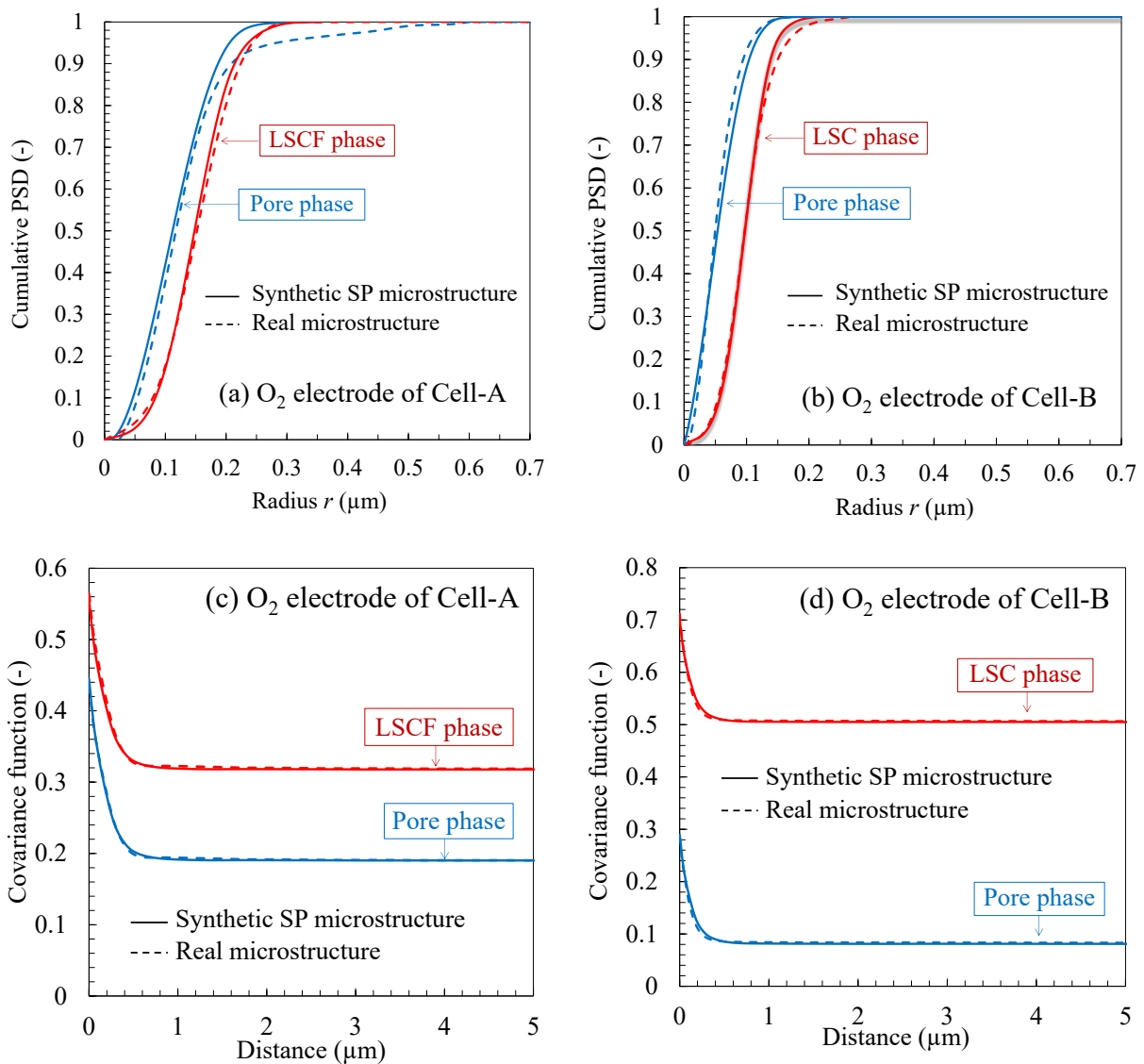


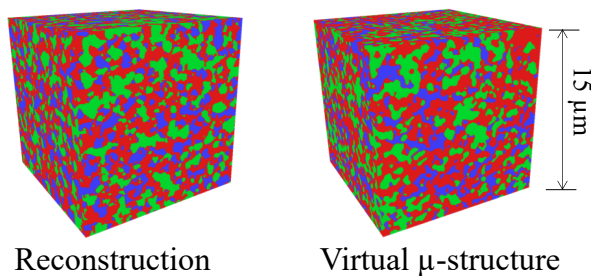
Fig. III.18 Comparison between the SP synthetic and real O_2 electrode microstructures in respect of (a,b) the cumulative PSDs and (c,d) the covariance functions for both Cell-A and Cell-B.

III.2.2.2 Validation for the three-phase electrodes

As shown in the previous section, the morphology characteristics between the Ni-YSZ cermet and LSCF-CGO composite are similar. Therefore, the validation has been restricted for the SP model to the Ni-YSZ electrodes of Cell-A and Cell-B. In this case, the Ni-YSZ synthetic microstructures have been generated with the proposed particle-based model extended to the porous composite materials. As previously checked for the random field method, it has been found that only one single synthetic microstructure generation of $15^3\mu\text{m}^3$ is needed for the cermet of Cell-A. However, 16 generations are required for the cermet of Cell-B, as a single Stochastic Volume Element (SVE) of $8.5^3\mu\text{m}^3$ is not representative of the whole electrode.

The 3D rendering volumes of the synthetic microstructures are compared to the Ni-YSZ cermet reconstructions in Fig. III.19. As for the LSCF or LSC electrode, their visual inspections reveal that the more complex microstructure of the three-phase electrodes can be correctly predicted by the model. This preliminary observation is also supported by the good agreement found between the phase size distribution of the real and synthetic microstructures (Fig. III.20a and III.20b). This good match is obviously obtained for the solid phases, but also on the complementary phase (i.e. porosity) for which the pore size distribution is not directly controlled by the model. This means that all the length scales present in the real reconstructions are accurately taken into consideration by the model, thus proving its relevance.

(a) H_2 electrode of Cell-A



(b) H_2 electrode of Cell-B

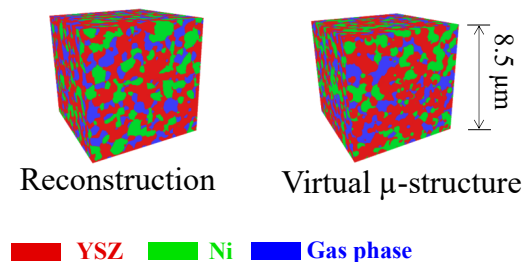


Fig. III.19 Visual comparison between the synthetic microstructures and the reconstructed volumes for the H_2 electrodes of (a) Cell-A and (b) Cell-B.

To check more in depth the model representativeness, the same approach has been adopted for the two-phase materials validation. Indeed, the covariance functions have been compared in

Figs. III.20c and III.20d and the microstructural properties have been summarized in Tables III.6 and III.7 for Cell-A and Cell-B respectively. The covariance functions computed for the three phases accurately fit the ones computed on the real reconstructions of both cells. This accordance was confirmed by the good agreement obtained on the metric properties extracted from these curves, namely the phase volume fractions and the specific surface areas. In fact, the errors obtained on these two properties do not exceed $\pm 4\%$ for the three phases of both cells. This result is of central importance in an electrochemical modeling framework where some kinetic rates (of adsorption/desorption for example) are directly scaled to the specific surface areas (c.f. Section V.3). One other essential parameter, that directly governs the Ni-YSZ electrode efficiency, is the TPBI density [Lay-Grindler2013]. The model is able to retrieve this property with negligible relative errors that does not exceed $\pm 6\%$, thus providing initial evidence of the model extension relevance to three-phase materials. Finally, the phase mean diameters were perfectly recovered by the model as expected from the PSD validation.

Once the metric properties are shown to be precisely simulated by the proposed model, the following step is to check if the three phases are properly distributed in the 3D space. For this purpose, the synthetic microstructures have been compared in terms of topological properties to the real reconstructions. As a first remark, the three simulated phases are almost totally connected as expected. The average relative error on this parameter is only 2.5%. The highest mismatch is found for the Ni phase of Cell-B for which a connectivity of 98.38% is obtained compared to 92.81% for the real electrode. This slight disagreement seems to be correlated to the rather low Ni volume fraction in Cell-B (i.e. 24.41%). The model has also been evaluated in terms of geometrical tortuosity and constrictivity. It can be noticed that these two properties were accurately retrieved for the YSZ backbone of both electrodes, which is the less tortuous and less constrictive phase as it exhibits the highest volume fraction ($>44\%$). For the more constrictive phases (i.e. Ni and porosity), the model succeeds to estimate the geometric tortuosity quite accurately (error $< \pm 6\%$), while a higher mismatch is obtained on the constrictivity factor, with a maximum error of $+18\%$ obtained for the Ni phase of Cell-A. As a general matter, the model does not seem to perfectly capture the high constrictivities. This finding is confirmed by the mismatch obtained on the M-factor of these two phases. Indeed, as explained previously, the effective conductivity and diffusivity are directly linked to the topological properties of the medium. A maximum error of $+21\%$ is detected on the M-factor

of the Ni phase of Cell-B, this error is the result of accumulation of the morphological errors obtained on this phase.

Table III.6

Microstructural properties for the H₂ electrode active layer of Cell-A computed on the tomographic reconstruction and the synthetic volume.

H ₂ electrode of Cell-A														
Properties	Gas phase							Electronic conducting phase (Ni)						
	S _p (μm ⁻¹)	δ (%)	ε (%)	d _p ^(*) (μm)	τ ^{geo} (-)	β (-)	M-factor (-)	S _p (μm ⁻¹)	δ (%)	ε (%)	d _p ^(*) (μm)	τ ^{geo} (-)	β (-)	M-factor (-)
Real μ-structure	2.67	94.74	28.04	0.28	1.67	0.09	0.030	2.30	97.45	27.88	0.33	1.75	0.08	0.041
Virtual μ-structure	2.62	99.51	27.87	0.28	1.62	0.10	0.035	2.25	99.34	28.12	0.33	1.65	0.09	0.049
Error	-2%	+4%	~0%	~0%	-3%	+16%	+17%	-2%	+2%	~0%	~0%	-6%	+18%	+21%
Properties	Ionic conducting phase (YSZ)							Density of TPBIs (Ni/YSZ/gas contact lengths)						
	S _p (μm ⁻¹)	δ (%)	ε (%)	d _p ^(*) (μm)	τ ^{geo} (-)	β (-)	M-factor (-)	ξ _{TPBIs} ^(**) (μm ⁻²)						
Real μ-structure	3.68	99.78	44.08	0.28	1.43	0.13	0.189	4.78						
Virtual μ-structure	3.83	99.99	44.01	0.28	1.42	0.12	0.193	4.97						
Error	+4%	~0%	~0%	~0%	-1%	-3%	+2%	+4%						

(*) mean phase diameter taken from the PSD. (**) density of 'active' TPBIs computed on the connected phases.

Table III.7

Microstructural properties for the the H₂ electrode active layer of Cell-B computed on the tomographic reconstruction and the synthetic SP volume.

H ₂ electrode of Cell-B														
Properties	Gas phase							Electronic conducting phase (Ni)						
	S _p (μm ⁻¹)	δ (%)	ε (%)	d _p ^(*) (μm)	τ ^{geo} (-)	β (-)	M-factor (-)	S _p (μm ⁻¹)	δ (%)	ε (%)	d _p ^(*) (μm)	τ ^{geo} (-)	β (-)	M-factor (-)
Real μ-structure	2.94	94.23	26.55	0.24	1.74	0.39	0.021	2.46	92.81	24.13	0.28	1.81	0.34	0.018
Virtual μ-structure	3.05	99.51	26.16	0.24	1.69	0.43	0.025	2.53	98.38	24.41	0.28	1.76	0.39	0.021
Error	+4%	+4%	~0%	~0%	-3%	+11%	+17%	+3%	+6%	+1%	+1%	-3%	+16%	+18%
Properties	Ionic conducting phase (YSZ)							Density of TPBIs (Ni/YSZ/gas contact lengths)						
	S _p (μm ⁻¹)	δ (%)	ε (%)	d _p ^(*) (μm)	τ ^{geo} (-)	β (-)	M-factor (-)	ξ _{TPBIs} ^(**) (μm ⁻²)						
Real μ-structure	3.42	99.92	49.55	0.31	1.14	0.44	0.243	6.20						
Virtual μ-structure	3.46	99.99	49.43	0.31	1.13	0.47	0.248	5.83						
Error	+3%	~0%	~0%	+1%	-1%	+8%	+2%	-6%						

(*) mean phase diameter taken from the PSD. (**) density of 'active' TPBIs computed on the connected phases.

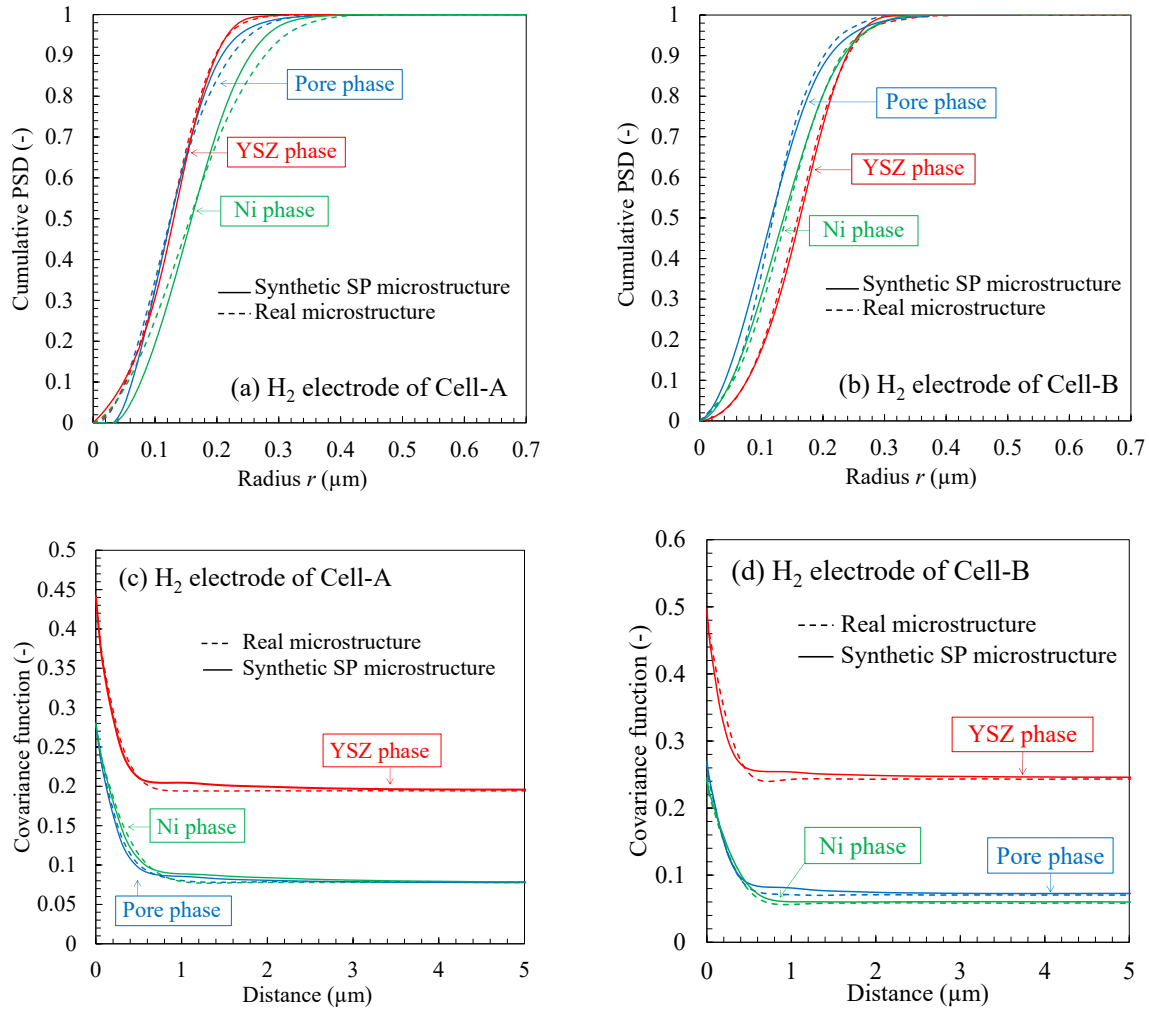


Fig. III.20 Comparison between the particle-based synthetic and real H₂ electrode microstructures in respect of (a,b) the cumulative PSDs and (c,d) the covariance functions for both Cell-A and Cell-B.

To sum up, it appears that the model is able to accurately reproduce the metric properties (i.e. volume fractions, specific surface areas, mean phase diameters and density of TPBIs), whereas a higher discrepancy on the topological parameters (i.e. constrictivity and tortuosity) is detected for the very high constrictive phases associated with low volume fraction. Nevertheless, it is worth mentioning that this limitation of the model remains acceptable for the investigated SOCs electrodes (in the worst case, the error on the microstructural factor does not exceed +/-21% for Cell A and +/-18% for Cell-B: cf. Tables III.6 and III.7). As a consequence, despite the limitation on the constrictivity factor, it can be concluded that the adapted particle-based model is able to accurately simulate the main electrode properties, and then to provide realistic and representative Ni-YSZ synthetic microstructures.

III.2.3 Model flexibility: illustration for a diffusion layer with a bimodal pore distribution

III.2.3.1 General discussion on the model flexibility

With the present validated numerical tool, different synthetic microstructures could be generated by changing the model input parameters. The proposed particle-based model has the advantage of being very close to the electrodes classical manufacturing routes (screen printing or tape casting). Indeed, the powder mix composition and the particle size distribution as well as the porosity can easily be controlled to generate a large set of different microstructures. This kind of sensitivity analysis can be used to establish the link between the parameters controlling the electrochemical reactions (S_{ij} and TPBI density) to the basic microstructural parameters (composition, porosity and PSD) that are directly controlled by the cell manufacturers (cf. chapter IV). These correlations are of capital importance in a numerical optimization framework of the SOC electrode microstructures in order to provide practical guidelines for the cell manufacturing.

Aside from the classical electrode microstructure, the sphere-packing algorithm can be easily adapted for the generation of promising electrode architectures. For instance, it is straightforward to introduce some spatial heterogeneities such as agglomerates by controlling the initial sphere allocation. Gradients in composition, particle size or porosities could also be considered by adding a spatial constraint on the volume fractions or particle size distributions. Anisotropies with oriented phases could be also obtained by creating privileged directions when positioning new spheres during the domain filling step (i.e. by using a non- uniformly distributed directions in eq. III.20). The spheres could also be changed into needle-like particles or nanofibers for the simulation of original microstructures obtained for instance by electrospinning [Enrico2018].

Finally, it would be very important to address the microstructural modeling for the Ni-YSZ cell support with a bimodal pore size distribution as observed for Cell-B. As detailed in chapter I, this substrate must hold the thin electrolyte and electrode active layers while promoting the gas diffusion. In that view, optimization of the porosity by virtual material design could be especially relevant. To date, there is no specific geometrical stochastic model available in the literature dedicated to this particular microstructure. For this reason, the sphere-packing model flexibility has been illustrated on this particular case.

III.2.3.2 Model adaptation to a bimodal pore size distribution

The actual configuration of the proposed particle-based model does not allow to take into account the macropores specificities, and an adaptation is then required. The first step was to accurately characterize this electrode layer in order to reproduce it numerically. For this end, a morphological procedure has been proposed to separate the large scale porosities from the microporosity network in the X-ray tomographic reconstruction of Cell-B substrate (cf. Section II). Isolating the macropores allowed to thoroughly characterize their morphology. It was shown that the disconnected macropores are homogeneously distributed within the diffusion layer, and have ellipsoid-like morphologies with varying degrees of flattening and tilt.

The sphere-packing algorithm has been modified and a three steps procedure has been proposed as detailed hereafter. A first synthetic microstructure is generated for the percolated micropores and solid phases. In this case, the same procedure than the one previously described is used as this microstructure results from the partial sintering of the initial powers. The second step of the process is devoted to producing a volume with the disconnected macropores (coming from the use of pore formers). In this case, a specific algorithm has been proposed. Finally, the two volumes are merged to model the microstructure with the bi-modal distribution on the pores.

For the second step related to the macropore modeling, the same rules than the ones defined for the initial particle positioning in the domain was followed. In this frame, the number of sub-volumes is directly given by the number of macropores. This method allows a uniform repartition of the macropores in the volume. Then, the morphology and the orientation of these macropores are modelled thanks to parameterized ellipsoid particles with a distribution on size, degree of flattening and orientation. The model input distributions were computed from the real microstructure presented in Chapter II. In practice, the ellipsoids are defined in a spherical coordinates system (Fig III.21) by using three space dimensions a , b , and c ; a polar angle θ to describe the volume tilt with respect to the z -axis, and an azimuth angle ϕ to introduce the xy -plane rotation:

$$x = a \cos(\theta) \cos(\Phi) \quad ; \quad y = b \cos(\theta) \sin(\Phi) \quad ; \quad z = c \sin(\theta) \quad (III.23)$$

As described in Chapter II, the macropores fitting to ellipsoid volumes allowed obtaining the real distribution of the voids dimensions (a , b , and c), and orientation (θ and ϕ).

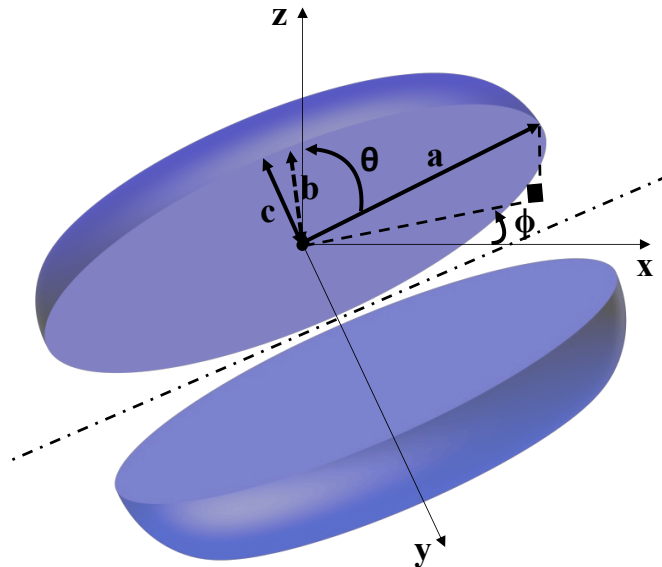


Fig. III.21 Schematic representation of an ellipsoid cut used in the macropores simulation. An illustration is given for the three space lengths a , b and c in a spherical coordinates system where θ is the polar angle (tilt angle with respects to z -axis) and ϕ is the azimuth angle (rotation within the xy -plane).

For the simulations, a large synthetic volume with size $200 \times 200 \times 200 \mu\text{m}^3$ was considered to ensure the statistical representativeness of the synthetic structure, and to achieve a good repetitiveness of the model. Thanks to the rather coarse microstructure of the substrates, a resolution of 50 nm has been used. Indeed, the voxel size is a good compromise to optimize as far as possible the computation time while keeping a fine description of the microstructure (with this resolution, the rule of 10-15 voxels per particle diameter is still respected: cf chapter II).

III.2.3.3 Element of model validation

The visual comparison of the 2D slice cuts of the real and synthetic microstructures is shown in figure III.22. It can be seen that the two structures are geometrically similar. In order to validate this finding, several $36 \times 36 \times 36 \mu\text{m}^3$ volumes were cut off the synthetic structure, and their microstructural parameters were averaged. It is worth noting that only 5 SVEs are requested to obtain very good statistics with a negligible standard deviation. From this point

of view, the error margins on the data computed on the single volume of $36 \times 36 \times 36 \mu\text{m}^3$ can be roughly considered acceptable.

The properties computed on the synthetic and real reconstruction are compared in Table III.8. It is worth reminding that the sphere-packing model was shown to be able to accurately simulate the morphological and physical properties of the Ni-YSZ ‘classical’ cermet (i.e. without macropores: cf. section III.2.2.2). Indeed, the relative mismatch between the real and numerical microstructures was quantified to $\sim 4\%$, while the highest discrepancy of $\sim 20\%$ was obtained for the very high constrictivities. As expected, the same general order of errors was obtained for the solid and micropore phases for the synthetic substrate cermet (Table III.8). For this reason, the following discussion will focus on the comparison of the parameters affected by the addition of macropores.

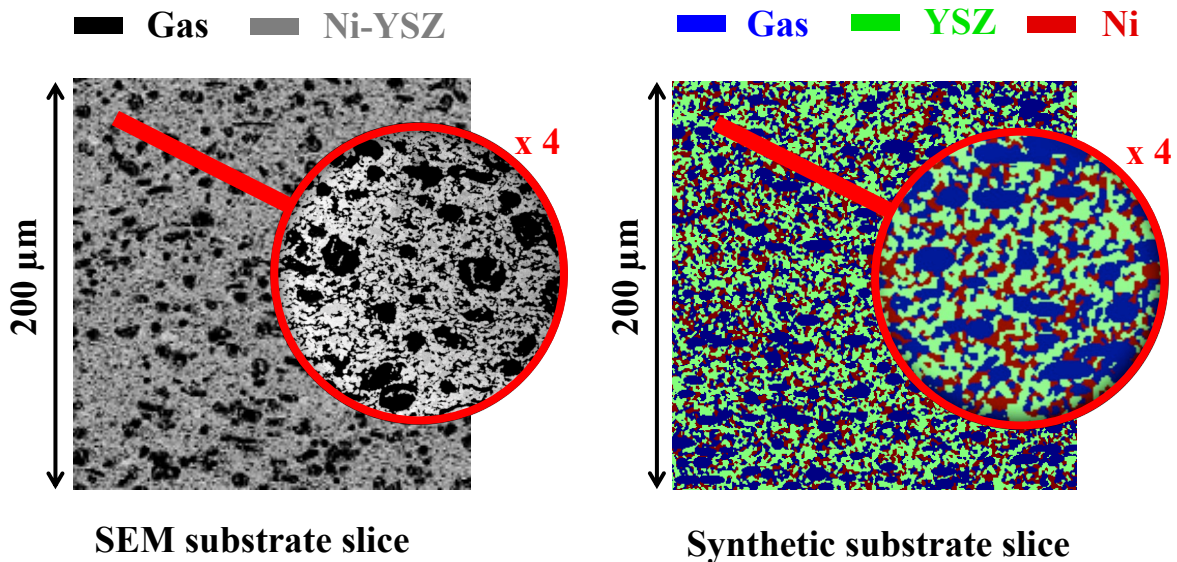


Fig. III.22 Comparison of the 2D slice cuts of the real and synthetic microstructures.

First and foremost, all the phase volume fractions were accurately retrieved as they are input model parameters. For the same reason, the macropores mean diameter is also precisely modeled. However, while the specific surface area developed by the micropores network $S_{p_{micropores}}$ is well simulated (-3% error), the one induced by the macropores $S_{p_{macropores}}$ is slightly under-estimated (-7% error). This disagreement can be explained by the roughness at the surface of the real macropores that is omitted by the fitted ideal ellipsoids.

A good agreement was also obtained for the topological properties including the connectivity, the geometrical tortuosity and the constrictivity factor, for which the errors do not exceed +/-2%, +/-5% and +/-10%, respectively. As already discussed in chapter II, the addition of macropores yields a rather low geometrical tortuosity and constrictivity for the gas phase. These specific features of the substrate are well retrieved by the model (Table III.8). As a consequence, a good agreement is also found for the M-factor of this phase.

Moreover, a noticeable anisotropy of the real substrate was detected thanks to the computation of the M-factors in the three direction of the space. It has been found for the synthetic microstructures that the M-factors are respectively 24%, 24% and 33% lower in the z-direction for the YSZ, Ni and pore phases than in the two other directions (compared to 26%, 25% and 36% for the real reconstruction). This quantification shows that the anisotropy is also well reproduced by the model thanks to the control of the macropores flattening and orientation.

Table III.8

Microstructural properties for the diffusion layers of the H₂ electrode of Cell-B computed on the tomographic reconstructions. The specific surface area, the connectivity, the volume fraction, the mean particle/pore diameter, the geometrical tortuosity, the constrictivity factor, the M-factor, and the connected TPBI density are given for each electrode phase. It can be noted the porosity is divided into microporosity and macroporosity

Properties Units	Cell-B H ₂ electrode diffusion layer							TPBI density μm ⁻²	
	S _p μm ⁻¹	δ %	ε %	d _p μm	τ ^{geo} -	β -	M-factor -		
Microporosity	1.92		31.25	0.61					
Macroporosity	0.28	99.94	14.21	2.48	1.62	0.20	0.131	3.19	Real
YSZ phase	1.79	99.22	34.85	0.56	1.78	0.43	0.100		
Ni phase	1.25	96.71	19.69	0.42	2.20	0.35	0.011		
Microporosity	1.86	99.97	31.51	0.63					
Macroporosity	0.26		13.46	2.42	1.57	0.22	0.140	3.08	Synthetic
YSZ phase	1.81	99.43	34.98	0.56	1.73	0.43	0.110		
Ni phase	1.28	98.46	20.05	0.43	2.08	0.36	0.013		
Microporosity									

It should be retained that the proposed ellipsoid-based model is able to correctly take into account all the macropore characteristics of Cell-B substrate. This result is very promising in an objective to optimize this electrode layer. Indeed, the macropores morphology, orientation and amount can easily be tuned in order to sweep a wide range of substrate architectures. The influence of these parameters on the cell transport properties can thus be investigated in order to optimize its performance. This analysis should give valuable insights for highly efficient cell substrates.

III.2.4 Conclusion

An original particle-based model has been developed in order to mimic the complex microstructure of SOC electrodes. The proposed stochastic geometrical model has the advantage of being very close to the ‘classical’ cell manufacturing routes via tape casting or screen printing. Indeed, the powder characteristics used in the process, namely proportions and PSD, as well as the densification extend can directly be controlled by the model parameters. This feature is of central importance in an objective to establish the complex relationships linking the SOC manufacturing parameters to the electrochemically controlling properties.

The representativeness of the synthetic microstructures has been checked on four X-ray synchrotron and FIB-SEM tomographic reconstructions of typical LSCF, LSC, and Ni-YSZ electrodes. Beyond a first visual examination, all the relevant microstructural parameters were computed on the virtual microstructures and compared to the real values. This validation step showed that the model is able to catch accurately all the morphological and physical parameters with a low average relative error of $\sim 4\%$. The highest discrepancy of $\sim 21\%$ was obtained on the constrictivity of the phases close to the percolation threshold, and thus having a pronounced bottle-neck effect. As a general matter, it was inferred from this analysis that the synthetic media emulate correctly the complex sintered structure of typical SOC electrodes.

Finally, the potential flexibility of this model to simulate a large range of microstructures has been discussed. To illustrate this statement, the proposed particle-based model has been extended to take into account the particular bimodal pore distribution for typical Ni-YSZ substrates. In this particular case, the generated synthetic medium has been found to mimic all the characteristics of this diffusion layer with a high level of confidence.

III.3 Concluding remarks: models comparison

Two different stochastic geometrical models have been developed and validated to simulate the microstructure of the different SOC electrodes layers. The two models are founded on two radically different considerations. The Gaussian Random Field (RF) is established on the covariance function which is considered to ‘fully’ characterize the stochastic morphology of a given material. On the other side, the proposed Sphere Packing (SP) model is an iterative

particle-based algorithm that builds a microstructure by positioning representative geometries following a given distribution on size and overlap. It can be inferred that if the RF model considers a statistical representation of the continuous medium as a whole, the SP model breaks it down to a discrete set of representative particles. This later model can thus be considered closer to the classical cell manufacturing process via powders sintering. Nevertheless, the non-iterative nature of the RF model allows drastically reducing the computational time compared to the common iterative methods. Indeed, only ~ 8 s is needed to generate a $9 \times 9 \times 9 \mu\text{m}^3$ microstructure using the RF model, while ~ 90 minutes is needed for the SP model.

Despite the fundamental difference between the two models, they exhibit a number of common points. Indeed, the morphological properties are precisely caught by both RF and SP methods with close relative mean errors of $\sim 5\%$ and $\sim 4\%$, respectively. Unfortunately, neither the RF nor the SP model succeeded to accurately reproduce the very high constrictive phases, on which the highest relative errors of 25% and 21% was obtained, respectively. Further investigations should be done to improve this ‘limitation’ for the phases close to the percolation threshold. Nevertheless, considering the negligible overall mismatches, both models can be used to generate synthetic but representative SOC microstructures.

It is worth underlining that the two different models are also complementary. Indeed, a large range of microstructures can be obtained by the models or even by their combination. For instance, the RF model feature allows generating some promising cell architectures like infiltrated electrodes. Moreover, a local thresholding of a random field allows to introduce some spatial heterogeneities like a graded structure. On the other side, the control of the sphere allocation and the particle size distribution in the particle based-model opens up the possibility to address a large variety of microstructures (infiltrated electrodes, gradients in composition and particle size, etc.). This model ability has been illustrated for the bimodal pore distribution of the diffusion layer.

Finally, the difference in the basic model assumptions allows obtaining two representations and thus two different approximations of a same medium. This fundamental difference between the two proposed models constitutes a strong asset in the frame of our study. Indeed, this allows to sweep a large range of promising microstructures, while giving two different approximations for the classical ones. This double estimation is significant to make sure that the conclusions drawn in the upcoming work do not depend on the chosen model. A large set

of synthetic microstructures will be generated by taking advantage of the models flexibility. This will serve to validate some proposed microstructural correlations linking the ‘primary’ parameters (materials proportions, mean diameters, and porosity), to the ‘electrochemically controlling’ properties (specific surface areas, and TPBIs density). These relationships will bridge the link between the parameters that are easily controlled by the cell manufacturers and the electrode performance indicators.

Chapter IV: Microstructural correlations

IV.1 Introduction

Microstructural engineering of composite electrode materials is a multivariate problem. Indeed, the density of TPBI and the interfacial specific surface areas, which are the key properties controlling the electrochemical response, depend on several “basic” microstructural parameters which can be linked to the powder before sintering [Zhang2011]. By considering the medium described by a random packing of convex particles, these “basic” parameters of the microstructure can be ascribed to the features of the particles collection that can be defined as follows [Gokhale2009, Zhang2010]:

(i) The phase volume fractions are expressed through the porosity (θ_p) and the ratio of the ionic to the electronic phase volume fractions ($\alpha = \theta_{io}/\theta_{el}$) with:

$$\theta_{io} + \theta_{el} + \theta_p = 1 \quad (\text{IV.1})$$

(ii) The morphology of the electrode particles can be described for each phase i by two shape factors K_{1i} and K_{2i} defined by:

$$K_{1i} = \frac{\langle S_i \rangle}{\langle D_i^2 \rangle} \text{ and } K_{2i} = \frac{\langle V_i \rangle}{\langle D_i^3 \rangle} \text{ with } i = \text{ionic or electronic particles}, \quad (\text{IV.2})$$

where D_i , S_i and V_i denote the mean diameter, the surface area and the volume for the ionic or electronic particle, respectively (note that $\langle X_i \rangle$ represents the arithmetic mean of X_i : $\langle X_i \rangle = \int_0^\infty X_i p(X_i) dX_i$ with $p(X_i)$ is the probability density function). For the ideal case of spherical particles, the ratio $\beta_i = K_{1i}/K_{2i}$ is equal to 6 [Gokhale2009].

(iii) The Particle Size Distribution (PSD_i) of each solid phase i is defined by the mean value $\langle D_i \rangle$, the standard deviation σ_i^2 , the Coefficient of Variation (CV_i) and the skewness γ_i :

$$\sigma_i^2 = \int_0^\infty [D_i - \langle D_i \rangle]^2 p(D_i) dD_i ; CV_i = \frac{\sigma_i}{\langle D_i \rangle}; \gamma_i = \frac{1}{\sigma_i^3} \int_0^\infty [D_i - \langle D_i \rangle]^3 p(D_i) dD_i \quad (\text{IV.3})$$

Therefore, the density of TPBI and the interfacial specific surface areas have to be expressed as a function of θ_p , α , β_i , $\langle D_i \rangle$, CV_i and γ_i .

In order to establish these electrode microstructural correlations, a first strategy is based on the manufacturing of several electrodes by changing the characteristics of the initial powder. The microstructural properties (L_{TPB} and $S_{i/j}$) can be measured on 3D reconstructions obtained by tomographic techniques described in Section II.2. However, this experimental approach requires the analysis of a large number of samples for parametric studies, which constitutes a limitation for this very time-consuming procedure [Chen2013, Gokhale2009]. For this reason, we proposed to use an alternative approach based on the concept of “extended” microstructure. This geometrical method has been initially employed by Gokhale et al. [Gokhale2009] to express L_{TPB} in composite electrodes, taking into account the actual PSD of spheres (eq. IV.4). From our best knowledge, no correlation has been proposed for the interfacial specific surface areas.

$$L_{TPB} = \frac{\pi}{4} \frac{\alpha}{(1 + \alpha)^2} \theta_p (\ln \theta_p)^2 \beta_{io} \beta_{el} \frac{1}{\langle D_{io} \rangle \langle D_{el} \rangle} \times \frac{(1 + CV_{io}^2)}{(1 + 3CV_{io}^2 + \gamma_{io} CV_{io}^3)} \frac{(1 + CV_{el}^2)}{(1 + 3CV_{el}^2 + \gamma_{el} CV_{el}^3)} \quad (IV.4)$$

In this work, semi-analytical expressions linking the density of TPBI and the interfacial specific surface areas to the “basic” parameters of the microstructure are studied and calibrated on two sets of synthetic 3D microstructures. These databases have been generated by using the two models detailed in the previous chapter. Finally, the reliability of the microstructural relationships has been checked with real 3D electrode reconstructions introduced in Chapter II. The current chapter is organized as follows: the theoretical development of semi-analytical correlations is detailed in Section IV.2. The fitting of the parametric equations are presented and discussed in Section IV.3. For each property (L_{TPB} and $S_{i/j}$), the correlations deduced from simulated microstructure datasets have been compared to the data extracted from the real reconstructions in Section IV.4. This work was the object of an article entitled “Microstructural correlations for specific surface area and triple phase boundary length for composite electrodes of solid oxide cells”, published in Journal of Power Sources [Moussaoui2019].

IV.2 Theoretical development and methodology

IV.2.1 Theoretical development: analytical expression for $S_{i/j}$ and S_i

In this work, we have derived the analytical expressions for the interfacial specific surface areas $S_{i/j}$ as a function of the microstructural parameters of the composite electrode. The electrode specific surface areas S_p can obviously be deduced from the former relations with $S_p = S_{io/p} + S_{el/p}$. The same procedure as the one proposed by Gokhale et al. [Gokhale2009] for the density of TPBI has been followed. The main steps of this study are detailed hereafter.

IV.2.1.1 Concept of “extended” microstructure

The approach is based on the concept of a virtual domain called the “extended” microstructure [Avrami1939, Avrami1940, Avrami1941]. In this domain, the centers of convex particles are randomly distributed by a homogeneous Poisson point process. The ionic and electronic particles in the “extended” microstructure are free to interpenetrate while the remaining empty space corresponds to the porosity (Fig. IV.1). With such a definition, the volumes of the ionic and electronic phases are overestimated in the “extended” domain since the particles cannot overlap in the “real” microstructure. Nevertheless, the properties of the “actual” microstructure can be deduced from the virtual domain by taking into account the particles overlap. Indeed, only a fraction of any incremental volume change in the “extended” microstructure dV_i^{ex} contributes to a change in the real microstructure dV_i (the subscript i denotes the ionic or electronic phase). Assuming that the particles are uniformly randomly distributed, this fraction of dV_i^{ex} corresponds to the volume in the extended microstructure which is formed in the complementary phase of the solid particles (i.e. the porosity); whereas the volume that drops within the overlap must be ignored (Fig. IV.1). On average, any increment of volume in the real medium is thus proportional to the volume increase in the extended microstructure as follows [Jones1997]:

$$dV_{el} = \left[1 - \frac{V_{el} + V_{io}}{V_{tot}}\right] dV_{el}^{ex} \quad \text{and} \quad dV_{io} = \left[1 - \frac{V_{el} + V_{io}}{V_{tot}}\right] dV_{io}^{ex} \quad (\text{IV.5})$$

Where V_{tot} denotes the volume of the considered domain. The terms V_i and V_i^{ex} are related to the volumes of the phase i for the real and extended microstructures, respectively. Knowing

that $\frac{\theta_{io}}{\theta_{el}} = \alpha$ (where θ_{io} and θ_{el} represent the phase volume fraction with $\theta_{io} = \frac{V_{io}}{V_{tot}}$ and $\theta_{el} = \frac{V_{el}}{V_{tot}}$). Jones and Bhadeshia [Jones1997] have integrated the increment of volumes to find the relations between the extended and real volumes for two phases:

$$\frac{V_{el}^{ex}}{V_{tot}^{ex}} = \frac{-1}{1+\alpha} \ln \left[1 - (1+\alpha) \frac{V_{el}}{V_{tot}} \right] \quad \text{and} \quad \frac{V_{io}^{ex}}{V_{tot}^{ex}} = \frac{-\alpha}{1+\alpha} \ln \left[1 - \left(\frac{1+\alpha}{\alpha} \right) \frac{V_{io}}{V_{tot}} \right] \quad (\text{IV.6})$$

It can be noticed that the two previous relations in eq. (IV.6) imply that:

$$\frac{\theta_{io}^{ex}}{\theta_{el}^{ex}} = \frac{\theta_{io}}{\theta_{el}} \quad (\text{IV.7})$$

The combination of eq. (IV.6) and eq. (IV.1) allows the volume fraction of the ionic and electronic conductors in the extended microstructure to be expressed as a function of the porosity of the real medium:

$$\theta_{el}^{ex} = \frac{-1}{1+\alpha} \ln[\theta_p] \quad \text{and} \quad \theta_{io}^{ex} = \frac{-\alpha}{1+\alpha} \ln[\theta_p] \quad (\text{IV.8})$$

These last equations will be used to express the interfacial specific surface areas.

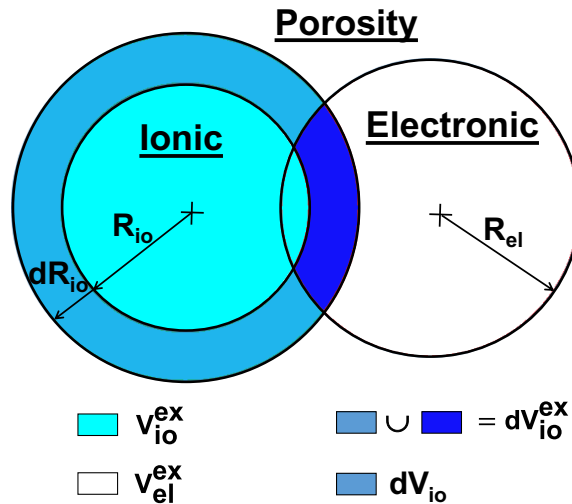


Fig. IV.1: Schematic representation of two overlapping particles in the “extended” microstructure (given here for two spherical particles in ionic and electronic conducting phases).

IV.2.1.2. Specific surface area in the “real” and “extended” microstructures for the ionic/pore and electronic/pore interfaces

In the following, S_{io}^{ex} and S_{el}^{ex} denote the specific surface areas for the ionic and electronic phases in the extended microstructure, whereas $S_{io/p}$ and $S_{el/p}$ represent the interfacial surface areas per unit volume of sample between the ionic/porosity and electronic/porosity phases in the corresponding real microstructure. As previously discussed for the volumes, only a part of the surface area in the extended microstructure can contribute to the surface area in the real microstructure. By analogy with the volume increments in eq. (IV.5), the interfacial surface area of the ionic or electronic particles in contact with porosity in the real microstructure is only equal to the fraction of the surface area that falls within the porosity in the extended microstructure. As a consequence, it can be shown starting from eq. (IV.5) [Gokhale1980, Gokhale1984] the following relations:

$$S_{el/p} = \theta_p S_{el}^{ex} \quad \text{and} \quad S_{io/p} = \theta_p S_{io}^{ex} \quad (\text{IV.9})$$

These last equations will be used to express the interfacial specific surface areas as a function of the geometrical characteristics of the electrode phases.

IV.2.1.3 Expression of the ionic/pore and electronic/pore interfacial specific surface areas versus the “basic” electrode microstructural parameters

The specific surface area for each solid phase in the extended microstructure, S_{el}^{ex} or S_{io}^{ex} , is directly given by the mean surface area of the electronic or ionic particles, $\langle S_{el} \rangle$ or $\langle S_{io} \rangle$, multiplied by the number of particles per unit volume, N_{el} or N_{io} :

$$S_{el}^{ex} = N_{el} \langle S_{el} \rangle \quad \text{and} \quad S_{io}^{ex} = N_{io} \langle S_{io} \rangle \quad (\text{IV.10})$$

The same relations can be also written for the volume fractions in the extended microstructure:

$$\theta_{el}^{ex} = N_{el} \langle V_{el} \rangle \quad \text{and} \quad \theta_{io}^{ex} = N_{io} \langle V_{io} \rangle \quad (\text{IV.11})$$

Where $\langle V_{el} \rangle$ and $\langle V_{io} \rangle$ denote the mean value for the volume of the electronic and ionic particles, respectively. For each solid phase, the combination of eq. (IV.9) to (IV.11) yields the following expressions:

$$S_{el/p} = \theta_p \frac{\langle S_{el} \rangle}{\langle V_{el} \rangle} \theta_{el}^{ex} \quad \text{and} \quad S_{io/p} = \theta_p \frac{\langle S_{io} \rangle}{\langle V_{io} \rangle} \theta_{io}^{ex} \quad (\text{IV.12})$$

The relations given in eq. (IV.8) can be introduced in eq. (IV.12) in order to express the interfacial specific surface area with the parameters of the “real” microstructure only:

$$S_{el/p} = \frac{-1}{1+\alpha} \theta_p \ln[\theta_p] \frac{\langle S_{el} \rangle}{\langle V_{el} \rangle} \quad \text{and} \quad S_{io/p} = \frac{-\alpha}{1+\alpha} \theta_p \ln[\theta_p] \frac{\langle S_{io} \rangle}{\langle V_{io} \rangle} \quad (\text{IV.13})$$

The first terms in eq. (IV.13) describe the variation of the interfacial specific surface areas with the volume fractions of the three ionic, electronic, and pore phases. The ratio, $\frac{\langle S_{el} \rangle}{\langle V_{el} \rangle}$ or $\frac{\langle S_{io} \rangle}{\langle V_{io} \rangle}$, is related to the morphology of the electronic or ionic particles. Indeed, by using eq. (IV.2), the ratio can be replaced by the mean diameter and the shape factor of particles as follows:

$$S_{el/p} = \frac{-1}{1+\alpha} \theta_p \ln[\theta_p] \beta_{el} \frac{\langle D_{el}^2 \rangle}{\langle D_{el}^3 \rangle} \quad \text{and} \quad S_{io/p} = \frac{-\alpha}{1+\alpha} \theta_p \ln[\theta_p] \beta_{io} \frac{\langle D_{io}^2 \rangle}{\langle D_{io}^3 \rangle} \quad (\text{IV.14})$$

The ratio, $\beta_{el}=K_{1el}/K_{2el}$ or $\beta_{io}=K_{1io}/K_{2io}$, depends only on the electronic or ionic particle shape whereas the last term, $\frac{\langle D_{el}^2 \rangle}{\langle D_{el}^3 \rangle}$ or $\frac{\langle D_{io}^2 \rangle}{\langle D_{io}^3 \rangle}$, contains the characteristics describing the particle size distribution. Indeed, with the definitions of the standard deviation σ_i^2 , the coefficient of variation CV_i and the skewness γ_i given in eq. (IV.3), it can be shown that:

$$\langle D_i^2 \rangle = \langle D_i \rangle^2 [1 + CV_i^2] \quad \text{and} \quad \langle D_i^3 \rangle = \langle D_i \rangle^3 [1 + 3CV_i^2 + \gamma_i CV_i^3] \quad (\text{IV.15})$$

Finally, the combination of eqs. (IV.15) and (IV.14) allows the surface areas versus the “basic” microstructural parameters of the electrode to be expressed for both the electronic/porosity and ionic/porosity interfaces:

$$S_{el/p} = \frac{-1}{1 + \alpha} \theta_p \ln[\theta_p] \beta_{el} \frac{1}{\langle D_{el} \rangle} \frac{[1 + CV_{el}^2]}{[1 + 3CV_{el}^2 + \gamma_{el}CV_{el}^3]} \quad (IV.16a)$$

$$S_{io/p} = \frac{-\alpha}{1 + \alpha} \theta_p \ln[\theta_p] \beta_{io} \frac{1}{\langle D_{io} \rangle} \frac{[1 + CV_{io}^2]}{[1 + 3CV_{io}^2 + \gamma_{io}CV_{io}^3]} \quad (IV.16b)$$

It is worth reminding that the “extended” microstructure is composed of ionic and electronic particles while the porosity is taken as the complementary phase (Fig. IV.1). With such a configuration, the contact surface between two overlapping particles is not well defined. Therefore, the same development cannot be applied to derive the formula expressing the interfacial specific surface area between the electronic and ionic particles $S_{io/el}$. From that point of view, further assumptions are required.

IV.2.2.4 Expression of the interfacial specific surface area between the ionic and electronic phases

With simple geometrical considerations, it can be shown that the surface area $S_{io/el}$ is linked to the density of TPBl. Indeed, the interfacial surface area between two convex ionic and electronic particles is proportional to the contact perimeter.

Assuming spherical particles, the density of TPBl is simply given by the number of ionic and electronic contacts per unit volume, N_c , multiplied by the mean circumference of the intersections:

$$L_{TPB} = N_c \pi \langle d_c \rangle \quad (IV.17)$$

Where $\langle d_c \rangle$ is the mean value of the contact diameter between the ionic and electronic particles. Accordingly, the interfacial specific surface area can be expressed as $S_{el/io} = a_1 \times N_c \pi \langle d_c \rangle^2 / 4$ where the term a_1 is a factor of proportionality taking into account a potential roughness of the solid/solid interface created during the sintering. The interfacial specific surface area between the electronic and ionic particles is then given by:

$$S_{el/io} = a_1 \times L_{TPB} \langle d_c \rangle / 4 \quad (IV.18)$$

Considering the geometry of a Hertzian contact force model for spheres, Amitai et al. [Amitai2017] have shown that $\langle d_c \rangle$ can be related to the mean diameters of the ionic and electronic particles:

$$\frac{\langle d_c \rangle^2}{4} = \frac{\langle D_{el} \rangle \langle D_{io} \rangle}{\langle D_{el} \rangle + \langle D_{io} \rangle} \ell \quad (\text{IV.19})$$

Where ℓ denotes the penetration length of the particles intersection. Unfortunately, this parameter depends on the local geometry of the intersections (contact angle and sphere radius). However, it varies over a limited range for “classical” electrode microstructures with a good estimation given by $\ell = a_2 \times \min \{ \langle D_{el} \rangle, \langle D_{io} \rangle \}$, where a_2 is a constant of proportionality depending on the mean contact angle $\langle \theta \rangle$. This approximation is rigorously fulfilled when the ionic and the electronic particles have the same size. Indeed, the penetration length is then simply given by $\ell = a_2 \times \langle D_{i=io \text{ or } el} \rangle$ (with $a_2 = (1 - \cos \langle \theta_{i=io \text{ or } el} \rangle)$). However, this relation is also valid when one of the mean phase diameters is significantly higher than the other (in this case, $\ell = a_2 \times \min \{ \langle D_{el} \rangle, \langle D_{io} \rangle \}$). Therefore, by combining (IV.4), (IV.18) and (IV.19), the interfacial specific surface area between the ionic and electronic phases can be given as a function of the geometrical attributes of the microstructure:

$$S_{el/io} = \frac{\pi}{8} \frac{\alpha}{(1 + \alpha)^2} \theta_p (\ln \theta_p)^2 \frac{\beta_{io} \beta_{el} a}{\sqrt{\max \{ \langle D_{el} \rangle, \langle D_{io} \rangle \} \times (\langle D_{io} \rangle + \langle D_{el} \rangle)}} \quad (\text{IV.20})$$

$$\times \frac{(1 + CV_{io}^2)}{(1 + 3CV_{io}^2 + \gamma_{io} CV_{io}^3)} \frac{(1 + CV_{el}^2)}{(1 + 3CV_{el}^2 + \gamma_{el} CV_{el}^3)}$$

Where a is a constant of proportionality (depending on a_1 and a_2). As for the TPBI, this correlation is expressed for the whole ionic/electronic surface area including the connected and disconnected phases. However, it must be still valid for the connected phases as long as all the electrode phases are above the percolation threshold.

IV.2.3 Methodology for calibrating and validating the microstructural correlations

IV.2.3.1 Calibration of the semi-analytical correlations

The “basic” microstructural parameters used in the correlations are associated to the geometric attributes that describe the morphology of the electrode particles collection. If the sintering temperature is not too high, these parameters must not be too far from the geometrical characteristics of the initial powders [Zhang2011]. However, the full relevance of this claim is questionable as the solid phases in real electrodes exhibit a continuous shape with no remanence of the initial geometry of the powder particles [Prakash2014, Moussaoui2018, Neumann2016]. Nevertheless, considering the real electrodes, the “basic” microstructural parameters can still be measured by image analysis on 3D reconstructions (or assessed on 2D micrographs with stereological assumptions). For example, the parameters $\langle D_i \rangle$, CV_i and γ_i can be measured using the concept of continuous PSD (cf. Section II.5.1.1). Therefore, the determination of the ratio β_{el} , β_{io} and the parameter a is not straightforward.

In the present work, the correlations have been calibrated thanks to the generation of a large database of representative 3D synthetic microstructures. In other words, the unknown parameters β_{el} , β_{io} and a of the correlations have been fitted on the numerical dataset computed on the 3D volumes. Besides, the consistency of the microstructural correlations have been checked by varying independently (i) the electrode composition, (ii) the porosity and (iii) the mean particle size of the ionic and electronic phases (which constitute the main parameters that can easily be adapted for an electrode microstructural optimization).

In practice, the two 3D stochastic geometrical models detailed in the previous chapter have been used. The same 3D reconstruction of the typical Ni-YSZ cermet of Cell-A (cf. Chapter II), which was used to check the representativeness of the two models, has been employed as reference for the database generation. It can be noticed that, being radically different, both approaches lead to produce distinct microstructures even if they have to emulate the same porous medium. Therefore, the two models must provide two approximations of the real microstructures, and hence, two approximations for the correlations calibrated on the two numerical datasets.

IV.2.3.2 Validation of the microstructural correlations

Finally, the validity of the correlations to predict the microstructural properties has been checked thanks to various reconstructions acquired on different electrodes. In this frame, the reconstruction of a second typical cermet of Cell-B in Chapter II has been used (Electrode_2). Besides, a typical O₂ electrode made of LSCF and CGO (Electrode_3) has been specifically reconstructed by FIB-SEM (cf. presentation of Cell-C in Chapter II). The ability of the correlation to reproduce the loss of TPBI after Ni agglomeration has also been checked on Electrode_1 thanks to 3D volumes reconstructed after long-term operation [Hubert2018].

IV.2.3.3 Visualization of the real and synthetic electrodes microstructures

The 3D rendering volumes of the three electrode reconstructions are provided in Fig. IV.2. The synthetic microstructures (digital twins) generated by the sphere-packing and the random fields methods are also given for Cell-A taken as reference for the sensitivity analysis. The simulated volumes obtained by changing the electrode porosity are also provided as an illustration. A volume of 15x15x15 μm³ with a resolution of 25 nm is taken for the synthetic microstructures. As already discussed in Section II.6, this size of the 3D volume is sufficiently large to reach a good representativeness of the heterogeneous electrode microstructure (so that it can be considered as a Representative Volume Element (RVE) of the microstructure for which only one realization is required).

The microstructural properties have been measured on the synthetic microstructures or real reconstructions thanks to the procedures already detailed in Section II.5. It can be noticed that, in our case, the continuous PSD is used to describe the smooth electrode phases and thus it is not related to a collection of discrete particles. As a consequence, the ratios β_{el} , β_{io} and the parameter a for the sintered SOC electrodes cannot be directly associated to the geometrical shapes of distinct particles. In the present work, the parameters β_{el} , β_{io} , a are thus fitted on the 3D microstructures, in such a way that the relationships for L_{TPB} and $S_{i/j}$ given by eqs (IV.4), (IV.16) and (IV.20) can be seen as semi-analytical correlations.

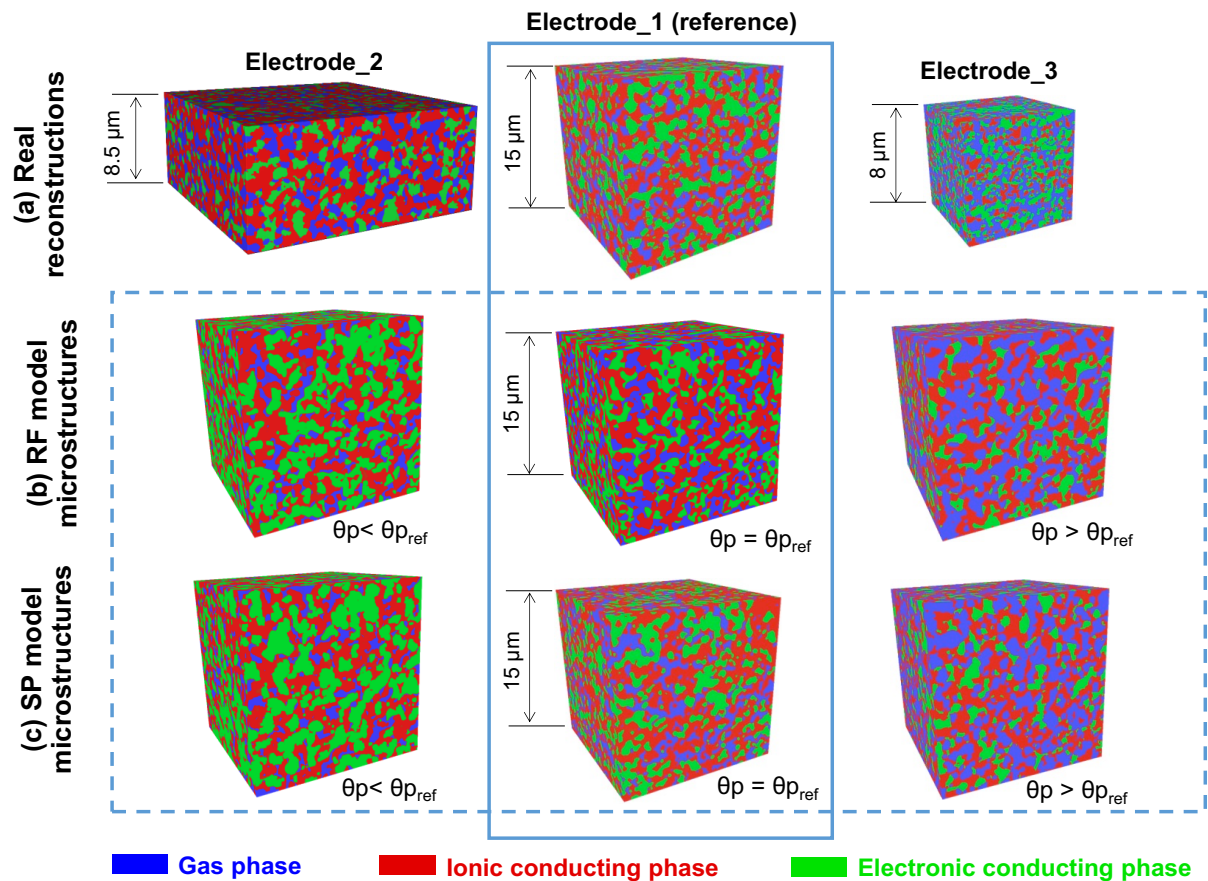


Fig. IV.2: (a): 3D rendering volumes for the reconstructions of Electrode_1 (Ni-YSZ), Electrode_2 (Ni-YSZ) and Electrode_3 (LSCF-CGO). (b) and (c): the synthetic microstructures of Electrode_1 generated by the Gaussian random field and the sphere packing models are shown with a sensitivity analysis on the porosity.

IV.3. Calibration of the microstructural correlations

IV.3.1 Correlations for the electronic/pores and ionic/pores interfacial specific surface area

As the correlations have been established for the specific surface area including the connected and disconnected phases, they have been calibrated on the 3D microstructures taking into account the total phases. However, the analyses have been conducted over a range of porosities and compositions for which each phase remains almost fully percolated. In practice, the fitting procedure has been performed while keeping the electrode porosity and the ionic and electronic volume fractions higher than the phase percolation threshold (around 18%). Over this range of electrode compositions, the phase percolation remains higher than 93% so that the correlations should be still valid if considering only the connected phases. The full

validity of this last assumption has been *a posteriori* verified by comparing the predicted surface area with the data obtained on the percolated phases.

IV.3.1.1 Ionic/pores interfacial specific surface area

The ionic/pores interfacial surface area $S_{io/p}$ calculated with eq. (IV.16b) is compared to the numerical values computed on the 3D microstructures by changing the porosity θ_p , the composition $\alpha = \theta_{io}/\theta_{el}$ and the mean phase diameters $\langle D_{io} \rangle$ and $\langle D_{el} \rangle$ in Fig. IV.3a, 3b and 3c, respectively. As a general comment, a good agreement is observed between the whole numerical dataset, generated either with the Random Field (RF) model or the Sphere Packing (SP) model, and the semi-analytical correlation (IV.16b) for which only one scaling parameter β_{io} has been fitted.

As previously mentioned, some specific surface areas have also been calculated on the 3D microstructures by considering only the connected phases. These computations have been performed for the microstructural parameters taken at three bounds in the sensitivity analysis: pores, Ni or YSZ volume fractions equal to 18%. As expected, it can be seen in Fig. IV.3 that the bias, which is introduced with only the percolated phases, remains negligible (as long as the phase volume fractions are not lower than $\approx 18\%$).

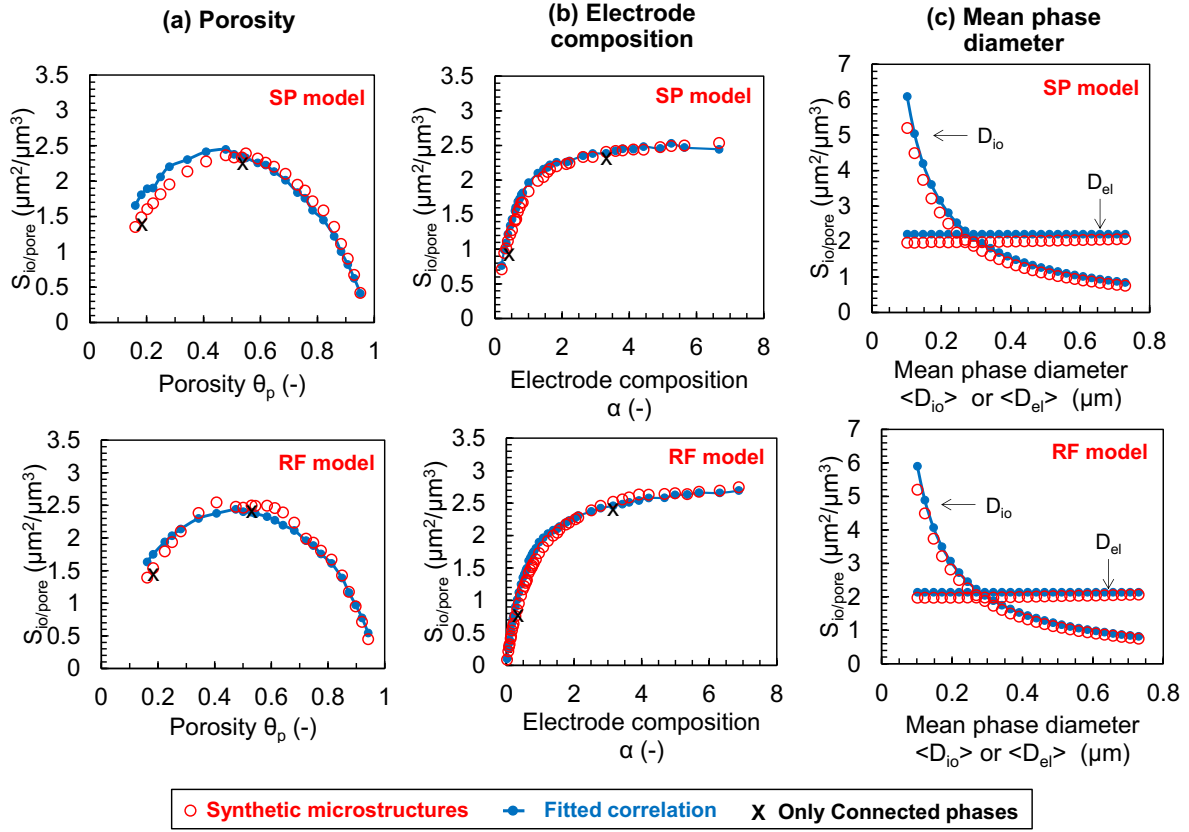


Fig. IV.3: Comparison between the interfacial specific surface area $S_{io/p}$ calculated with the correlation (IV.16b) and the data measured on the 3D volumes generated by the RF and SP models. The surface area $S_{io/p}$ is plotted versus the porosity (a), the electrode composition (b) and the mean phase diameters (c). The crosses indicate the values for $S_{io/p}$ calculated with (IV.16b) considering only the connected phases (for θ_{Ni} , θ_{YSZ} or $\theta_p = 0.18$). The scaling parameter β_{io} in (IV.16b) has been fitted to $\beta_{io}^{RF} = 3.369$ and $\beta_{io}^{SP} = 3.476$ on the RF and SP microstructures, respectively.

According to eq. (IV.16b), the ionic/pores interfacial surface area is proportional to $S_{io/p} \propto -\theta_p \ln[\theta_p]$ meaning that the property exhibits a maximum at intermediate porosities. This evolution is well retrieved by both SP and RF models as shown in Fig. IV.3a. This behavior is easily explained since the surface area tends to zero in the case of a dense or a highly porous medium. Moreover, the surface area $S_{io/p}$ is a function of the electrode composition with a relation $S_{io/p} \propto \frac{\alpha}{1+\alpha} = \frac{\theta_{io}}{\theta_{el}+\theta_{io}}$ given in eq. (IV.16b). As discussed for the porosity, this dependence is also rather well reproduced by the numerical data (Fig. IV.3b). It can also be noticed that the ionic/pore surface area increases with the ratio α up to reach a plateau. Indeed, the contact surface area between the ionic phase and the porosity must increase by increasing the ionic content in the electrode composition. Finally, regarding eq. (16b), $S_{io/p}$

must be independent on the mean diameter of the electronic conducting phase whereas it is inversely proportional to the mean diameter of the ionic phase. Both of these dependences are perfectly confirmed by the RF and SP numerical models (Fig. IV.3c). This behavior is explained since a very fine microstructure for the ionic network must result in a high ionic/pore surface area irrespective of the size of the electronic phase.

IV.3.1.2 Electronic/pores interfacial specific surface area

Following the same procedure as $S_{io/p}$, the semi-analytical expression (IV.16a) for the electronic/pores interfacial surface area $S_{el/pore}$ has been calibrated with the same database of numerical microstructures. Similarly to the previous property, a general good consistency has been found with the two datasets obtained with the RF and SP models. The reader is invited to refer to Appendix A.3 for the plots of $S_{el/pore}$ as a function of θ_p , α and $\langle D_i \rangle$. It has been confirmed using the numerical dataset that $S_{el/pore}$ follows the same evolution with the porosity as $S_{io/pore}$. Besides, the electronic/pore surface area has been found to be inversely proportional to the mean electronic phase diameter as predicted by eq. (IV.16a). Finally, it has also been checked that $S_{el/pore}$ is directly proportional to the relative volume fraction of the electronic phase in the solid (i.e. $\frac{1}{1+\alpha} = \frac{\theta_{el}}{\theta_{el}+\theta_{io}}$).

In order to summarize all the results, the ionic/pores and electronic/pores interfacial specific surface areas measured on the set of synthetic microstructures have been plotted as a function of the semi-analytical estimations in Fig. IV.4. In this representation, all the points are rather well aligned proving the reliability of the proposed correlation for both RF and SP models.

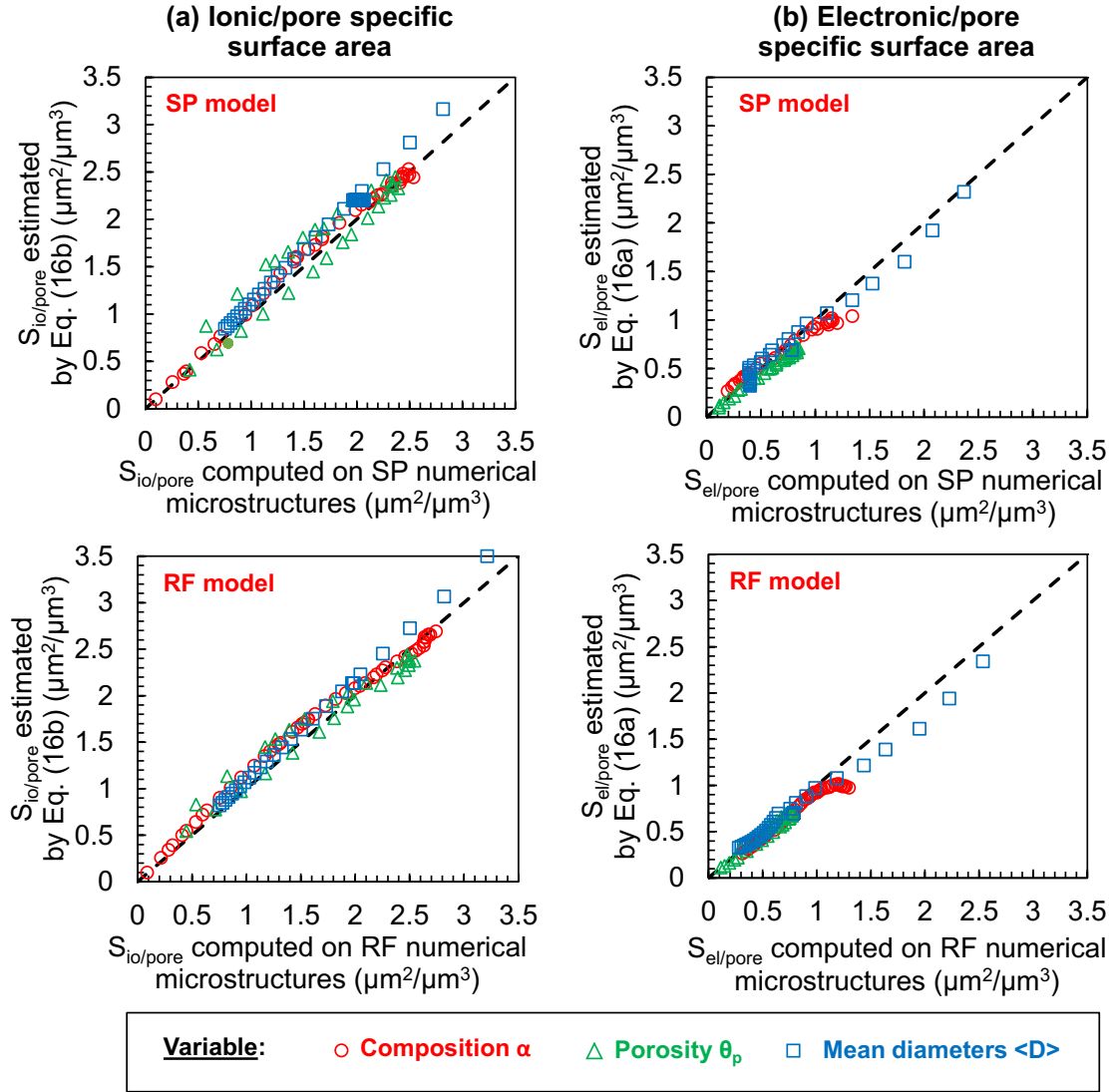


Fig. IV.4: Ionic/pores and electronic/pores interfacial specific surface areas estimated with the semi-analytical eqs. (16b) and (16a) are plotted as a function of the data measured on the set of RF and SP synthetic microstructures. The scaling parameters β_{io} and β_{el} have been fitted on the RF and SP microstructures to: $\beta_{io}^{RF} = 3.369$, $\beta_{io}^{SP} = 3.476$, and $\beta_{el}^{RF} = 2.476$, $\beta_{el}^{SP} = 2.454$.

IV.3.2 Correlation for the electronic/ionic interfacial specific surface area

As shown in eq. (IV.20), the expression of the electronic/ionic interfacial specific surface area is scaled by the product $\beta_{io} \times \beta_{el} \times a$. Knowing that β_{io} and β_{el} have already been determined with the previous relationships, only the scaling parameter a has been fitted for this correlation. The dependences of $S_{el/io}$ with the porosity, the composition and the mean phase diameters are shown in Fig. IV.5a, 5b and 5c. It can be seen that the proposed equation is able to accurately predict all the evolutions of the studied property measured on the synthetic microstructures for both the RF and SP models. Moreover, in accordance with the previous relations for $S_{el/pore}$ and $S_{io/pore}$, it has been checked that the semi-analytical

relation for $S_{el/io}$ is still valid for the percolated phases over the investigated range of microstructures (Fig. IV.5).

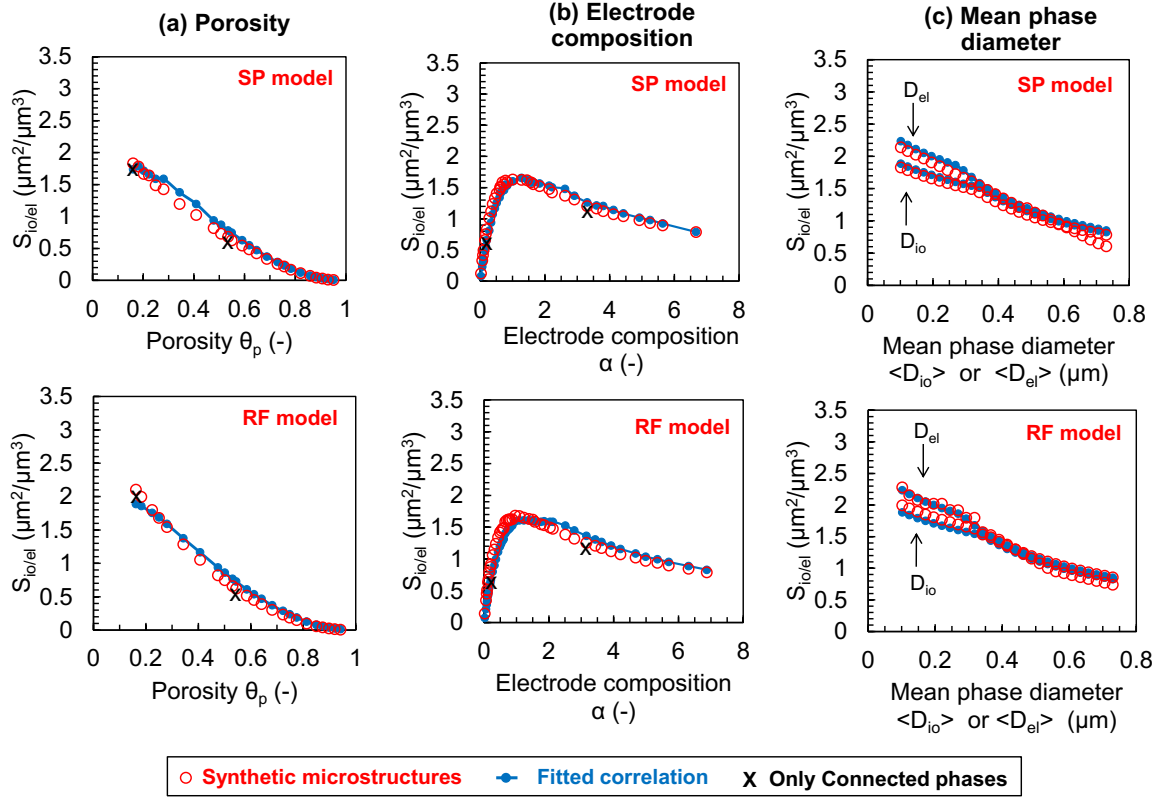


Fig. IV.5: Comparison between the specific interfacial surface area $S_{el/io}$ calculated with the correlation (IV.20) and the data measured on the 3D dataset for the RF and SP models. The surface area $S_{el/io}$ is plotted versus the porosity (a), the electrode composition (b) and the mean phase diameters (c). The crosses indicate the values for $S_{el/io}$ calculated with (IV.20) considering only the connected phases (for θ_{Ni} , θ_{YSZ} or $\theta_p = 0.18$). Correlation calibrated with $\beta_{io}^{RF} = 3.369$, $\beta_{el}^{RF} = 2.476$, $a^{RF} = 3.661$ and $\beta_{io}^{SP} = 3.476$, $\beta_{el}^{SP} = 2.454$ and $a^{SP} = 3.580$ on the RF and SP microstructures, respectively.

Unlike the specific surface area at electronic/pore or ionic/pore interfaces, the contact surface area between the two solid phases decreases continuously as a function of the porosity (Fig. IV.5a). Indeed, the volume fractions of both solid phases, and hence their surface contact, decreases when the microstructure is more porous. Besides, $S_{el/io}$ presents a maximum for $\alpha = 1$ when the amounts of ionic and electronic phases are equal (Fig. IV.5b).

As shown in eq. (IV.20), the dependence of $S_{el/io}$ with the mean phase diameter is more complex than the one established for the surface area between the solid phases and the

porosity. Indeed, the analytical correlation (IV.20) predicts a coupled dependence in the mean diameters for both solid phases: $S_{el/io} \propto \frac{1}{\sqrt{\max\{\langle D_{el}\rangle, \langle D_{io}\rangle\} \times (\langle D_{io}\rangle + \langle D_{el}\rangle)}}$. Therefore, the electronic/ionic surface area must decrease when both mean diameters increase. More precisely, two regimes can be distinguished when changing one diameter (while the other remains constant in the sensitivity analysis). For instance, let one consider in Fig. IV.5c the case of changing $\langle D_{el}\rangle$ while $\langle D_{io}\rangle$ is kept constant to the reference value $\langle D_{io}\rangle = 0.34 \mu\text{m}$. If $\langle D_{el}\rangle > \langle D_{io}\rangle$, then the specific surface area is given by $S_{el/io} \propto \frac{1}{\sqrt{\langle D_{el}\rangle} \sqrt{\langle D_{el}\rangle + 0.34}}$. Inversely, when $\langle D_{el}\rangle < \langle D_{io}\rangle$, the equation is reduced to $S_{el/io} \propto \frac{1}{\sqrt{\langle D_{el}\rangle + 0.34}}$. This behavior predicted by the analytical model involves two slopes in the curve $S_{el/io} = f(\langle D_{el}\rangle)$ plotted in Fig. IV.5c. This evolution is perfectly reproduced by the data computed on the synthetic microstructures generated by the two models (Fig IV.5c). This result allows validating the mean diameters dependency depicted in eq. (IV.20).

As expected, the error given by the correlation is minimum when the two mean diameters are similar in the sensitivity analysis (*i.e.* around the reference electrode for $\langle D_{io}\rangle \approx 0.34 \mu\text{m}$). Indeed, there is no approximation in the expression of the penetration length when the two diameters are equal as discussed in Section IV.2.2.4. Nevertheless, the error introduced when the two mean diameters differ from each other remains negligible as it can be seen in Fig. IV.5c. Consequently, the expression remains valid over a wide range of fine or coarse microstructures for the ionic or electronic phases.

All the results of the sensitivity analysis are reported in Fig. IV.6a. The values coming from the analytical correlation are compared to the numerical data measured on the 3D volumes for both SP and RF models. For all the dataset, the analytical predictions well match all the values measured on the synthetic microstructures, highlighting the global consistency of the proposed correlations.

IV.3.3 Correlation for the density of TPBI

The density of TPBI has been calculated with the correlation (IV.4) by keeping the same scaling parameters β_{io} and β_{el} previously determined for the specific surface areas. In other words, no additional fitting parameter has been considered at this stage.

In this way, it has been found that the correlation (IV.4) is able to accurately capture the TPBI evolutions as a function of the porosity, the electrode composition and the mean diameters of the electronic and ionic conducting phases measured on the synthetic microstructures (cf. supplementary). All the results are summarized in Fig. IV.6b where the densities of TPBI calculated with the semi-analytical correlation have been confronted to the data measured on the RF and SP synthetic microstructures. As shown in Fig. IV.6b, a good agreement is found between the analytical predictions and the numerical dataset, meaning that eq. (IV.4) provides an accurate estimation of TPBI density for a large range of representative microstructures.

It is worth reminding that Zhang et al. [Zhang2012] have already checked the validity of eq. (IV.4) with simulated microstructures made of spherical powders or needle-shape particles (cf. Section IV.2.1). In their case, the electrode was thus composed by a collection of well-defined particles. Therefore, as predicted by the theory, it was possible to ascribe β_{io} and β_{el} to the shape of the constitutive element of the microstructures. In this work, it has been shown that the correlation can still be used for typical sintered SOCs electrodes with phases exhibiting a continuous and smooth shape (Fig. IV.2). However, in this particular case, it is reminded that the correlation is not fully analytical since β_{io} and β_{el} , which can not be related to the particle shape, have to be considered as simple scaling parameters (without any geometrical meaning).

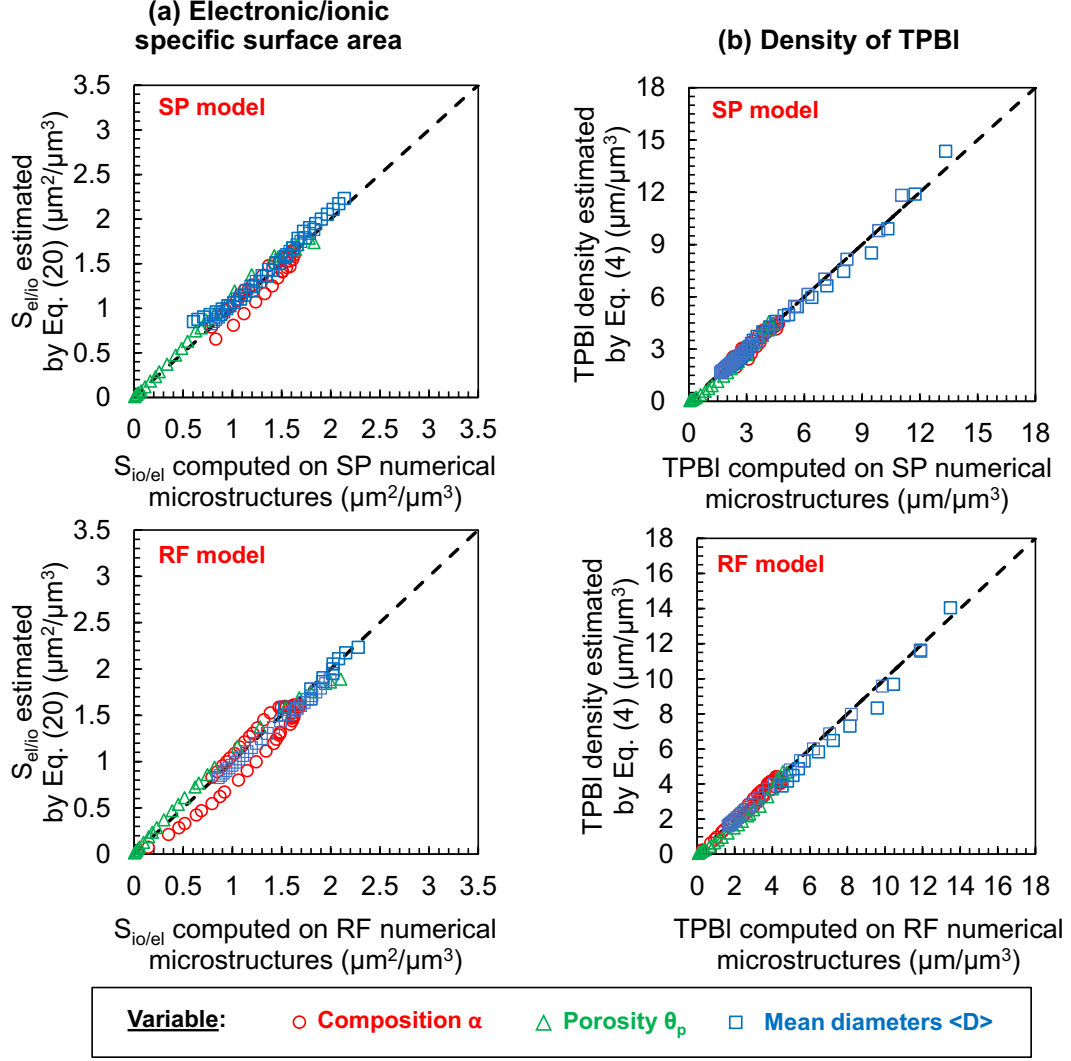


Fig. IV.6: Electronic/ionic interfacial specific surface area and density of TPBI estimated with the semi-analytical eqs (IV.20) and (IV.4) are plotted as a function of the data measured on the set of RF and SP synthetic microstructures. Correlation calibrated with $\beta_{io}^{RF} = 3.369$, $\beta_{el}^{RF} = 2.476$, $a^{RF} = 3.661$ and $\beta_{io}^{SP} = 3.476$, $\beta_{el}^{SP} = 2.454$ and $a^{SP} = 3.580$ on the RF and SP microstructures, respectively.

As done before with the interfacial specific surface areas, the active density of TPBI has been computed on the synthetic volumes by considering only the percolated phases. The dataset has been compared to the prediction of the semi-analytical correlation (IV.4) depending on the phase volume fractions. The results are illustrated in Fig IV.7 changing the ionic content in the electrode. As mentioned for the specific surface area, it can be observed that eq. (IV.4) is able to accurately predict the active TPBI as long as the electrode phases are well connected. Indeed, it has been found that the TPBI calculated with eq. (IV.4) matches the data measured on the percolated microstructures as long as each volume fraction is higher than $\approx 18\%$. It can be noticed that the condition to calculate the active density of triple-phase

boundary is more restrictive than the one requested for the specific surface area. Indeed, the three electrode phases have to be connected at the same time for the active TPBIs whereas only two are necessary for S_{ij} .

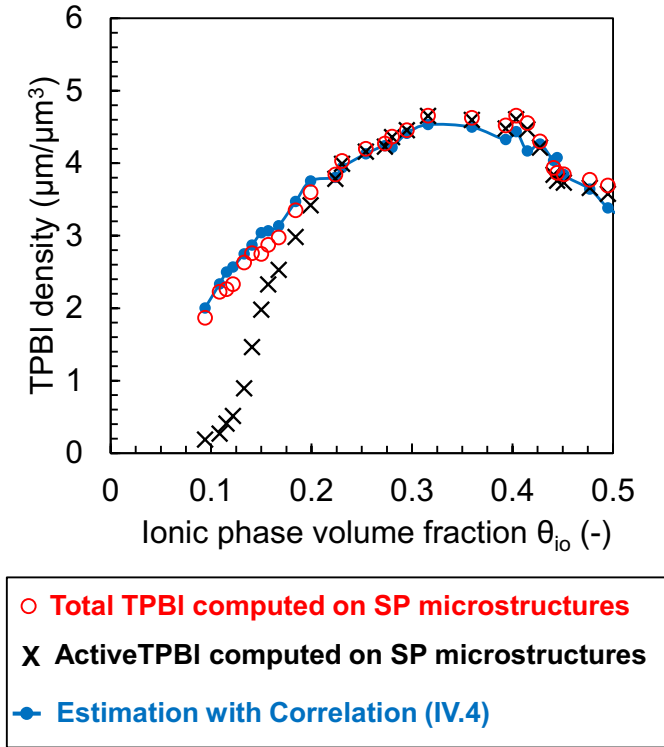


Fig. IV.7: Comparison between the density of TPBI calculated with the correlation (IV.4) and the ones measured on the total and connected phases on the SP synthetic microstructures as a function of the ionic content in the electrode ($\beta_{io}^{SP} = 3.476$, $\beta_{el}^{SP} = 2.454$).

IV.4. Discussion and validation

The consistency of the calibrated correlations with respect to the RF and SP models are discussed as a first element of validation. The final check-up of the model reliability is then conducted by comparing the predictions with the properties measured on the real electrode reconstructions.

IV.4.1 Model prediction with respect to the RF and SP microstructures

The calibration of the previous correlations for S_{ij} and TPBI has been carried out on two sets of representative synthetic microstructures generated by two fundamentally different mathematical models. In spite of the large range of investigated cases in the sensitivity analyses, it has been shown that the semi-analytical equations are able to capture all the

microstructural evolutions with only three fitting parameters. This preliminary remark constitutes a first evidence for the model validation.

Moreover, the scaling parameters are equal to $\beta_{io}^{RF} = 3.369$, $\beta_{el}^{RF} = 2.476$ and $a^{RF} = 3.661$ for the correlations calibrated on the dataset coming from the random field microstructures. By using the sphere packing algorithm, the fitting parameters have been estimated to $\beta_{io}^{SP} = 3.476$, $\beta_{el}^{SP} = 2.454$ and $a^{SP} = 3.580$. Therefore, it can be claimed that there is a very good consistency between the two sets of scaling parameters fitted on the RF and SP microstructures. It is worth reminding that the two numerical models, which have been validated on one single electrode reconstruction, must provide two approximations of the real electrodes when changing the ‘basic’ parameters of the microstructure such as the porosity. From that point of view, the two sets of calibrated semi-analytical correlations should converge toward two independent estimations of the reality. As the scaling parameters are very close to each other, it means that the two predictions remain fully coherent when considering the two approximations given by the RF and SP models. As a consequence, the semi-analytical correlations should provide two accurate predictions over a large range of real electrodes microstructures. In order to check this assertion, the predictions of the correlations have been compared to the properties measured on various electrode reconstructions.

IV.4.2 Model validation on diverse electrodes reconstructions

In Table IV.1, the properties measured on the reconstructions of Electrode_1, electrode_2 and electrode_3 (Fig. IV.2a) are compared to the data calculated with the semi-analytical correlations. As a general comment, it can be seen that a good agreement is found between the properties measured on the 3D volumes and the ones calculated with the calibrated semi-analytical equations. Indeed, whatever the electrodes or the calculated properties are, the error on the parameters estimations does not exceed 12% with an average of 5.4%. More precisely, the inspection of the data reported in Table IV.1 reveals that the correlations calibrated on the SP and RF microstructures provide in average almost the same estimation with respect to the real electrode properties (mean error of 5.5% and 5.3% for the SP and RF models, respectively). Therefore, the difference in the parameters coming from the two calibrations on the RF and SP microstructures is quite negligible, confirming that both sets of correlations provide a good approximation of the reality.

Table IV.1 Summary of the relative errors between the properties measured on the 3D reconstructions and the predictions given by the correlations for (L_{TPB} and S_{ij}).

	L_{TPB} (μm^2)		$S_{io/el}$ (μm^{-1})	
	Correlation (4) calibrated with SP model	Correlation (4) calibrated with RF model	Correlation (20) calibrated with SP model	Correlation (20) calibrated with RF model
Electrode_1 (Ni_YSZ)	4.28 (Error=-9.8%)	4.19 (Error=-11.8%)	1.59 (Error=+0.0%)	1.59 (Error=+0.0%)
Electrode_2 (Ni-YSZ)	5.19 (Error=-5.0%)	5.07 (Error=-7.1%)	1.83 (Error=-0.9%)	1.83 (Error=-1.0%)
Electrode_3 (LSCF-CGO)	8.12 (Error=-7.5%)	7.94 (Error=-9.5%)	1.67 (Error=+1.2%)	1.67 (Error=+1.2%)
	$S_{io/pore}$ (μm^{-1})		$S_{el/pore}$ (μm^{-1})	
	Correlation (16b) calibrated with SP model	Correlation (16b) calibrated with RF model	Correlation (16a) calibrated with SP model	Correlation (16a) calibrated with RF model
Electrode_1 (Ni_YSZ)	2.20 (Error=+9.7%)	2.14 (Error=+6.4%)	0.69 (Error=+9.9%)	0.70 (Error=+10.9%)
Electrode_2 (Ni-YSZ)	1.87 (Error=+7.0%)	1.81 (Error=+3.7%)	0.94 (Error=+5.2%)	0.94 (Error=+6.1%)
Electrode_3 (LSCF-CGO)	2.24 (Error=+6.0%)	2.18 (Error=+2.7%)	2.01 (Error=-3.8%)	2.03 (Error=-2.9%)

The semi-analytical equations are thus able to accurately predict the properties for the typical Ni-YSZ cermets of Electrode_1 and Electrode_2 as well as for the LSCF-CGO composite of Electrode_3. In the latter case, the electrode microstructure is much finer than the two cermets with lower mean diameters for the ionic and electronic conducting phases (cf. microstructures displayed in Fig. IV.2a with $\{\langle D_{LSCF} \rangle = 0.17 \mu\text{m}; \langle D_{CGO} \rangle = 0.16 \mu\text{m} \text{ for Electrode}_3\} < \{\langle D_{Ni} \rangle = 0.34 \mu\text{m}, \langle D_{YSZ} \rangle = 0.28 \mu\text{m} \text{ for Electrode}_1\}$). This finer microstructure for Electrode_3 results in a significantly higher density of TPBI that is well captured by the semi-analytical relation. As a conclusion, it can be inferred from this analysis that the proposed correlations are able to accurately predict the density of TPBI and the interfacial surface areas for different kinds of SOC electrodes (manufactured by the classical manufacturing routes for ceramics).

IV.4.3 Model validation on the loss of TPBI after Ni agglomeration

For Electrode_1, some reconstructions have been also acquired after ageing at 850°C. The experimental conditions of the long-term testing and the microstructural characterization have been detailed in [Hubert2018]. It was found that the Ni phase undergoes a substantial particle coarsening in operation that was modeled by a standard Ostwald ripening power-law equation:

$$[\langle D_{Ni}(t) \rangle^n - \langle D_{Ni}(t=0) \rangle^n] = k_{pow} \times t \quad (IV.21)$$

Where t is the time, k_{pow} the rate constant and n an exponent which is characteristic of the predominant mass transport in the sintering process. The grain-size growth in the cermet was measured on the reconstructed electrodes and the best adjustment of eq. (IV.21) on the experimental data was found for $n = 8$. It was also highlighted that the Ni phase coarsening leads to a substantial decrease in TPBI whereas the volume fractions and the mean phase diameters for the complementary phases remain quite unaffected by the agglomeration.

To check the possibility to use the present microstructural modeling to reproduce the loss of TPBI, eq. (IV.21) has been combined with the correlation (IV.4) calibrated with the SP microstructures. Without any supplementary fitting, the loss of TPBI given by the semi-analytical relations (IV.4) and eq. (IV.21) is compared in Fig. IV.8 to the values measured on the reconstructions. Even if the scattering on the experimental data is rather significant, the two equations are able to predict the evolution of TPBI over the time. This result brings a supplementary evidence on the reliability of the correlation. Besides, it can be mentioned that the system of eqs. (IV.4) and (IV.21) constitutes a physically-based model to compute the loss of TPBI induced by the Ni agglomeration.

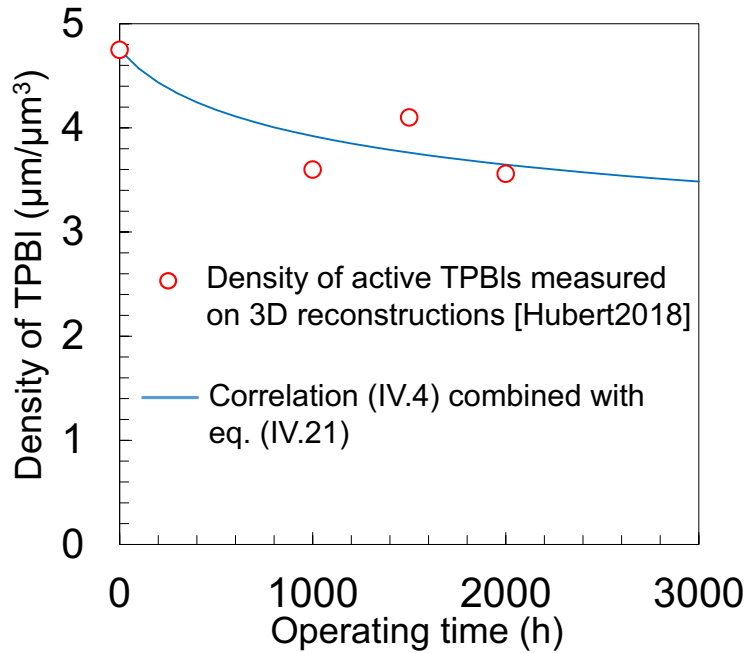


Fig. IV.8: Comparison between the loss of active TPBI measured on several 3D reconstructions after operation and the prediction combining the correlation (IV.4) with the power-law model (IV.21) for the Ni particle coarsening ($\beta_{io}^{SP} = 3.476$, $\beta_{el}^{SP} = 2.454$).

Finally, some authors have also investigated the evolution of the cermet microstructural properties before and after Ni agglomeration by 3D electrode reconstructions [Faes2009, Lee2014]. For instance, Faes et al. [Faes2009] have reported a percentage decrease of 25% in the density of TPBI (after 1130h for ‘Stack A’) whereas Lee et al. [Lee2014] have found, in their experimental conditions, a percentage drop of 55% (after 50h at 1200°C). The change in the ‘basic’ microstructural parameters provided in the two articles have been used to calculate the TPBI decrease with the correlation (IV.4). The model leads to an estimation of the percentage loss of 26% and 50% (instead of 25% and 55%, respectively). The good agreement between the published data and the estimated values also highlights the model validity.

IV.5 Conclusion

The concept of “extended” microstructure has been applied to express the correlations relating the key microstructural properties, which control the electrochemistry, to the ‘basic’ parameters of the microstructure. This approach was initially employed in [Gokhale2009] to establish the relation linking the density of TPBI as a function of (i) the porosity, (ii) the electrode composition, (iii) the geometrical shape and size distribution of particles for the electronic and ionic conducting phases. Following the same approach, the method has been applied in the present work to derive the equations for the ionic/pore, electronic/pore and ionic/electronic interfacial specific surface areas.

The correlations have been studied for the classical SOCs electrodes for which the phases exhibit a continuous shape without remanence of the initial powder particles after sintering. In that case, the three parameters associated to the geometry of the particles and their contacts in the final microstructure have been considered as simple scaling factors.

These scaling parameters have been determined by fitting the semi-analytical relations on a large dataset of properties measured on representative synthetic microstructures generated by two different mathematical methods (i.e. the Gaussian Random Field and the Sphere Packing models). In both cases, the semi-analytical correlations have been found to capture all the evolutions in terms of porosity, electrode composition and mean phase diameters. As long as the phases are well percolated (i.e. for volume fractions higher than $\approx 18\%$), it has been found that the correlations remain valid.

The validity of the calibrated correlations has been discussed with respect to the two numerical methods used for the microstructural generation. It has been shown that the correlations were able to accurately fit the two datasets that provide two independent but close estimations of the real microstructures. To go further in the model validation, the properties calculated by the semi-analytical equations have been also compared to the data measured on several 3D electrode reconstructions. It has been found that the correlations provide accurate predictions for typical Ni-YSZ cermets and LSCF-CGO composite electrodes. Indeed, the estimated average on the error between the estimated properties and the real data are lower than 5.4%, demonstrating the reliability of the proposed semi-analytical correlations. Finally, it has also been shown that the TPBl correlation combined with a power-law model describing the particle growth due to Ni coarsening is able to capture the loss of active TPBl in operation.

These findings unravel the relationships between the “basic” microstructural parameters, which can be linked to the characteristics of the powders before sintering, to the electrode reaction sites density, which are the key properties controlling the electrochemical response. This gives clear insights to cell manufacturers towards engineering highly efficient SOC electrodes. Nevertheless, microstructural optimization is a more complex multivariate task because the reaction sites cannot be maximized at the same time.

Indeed, the electrode response depends on the reaction mechanism divided in a sequence of elementary steps. The kinetic rate of each step is scaled by some microstructural properties. For instance, some reactions occur at the surface of the electrodes while others take place at the triple lines in the microstructure. In that view, the contribution of each reaction to the global electrode performances has to be assessed as function of the microstructural properties. With this approach, the microstructure can be tuned in order to optimize the electrode performances depending on the co-limiting reactions of the global electrochemical process.

In this frame, an in-house electrochemical model is used in the following chapter to link the electrode microstructure to its performance. The LSCF-CGO composite was chosen to be studied in this case as a promising material for O₂ electrode.

Chapter V: Impact of microstructure on the LSCF-CGO composite electrode performance

One of the most commonly used O₂-electrode materials for Intermediate Temperature SOC (IT-SOC) is La_{1-x}SrCo_yFe_{1-y}O_{3-δ} (LSCF) because of its Mixed Electronic and Ionic Conductivity (MIEC) [Menzler2010]. Recent studies have shown that adding a high ionic conducting material like Ce_xGd_{1-x}O_{2-δ} (CGO) into LSCF is liable to enhance the electrode performances [Dusastre1999, Hwang2005]. Indeed, it has been reported by several authors [Dusastre1999, Leng2008, Wang2005] that the porous LSCF-CGO composite exhibits a higher effective ionic conductivity than the LSCF electrode. Furthermore, it is suspected that the presence of CGO could also modify the global reaction mechanism in electrolysis and fuel cell modes [Dusastre1999, Laurencin2015]. Indeed, for a porous electrode of pure LSCF, the oxygen reduction under cathodic polarization occurs on the surface of the MIEC particles according to a reaction mechanism named the “bulk path” [Laurencin2015, Adler1996], whereas the oxidation under anodic current takes place at the Triple Phase Boundary lengths (TPBLs) (defined by the lines where the LSCF, the pure ionic conducting material and the gas phase meet). In this case, the electrochemical reaction is thus restricted at the interface with the electrolyte according to the so-called “surface path” [Laurencin2015, Monaco2018]. For the LSCF-CGO composite, it is worth reminding that the TPBLs extend into the whole electrode thickness. For this reason, it has been suggested by some authors that the reaction at TPBLs could also play a major role in the electrode reaction mechanism [Dusastre1999, Fu2007, Kim2017].

In order to better understand the role of electrode microstructure on the performances, a coupled experimental and modeling approach has been used. The method is based on (i) electrochemical measurements on symmetrical cells, (ii) 3D reconstruction of the tested electrode (cf. Chapter II) and (iii) an integrated microstructural and electrochemical modeling. This trifold methodology enabled to quantify the contribution of the bulk and surface path for the LSCF/CGO composite and to address some numerical microstructural optimizations. This analysis has been conducted at the intermediate temperature of 700°C in the frame of IT-SOC optimization, as discussed in chapter I.

V.1 Experimental conditions, modeling and methodology

V.1.1 Testing conditions

A LSCF-CGO symmetrical cell has been specifically manufactured for this study. The fabrication details of this cell, named Cell-C, are given in Section II.1.3. It has been tested using a three-electrode experimental setup. The reference electrode (RE) consisted in a platinum wire ring applied on the periphery of the YSZ membrane as far as possible from the working electrode as shown in Fig. V.1. Considering the dimensions of the symmetrical cell (Fig. V.1), it is worth mentioning that the rules for positioning the reference electrode were fulfilled [Rutman2008]. Moreover, two gold grids with a mesh of 100 squares.cm⁻² and a surface equal to the area of the symmetrical electrodes were used as current collectors. A weight of around 0.7 kg was also applied on the cell in order to reduce the electrical contact resistances between the grids and the electrodes.

During the experiment, the cell was initially heated up to 800°C with a ramp of 1°C·min⁻¹ in order to avoid the damaging of the sample due to sharp thermal gradients. The cell was then maintained at this temperature for 24h under air. This preliminary annealing was done to optimize the electrical contacts and to stabilize the cell electrochemical response. Afterwards, the electrochemical characterizations were carried out at 650°C, 700°C and 750°C by feeding the cell under synthetic air with a high flow rate in order to limit the electrode overpotential due the O₂ conversion (with O₂ and N₂ flow rates of 0.44 NL·min⁻¹ and 1.56 NL·min⁻¹ respectively). All the measurements were conducted using an Autolab potentiostat/impedance frequency analyzer (PGSTAT302N). At each temperature, the polarization curve of the working electrode was recorded in galvanostatic mode with a current step of 1 mA·s⁻¹. Electrochemical Impedance Spectroscopy (EIS) measurements were carried out at OCP for the three studied temperatures. At 700°C, the experimental dataset was complemented by impedance spectra obtained under anodic and cathodic steady-state currents, $i_{dc} = \pm 50$ mA·cm⁻² and ± 30 mA·cm⁻². All the diagrams were acquired in the frequency range of 10 kHz–0.01 Hz by applying a sinusoidal perturbation on the current with an amplitude of $|i_{ac}| = \pm 10$ mA·cm⁻². For all presented impedance diagrams, the series resistances (the resistive contribution of YSZ pellet and the contact resistances) were subtracted for the sake of clarity.

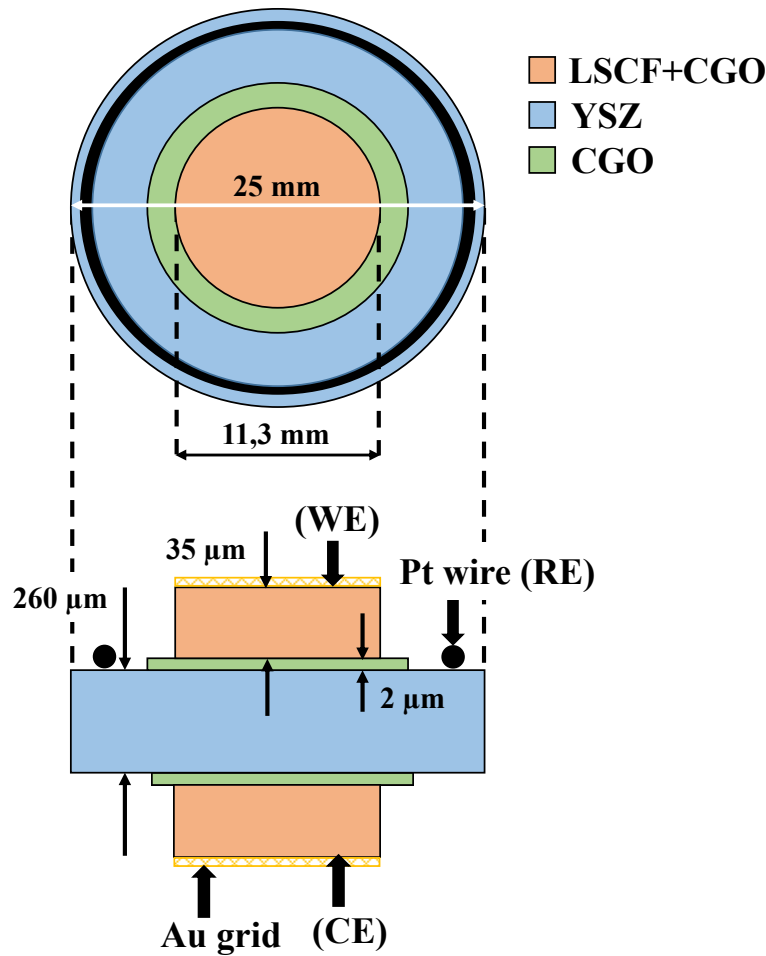


Figure V.1 Three-electrode setup with a symmetrical cell configuration.

V.1.2 Electrochemical model description

Since the reaction mechanism of LSCF-CGO electrodes is still not precisely understood, an in-house model was used to analyze the electrode operating pathways and their dependence on the electrode microstructure. This microscale model was developed in order to compute the stationary and dynamic response of the electrode under anodic and cathodic dc currents. The model was built by considering an equivalent homogenous medium of the composite porous electrode for which the effective properties are computed on the 3D reconstruction. The full description of the model has been already published elsewhere [Laurencin2015, Hubert2016] and only a brief description is thus provided below.

The reaction mechanism was divided into a sequence of reaction steps with two parallel pathways illustrated in Fig. V.2 in anodic polarization (i.e. electrolysis mode) The first pathway ('bulk path') is composed of an oxygen ionic transfer at the LSCF/CGO interface (R1) followed by an oxygen excorporation step (R2); while the second pathway ('surface

path') is defined by a direct electrochemical oxidation taking place at TPBLs (R3). As depicted in Fig. V.2, both pathways lead to form adsorbed oxygen atoms on the surface of the LSCF particles which are finally released into the porosity by a common associative desorption step (R4).

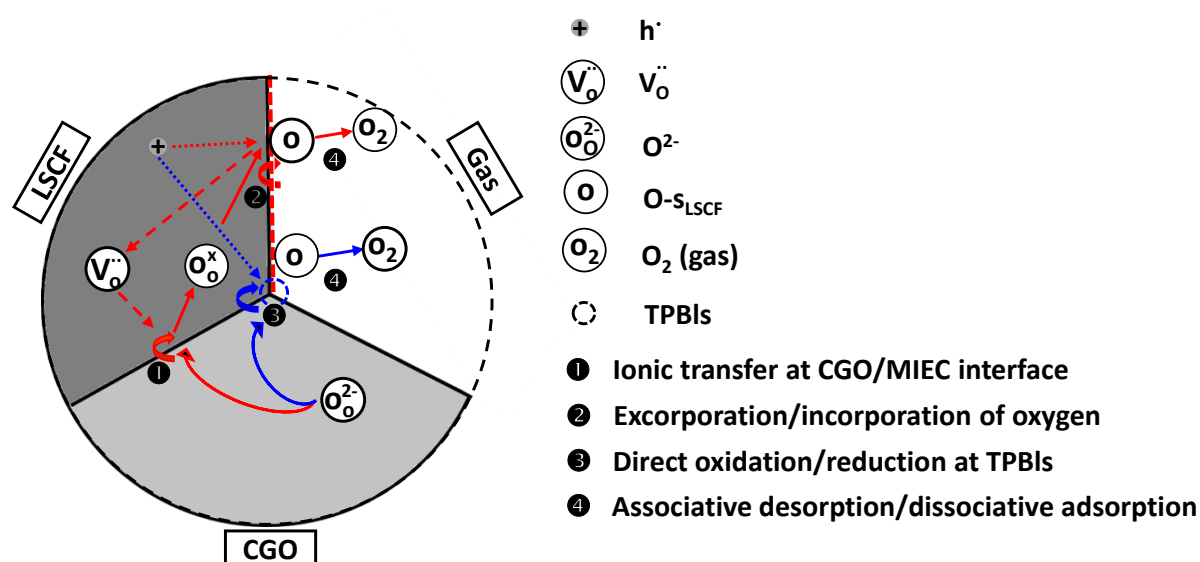


Figure V.2. Schematic representation of the two reaction pathways implemented in the O_2 electrode microscale model. The so-called 'bulk path' and the 'surface path' are represented with red and blue arrows, respectively.

All the equations for the reactions (R1) to (R4) are listed in Table V.1 using the 'Kröger-Vink' notation (the meaning of each parameter is given in the list of symbols). It can be noticed that all the reactions were written in this work by considering one single exchanged oxygen. The associated equations for expressing the electrochemical and chemical kinetic rates are provided in Table V.1. A classical Butler-Volmer formalism was used for the kinetic of the ionic transfer at the LSCF/CGO interface (R1) and the charge transfer at TPBLs (R3). The kinetic rate for the oxygen excorporation/incorporation from the LSCF lattice (R2) was written assuming a pure chemical oxidation/reduction as discussed in [Laurencin2015]. The forward and backward kinetic constants of each reaction are linked in the model through their respective thermodynamic equilibrium constant [Laurencin2015]. Finally, it is worth noting that all the kinetic rates were scaled by the corresponding microstructural parameters. For instance, the oxidation/reduction at TPBLs is directly proportional to the density of active TPBLs while reactions (2) and (4) taking place at the surface of the LSCF particles are dependent on the LSCF/gas specific surface area.

The equations related to the flows, currents, mass and charges balances, which are taken into account in the modelling, are given in Table V.1. The ionic and electronic currents in the CGO and LSCF materials have been assumed to obey to a classical Ohm's law. The electronic conductivity in the MIEC phase is dependent on the oxygen partial pressure with an exponent varying from $n=+1/5$ to $n=+1/20$ [Laurencin2015, Lane2000]. A Fick's law was used to compute the fluxes of the adsorbed oxygen atoms and the solid-state diffusion of vacancies in the LSCF. In the latter case, the coefficient is expressed through a chemical diffusivity that depends on the oxygen partial pressure. The gas transport in the electrode porosity was computed in the frame of the Dusty Gas Model (DGM). It can be noticed that all the effective transport parameters (i.e. effective conductivities and diffusivities) are calculated on the 3D microstructure by homogenization (cf. M-factor in Table II.3 of chapter II).

Table V.1

Reactions, expressions of the kinetic rate and equations of charge and mass conservations associated to the current and fluxes taken into account in the physically-based model (cf. List of symbols).

Electrode		
	Reactions	Kinetic rates
R1	$O_o^x(CGO) + V_o^{\bullet\bullet}(LSCF) \xrightleftharpoons[k_-]{k_+} O_o^x(LSCF) + V_o^{\bullet\bullet}(CGO)$	$v_{(1)} = S_p^{CGO/LSCF} \left\{ k_+ \exp\left(\frac{2\alpha_{(R1)}^{ox} FE}{RT}\right) \left(\frac{C_{V_o^{\bullet\bullet}}}{C_{O_o^x}^{max}}\right) - k_- \exp\left(\frac{-2\alpha_{(R1)}^{red} FE}{RT}\right) \left(\frac{C_{O_o^x}}{C_{O_o^x}^{max}}\right) \right\}$
R2	$O_o^x(LSCF) + 2h^* + s_{LSCF} \xrightleftharpoons[k_{red}^{(2)}]{k_{ox}^{(2)}} V_o^{\bullet\bullet}(LSCF) + O_{sLSCF}$	$v_{(2)} = S_p^{LSCF/gas} \left\{ k_{ox}^{(2)} (C_{O_o^x} \Gamma \theta_{sLSCF}) - k_{red}^{(2)} (\Gamma \theta_{O_{sLSCF}} C_{V_o^{\bullet\bullet}}) \right\}$
R3	$O_o^x(CGO) + 2h^* + s_{LSCF} \xrightleftharpoons[k_{red}^{TPB}}{k_{ox}^{TPB}} O_{sLSCF} + V_o^{\bullet\bullet}(CGO)$	$v_{(3)} = \xi_{TPBs} \left\{ k_{ox}^{TPB} \exp\left(\frac{2\alpha_{(R3)}^{ox} FE}{RT}\right) \Gamma \theta_{sLSCF} - k_{red}^{TPB} \exp\left(\frac{-2\alpha_{(R3)}^{red} FE}{RT}\right) \Gamma \theta_{O_{sLSCF}} \right\}$
R4	$O_{sLSCF} \xrightleftharpoons[k_{ads}]{k_{des}} \frac{1}{2} O_2(gas) + s_{LSCF}$	$v_{(4)} = S_p^{LSCF/gas} \left\{ k_{des} \Gamma \theta_{O_{sLSCF}} - k_{ads} P_{O_2}^{1/2} \Gamma \theta_{sLSCF} \right\}$
Transport phenomena		Conservation equations
	$\vec{i}_{i_o} = -\sigma_{i_o,CGO}^{eff} \times \vec{\nabla} \phi_{CGO}$	$\vec{\nabla} \cdot \vec{i}_{i_o} = +2F(v_{(R1)} + v_{(R3)}) - S_p^{CGO/LSCF} C_{dl} \frac{\partial E}{\partial t}$
	$\vec{N}_{V_o^{\bullet\bullet}} = -\tilde{D}_{chem}^{eff} \times \vec{\nabla} C_{V_o^{\bullet\bullet}}$	$\vec{\nabla} \cdot \vec{N}_{V_o^{\bullet\bullet}} = (v_{(R2)} - v_{(R1)}) - \epsilon_{LSCF} \frac{\partial C_{V_o^{\bullet\bullet}}(z,t)}{\partial t}$
	$\vec{N}_{O_{sLSCF}} = -S_p^{LSCF/gas} D_{O_{sLSCF}} \Gamma \times \vec{\nabla} \theta_{O_{sLSCF}}$	$\vec{\nabla} \cdot \vec{N}_{O_{sLSCF}} = (v_{(R2)} + v_{(R3)} - v_{(R4)}) - S_p^{LSCF/gas} \Gamma \frac{\partial \theta_{O_{sLSCF}}(z,t)}{\partial t}$
	$\vec{V} \cdot \vec{N}_{O_2} = -\frac{RT}{P_t} \left(\frac{N_{O_2}}{D_{k,O_2}^{eff}} + \frac{N_{O_2}^y N_2}{D_{O_2,N_2}^{eff}} \right)$	$\vec{\nabla} \cdot \vec{N}_{O_2} = \frac{1}{2} v_{(R4)} - \frac{\epsilon_{pores}}{RT} P_t \frac{\partial y_{O_2}(z,t)}{\partial t}$
	$\vec{i}_{e^-} = -\sigma_{h_{LSCF}}^{eff} \times \vec{\nabla} \phi_{LSCF}$	$\vec{\nabla} \cdot \vec{i}_{e^-} = -2F(v_{(R2)} + v_{(R3)}) + S_p^{CGO/LSCF} C_{dl} \frac{\partial E}{\partial t}$
Electrolyte		Conservation equation
	Transport phenomenon	Conservation equation
	$\vec{i}_{i_o} = -\sigma_{i_o,CGO}^{eff} \times \vec{\nabla} \phi_{CGO}$	$\vec{\nabla} \cdot \vec{i}_{i_o} = 0$

The set of equations given in Table V.1 was implemented in the mathematical toolbox of COMSOL Multiphysics® software using the external boundary conditions previously detailed in Refs. [Laurencin2015, Hubert2016]. The EIS are calculated in the time domain by applying a sinusoidal perturbation on the ionic current keeping the same conditions than the experiments.

V.2. Experimental results and models validation

V.2.1 Electrochemical measurements

The experimental electrode polarization curves measured at 650°C, 700°C and 750°C under air are provided in Fig. V.3a. As expected, the overpotential is strongly lowered by increasing the temperature meaning that the electrode performances are strongly thermally activated. More interestingly, it can be remarked that the i - η curves recorded at 750°C and 700°C present a symmetrical shape with respect to the OCP. This observation is confirmed by the plots of the polarization resistance R_p as a function of the electrode overpotential at these two temperatures (illustrated in Fig. V.3b at 750°C and V.3c at 700°C). Indeed, the R_p - η curves also exhibit a symmetrical behavior with the same evolution for cathodic or anodic polarization. This characteristic of the macroscopic electrode response suggests that the mechanism for the LSCF-CGO composite could be dominated by the same reaction pathway at 750°C and 700°C whatever the polarizations are. In other words, the steady-state response of the electrode would indicate that there is no change in the reaction mechanism of the LSCF-CGO composite in fuel cell or electrolysis mode.

In contrast to 750°C and 700°C, the i - η and R_p - η curves plotted at 650°C in Fig. V.3a and 3d respectively are clearly dissymmetric. From this observation, it turns out that the global reaction pathway at low temperature could be modified when changing the operating mode from cathodic to anodic polarization.

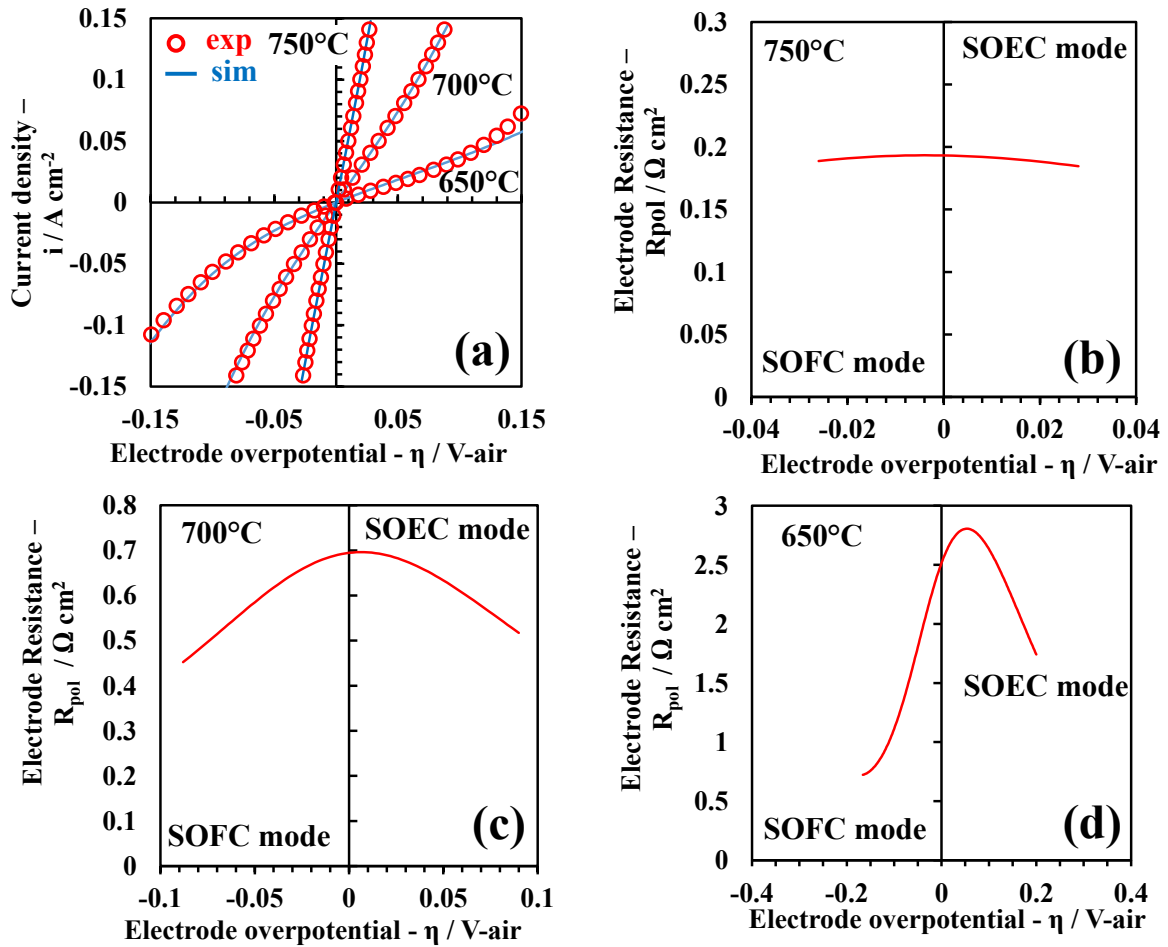


Figure V.3. Experimental and simulated experimental i - η curves at 650°C, 700°C and 750°C under air (a). Experimental electrode polarization resistance plotted as a function of the overpotential at 750°C (b), 700°C (c) and 650°C (d).

The electrochemical impedance diagrams recorded at OCP for the three temperatures under air, are reported in Fig. V.4. When plotted in the Nyquist plan (Fig. V.4a-c), it can be remarked that all the diagrams exhibit a kind of ‘classical’ Gerischer-type element. This general shape of the impedance spectra at OCP has been already highlighted by many other authors for the LSCF-CGO composite electrode [Hwang2005, Leng2008, Mortensen2014, Yurkiv2014, Choi2013]. The frequency distributions of the impedances at OCP are plotted in Fig. V.4d-f in the Bode plan. It can be seen that the frequency peak only slightly increases by increasing the temperature (i.e. $f_c \approx 2$ Hz, 8 Hz and 25 Hz at 650°C, 700°C and 750°C, respectively). This trend is consistent with the evolution of characteristic frequencies reported by Nielsen et al. [Nielsen2011] for a LSCF-CGO electrode (exhibiting a ‘moderate coarse microstructure’ with $f_c \approx 6$ Hz, 12 Hz and 18 Hz at 650°C, 700°C and 750°C, respectively). The fact that both shape and repartition of the frequencies in the impedance spectra are not

strongly affected by the temperature would also suggest that the electrode mechanism at OCP does not change in the investigated temperature range.

As shown in Fig. V.5, impedance diagrams were also recorded under polarization at intermediate temperature (700°C). Even if the impedance diagrams in Nyquist plane appear to be slightly depressed under cathodic polarization, it is worth noting that the global shape does not completely change under the different electrode polarizations. This ‘stability’ of the electrode impedance response under current is radically different to the behavior highlighted for the pure LSCF electrode. In the latter case, it was found the impedance was completely changed from a well-defined Gerischer element at OCP toward a flattened and convoluted semi-circle under anodic current [Monaco2018]. The evolution was explained by a modification of the dominant reaction mechanism passing from a ‘bulk’ to a ‘surface’ path. In the present study, the shape but also the frequency peak (changing from $f_c \approx 6$ Hz at $i_{dc} = -50$ mA cm⁻² to $f_c \approx 10$ Hz at $i_{dc} = +50$ mA cm⁻²: cf. Fig. V.5e–h) are not strongly affected by the polarization. This statement tends to reinforce the claim that only one single reaction mechanism is dominant at this temperature for the LSCF-CGO composite.

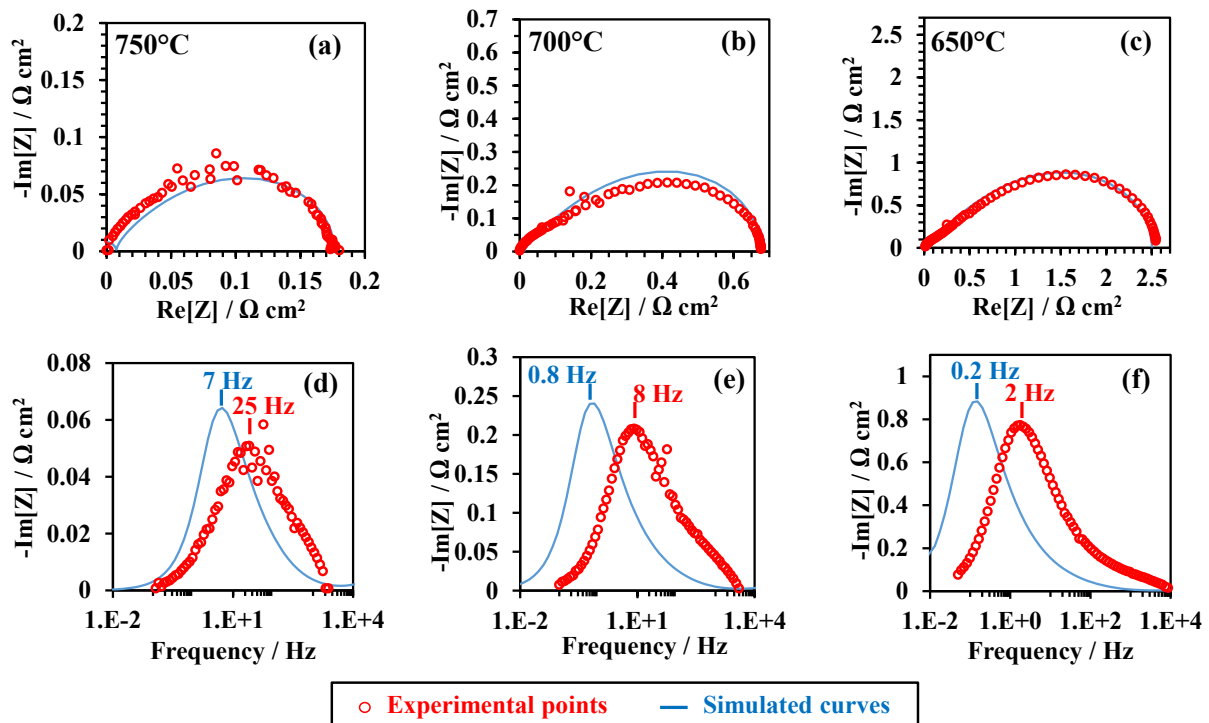


Figure V.4 Nyquist (a) and Bode (b) plots of the experimental and simulated impedance spectra at OCP for T=750°C, 700°C and 650°C.

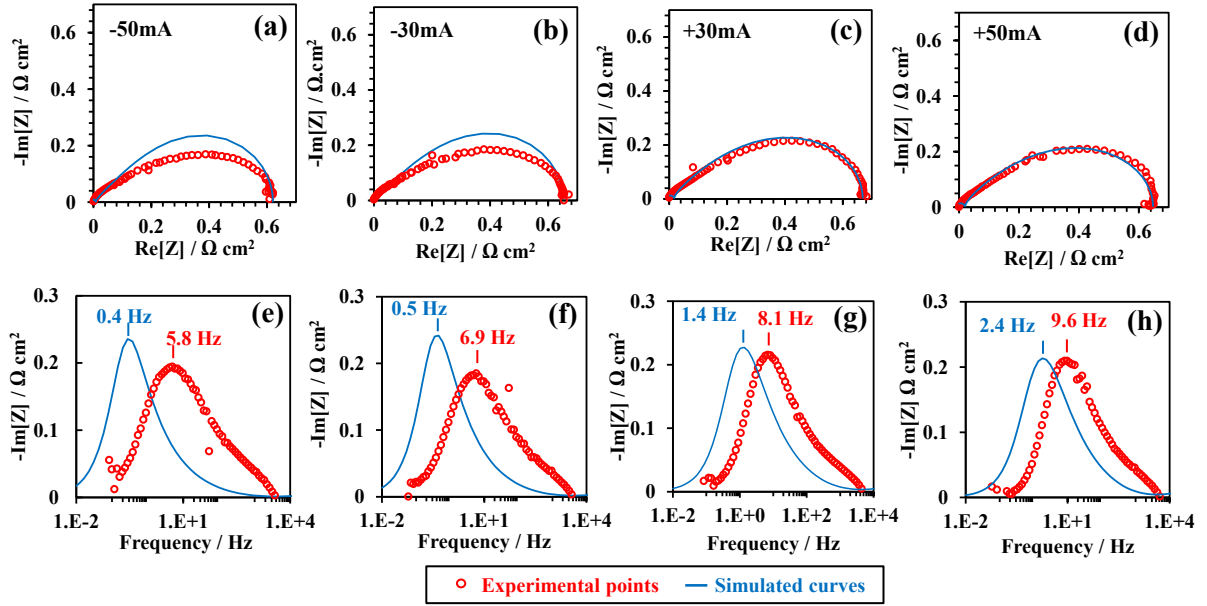


Figure V.5 Nyquist (a) and Bode (b) plots of the experimental and simulated impedance spectra at 700°C for $i_{\text{dc}}=-50 \text{ mA}\cdot\text{cm}^{-2}$, $i_{\text{dc}}=-30 \text{ mA}\cdot\text{cm}^{-2}$, $i_{\text{dc}}=+30 \text{ mA}\cdot\text{cm}^{-2}$, and $i_{\text{dc}}=+50 \text{ mA}\cdot\text{cm}^{-2}$.

V.2.2 Calibration and validation of the electrochemical model

First, it is worth reminding that all the microstructural parameters of the LSCF-CGO composite are identified thanks to the electrode reconstruction (cf. Table II.3). This enables to reduce the number of unknown input parameters of the electrochemical model. Regarding the transport properties used as input data, the oxygen molecular and gas diffusivities are calculated as a function of the temperature with the relations given in Ref. [Laurencin2015]. The ionic and electronic conductivities under air of CGO and LSCF used in the simulations are provided in Table V.2 at 700°C [Tanaka2012]. The evolution of the CGO ionic conductivity with the temperature is taken into account in the model with a thermal activation of 65 kJ mol^{-1} [Tanaka2012]. Regarding the oxygen chemical diffusivity in the LSCF lattice, there is a rather large scattering for the reported values in the literature and the activation energy can spread from 116 to 145 kJ mol^{-1} [Bouwmeester2004, Yashiro2011]. As a consequence, the value given in Table V.2 at 700°C under air was arbitrarily chosen to be consistent with the published data while the activation energy was fixed to an average at 128 kJ mol^{-1} .

For the thermodynamic calculation, the LSCF oxygen under-stoichiometry and the lattice parameter at equilibrium (for a given oxygen partial pressure and temperature) were respectively taken from the data provided by Bouwmeester et al. [Bouwmeester2004] and

Hashimoto et al. [Laurencin2015, Hashimoto2011] (cf. resulting data at 700°C under air in Table V.2). In agreement with the literature [Deseure2005, Gong2012, Svensson1998], a low oxygen coverage rate was assumed on the LSCF surface ($\theta_{LSCF}^{eq} = 10^{-4}$ under $P_{O_2} = 1$ atm leading to $\theta_{LSCF}^{eq} = 4.58 \times 10^{-5}$ under $P_{O_2} = 0.21$ atm: cf. Table V.2). As already discussed by Monaco et al. [Monaco2018], it can be reasonably supposed that the oxygen coverage remains at a very low level over the studied range of temperatures so that its evolution from 650°C to 750°C has been neglected in the present study.

Finally, the reaction of oxygen ionic transfer (R1) across the LSCF/CGO interface has been supposed to be not limiting [Adler2004] and its kinetic constant has been fixed to $k_+ = 50 \text{ mol s}^{-1} \text{ m}^{-2}$ whatever the temperature. For the transient simulations, the capacitance of the LSCF/CGO double layer has been taken to $50 \text{ } \mu\text{F cm}^{-2}$ estimated by Monaco et al. [Monaco2018]. Considering all these input data, the number of unknown parameters for the modeling was drastically reduced. Only the oxygen surface diffusivity and the forward kinetics constants for the reactions of oxygen desorption (R4), excorporation (R2) and charge transfer at TPBLs (R3) were missing.

The four missing parameters have been determined by adjusting in an iterative process the simulated polarization curves on the three experimental i - η curves recorded at 650°C, 700°C and 750°C. Thanks to the non-linear evolution of the current under polarization especially at low temperature, only one single solution for each unknown model parameter was possible to adjust accurately the experiments. The result of the model calibration is shown on Fig. V.3a whereas the values of the fitted data are listed in Table V.3. It can be noticed that the estimated activation energies are quite consistent with the ones previously determined for a pure LSCF electrode (for a temperature range of 700°C-800°C under air) [Monaco2018]. For instance, the activation energy was estimated to 180 kJ mol^{-1} for the oxygen surface diffusivity instead of 179 kJ mol^{-1} in the present study. Nevertheless, it can be pointed out that a substantial lower activation energy for the charge transfer at TPBLs was previously found (of 260 kJ mol^{-1} [Monaco2018]). This apparent discrepancy could be explained by the lowest temperature range in the present study that could exacerbate the role of the thermal activation for the charge transfer at TPBLs. In other word, the global performances of the LSCF-CGO electrode starts to be limited at 650°C as shown in Fig.V.3a.

After the model calibration on the polarization curves, the impedance spectra have been computed in the same conditions as the experiments. The calculated diagrams are compared to the experimental EIS diagrams in Fig. V.4 for the measurements at OCP and in Fig. V.5 for the measurements under dc currents.

Without any additional fitting, it is found that the model is able to accurately predict the shape of the impedance at OCP for the three temperatures in the Nyquist plan (Fig. V.4a–c). The simulated EIS diagrams also capture the evolution of the impedance under dc current even if the ‘flattening’ of the diagram under cathodic polarization was not perfectly reproduced by the model (Fig. V.5a–b). In the Bode plan, a frequency lag between the simulations and the experimental results is clearly highlighted. For a better analysis, the calculated and measured frequency peaks are marked in Fig. V.4d–f and Fig. V.5e–h. It can be seen that the model is able to correctly predict the frequency peak evolution with the temperature and the polarization (the frequency peak increases with increasing the temperature and slightly decreases with the applied dc current). Moreover, the frequency shift is rather limited meaning that simulated and experimental data are lying in the same order of magnitude. However, the origin of this discrepancy is still not clearly understood. It could be due to an uncertainty on the microstructural parameters determination from the 3D reconstruction coming from heterogeneities in the batch of the studied electrodes. Indeed, it has been shown by Nielsen et al. [Nielsen2011] that any change in the microstructure of the composite has a huge impact on the frequency distribution in the impedance spectra. For instance, the characteristic frequency of a LSCF-CGO electrode with a ‘moderate coarse microstructure’ was found equal to 5.6 Hz (at 650°C) while the one measured in the same conditions for a ‘fine microstructure’ increases up to 261 Hz. Nevertheless, it cannot be excluded that the model needs to be improved by taking a more complex reaction pathway of elementary steps to better catch the frequency response of the electrode. Despite this discrepancy on the frequency distribution, it is worth mentioning that the model is able to simulate without any fitting quite correctly the impedance spectra at the different investigated temperatures and polarizations. Therefore, the model can be regarded as validated to be used at least in the same conditions of its calibration and validation (between 650°C to 750°C under air).

Table V.2

Model input parameters at 700°C under air used for the simulations.

Parameter	Value	Units
Maximum oxygen concentration in the LSCF ($C_{O_2}^{\max}$)	83108	mol m ⁻³
Equilibrium oxygen concentration in the LSCF ($C_{O_2}^{\text{eq}}$) at 700°C under air	82491	mol m ⁻³
Bulk electronic conductivity of LSCF ($\sigma_{h,LSCF}$) at 700°C under air	33738	S m ⁻¹
Bulk ionic conductivity of CGO ($\sigma_{io,CGO}$) at 700°C under air	2.9	S m ⁻¹
Oxygen coverage rate at equilibrium ($\theta_{O-SLSCF}^{\text{eq}}$)	4.6 10 ⁻⁰⁵	–
Maximum density of adsorption sites (Γ)	10 ⁻⁰⁵	mol m ⁻²
Double layer capacitance (for EIS modeling) (C_{dl})	0.5	F m ⁻²
Chemical diffusivity at 700°C under air	3.7 10 ⁻¹⁰	m ² s ⁻¹

Table V.3

Model parameters fitted on the i - η curves.

Parameter	700°C	Activation energy (kJ mol ⁻¹)
Oxygen adsorbates diffusion coefficient $D_{O-SLSCF}$ (m ² s ⁻¹)	2.5 10 ⁻⁷	179
Kinetic constant for adsorption (atm ^{-1/2} s ⁻¹)	60	203
Kinetic constant for oxidation at TPBs (m s ⁻¹)	2.3 10 ⁻⁵	475
Kinetic constant for oxygen excorporation (m ³ mol ⁻¹ s ⁻¹)	2.5 10 ⁻⁵	43

V.3. Role of the LSCF-CGO microstructure on the reaction mechanism

V.3.1 Reaction mechanism at 700°C and impact on the electrode performances

As previously discussed in the first chapter, the operating temperature of SOCs needs to be reduced in order to mitigate the associated degradation. In this case, a microstructural optimization is needed to maintain a good performance at intermediate temperatures. For this purpose, the reaction mechanism need to be better understood at around a chosen temperature of 700°C. The full and deep analyses of the reaction mechanism at all the temperatures can be found in the paper published in ‘Fuel Cells’ journal [Effori2019]. As already mentioned in Chapter I, this article is the result of collaboration with the thesis of Elisa Effori.

In order to analyze the reaction mechanism, the ratio of the surface to bulk path has been computed with the electrochemical model (note that the ratio is simply given by the integration of R3 and R2 over the electrode thickness: $ratio = \int_{z=0}^{z=h} \frac{v_{R3}(z)}{v_{R2}(z)} dz$). The result is plotted in Fig. V.7a at 700°C as a function of the current density.

At this temperature, it is found that the ratio increases steeply with increasing the current density. As already analyzed in the previous articles [Laurencin2015, Hubert2016], this evolution is due to the dependence of the electrode polarization with the oxygen content in the MIEC material. Indeed, under cathodic polarization, the LSCF is depleted in oxygen while the oxygen concentration increases above the equilibrium under anodic current. In other words, the LSCF under-stoichiometry (associated to the concentration of oxygen vacancies) decreases with increasing the current density up to vanish at high anodic polarizations. In this condition, the successive steps of (i) the ionic transfer at the CGO/LSCF interface, (ii) the solid-state diffusion and (iii) the oxygen exorporation become bounded altogether so that the bulk path is limited. This behavior induces a decrease of the oxygen concentration adsorbed onto the LSCF surface leading to promote the direct oxidation at TPBLs (cf. expression the kinetic rate in Table V.1). As a consequence, the surface path is strongly favored by increasing the polarization from cathodic to anodic currents as shown in Fig. V.7a.

Nevertheless, in contrast to the LSCF electrode [Monaco2018], it is found that the ratio of the surface to the bulk path is much higher than unity whatever the polarization at 700°C (Fig. V.7a). This result means that, even under cathodic current, the reaction mechanism for the LSCF-CGO composite is fully controlled by the surface path at ‘intermediate’ temperatures ($T \geq 700^\circ\text{C}$). This statement is obviously explained by the extent of the TPBLs into the whole electrode thickness and the possibility for the reaction R3 to spread into the depth of the electrode. Therefore, conversely to the LSCF electrode for which the charge transfer at TPBLs is only restricted at the interface with the electrolyte, the surface path is highly favored by the multiplication of the active sites within the LSCF-CGO electrode. In this condition, it is found that the reaction mechanism at $T=700^\circ\text{C}$ is entirely governed by the surface path. This conclusion coming from the modeling is in perfect line with the experimental results (see section V.2.1) for which it was highlighted that only one single pathway is dominant at temperatures higher than 700°C.

The polarization curve for the studied LSCF-CGO composite and the one obtained for a pure LSCF electrode [Monaco2018] are compared in Fig. V.7b at 700°C under air. As expected, the performances are significantly higher for the composite electrode. For instance, at a current density of $-0.1 \text{ A}\cdot\text{cm}^{-2}$, the electrode overpotential decreases from $-0.17 \text{ V}/\text{air}$ for the LSCF to $-0.05 \text{ V}/\text{air}$ for the LSCF-CGO. As discussed in the introduction, this improvement is explained by the addition of CGO leading to enhance the ionic conductivity of the electrode and to extend the TPBLs in the electrode thickness. Nevertheless, the electrode performance is a combination of several microstructural parameters such as the phase volume fraction, the specific surface area or the density of TPBLs, etc. In order to unravel the impact of each parameter on the electrode response, a sensitivity analysis of the microstructural properties is thus required.

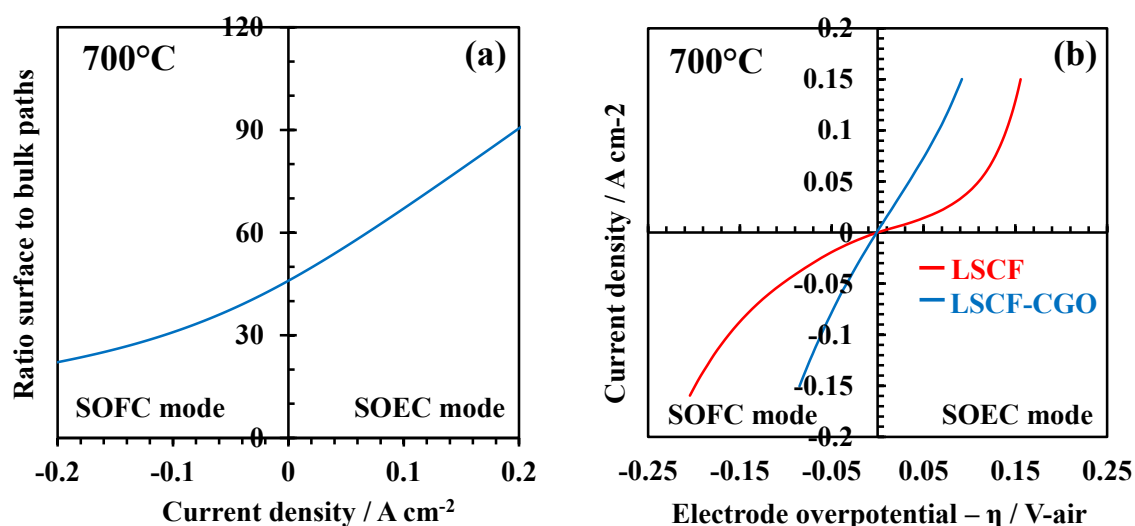


Figure V.7 Ratio of surface to bulk path for the LSCF-CGO electrode under air at 700°C (a) Comparison of the polarization curves at 700°C for the single LSCF [Monaco2018] and the studied LSCF-CGO composite (b).

V.3.2 Role of microstructure on the electrode response: effect of composition, porosity and particle size

To better understand the role of the microstructure on the electrode performance, a dataset of synthetic electrode volumes have been generated with the Random Fields model. In the sensitivity analysis, the tested electrode was taken as reference, while the composition, the porosity and the mean particle size have been changed independently. For instance, the relative phase volume fraction of CGO in the solid phase was modified whereas the electrode

porosity and the Particle Size Distributions (PSDs) were kept constant. In addition, the effect of adding a gradient of composition in the LSCF-CGO electrode was examined subsequently.

In the frame of this sensitivity analysis, the adaptation of the plurigaussian random field model has been employed for its very fast execution time. A dataset of synthetic electrodes with the studied LSCF-CGO composite taken as reference have then been generated, and all the microstructure properties have been then extracted from the 3D volumes and implemented in the electrochemical model to simulate the impedance spectra at OCP. All the present study has been carried out at the intermediate operating temperature for SOCs of 700°C under air (cf. Introduction and chapter I).

V.3.2.1 Effect of electrode composition and porosity

The synthetic microstructures have been computed for two levels of porosity (43.5% corresponding to the reference and 33.3%). For each case, the electrode composition was progressively changed by increasing the CGO volume fraction in the solid phase from 0 vol.% to 92 vol.%. The evolution of the density of active TPBIs, the LSCF/gas specific surface area and the M-factors (i.e. ratio between the effective and bulk conductivities) have been plotted in Fig. V.8 as a function of the volume content of CGO.

As already discussed in the previous chapter, it can be remarked in Fig. V.8a that the density of TPBIs is the largest when the volume fractions of LSCF and CGO in the solid phase are equivalent. A sharp evolution is observed to around 20% and 80% of CGO. Since these values correspond approximately to the percolation thresholds for the CGO and the LSCF networks, the active density of TPBIs drops to zero below and above these two limits. As expected, the CGO effective conductivity decreases with decreasing the CGO content and becomes nil below the percolation threshold (Fig. V.8c). An opposite evolution is obviously found for the LSCF effective conductivity. It can be also noticed that the LSCF/gas specific surface area decreases continuously when decreasing the LSCF content in the solid phase (Fig. V.8b). Besides, when the porosity is changed from 43.5% to 33.3%, the density of TPBIs is significantly increased while the LSCF/gas specific surface area is slightly decreased (Fig. V.8a and 8b). Both evolutions are in good agreement with the microstructural correlations given in the previous chapter. Finally, the effective conductivities for CGO and LSCF are enhanced by decreasing the pore volume fraction (Fig. V.8c).

The electrode polarization resistances determined from the simulated impedance diagrams at OCP are provided in Fig. V.8d as a function of the electrode composition. The plots exhibit a reverse behavior with respect to the density of TPBLs (Fig. V.8a). The correlation between the two curves is explained since the reaction mechanism for the composite electrode is mainly governed by the surface path. In this condition, it is directly dependent on the rate of reaction R3 proportional to the density of TPBLs (Table V.1). Nevertheless, it is worth mentioning that the minimum of the polarization resistance is not found for a composition of LSCF:CGO = 50:50 vol.% which corresponds to the maximum of TPBLs, but it is shifted to around LSCF:CGO = 32:68 vol.% regardless of the porosity value. Indeed, even if some active TPBLs are lost, the increase of CGO content above 50% improves the effective ionic conduction leading to enhance the oxygen transport up the TPBLs. From this point of view, the best compromise for the surface path between optimizing the density of TPBLs and the CGO ionic conduction is identified to around 68 vol.% of CGO.

When approaching the percolation threshold for the LSCF, the polarization resistance tends to an unbounded value (Fig. V.8d). Indeed, the LSCF network starts to lose its connectivity so that the electrode cannot work anymore. Conversely, the polarization resistance reaches a bounded value when the CGO content is equal to zero corresponding to the resistance of the pure LSCF electrode. It can be noticed in Fig. V.8d that adding CGO to a pure LSCF electrode slightly decreases its performances for very low amounts of CGO (vol% CGO<5). Indeed, in this configuration, the CGO network is poorly connected so that its effective ionic conductivity remains nil (Fig. V.8c) while the loss in LSCF/gas surface area (Fig. V.8b) is much more important than the gain in active TPBLs density (Fig. V.8a).

Except for very low CGO content in the composite decreasing porosity from 43.5% to 33.3% yields an overall improvement in the electrode performances (Fig. V.8d). The optimum composition to minimize the polarization resistance is found to be unchanged (to around LSCF:CGO = 32:68 vol.%). At this optimum, the polarization resistance is divided by a factor of ≈ 2 decreasing from $0.51 \text{ } \Omega \cdot \text{cm}^2$ to $0.26 \text{ } \Omega \cdot \text{cm}^2$ at 700°C . At the same composition, the density of active TPBLs and the CGO effective conductivity are increased from 9.5 to $14.5 \text{ } \mu\text{m} \cdot \mu\text{m}^{-3}$ and 0.32 to $1.1 \text{ S} \cdot \text{m}^{-1}$, respectively. This correlation brings new evidence on the predominance of the surface path, and consequently, the critical contribution of the density of TPBLs and the effective ionic conductivity of CGO on the electrode performances.

It can be noticed that the porosity decrease widens the window of electrode composition for which both LSCF and CGO phases are percolated at the same time (as the solid fraction is higher). In this condition, the range for which the composite electrode performance is improved thanks to the surface path (reaction at the active TPBs for the connected phases) is enlarged from $25.96 < \text{vol.}\% \text{ CGO} < 75.39$ (for a porosity of 43.5%) to $17.55 < \text{vol.}\% \text{ CGO} < 78.98$ vol.% (for a porosity of 33.3%).

As already mentioned, an optimum for the two studied porosities has been identified for a composition of LSCF:CGO = 32:68 vol.%. It is worth underlining that this result is in perfect line with the experimental study reported by Kim et al. [Kim2017] on the same LSCF/CGO system (electrodes tested at 700°C but under 100% O₂ with porosities ranging between 32% and 42.5%). Indeed, the authors have identified an optimum in terms of electrode performances for a CGO volume fraction of 70%. The very good agreement between our numerical analyses and the experimental results of Kim et al. [Kim2017] further suggests the full reliability of the modeling approach combining the microstructural computations to the electrochemical simulations.

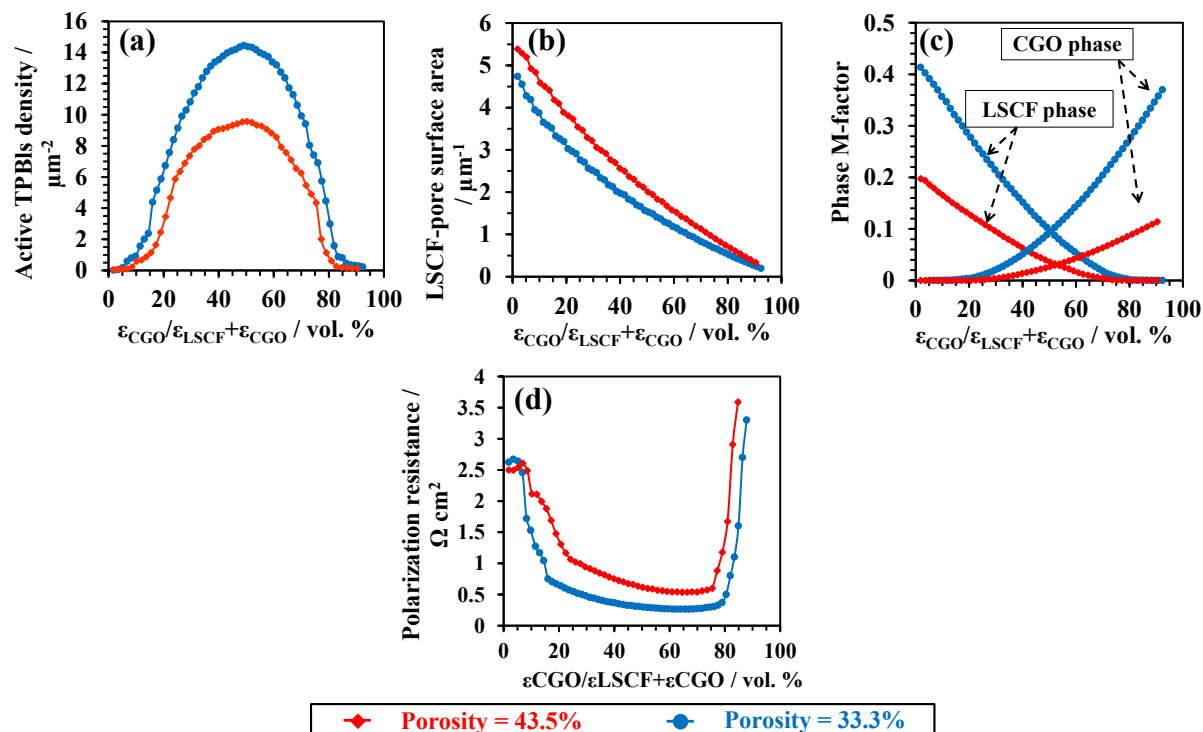


Figure V.8. Active TPB density (a), LSCF/gas specific surface area (b), LSCF and CGO M-factors (c) and electrode polarization resistance (d) as functions of the volume fraction of CGO in the solid-phase (for a porosity=43.5% in red and porosity=33.3% in blue at 700°C).

V.3.2.2 Investigation of the effect of LSCF and CGO particle sizes

The density of TPBls or the specific surface area is dependent on the mean particle size of both electronic and ionic conducting phases [Moussaoui2019]. Since this parameter can be also controlled during the cell manufacturing, the particle size can be tuned to optimize the electrode performances. In the following study, the CGO mean phase diameter was fixed at the reference electrode value of $d_{\text{CGO}} = 0.16 \mu\text{m}$ and the LSCF diameter was changed (while keeping the composition and porosity equal to the reference electrode values). The results of this sensitivity analysis are presented in red in Fig. V.9. A complementary analysis was conducted while fixing the LSCF mean diameter at the reference electrode value of $d_{\text{LSCF}} = 0.19 \mu\text{m}$ and varying the CGO one (curves in blue in Fig. V.9).

As expected from the microstructural correlations in Chapter IV, it is found that the density of TPBls is inversely proportional to the CGO and LSCF mean particle diameters. In other words, a very fine microstructure leads to a high density of TPBls as shown in Fig. V.9a. Still in good agreement with the correlations established in the previous chapter, the LSCF/pore specific surface area is observed to follow the same evolution than the TPBls when changing the LSCF particle size (Fig. V.9b). Moreover, the surface of contact between the LSCF and the gas is independent on the particle size distribution of the ionic conducting material. Finally, the effective ionic conductivity for the CGO network is improved when its mean particle size is increased (Fig. 9c). The same trend is obviously highlighted for the LSCF effective conductivity.

The impact of the mean particle size on the electrode polarization resistance is given in Fig. V.9d. As a general comment, the performances are significantly increased for a finer electrode microstructure. These improvements are mainly ascribed to the higher density of active TPBls despite the lower conductivity of the materials. It can be noticed that the decrease of the polarization resistance is more sensitive to the LSCF particle size than to the CGO one. Indeed, the lowest polarization resistances are reached for the smallest LSCF particles. This result is due to the steep increase of the LSCF/gas specific surface area that favors the surface diffusion and the gas adsorption/desorption for the surface path (Table V.1).

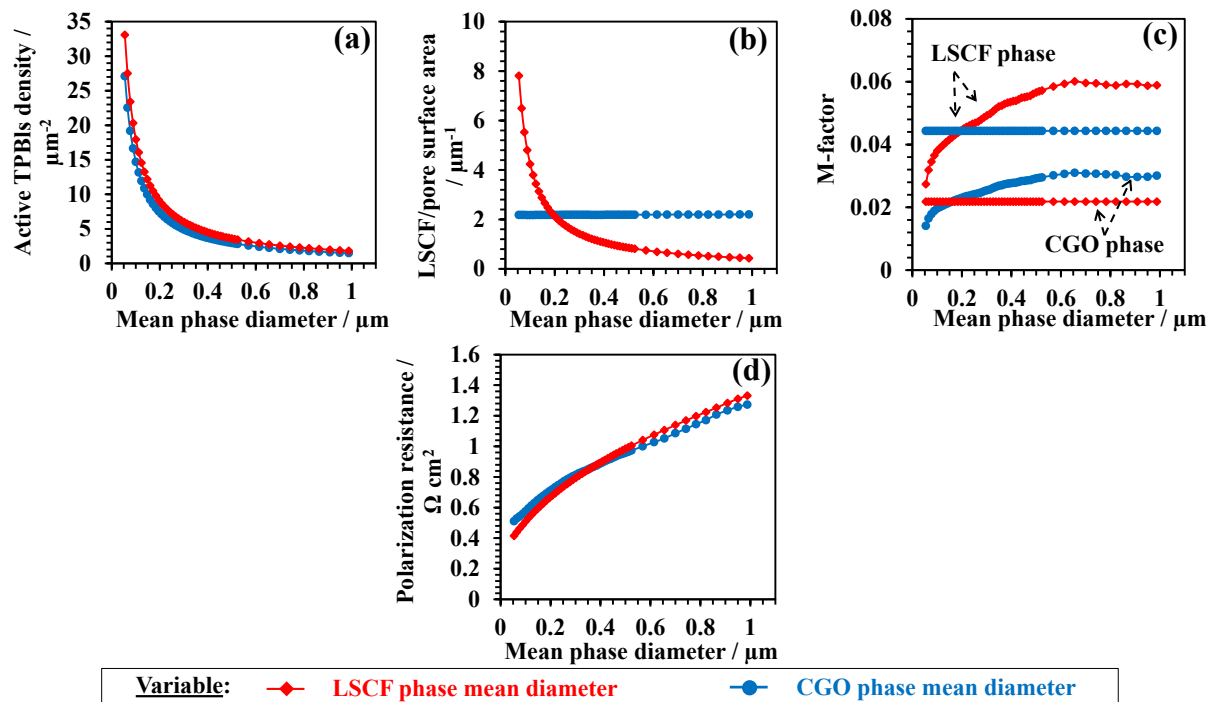


Figure V.9 Active TPB density (a), LSCF/gas specific surface area (b), LSCF and CGO M-factors (c) and electrode polarization resistance (d) as functions of the LSCF mean phase diameter in red and CGO mean phase diameter in blue (with porosity=43.5% and at 700°C under air).

V.4 Conclusion

A coupled experimental and modeling method was used to investigate the reaction mechanism and the role of microstructure for a LSCF-CGO composite used as O₂ electrode in SOCs. The overall approach combines (i) electrochemical testing with a three-electrode setup, (ii) microstructural characterization by FIB-SEM tomography and (iii) an in-house multi-physics modeling. The numerical tool is composed of two modules for the microstructural and the electrochemical modeling. The first one is based on the truncated Gaussian random field method for the generation of representative synthetic electrodes. The second one includes a description of the reaction mechanism in a series of steps divided in two parallel pathways (the surface path and the bulk path). The microstructural model is used to calculate all the microstructural properties as a function of the basic geometrical attributes of the electrode (porosity, composition, particle size distribution) and the electrochemical model allows simulating the stationary and the dynamic response of the electrode versus the electrode microstructure.

Thanks to the knowledge of the electrode microstructural properties detailed in the chapter II, the number of unknown parameters for the electrochemical model was drastically reduced in such a way that only the kinetic constant and the surface diffusivity were missing for the simulations. These data were estimated by fitting the experimental electrode polarization curves with the simulated ones. The model was then validated by comparing the simulated and the experimental impedance spectra.

In our experimental conditions, the electrochemical characterizations have revealed that the LSCF-CGO composite is controlled by the same reaction mechanism at 700°C under air. It has been shown with the simulations that the electrode response at this temperature is fully controlled by the charge transfer at TPBIs (surface path). The integrated modeling approach has been employed to unravel the role of microstructure on the electrode performances. A large dataset of synthetic microstructures was generated by changing the electrode composition, the porosity and the particle size. All the properties computed on the 3D volumes were introduced in the electrochemical model. The simulations have shown that the electrode performances are mainly controlled by the density of TPBIs and the effective ionic conductivity of the CGO network. Moreover, an optimum in terms of electrode polarization resistance has been identified for a composition of LSCF:CGO = 32:68 vol.%. The performances are also improved by decreasing the porosity from 43% to 33% and for a fine particle size distribution of the LSCF network into the CGO backbone. All these statements constitute a set of guidelines to improve the efficiency of the promising LSCF-CGO electrode.

Conclusions & Perspectives

This section provides a brief summary of the results and the main findings of this work. Furthermore, a discussion about their generalization to other applications is given and different perspectives are proposed.

The main objective of this thesis was to improve the understanding of how Solid Oxide Cells (SOCs) microstructure controls their performance, with the purpose of optimizing them. Indeed, the durability of SOCs is the main technological lock towards their industrial deployment. As the degradation mechanisms are found to be thermally activated, lowering the operating temperature (from $\sim 800^{\circ}\text{C}$ to $600\text{-}700^{\circ}\text{C}$) has recently attracted an increasing interest. Nevertheless, as the activation losses are particularly exacerbated with the temperature decrease, some cell improvements are necessary to maintain high performances at these ‘intermediate’ temperatures. In this condition, a microstructural optimization is necessary to bring back the cell performance to the industry requirement level.

For this objective, an integrated multi-scale and multi-disciplinary approach, coupling advanced 3D characterization, experimental tests and numerical modeling, was adopted to understand the microstructural correlations and to link the electrode microstructure to its electrochemical performance.

Four distinct, but complementary, domains can be identified in the proposed methodology, which correspond to the main milestones of this work: ‘3D characterization and geometrical modeling’, ‘microstructural correlations’, ‘ O_2 electrode electrochemical modeling’, and ‘microstructural optimization’. A brief summary of the main findings will be provided for each section, then some perspectives are proposed.

‘3D characterization and geometrical modeling’ - The first step towards this objective was to perform a fine 3D microstructural characterization of the studied electrodes and to develop a stochastic geometrical tool able to mimic the specific morphology of these porous media. In this frame, state-of-the-art imaging techniques have been used to reconstruct several commercial and fabricated cells. Then a number of in-house multi-scale methods have been used, or adapted, to process the raw reconstructions and extract all the relevant morphological and physical properties from the identified phases. A special focus has been paid to the H_2 electrode substrate, for which the macropores have been separated from the microporosity

network and analyzed meticulously, for the first time. This allowed separating the contribution of each porosity length scale to the electrode diffusion process. As the image reconstruction and processing techniques are very time- and -resources consuming procedures, two numerical tools have been developed to generate synthetic but realistic microstructures. The proposed methods are based on two different considerations; the first one is built on an original particle-based algorithm, while the second one is founded on the Random Fields method from geostatistics. This difference was necessary to obtain two approximations of the same media and thus to make sure that the drawn conclusions do not depend on the chosen model. The validation of both models on the reconstructed two- and three-phase electrodes showed that the numerical volumes mimic quite accurately all the morphological and physical properties of the electrodes. Nevertheless, both tools fell short from perfectly retrieving the high constrictivities of the phases with low volume fractions, and thus close to the percolation threshold. Finally, the models flexibility to generate ‘non classical’, but promising, electrode architectures was discussed and illustrated for different cases (graded electrodes, diffusion layers, impregnated electrodes, etc.).

Naturally, the first perspective to this part is to address the common ‘limitation’ of both models concerning high constrictivities simulation. In this frame the morphological evolution of a phase close to its percolation threshold should be meticulously examined. For example, the Euler-Poincaré characteristic could be computed at the edge of this threshold, for real and synthetic volumes, to investigate the eventual change in phase topology. Once the problem is clearly identified, the models need to be adapted accordingly. A second perspective would be to introduce some spatial heterogeneities in the synthetic microstructures as it was detected in some real reconstructions [Grew2010]. In this case, a local thresholding or a non-stationarity should be introduced in the proposed Random Fields model, while a heterogeneous seeds allocation could be chosen by using the original sphere-packing method. A third perspective would be to generate representative 3D microstructures based on 2D cross sectional images. Indeed, all the models input data can be estimated on a 2D image. The Representative Surface Element (RSE) size, for which a good statistics are obtained, should be identified in the same way as the Representative Volume Element (RVE) size identification. This tool could be very beneficial as it could reduce drastically the number of time-consuming 3D tomographic reconstructions in an experimental work. A fourth and last perspective in this section is the generation of other ‘non-classical’ microstructures, like partially impregnated electrodes [Jiang2005, Wang2006, Wei2007, Zhao2009, Meng2014] (by using both models combination

for example), or some promising nano-fiber based electrodes [Hieu2012, Enrico2014, Lubini2017].

'Microstructural correlations' – The concept of “extended” microstructure has been applied to express the correlations relating the ‘key’ microstructural properties (TPBLs density and S_{ij}), controlling the electrochemical response, to the ‘basic’ parameters of the microstructure (composition, porosity, and particle size), which can be linked to the characteristics of the powders before sintering. The novel semi-analytical equations have been calibrated by using two sets of synthetic microstructures generated by using the previously developed models. The validation of these relationships on several tomographic reconstructions showed that they are able to capture all the evolutions in terms of porosity, electrode composition and mean phase diameters. These findings provide therefore clear insights for a microstructural optimization of electrodes manufactured by ‘classical’ routes of screen-printing or tape casting.

As a perspective to this work, the correlations could be extended to physical properties like transport and mechanical parameters. Either analytical or phenomenological relationships could be used in this frame, and the previously available dataset of synthetic microstructures could be used for the equations calibration. Besides, the same procedure could be applied to investigate the microstructural correlations for ‘non-classical’ promising architectures, like impregnated electrodes.

'O₂ electrode electrochemical modeling' - An in-house electrochemical model has been used to investigate the reaction mechanisms for the LSCF-CGO composite used as O₂ electrode material. For this purpose, a symmetrical cell has been manufactured and electrochemically tested in terms of stationary polarization curves ($i-V$) and Electrochemical Impedance Spectroscopy (EIS). These experimental results along with the 3D microstructural characterization data allowed fitting the model on the $i-V$ curves and thus identifying the kinetic constants and the surface diffusivity that were missing for the simulations. Without any additional fitting, the model has been shown to reproduce quite accurately the impedance diagrams recorded at different temperatures and polarizations. Thanks to this result, the model was considered validated. It was then shown with the simulations that the electrode response is fully controlled by the charge transfer at TPBLs (surface path) for a chosen temperature of 700°C, while the oxygen incorporation at the surface of the LSCF particles (bulk path) is

negligible. The underlying phenomena at the origin of this electrode behavior were also discussed.

In terms of perspectives to this work, as a slight shift has been obtained on the frequency distribution of the simulated EIS diagrams, it could be interesting to investigate the origin of this mismatch. A plausible track could be an uncertainty in the microstructural parameters, or an imprecision in the proposed reaction mechanisms. Therefore, it could be worth proposing a full elementary reactions model. Moreover, it could be interesting as well to examine the effect of other operating conditions like O₂ partial pressure. Besides, this methodology could be applied as well for other O₂ electrode materials like Nickelates, or for the H₂ electrode classically made of Ni-YSZ.

'Microstructural optimization' - The integration of the stochastic geometrical and electrochemical modeling enabled the investigation of the role of microstructure on the electrode performances. It was shown that the electrode performances are mainly controlled by the density of TPBLs and the effective ionic conductivity of the CGO network. Moreover, an optimum in terms of electrode polarization resistance has been identified for a composition of LSCF:CGO = 32:68 vol.%. The performances are also improved by decreasing the porosity from 43% to 33% and for a fine particle size distribution of the LSCF network into the CGO backbone. All the statements constitute a set of guidelines to improve the efficiency of the LSCF-CGO electrode. These recommendations are currently used by the cell manufacturing laboratory to increase the electrode performances. A work is still in progress to assess the real gain with respect to the studied reference electrode.

An outlook to this optimization section is to address 'non-classical' but promising LSCF-CGO electrode architectures. This includes the impregnated electrodes, graded electrodes (in terms of composition, porosity or particle size), or a diffusion layer with a bimodal pore-size distribution. Moreover, besides the electrochemical optimization, other criteria could be taken into account like mechanical robustness and degradation overtime. This last point will allow conducting a time dependent optimization and thus identifying a global optimum for all the electrode life span. Furthermore, the proposed methodology could be applied as well for other electrode materials. For instance, the same procedure could be applied for the optimization of the O₂ composite electrodes made of Nickelates and CGO. Moreover, the optimization of the cermet Ni-YSZ could be particularly interesting. Indeed, the classical cermet is subjected to Ni coarsening and volatilization upon steady-state operation. Moreover, micro-cracking in the

electrode can occur after (i) partial Ni (re)oxidation and (ii) thermal cycling. This damaging could become more problematic when decreasing the thickness of the Ni-YSZ substrate (used as support for the cell). Therefore, a tradeoff between robust but also stable microstructure upon steady-state operation must be identified.

Appendix

A.1 Expression of the correlation $\rho_X(h)$ as a function of the weight function $\omega(h)$

By definition, the correlation function $\rho_X(h)$ is the covariance of the random field $G_X(z)$:

$$\rho_X(h) = \text{cov}\{G_X(z), G_X(z+h)\} \quad (\text{A1})$$

Since G_X is defined as the convolution of an uncorrelated Gaussian random noise $U(z)$ with the weight function $\omega(h)$ (cf. eq. (7)), $\rho_X(h)$ can be expressed as follows:

$$\rho_X(h) = \text{cov}\left\{ \sum_{h_1 \in \Omega} U(z-h_1)\omega(h_1), \sum_{h_2 \in \Omega} U(z+h-h_2)\omega(h_2) \right\} \quad (\text{A2})$$

Considering the basic linear property of the covariance, the previous equation can be rewritten as follows:

$$\rho_X(h) = \sum_{h_1 \in \Omega} \sum_{h_2 \in \Omega} \omega(h_1)\omega(h_2) \text{cov}\{U(z-h_1), U(z+h-h_2)\} \quad (\text{A3})$$

The covariance of the random noise is equal to 1 if $h_1 = h_2 - h$ and 0 otherwise. Besides, considering the symmetry of the weight function ($\omega(h) = \omega(-h)$), Eq. (A4) becomes:

$$\rho_X(h) = \sum_{h_2 \in \Omega} \omega(h_2 - h)\omega(h_2) = (\omega * \omega)(h) \quad (\text{A4})$$

A.2 Relation between $C_X(h)$, $\rho_X(h)$ and λ_X

The covariance $C_X(h)$ is defined as follows:

$$C_X(h) = P(z \in X, z+h \in X) = \int_{\lambda_X}^{+\infty} \int_{\lambda_X}^{+\infty} p(x_1, x_2) dx_1 dx_2 \quad (\text{A5})$$

Where $p(x_1, x_2)$ is the bivariate distribution or probability density function given by:

$$p(x_1, x_2) = \frac{1}{2\pi\sqrt{1-\rho^2}} \exp\left\{ -\frac{(x_1^2 + x_2^2 + 2\rho x_1 x_2)}{2(1-\rho^2)} \right\} \quad (\text{A6})$$

It can be easily demonstrated that $\frac{\partial p}{\partial \rho} = \frac{\partial^2 p}{\partial x_1 \partial x_2}$ and then:

$$\frac{\partial C_X(h)}{\partial \rho} = \int_{\lambda_X}^{+\infty} \int_{\lambda_X}^{+\infty} \frac{\partial^2 p(x_1, x_2)}{\partial x_1 \partial x_2} dx_1 dx_2 = p(\lambda_X, \lambda_X) \quad (\text{A7})$$

The integration of the previous equation, $\int_{r=1}^{r=\rho} \frac{\partial C_X(h)}{\partial \rho} dr = \int_{r=1}^{r=\rho} p(\lambda_X, \lambda_X) dr$, leads to the relation used in the method:

$$C_X(h) - \varepsilon_X = \frac{1}{2\pi} \int_1^{\rho_X(h)} \frac{1}{\sqrt{1-r^2}} \exp\left\{\frac{-\lambda_X^2}{1+r}\right\} dr \quad (\text{A8})$$

A.3 Correlations for the specific surface area between the electronic and pore phases

In Fig. S1, the electronic/pore interfacial surface area calculated with (IV.16a) is confronted to the data measured on the RF and SP microstructures. The correlation allows reproducing the dependencies of the property with the porosity, the electrode composition and the mean phase diameters (Fig. S1).

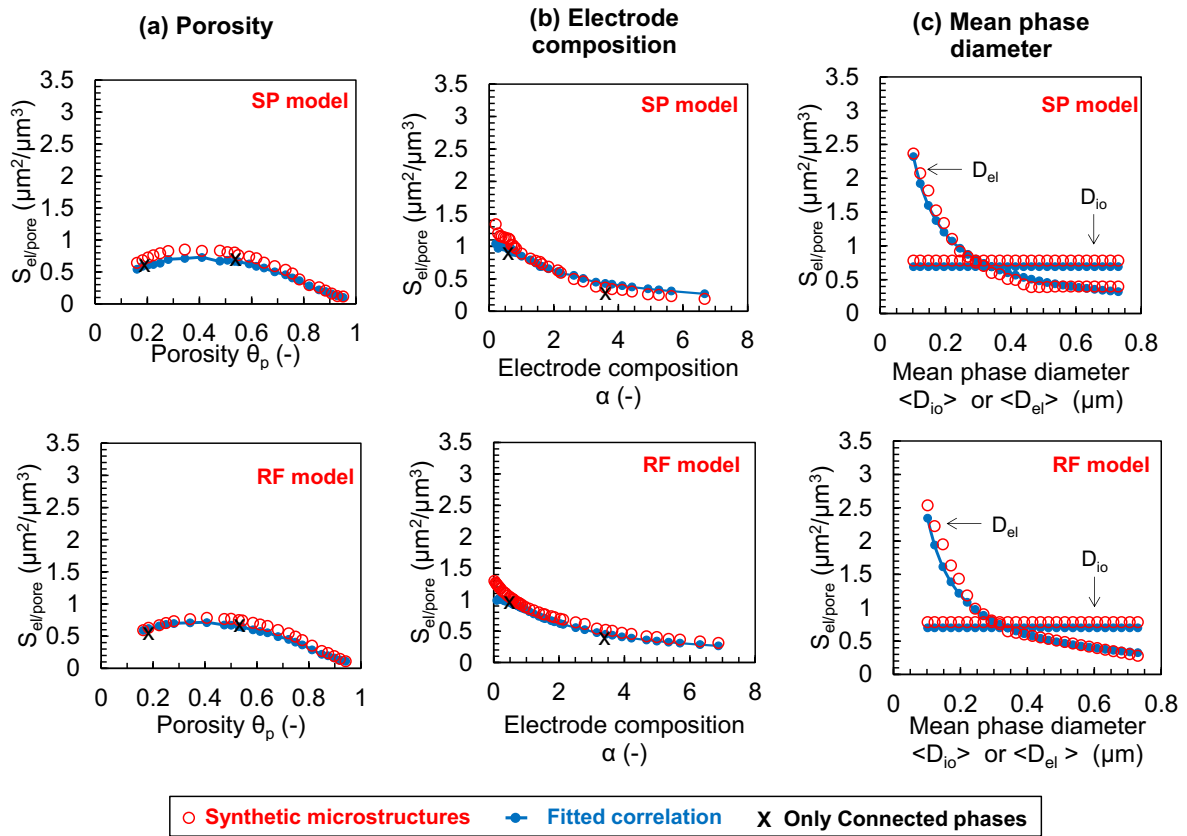


Fig. A1: Comparison between the specific interfacial surface area $S_{el/p}$ calculated with the correlation (eq. IV. 16a) and the data measured on the 3D volumes generated by the RF and SP models. The surface area $S_{el/p}$ is plotted versus the porosity (a), the electrode composition (b) and the mean phase diameters (c). The crosses indicate the values for $S_{el/p}$ calculated with (eq. IV. 16a) considering only the connected phases (for θ_{Ni} , θ_{YSZ} or $\theta_p = 0.18$). The scaling parameter β_{el} in (eq. IV. 16a) has been fitted to $\beta_{el}^{RF} = 2.476$ and $\beta_{el}^{SP} = 2.454$ on the RF and SP microstructures, respectively.

A.4 Correlations for the Triple Phase Boundary lengths TPBIs density

In Fig. S2, the density of TPBI calculated with (Eqn. IV.4) is confronted to the data measured on the RF and SP microstructures. The correlation allows reproducing the dependencies of the property with the porosity, the electrode composition and the mean phase diameters (Fig. S2).

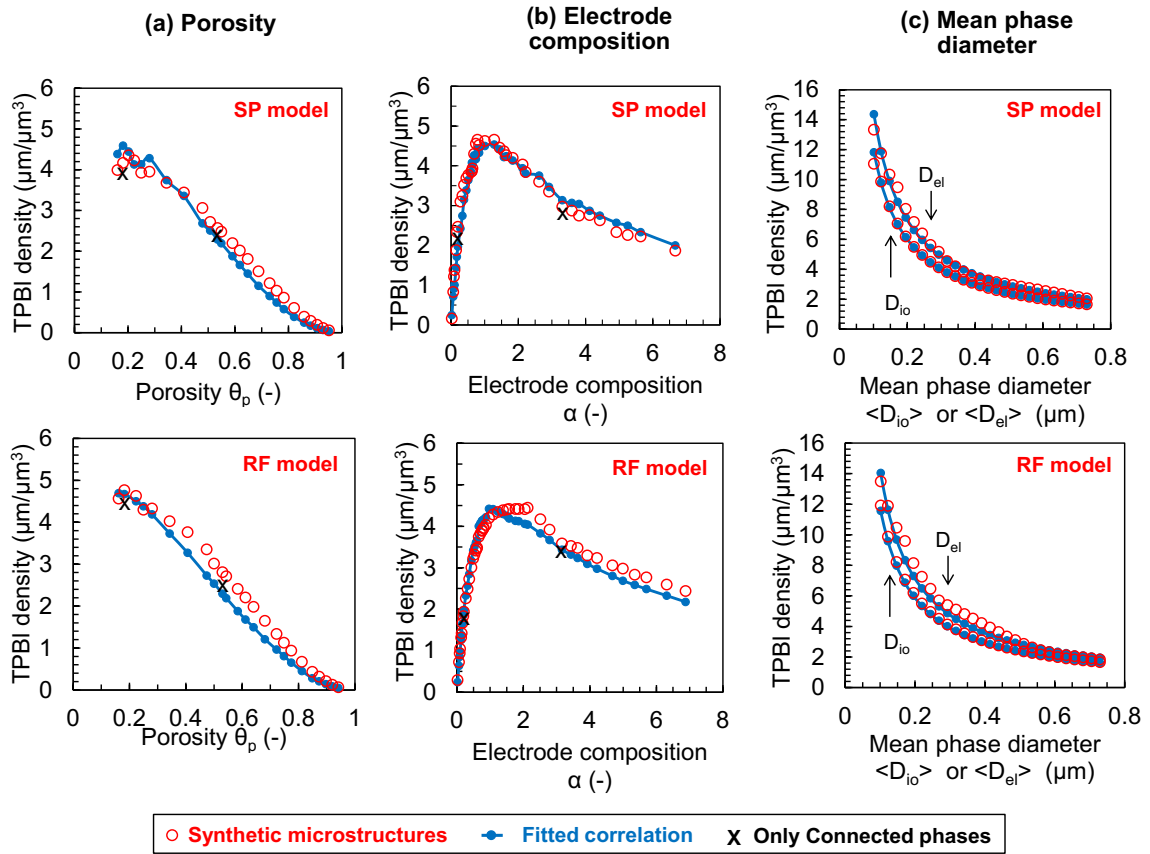


Fig. A2: Comparison between the density of TPBI L_{TPB} calculated with the correlation (eq. IV.4) and the data measured on the 3D volumes generated by the RF and SP models. The density of TPBI L_{TPB} is plotted versus the porosity (a), the electrode composition (b) and the mean phase diameters (c). The crosses indicate the values for L_{TPB} calculated with (eq. IV.4) considering only the connected phases (for θ_{Ni} , θ_{YSZ} or $\theta_p = 0.18$).

References

- [Aarberg1998] R. J. Aaberg, R. Tunold, M. Mogensen, R. W. Berg, R. Ødegaard, "Morphological Changes at the Interface of the Nickel-Yttria Stabilized Zirconia Point Electrode", *Journal of The Electrochemical Society* 145(7) (1998) 2244-2252
- [Abdallah2016] B. Abdallah, F. Willot, D. Jeulin, *J. Microscopy*, 263(1) (2016) 51-63.
- [Abe2006] H. Abe, K. Murata, T. Fukui, W.-J. Moon, K. Kaneko, M. Naito, Microstructural control of Ni-YSZ cermet anode for planer thin-film solid oxide fuel cells, 496 (2006) 49-52.
- [Abrahamsen1997] P. Abrahamsen, A review of Gaussian random fields and correlation functions, Research Council of Norway, 1997.
- [Adijanto2011] L. Adijanto, R. Kungas, F. Bidrawn, R. J. Gorte, J. M. Vohs, "Stability and performance of infiltrated La_{0.8} Sr_{0.2} Co_x Fe_{1-x} O₃ electrodes with and without Sm_{0.2} Ce_{0.8} O_{1.9} interlayers", *Journal of Power Sources* 196(14) (2011) 5797-5802
- [Alder1990] P.M. Alder, C.G. Jacquin, J.A. Quiblier, *Int. J. Multiphase Flow*, 16 (July-August (4)) (1990) 691-712.
- [Adler96] S.B. Adler, J.A. Lane, B.C.H. Steele, *Electrode Kinetics of Porous Mixed-Conducting Oxygen Electrodes*, *J. Electrochem. Soc.* 143 (1996) 3554-3564.
- [Adler2004] S.B. Adler, *Chem. Rev.*, 2004, 104, 4791.
- [Adler2010] R.J. Adler, *The geometry of random fields*, *Classics in applied mathematics*, Siam, 2010.
- [Aicart2014] J. Aicart, J. Laurencin, M. Petitjean, L. Dessemond, "Experimental Validation of Two-Dimensional H₂O and CO₂ Co-Electrolysis Modeling", *Fuel Cells* 14(3) (2014) 430-447
- [Ali2008] A. Ali, X. Wen, K. Nandakumar, J. Luo, K.T. Chuang, *J. Power Sources*, 185 (2008) 961-966.
- [Anandakumar2010] G. Anandakumar, N. Li, A. Verma, P. Singh, J.-H. Kim, *J. Power Sources*, 195 (2010) 6659-6670.
- [Anderson2004] M.D. Anderson, J.W. Stevenson, S.P. Simner, *J. Power Sources* 2004, 129, 188.
- [Armstrong2011] M. Armstrong, A. Galli, H. Beucher, G. Le Loc'h, D. Renard, B. Doligez, R. Eschard, F. Geffroy, *Plurigaussian Simulations in Geosciences*, Springer Heidelberg Dordrecht London New York, 2011
- [Avrami2039] M. Avrami, *Kinetics of Phase Change. I: General Theory*, *The Journal of Chem. Phys.*, 7 (1939) 1103-1112.
- [Avrami1940] M. Avrami, *Kinetics of Phase Change. II: Transformation-Time Relations for Random Distribution of Nuclei*, *The Journal of Chem. Phys.*, 8 (1940) 212-224.
- [Avrami1941] M. Avrami, *Kinetics of Phase Change. III: Granulation, Phase Change, and Microstructure*, *The Journal of Chem. Phys.*, 9 (1941) 177-184.
- [Amitai2017] S. Amitai, A. Bertei, R. Blumenfeld, Theory-based design of sintered granular composite triples three-phase boundary in fuel cells, *Physical review E*, 96 (2017) 052903 1-10.

- [Baniassadi2011] M. Baniassadi, H. Garmestani, D.S. Li, S. Ahzi, M. Khaleel, X. Sun, *Acta Mater.*, 59 (2011) 30-43.
- [Bernadet2015] L. Bernadet, G. Gousseau, A. Chatroux, J. Laurencin, F. Mauvy, M. Reytier, *Int. J. of Hydrogen Energy*, 40 (2015) 12918-12928.
- [Bathia1985] S.K. Bathia, *J. Catalysis*, 93 (1985) 192-196
- [Bertei2011] A. Bertei, C. Nicolella, Percolation theory in SOFC composite electrodes: effects of porosity and particle size distribution on effective properties, *J. Power Sources*, 196 (2011) 9429-9436.
- [Bertei2012] A. Bertei, H.-W. Choi, J.G. Pharoah, C. Nicolella, *Powder Tech.*, 231 (2012) 44-53.
- [Bertei2013] A. Bertei, B. Nucci, C. Nicolella, *Chemical Engineering Science*, 101 (2013) 175-190.
- [Bidrawn2011] F. Bidrawn, R. Küngas, J.M. Vohs, R.J. Gorte, *J. Electrochem. Soc.*, 158(5) (2011) B514-B525.
- [Blum2013] L. Blum, U. Packbier, I. C. Vinke, L. G. J. de Haart, "Long-Term Testing of SOFC Stacks at Forschungszentrum Jülich", *Fuel Cells* 13(4) (2013) 646-653
- [Bouwmeester2004] H.J.M. Bouwmeester, M.W. Den Otter, B.A. Boukamp, *J. Solid State Electrochem.* 2004, 8, 599.
- [Borglum2015] B. P. Borglum, H. Ghezal-Ayagh, "Development of Solid Oxide Fuel Cells at Versa Power Systems and FuelCell Energy", *ECS Transactions* 68(1) (2015) 89-94
- [Brandon2004] N. P. Brandon, A. Blake, D. Corcoran, D. Cumming, A. Duckett, K. El-Koury, D. Haigh, C. Kidd, R. Leah, G. Lewis, C. Matthews, "Development of metal supported solid oxide fuel cells for operation at 500–600 C", *Journal of Electrochemical Energy Conversion and Storage* 1(1) (2004) 61-65
- [Brisse2008] A. Brisse, J. Schefold, M. Zahid, "High temperature water electrolysis in solid oxide cells", *International Journal of Hydrogen Energy* 33(20) (2008) 5375-5382 177
- [Cai2011] Q. Cai, C.S. Adjiman, N. Brandon, *Electrochimica Acta*, 56 (2011) 5804-5814.
- [Çelikbilek2016] Ö. Çelikbilek, D. Jauffrès, E. Siebert, L. Dessemond, M. Burriel, C.L. Martin, E. Djurado., *J. Power Sources* 2016, 333, 72.
- [Chan2004] S.H. Chan, X.J. Chen, K.A. Khor, Cathode micromodel of solid oxide fuel cell, *J. Electrochem. Soc.*, 151 (2004) A164-A172.
- [Chen2010] X. Chen, Y. Zhen, J. Li, S. P. Jiang, "Chromium deposition and poisoning in dry and humidified air at (La 0.8 Sr 0.2) 0.9 MnO 3+ δ cathodes of solid oxide fuel cells", *International Journal of Hydrogen Energy* 35(6) (2010) 2477-2485
- [Chen2011] D. Chen, L. Lu, J. Li, Z. Yua, W. Kong, H. Zhu, Percolation micro-model to predict the effective properties of the composite electrode with poly-dispersed particle sizes, *J. Power Sources* 196 (2011) 3178-3185.
- [Chen2013] D. Chen, H. He, D. Zhang, H. Wang, M. Ni, *Energies*, 6 (2013) 1632-1656.
- [Choi2011] H.-W. Choi, D. Gawel, A. Berson, J.G. Pharoah, K. Karan, *ECS Trans.*, 35(1) (2011) 997-1005.
- [Choi2013] M.-B. Choi, B. Singh, E.D. Wachsman, S.-J. Song, *J. Power Sources* 2013, 239, 361.

- [Cooper2014] S.J. Cooper, D.S. Eastwood, J. Gelb, G. Damblanc, D.J.L. Brett, R.S. Bradley, P.J. Withers, P.D. Lee, A.J. Marquis, N.P. Brandon, P.R. Shearing, *J. Power Sources*, 247 (2014) 1033-1039.
- [Costamagna1998] P. Costamagna, P. Costa, V. Antonucci, *Micro-modelling of solid oxide fuel cell electrodes*, *Electrochimica Acta*, 43 (1998) 375-394.
- [Cronin2013] J.S. Cronin, Y.C.K. Chen-Wiegart, J. Wang, S.A. Barnett, *J. Power Sources* 233 (2013) 174–179.
- [Delette2013] G. Delette, J. Laurencin, F. Usseglio-Viretta, J. Villanova, P. Bleuet, E. Lay, T. Le Bihan, *Inter. J. Hydrogen Energy*, 38 (2013) 12379-12391.
- [Deseure2005a] J. Deseure, L. Dessemond, Y. Bultel, E. Siebert, *J. Euro. Ceram. Soc.*, 25 (2005) 26-73-2676.
- [Deseure2005b] J. Deseure, Y. Bultel, L. Dessemond, E. Siebert, *Solid State Ionics* 2005, 176, 235.
- [Ding2014] D. Ding, X. Li, S.Y. Lai, K. Gerdes, M. Liu, *Energy Environ. Sci.*, 7 (2014) 552-575.
- [Duhamel1990] Duhamel, P. and M. Vetterli, "Fast Fourier Transforms: A Tutorial Review and a State of the Art," *Signal Processing*, Vol. 19, April 1990, pp. 259-299.
- [Dusastre1999] V. Dusastre, J.A. Kilner, *Optimisation of composite cathodes for intermediate temperature SOFC applications*, *Solid State Ionics*, 126 (1999) 163-174.
- [Effori2019] E. Effori, H. Moussaoui, F. Monaco, J. Debayle, Y. Gavet, G. Delette, E. Siebert, J. Vulliet, B. Morel, L. Dessemond, J. Laurencin, accepted in 'Fuel Cells'.
- [Faes2009] A. Faes, A. Hessler-Wyser, D. Presvytes, C. G. Vayenas, *Nickel–zirconia anode degradation and triple phase boundary quantification from microstructural analysis*, *Fuel cells* 9(6) (2009) 841-851.
- [Fu2007] C. Fu, K. Sun, N. Zhang, X. Chen, D. Zhou, *Electrochim. Acta* 2007, 52, 4589.
- [Gaiselmann2014] G. Gaiselmann, M. Neumann, V. Schmidt, O. Pecho, T. Hocker, L. Holzer, *AIChE Journal*, 60(6) (2014) 1983-1999.
- [Gostovic2007] D. Gostovic, J.R. Smith, D.P. Kundinger, K.S. Jones, E.D. Wachsmann, *Electrochem. Solid State Letters*, 10(12) (2007) B214-B217.
- [Enrico2018] Anna Enrico, Wenjing Zhang, Marie Lund Traulsen, Elena Marzia Sala, Paola Costamagna, Peter Holtappels, *Journal of the European Ceramic Society* Volume 38, Issue 7, July 2018, Pages 2677-2686.
- [Epstein1989] N. Epstein, *Chem. Eng. Sci.*, 44(3) (1989) 77-779.
- [Galli1994] A. Galli, H. Beucher, G. Le Loc'h, B. Doligez, In "Geostatistical simulations", Ed. by M. Armstrong and P.A. Dowd, *Quantitative Geology and Geostatistics: vol. 7*, Springer Science+Business Media Dordrecht, 1994, 217-233.
- [Gao2016] Z. Gao, L. V. Mogni, E. C. Miller, J. G. Railsback, S. A. Barnett, "A perspective on low-temperature solid oxide fuel cells", *Energy & Environmental Science* 9(5) (2016) 1602-1644
- [Gelb1999] L.D. Gelb, K.E. Gubbins, *Pore size distributions in porous glasses: a computer simulation study*, *Langmuir*, 15 (1999) 305-308.
- [Ghezel2013] H. Ghezel-Ayagh, "Advances in SOFC Development at FuelCell Energy ", 14th Annual SECA Workshop Pittsburgh (2013)
- [Godula-Jopek2015] A. Godula-Jopek, "Hydrogen Production by Electrolysis", Wiley, 2015.

- [Gokhale1980] A.M. Gokhale, C.V. Iswaran, R.T. Dehoff, Application of microstructure modelling to the kinetics of recrystallization, *Metall. Trans. A*, 11A (1980) 1377-1383.
- [Gokhale1984] A.M. Gokhale, A test for randomness of the spatial distribution of particles during phase transformation, *Metall. Trans. A*, 15A (1984) 243-245.
- [Gokhale1909] A.M. Gokhale, S. Zhang, M. Liu, *J. Power Sources*, 194 (2009) 303-312.
- [Golbert2008] J. Golbert, C.S. Adjiman, N. Brandon, *Ind. Eng. Chem. Res.*, 47 (2008) 7693-7699.
- [Gong2012] M. Gong, R.S. Gemmen, X. Liu, *J. Power Sources* 2012, 201, 204.
- [Graves2015] C. Graves, S.D. Ebbesen, S.H. Jensen, S.B. Simonsen, M.B. Mogensen, *Nature Materials*, 14 (2015) 239-244.
- [Grew2010] K.N. Grew, Y.S. Chu, J. Yi, A.A. Peracchio, J.R. Izzo, Y. Hwu, F. De Carlo, W.K. Chiu, *J. Electrochem. Soc.* 157 (6) (2010) B783–B792.
- [Haering2005] C. Haering, A. Roosen, H. Schichl, "Degradation of the electrical conductivity in stabilised zirconia system: Part I: yttria-stabilised zirconia", *Solid State Ionics* 176(3)
- [Hagen2006] A. Hagen, R. Barfod, P. V. Hendriksen, Y.-L. Liu, S. Ramousse, "Degradation of anode supported SOFCs as a function of temperature and current load", *Journal of The Electrochemical Society* 153(6) (2006) A1165-A1171
- [Hanna2014] J. Hanna, W.Y. Lee, Y. Shi, A.F. Ghoniem, Fundamentals of electro- and thermochemistry in the anode of solid-oxide fuel cells with hydrocarbon and syngas fuels, *Progress in Energy and Combustion Science*, 40 (2014) 74-111.
- [Hashimoto2011] S. Hashimoto, Y. Fukuda, M. Kuhn, K. Sato, K. Yashiro, J. Mizusaki, *Solid State Ionics* 2011, 186, 37.
- [Hatae2015] T. Hatae, K. Sato, T. Somekawa, Y. Matsuzaki, S. Amaha, M. Yoshikawa, Y. Mugikura, K. Miyara, T. Oshima, S. Taniguchi, K. Sasaki, "Durability Assessment of SOFC Stacks with Several Types of Structures for Thermal Cycles during Their Lifetimes on Residential Use", *ECS Transactions* 68(1) (2015) 2209-2216
- [Hauch2006] A. Hauch, S. H. Jensen, S. Ramousse, M. Mogensen, "Performance and durability of solid oxide electrolysis cells", *Journal of The Electrochemical Society* 153(9) (2006) A1741-A1747
- [Hauch2008] A. Hauch, S. D. Ebbesen, S. H. Jensen, M. Mogensen, "Solid oxide electrolysis cells: microstructure and degradation of the Ni/yttria-stabilized zirconia electrode", *Journal of The Electrochemical Society* 155(11) (2008) B1184-B1193
- [Hilpert1996] K. Hilpert, D. Das, M. Miller, D. H. Peck, R. Weiss, "Chromium vapor species over solid oxide fuel cell interconnect materials and their potential for degradation processes", *Journal of The Electrochemical Society* 143(11) (1996) 3642-3647
- [Hino2004] R. Hino, K. Haga, H. Aita, K. Sekita, "38. R&D on hydrogen production by hightemperature electrolysis of steam", *Nuclear Engineering and Design* 233(1) (2004) 363-375
- [Holzer2011] L. Holzer, B. Münch, B. Iwanschitz, M. Cantoni, T. Graule, *J. Power Sources* 196 (2011) 7076–7089.
- [Holzer2013] L. Holzer, D. Wiedenmann, B. Münch, L. Keller, M. Prestat, Ph. Gasser, I. Robertson, B. Grob ty, *J. Mater. Sci.*, 48 (2013) 2934-2952.
- [Harris2015a] W. M. Harris, W. K. S. Chiu, *Journal of Power Sources* 282 (2015) 552-561.
- [Harris2015b] W. M. Harris, W. K. S. Chiu, *Journal of Power Sources* 282 (2015) 622-629.

- [Hjalmarsson2014] P. Hjalmarsson, X. Sun, Y.-L. Liu, M. Chen, J. Power Sources 2014, 262, 316.
- [Hsiao1997] Y.C. Hsiao, J. Robert Selman, Solid State Ionics 1997, 98, 33.
- [Hubert2016] M. Hubert, J. Laurencin, P. Cloetens, J.C. da Silva, F. Lefebvre-Joud, P. Bleuet, A. Nakajo, E. Siebert, Solid State Ionics, 294 (2016) 90-107.
- [Hubert2017a] M. Hubert, Durability of Solid Oxide Cells: an experimental and modelling investigation based on synchrotron X-ray nano-tomography characterization, Thesis of Grenoble University, 2017.
- [Hubert2017b] M. Hubert, A. Pacureanu, C. Guilloud, Y. Yang, J.C. da Silva, J. Laurencin, F. Lefebvre-Joud, P. Cloetens, Submitted in: Applied Physics Letters (2017).
- [Hubert2018a] M. Hubert, J. Laurencin, P. Cloetes, B. Morel, D. Montinaro, F. Lefebvre-Joud, J. Power Sources 2018, 397, 240.
- [Hubert2018b] M. Hubert, A. Pacureanu, C. Guilloud, Y. Yang, Julio C. da Silva, J. Laurencin, F. Lefebvre-Joud, Peter Cloetens, Efficient correction of wavefront inhomogeneities in X-ray holographic nanotomography by random sample displacement, Applied Physic Letters, 112 (2018) 203704 1-5.
- [Hwang2005] H.J. Hwang, J.-W. Moon, S. Lee, E.A. Lee, J. Power Sources 2005, 145, 243. (2005) 261-268
- [Irvine2016] John T.S. Irvine, D. Neagu, M.C. Verbraeken, C. Chatzichristodoulou, C. Graves, M.B. Mogensen, Nature Energy, 1 (2016) 1-13.
- [Janardhanan08] V.J. Janardhanan, V. Heuveline, O. Deutschmann, Three-phase boundary length in solid-oxide fuel cells: a mathematical model, J. Power Sources, 178 (2008) 368-372.
- [Jia2012] Z. Jiao, N. Shikazono, N. Kasagi, Quantitative Characterization of SOFC Nickel-YSZ Anode Microstructure Degradation Based on Focused-Ion-Beam 3D-Reconstruction Technique, J. Electrochem. Soc., 159 (3) (2012) B285-B291.
- [Jiang1999] S. P. Jiang, J. G. Love, J. P. Zhang, M. Hoang, Y. Ramprakash, A. E. Hughes, S. P. S. Badwal, "The electrochemical performance of LSM/zirconia–yttria interface as a function of a-site non-stoichiometry and cathodic current treatment", Solid State Ionics 121(1) (1999) 1-10.
- [Jiang2003] S. P. Jiang, "Sintering behavior of Ni/Y2O3-ZrO2cermet electrodes of solid oxide fuel cells", Journal of Materials Science 38(18) (2003) 3775-3782
- [Jiang2014] S. P. Jiang, X. Chen, "Chromium deposition and poisoning of cathodes of solid oxide fuel cells—a review", International Journal of Hydrogen Energy 39(1) (2014) 505-531
- [Jones1997] S.J. Jones, H.K.D.H. Bhadeshia, Kinetics of the simultaneous decomposition of austenite into several transformation products, Acta Mater. 45 (1997) 2911-2920.
- [Joos2012] J. Joos, M. Ender, T. Carraro, A. Weber, E. Ivers-Tiffée, "Representative volume element size for accurate solid oxide fuel cell cathode reconstructions from focused ion beam tomography data", Electrochimica Acta 82 (2012) 268-276
- [Kiburakaran2009] A. Kirubakaran, S. Jain, R. K. Nema, "A review on fuel cell technologies and power electronic interface", Renewable and Sustainable Energy Reviews 13(9) (2009) 2430-2440
- [Kim2017a] Y.T. Kim, Z. Jiao, N. Shikazono, Evaluation of La_{0.6}Sr_{0.4}Co_{0.2}Fe_{0.8}O₃-Gd_{0.1}Ce_{0.9}O_{1.95} composite cathode with three dimensional microstructure reconstruction, J. Power Sources, 342 (2017) 787-795.

- [Kim2017b] Y.T. Kim, N. Shikazono, Investigation of $\text{La}_{0.6}\text{Sr}_{0.4}\text{CoO}_{3-\delta}\text{-Gd}_{0.1}\text{Ce}_{0.9}\text{O}_{1.95}$ composite cathode with different volume ratios by three dimensional reconstruction, *Solid State Ionics*, 309 (2017) 77-85.
- [Kishimoto2012] H. Kishimoto, K. Yashiro, T. Shimonosono, M. E. Brito, K. Yamaji, T. Horita, H. Yokokawa, J. Mizusaki, "In situ analysis on the electrical conductivity degradation of NiO doped yttria stabilized zirconia electrolyte by micro-Raman spectroscopy", *Electrochimica Acta* 82 (2012) 263-267
- [Kenney09] B. Kenney, M. Valdmanis, C. Baker, J.G. Pharoah, K. Karan, *J. Power Sources*, 189 (2009) 1051-1059.
- [Kong2007] J. Kong, K. Sun, D. Zhou, N. Zhang, J. Mu, J. Qiao, *J. Power Sources*, 166 (2007) 337-342.
- [Konysheva2006] E. Konysheva, H. Penkalla, E. Wessel, J. Mertens, U. Seeling, L. Singheiser, K. Hilpert, "Chromium poisoning of perovskite cathodes by the ODS alloy $\text{Cr}_5\text{Fe}_1\text{Y}_2\text{O}_3$ and the high chromium ferritic steel Crofer22APU", *Journal of The Electrochemical Society* 153(4) (2006) A765-A773
- [Laguna2012] M. A. Laguna-Bercero, "Recent advances in high temperature electrolysis using solid oxide fuel cells: A review", *Journal of Power Sources* 203 (2012) 4-16
- [Lane2000] J.A. Lane, J.A. Kilner, *Solid State Ionics* 2000, 136–137, 997.
- [Lang2011] A. Lang, J. Potthoff, *Monte Carlo Methods Appl.*, 17 (2011) 195-214.
- [Lantuéjoul2002] C. Lantuéjoul, *Geostatistical Simulation, Model and Algorithms*, Springer, 2002.
- [Lanzini2009] A. Lanzini, P. Leone, P. Asinari, *J. Power Sources*, 194 (2009) 408–422.
- [Laurencin2008] J. Laurencin, F. Lefebvre-Joud, G. Delette, "Impact of cell design and operating conditions on the performances of SOFC fuelled with methane", *Journal of Power Sources* 177(2) (2008) 355-368
- [Laurencin2012] J. Laurencin, R. Quey, G. Delette, H. Suhonen, P. Cloetens, P. Bleuet, *J. Power Sources*, 198 (2012) 182-189.
- [Laurencin2015] J. Laurencin, M. Hubert, K. Couturier, T. Le Bihan, P. Cloetens, F. Lefebvre-Joud, E. Siebert, *Electrochimica Acta*, 174 (2015) 1299-1316.
- [Laurencin2017] J. Laurencin, M. Hubert, D. Ferreira Sanchez, S. Pylypko, M. Morales, A. Morata, B. Morel, D. Montinaro, F. Lefebvre-Joud, E. Siebert, *Electrochim. Acta* 2017, 241, 459.
- [Lay-Grindler2013] E. Lay-Grindler, J. Laurencin, G. Delette, J. Aicart, M. Petitjean, L. Dessemond, *Int. J. of Hydrogen Energy*, 38 (2013) 6917-6929.
- [Lay-Grindler2013b] E. Lay-Grindler, J. Laurencin, J. Villanova, I. Kieffer, F. Usseglio-Viretta, T. Le Bihan, P. Bleuet, A. Mansuy, G. Delette, *ECS Trans.* 57(1) (2013) 3177-3187.
- [Lay-Grindler2014] E. Lay-Grindler, J. Laurencin, J. Villanova, P. Cloetens, P. Bleuet, A. Mansuy, J. Mouglin, G. Delette, Degradation study by 3D reconstruction of a nickel-yttria stabilized zirconia cathode after high temperature steam electrolysis operation, *Journal of Power Sources* 269 (2014) 927-936.
- [Leng2008] Y. Leng, S.H. Chan, Q. Liu, *Int. J. Hydrogen Energy* 2008, 33, 3808.
- [Liang1998] Z.R. Liang, C.P. Fernandes, F.S. Magnani, P.C. Philippi, *J. Petrol. Sci. Eng.* 21 (1998) 273-283.

- [Linderoth2001] S. Linderoth, N. Bonanos, K. V. Jensen, J. B. Bilde-Sørensen, "Effect of NiO-to-Ni Transformation on Conductivity and Structure of Yttria-Stabilized ZrO₂", *Journal of the American Ceramic Society* 84(11) (2001) 2652-2656
- [Liu2011] X. Liu, C. Martin, G. Delette, J. Laurencin, D. Bouvard, T. Delahaye, J. Power Sources, 196 (2011) 2046-2054.
- [Liu2012] Y. L. Liu, K. Thydén, M. Chen, A. Hagen, "Microstructure degradation of LSMYSZ cathode in SOFCs operated at various conditions", *Solid State Ionics* 206 (2012) 97-103
- [Leng2008] Y. Leng, S. Hwa Chan, Q. Liu, Development of LSCF-GDC composite cathodes for low-temperature solid oxide fuel cells with thin film GDC electrolyte, *Int. J. Hydrogen Energy*, 33 (2008) 3808-3818.
- [Mai2006] A. Mai, V. AC Haanappel, F. Tietz, D. Stöver, "Ferrite-based perovskites as cathode materials for anode-supported solid oxide fuel cells: Part II. Influence of the CGO interlayer", *Solid State Ionics* 177(19) (2006) 2103-2107
- [Marinha2011] D. Marinha, L. Dessemond, J. Scott Cronin, James R. Wilson, E. Djurado, *Chem. Mater.*, 23 (24) (2011) 5340–5348.
- [Matsui2012] T. Matsui, R. Kishida, H. Muroyama, K. Eguchi, "Comparative Study on Performance Stability of Ni–Oxide Cermet Anodes under Humidified Atmospheres in Solid Oxide Fuel Cells", *Journal of The Electrochemical Society* 159(8) (2012) F456-F460
- [Matsuzaki2001] Y. Matsuzaki, I. Yasuda, "Dependence of SOFC cathode degradation by chromium-containing alloy on compositions of electrodes and electrolytes", *Journal of The Electrochemical Society* 148(2) (2001) A126-A131
- [Mekhilef2012] S. Mekhilef, R. Saidur, A. Safari, "Comparative study of different fuel cell technologies", *Renewable and Sustainable Energy Reviews* 16(1) (2012) 981-989
- [Menzler2010] N.H. Menzler, F. Tietz, S. Uhlenbruck, H.P. Buchkremer, D. Stöver, *J. Mater. Sci.*, 45 (2010) 3109-3135.
- [Metcalf2010] C. Metcalfe, O. Kesler, T. Rivard, F. Gitzhofer, N. Abatzoglou, *J. Electrochem. Soc.*, 157(9) (2010) B1326-B1335.
- [Minh1993] N. Q. Minh, "Ceramic fuel cells", *Journal of the American Ceramic Society* 76(3) (1993) 563-588
- [Moçoteguy2013] P. Moçoteguy, A. Brisse, A review and comprehensive analysis of degradation mechanisms of solid oxide electrolysis cells, *Inter. J. Hydrogen Energy*, 38 (2013) 15887-15902.
- [Monaco2018] F. Monaco, V. Tezyk, E. Siebert, S. Pylypko, B. Morel, J. Vulliet, T. Le Bihan, F. Lefebvre-Joud, J. Laurencin, Experimental validation of a La_{0.6}Sr_{0.4}Co_{0.2}Fe_{0.8}O_{3-δ} electrode model operated in electrolysis mode: Understanding the reaction pathway under anodic polarization, *Solid State Ionics*, 319 (2018) 234-246.
- [Morel2005] B. Morel, J. Laurencin, Y. Bultel, F. Lefebvre-Joud, "Anode-supported sofc model centered on the direct internal reforming", *Journal of The Electrochemical Society* 152(7) (2005) A1382-A1389
- [Mortensen2014] J.E. Mortensen, M. Søgaard, T. Jacobsen, *J. Electrochem. Soc.* 2014, 161, 161.
- [Moussaoui2017] H. Moussaoui, J. Debayle, Y. Gavet, J. Laurencin, *Proc. SPIE – Int. Soc. Optical Eng.*, Vol. 10338 (2017) doi:10.1117/12.2264376.

- [Moussaoui2018] H. Moussaoui, J. Laurencin, Y. Gavet, G. Delette, M. Hubert, P. Cloetens, T. Le Bihan, J. Debayle, Stochastic Geometrical Modeling of Solid Oxide Cells Electrodes Validated on 3D Reconstructions, *Computational Materials Science*, 143 (2018) 262-276.
- [Moussaoui2019] H. Moussaoui, R.K. Sharma, J. Debayle, Y. Gavet, G. Delette, J. Laurencin, *Journal of Power Sources*, Volume 412, 1 February 2019, Pages 736-748.
- [Murray2002] P.E. Murray, M.J. Server, S.A. Barnett, *Solid State Ionics* 2002, 148, 27.
- [Naebe2016] M. Naebe, K. Shirvanimoghaddam, *Applied Materials Today*, 5 (2016) 223-245.
- [Nelson2012] G. J. Nelson, K. N. Grew, J. R. Izzo, J. J. Lombardo, W. M. Harris, A. Faes, A. Hessler-Wyser, J. Van herle, S. Wang, Y. S. Chu, A. V. Virkar, W. K. Chiu, "three-dimensional microstructural changes in the Ni-YSZ solid oxide fuel cell anode during operation", *Acta Materialia* 60(8) (2012) 3491-3500
- [Neumann2016] M. Neumann, J. Staněk, O.M. Pecho, L. Holzer, V. Beneš, V. Schmidt, *Comput. Mater. Sci.*, 118 (2016) 353-364.
- [Ni2008] M. Ni, M. K. H. Leung, D. Y. C. Leung, "Technological development of hydrogen production by solid oxide electrolyzer cell (SOEC)", *International Journal of Hydrogen energy* 33(9) (2008) 2337-2354
- [Nie2015] L. Nie, Q. Sun, Z. Liu, M. Liu, *Inter. J. Hydrogen Energy*, 40 (2015) 16503-16508.
- [Nielsen2011] J. Nielsen, T. Jacobsen, M. Wandel, *Electrochimica Acta* 2011, 56, 7963.
- [Nishida2011] Y. Nishida, S. Itoh, *Electrochimica Acta*, 56 (2011), 2792-2800.
- [O'Brien2008] J. E. O'Brien, M. G. McKellar, C. M. Stoots, J. S. Herring, G. L. Hawkes, "Parametric study of large-scale production of syngas via high-temperature co-electrolysis", *International Journal of Hydrogen Energy* 34(9) (2009) 4216-4226
- [Ormerod2003] R. Mark Ormerod, *Chemical Society Reviews*, 32 (2003), 17-28.
- [Ostergard1995] M. Ostergard, C. Clausen, C. Bagger, M. Mogensen, Manganite-zirconia composite cathodes for SOFC: influence of structure and composition, *Electrochimica Acta*, 40 (12) (1995) 1971-1981.
- [Orui2008] H. Orui, K. Nozawa, K. Watanabe, S. Sugita, R. Chiba, T. Komatsu, H. Arai, M. Arakawa, "Development of practical size anode-supported solid oxide fuel cells with multilayer anode structures", *Journal of The Electrochemical Society* 155(11) (2008) B1110-B1116
- [Pihlatie2011] M. H. Pihlatie, A. Kaiser, M. Mogensen, M. Chen, "Electrical conductivity of Ni-YSZ composites: Degradation due to Ni particle growth", *Solid State Ionics* 189(1) (2011) 82-90
- [Prakash2014] B.S. Prakash, S.S. Kumar, S.T. Aruna, *Renew. Sustain. Ener. Rev.*, 36 (2014) 149-179.
- [Qiang2007] F. Qiang, K. Sun, N. Zhang, X. Zhu, S. Le, D. Zhou, *J. Power Sources* 2007, 168, 338.
- [Rhazaoui2011] K. Rhazaoui, Q. Cai, P. Shearing, C.S. Adjiman, N.P. Brandon, *ECS Transactions*, 35(1) (2011) 1097-1105.
- [Rutman2008] J. Rutman, I. Riess, *Solid State Ionics* 2008, 179, 913.
- [Sanyal2010] J. Sanyal, G.M. Goldin, H. Zhu, R.J. Kee, *J. Power Sources*, 195 (2010) 6671-6679.
- [Schefold2013] J. Schefold, A. Brisse, "Steam electrolysis in reversibly operated SOFC: Longterm cell testing beyond 1000 h", *ECS Transactions* 53(9) (2013) 53-61

- [Schneider2007] L.C.R. Schneider, C.L. Martin, Y. Bultel, L. Dessemond, D. Bouvard, *Electrochimica Acta*, 52 (2007) 3190-3198.
- [Schuler2012] J. A. Schuler, Z. Wuillemin, A. Hessler-Wyser, C. Comminges, N. Yousfi Steiner, J. Van Herle, "Cr-poisoning in (La, Sr)(Co, Fe) O₃ cathodes after 10,000 h SOFC stack testing", *Journal of Power Sources* 211 (2012) 177-183
- [Serra1988] J. Serra, *Image analysis and mathematical morphology: Theoretical advances*, Academic Press, Cornell University, 1988.
- [Sharma2016] R.K. Sharma, M. Burriel, L. Dessemond, V. Martin, J.-M. Bassat, E. Djurado, *J. Power Sources*, 316 (2016) 17-28.
- [Serra1988] J. Serra, *Image analysis and mathematical morphology: Theoretical advances*, Academic Press, Cornell University, 1988.
- [Shearing2012] P.R. Shearing, R.S. Bradley, J. Gelb, F. Tariq, P.J. Withers, N.P. Brandon, *Solid State Ionics* 216 (2012) 69–72.
- [Shimonosono2012] T. Shimonosono, H. Kishimoto, M. E. Brito, K. Yamaji, T. Horita, H. Yokokawa, "Phase transformation related electrical conductivity degradation of NiO doped YSZ", *Solid State Ionics* 225 (2012) 69-72
- [Singhal2003] S.C. Singhal and K. Kendall, "High Temperature Solid Oxide Fuel cells, Fundamental, Design and Applications", Elsevier, 2003.
- [Simner2005] S. P. Simner, M. D. Anderson, G-G. Xia, Z. Yang, Larry R. Pederson, J. W. Stevenson, "SOFC performance with Fe-Cr-Mn alloy interconnect", *Journal of The Electrochemical Society* 152(4) (2005) A740-A745
- [Simner2006] S. P. Simner, M. D. Anderson, M. H. Engelhard, J. W. Stevenson, "Degradation Mechanisms of La–Sr–Co–Fe–O₃ SOFC Cathodes", *Electrochemical and Solid-State Letters* 9(10) (2006) A478-A481
- [Simwonis2000] D. Simwonis, F. Tietz, D. Stöver, "Nickel coarsening in annealed Ni/8YSZ anode substrates for solid oxide fuel cells", *Solid State Ionics* 132(3) (2000) 241-251
- [Skaft2016] T.L. Skaft2, J. Hjelm, P. Blennow, C.R. Graves, Proc. 12th European SOFC & SOE Forum, (European Fuel Cell Forum), Lucerne, Switzerland 2016, pp 8.
- [Smith2009] J.R. Smith, A. Chen, D. Gostovic, D. Hickey, D. Kundinger, K.L. Duncan, R.T. DeHoff, K.S. Jones, E.D. Wachsman, *Solid State Ionics*, 180 (2009) 90–98.
- [Stenzel2016] O. Stenzel, O. Pecho, L. Holzer, M. Neumann, V. Schmidt, *AIChE Journal*, 62(5) (2016) 1834-1843.
- [Stenzel2017] O. Stenzel, O. Pecho, L. Holzer, M. Neumann, V. Schmidt, Big data for microstructure-property relationships: a case study of predicting effective conductivities, *AIChE Journal*, 63 (2017) 4224-4232.
- [Sunde1996] S. Sunde, Monte Carlo simulations of polarization resistance of composite electrodes for solid oxide fuel cells, *J. Electrochem. Soc.*, 143 (1996) 1930-1939.
- [Sunde2000] S. Sunde, Simulations of composite electrodes in fuel cells, *Journal of Electroceramics*, 5 (2000) 153-182.
- [Suzue2008] Y. Suzue, N. Shikazono, N. Kasagi, *J. Power Sources*, 184 (2008) 52-59.
- [Suzuki2009] Toshio Suzuki, Z. Hasan, Y. Funahashi, T. Yamaguchi, Y. Fujishiro, M. Awano, Impact of Anode Microstructure on Solid Oxide Fuel Cells, *Science*, 325 (2009) 852-855.

- [Svensson1998] A.M. Svensson, S. Sunde, K. Nişancıoğlu, J. Electrochem. Soc.1998, 145, 1390.
- [Tanaka2012] S. Tanaka, W.S. Oliveira, A. Brandão, J.C.C. Abrantes, J.R. Frade, *Electrochim. Acta* 2012, 85, 116.
- [Tanasini2009] P. Tanasini, M. Cannarozzo, P. Costamagna, A. Faes, J. Van Herle, A. Hessler-Wyser, C. Comninellis, "Experimental and theoretical investigation of degradation mechanisms by particle coarsening in SOFC electrodes", *Fuel Cells* 9(5) (2009) 740-752
- [Tietz2002] F. Tietz, H-P. Buchkremer, D. Stöver, "Components manufacturing for solid oxide fuel cells", *Solid State Ionics* 152 (2002) 373-381
- [Tietz2006] F. Tietz, V. A. C. Haanappel, A. Mai, J. Mertens, D. Stöver, "Performance of LSCF cathodes in cell tests", *Journal of Power Sources* 156(1) (2006) 20-22
- [Tu2004] H. Tu, U. Stimming, "Advances, aging mechanisms and lifetime in solid-oxide fuel cells", *Journal of Power Sources* 127(1) (2004) 284-293
- [Tucker2006] M. C. Tucker, H. Kurokawa, C. P. Jacobson, L. C. De Jonghe, S. J. Visco, "A fundamental study of chromium deposition on solid oxide fuel cell cathode materials", *Journal of Power Sources* 160(1) (2006) 130-138
- [Villanova13] J. Villanova, J. Laurencin, P. Cloetens, P. Bleuet, G. Delette, H. Suhonen, F. Usseglio-Viretta, *J. Power Sources* 243 (2013) 841–849.
- [Uhlenbruck2009] S. Uhlenbruck, T. Moskalewicz, N. Jordan, H-J. Penkalla, H. P. Buchkremer, "Element interdiffusion at electrolyte–cathode interfaces in ceramic high temperature fuel cells", *Solid State Ionics* 180(4) (2009) 418-423
- [Usseglio-Viretta2014] F. Usseglio-Viretta, J. Laurencin, G. Delette, J. Villanova, P. Cloetens, *J. Power Sources*, 256 (2014) 394-403.
- [Usseglio-Viretta2015] F. Usseglio-Viretta, Ph.D. Thesis, Université Grenoble Alpes, Grenoble, France, 2015.
- [Vernoux2000] P. Vernoux, M. Guillodo, J. Fouletier, A. Hammou, "Alternative anode material for gradual methane reforming in solid oxide fuel cells", *Solid State Ionics* 135(1) (2000) 425-431
- [Virkar2000] A.V. Virkar, J. Chen, C.W. Tanner, J.-W. Kim, *Solid State Ionics*, 131 (2000) 189-198.
- [Vivet2011a] N. Vivet, S. Chupin, E. Estrade, T. Piquero, P.L. Pommier, D. Rochais, E. Bruneton, *J. Power Sources* 196 (2011) 7541–7549.
- [Vivet2011b] N. Vivet, S. Chupin, E. Estrade, A. Richard, S. Bonnamy, D. Rochais, E. Bruneton, *J. Power Sources* 196 (2011) 9989–9997.
- [Virkar2000] A.V. Virkar, J. Chen, C.W. Tanner, J.-W. Kim, the role of electrode microstructure on activation and concentration polarizations in solid oxide fuel cells, *Solid State Ionics*, 131 (2000) 189-98.
- [Wei2015] B. Wei, K. Chen, C. C. Wang, Z. Lü, S. P. Jiang, "Cr deposition on porous La 0.6 Sr 0.4 Co 0.2 Fe 0.8 O 3– δ electrodes of solid oxide cells under open circuit condition", *Solid State Ionics* 281 (2015) 29-37
- [Wilson2001] R.J. Wilson, D.J. Nott, *Image Anal. Stereol.*, 20 (2001) 71-78.
- [Wilson2006] J.R. Wislon, W. Kobsiriphat, R. Mendoza, H.Y. Chen, J.M. Hiller, D.J. Miller, K. Thorton, P.W. Voorhees, S.B. Adler, S.A. Barnett, *Nat. Mater.* 5 (2006) 541–544.

- [Wilson2010] J.R. Wilson, J.S. Cronin, A.T. Duong, S. Rukes, H.-Y. Chen, K. Thornton, D.R. Mumm, S.A. Barnett, *J. Power Sources* 195 (2010) 1829–1840.
- [Wang2005] W.G. Wang, M. Mogensen, *Solid State Ionics* 2005, 176, 457.
- [Wilson2011] J.R. Wilson, J.S. Cronin, S.A. Barnett, *Scripta Materialia*, 65 (2011) 67-72.
- [Yamamoto2000] O. Yamamoto, "Solid oxide fuel cells: fundamental aspects and prospects", *Electrochimica Acta* 45(15) (2000) 2423-2435
- [Yan2017] Z. Yan, S. Hara, Y. Kim, N. Shikazono, *Int. J. Hydrogen Energy* 2017, 42, 30166.
- [Yashiro2011] K. Yashiro, I. Nakano, M. Kuhn, S. Hashimoto, K. Sato, J. Mizusaki, *ECS Trans.*, 2011, 35, 1899.
- [Yokokawa1992] H. Yokokawa, N. Sakai, T. Kawada, M. Dokiya, *Solid State Ionics* 1992, 52, 43.
- [Yokokawa2008] H. Yokokawa, H. Tu, B. Iwanschitz, A. Mai, *J. Power Sources* 2008, 182, 400.
- [Yurkiv2014] V. Yurkiv, R. Costa, Z. Ilhan, A. Ansar, W.G. Bessler, *J. Electrochem. Soc.* 2014, 161, 480.
- [Zhang2010a] S. Zhang, Quantitative characterization and modelling of the microstructure of solid oxide fuel cell composite electrodes, Ph.D. dissertation, School of Materials Science and Engineering, Georgia Institute of Technology, Atlanta (2010).
- [Zhang2010b] S. Zhang, A.M. Gokhale, Computer simulations of topological connectivity of the triple phase boundaries in solid oxide fuel cell composite cathodes, *J. Power Sources*, 219 (2012) 172-179.
- [Zhang2011] Y. Zhang, Y. Wang, Y. Wang, F. Chen, C. Xia, *J. Power Sources*, 196 (2011) 1983-1991.
- [Zheng2016] K. Zheng, M. Ni, *Sci. Bull.*, 61(1) (2016) 78–85.
- [Zhu2003] W. Z. Zhu, S. C. Deevi, "A review on the status of anode materials for solid oxide fuel cells", *Materials Science and Engineering A* 362(1) (2003) 228-239

Microstructural optimization of Solid Oxide Cells: a coupled stochastic geometrical and electrochemical modeling approach applied to LSCF-CGO electrode

This work aims at better understanding the impact of the electrode microstructure on the performances of Solid Oxide Cells (SOCs). The method has been employed for a numerical optimization of the LSCF-CGO composite used as O₂ electrode. In this frame, an integrated approach coupling 3D stochastic geometrical and electrochemical models has been adopted. A plurigaussian random field model and an original sphere packing algorithm have been developed to simulate the SOCs electrode microstructure. The geometrical models have been validated on different electrode reconstructions obtained by synchrotron X-ray nano-holotomography or focused ion-beam tomography. Afterwards, semi-analytical microstructural correlations have been proposed and validated on a large dataset of representative synthetic microstructures. These equations allow establishing the links between ‘key’ microstructural properties controlling the performances (Triple Phase Boundary length density and specific surface areas) to the ‘basic’ geometric attributes of the electrode (composition, porosity and particle size distribution). The microstructural parameters have been implemented in an existing electrochemical model for the LSCF-CGO electrode. This model has been validated thanks to electrochemical characterizations of a reference symmetrical cell. The geometrical and electrochemical models have been used to investigate the impact of the electrode composition, the porosity and the particle size on the cell electrochemical performance, and thus providing useful recommendations to cell manufacturers.

Optimisation microstructurale des cellules à oxydes solides : approche numérique couplant modélisation géométrique et électrochimique appliquée à l'électrode LSCF-CGO

Ce travail a porté sur la compréhension du lien entre la microstructure des électrodes et la performance des cellules à oxydes solides (SOC). La méthodologie développée a été mis en œuvre pour optimiser l'électrode à oxygène constituée d'un composite LSCF-CGO. Une approche couplant une modélisation géométrique et électrochimique des électrodes a été proposée. Un modèle basé sur les champs aléatoires gaussiens tronqués et un second basé sur des empilements de sphères ont été développés et adaptés pour simuler les microstructures d'électrodes. Ces deux méthodes ont été validées sur différentes électrodes reconstruites par nano-holotomographie des rayons X au synchrotron ou par tomographie avec un microscope électronique à balayage couplé à un faisceau d'ions focalisé. Ensuite, des corrélations semi-analytiques ont été proposées et validées grâce à une large gamme de microstructures synthétiques. Ces relations permettent de relier les paramètres morphologiques ‘primaires’ de la microstructure (composition, porosité et diamètres des phases) aux propriétés qui pilotent les réactions électrochimiques (densité de points triples, surfaces spécifiques). Les paramètres microstructuraux ont été implémentés dans un modèle électrochimique du composite LSCF-CGO. Ce modèle a été validé grâce à des caractérisations électrochimiques conduites sur une cellule symétrique de référence. L'approche intégrée a été finalement utilisée pour étudier l'effet de la composition, de la porosité ou encore de la taille des particules sur les performances de l'électrode. Ces résultats ont permis d'identifier des microstructures optimisées.